Theoretical and Computational Studies of Active Topological Graphene Metasurfaces

Yupei Wang

A dissertation submitted in partial fulfillment

of the requirements for the degree of

Doctor of Philosophy

of

University College London.

Electronic and Electrical Engineering

University College London

January 5, 2023

I, Yupei Wang, confirm that the work presented in this thesis is my own. Where information has been derived from other sources, I confirm that this has been indicated in the work.

Abstract

In this thesis, we present theoretical and computational studies of topological valley plasmon transport on graphene metasurfaces, which were further applied to active optically and chemically controllable nanodevices. The presented results and designs may not only provide deeper insights into topological metasurface with novel symmetry-breaking, but also lead to active photonic nanodevices implemented in robust topological systems. Three configurations of graphene metasurfaces created with the required symmetry to possess valley topological plasmonic modes have been developed: i) a single graphene nanohole metasurface, ii) bilayer graphene metasurfaces, and iii) layered graphene metasurfaces. In all cases, the underlying graphene metasurfaces consist of a hexagonal periodic distribution of circular or triangular air-holes. By introducing additional nanoholes in a single graphene metasurface to break its spatial-inversion symmetry, or by horizontally shifting layers of bilayer graphene metasurfaces with a novel mirror symmetry breaking, or by simply rotating triangular holes in multilayer graphene metasurfaces to break their spatial-inversion or mirror symmetries, the symmetry-protected Dirac cones associated to the three configurations are gapped out. As a result, topological valley interface modes emerge inside the nontrivial bandgap, and the light propagation of the corresponding topological modes along the domain-wall interface shows unidirectional features. Taking advantage of the strong Kerr effect and chemically-tunable optical property of graphene, an active optical switch and an efficient approach to transfer power to topological modes are designed by optically tuning the frequency dispersion of graphene metasurfaces via the Kerr effect, and a molecular gas sensor using the fact that Fermi energy of graphene varies upon chemical doping are investigated.

Acknowledgements

First and foremost, I would like to express my sincere gratitude to my supervisor, Prof. Nicolae C. Panoiu, for the continuous support and guidance throughout my PhD study. It is he who led me into the research field of topological photonics and gave me the opportunity to work on this. His scientific insight, profound knowledge, impressive diligence, and infinite patience always motivate and inspire me to keep going, especially when I faced challenges during my research. His support has always been greatly appreciated for the rest of my professional career.

Second, I would like to thank my secondary supervisor, Prof. Paul Warburton, for his kind inspiration and brilliant comments during my transfer viva, together with Prof. Oleg Mitrofanov. Their questions and suggestions indeed broaden my horizons and make me from different perspectives.

My sincere thanks also go to my group colleagues (Dr. Jian Wei You, Dr. Zhihao Lan, Dr. Wei. E. I. Sha, Dr. Ivan Sekulic, Victor Manuel Fernandez Laguna, Jitong Wang, Zhaojian Zhang, and Gabriel Mihai Dumitrache) as well as the visiting students (Jikui Zhang and Fengxia Li) for their theoretical discussions and computational help during my PhD research. My life is filled with fun and excitement even during pandemic years because of their encouragement.

Finally, I would like to thank my parents and family members for their warmest concern and unwavering support of my study and life. In particular, I would like to thank my boyfriend, Chengqi Ma, for his love and companionship. For my grandma, I would like to say you will always be remembered and I love you.

It is with great gratitude that I thank the China Scholarship Council and the UCL Dean's Prize Scholarship for their financial support for my PhD study.

Impact Statement

Inspired by the unique and novel properties of topologically protected modes, I theoretically and computationally studied the topological valley plasmon transport on graphene nanohole metasurfaces in this thesis, which has been further applied to active optically and chemically controllable nanodevices. My work in the thesis not only offers a route toward the observation of valley-chirality-locked topological modes in the graphene-based topological photonic systems, but also opens up new ways of developing active topological photonic devices with new or improved functionality and robust integrated plasmonic devices for molecular sensing.

The topological valley graphene metasurfaces I studied are playing an important role in the development of the time-reversal invariant topological system with inversion symmetry breaking in the absence of an external magnetic field. The precise shape, geometry, size, orientation, and arrangement of the proposed graphene metasurfaces give them remarkable properties capable of manipulating electromagnetic waves: by enhancing, scattering, or blocking waves to achieve advantages beyond the optical response of conventional materials. My research provides three different ways to design and characterization of topological photonic waveguides with unidirectional light propagation without back-scattering, which will benefit national and international researchers in the field and related disciplines, especially nanophotonics, integrated photonic devices, and molecular sensing.

The absence of backscattering modes opens new avenues for the realization of topological photonics in practical applications. In particular, topologically protected characteristics of a nontrivial waveguide can enable dissipationless light propagation, leading to efficient photonic devices that are beneficial for optical

communication. This property is in contrast to applications implemented on trivial photonic waveguides, based on the fact that energy losses in such trivial systems are strongly influenced by the defects and disorders inside the photonic device. Furthermore, topologically protected transport in electronics requires low temperatures, whereas topologically protected transport in photonics operates at room temperature and can be much easier to be realized on practical platforms.

Potential applications for my proposed topological graphene plasmonic waveguide are diverse and can operate in a broad frequency range from mid-infrared to microwave regime, which includes topological insulator laser, nanocavities with a high-quality factor, and photonic delay line. Moreover, the proposed layered graphene-based topological valley systems with novel mirror symmetry breaking, could support two kinds of topological interface modes with layer-polarized and valley-chirality-locked properties inside the nontrivial bandgap. This remarkable property has great potential in the development of topological layer convertors and topological layer-selected delay lines.

Apart from the linear response of topological mode in graphene metasurfaces, key functionalities of active photonic devices, such as tunability, optical frequency generation, and sensing, can most effectively be implemented by employing the nonlinear optical response of the topological waveguides. The nonlinear optical response inside a topological waveguide could unlock active tunable functionalities. First, the study about the Kerr effect of the active ultra-fast optical switch could open up new routes towards active photonic nanodevices whose underlying functionality stems from their topological characteristics. Second, the proposed efficient nonlinear coupler between the topological interface and trivial edge modes provides an alternative way to transfer a large amount of light to the topological mode as a novel kind of excitation method in topological photonics.

List of Journal Publications

1. Yupei Wang, Jian Wei You, Zhihao Lan and Nicolae C. Panoiu, "Topological valley plasmon transport in bilayer graphene metasurfaces for sensing applications," (editor's pick) *Opt. Lett.* **45**, 3151-3154 (2020).

2. Yupei Wang and Nicolae C. Panoiu, "Optically controllable coupling between edge and topological interface modes of graphene metasurfaces," *J. Opt.* **24**, 104002 (2022).

3. Murat Can Sarihan, Alperen Govdeli, Zhihao Lan, Yildirim Batuhan Yilmaz, Mertcan Erdil, Mehmet Sirin Aras, Cenk Yanik, Yupei Wang, Nicolae C. Panoiu, Chee Wei Wong, and Serdar Kocaman, "Isotropic gap formation, localization, and waveguiding in mesoscale Yukawa-potential amorphous structures," *Nat. Commun. Phys.* (in review)

4. Yupei Wang, Jian Wei You and Nicolae C. Panoiu, "All-optical control of topological valley transport in graphene metasurfaces," *Opt. Express* (in review)

5. Yupei Wang, Zhihao Lan and Nicolae C. Panoiu, "Layer pseudospin of plasmonic interfacial supermodes of layered graphene metasurfaces possessing distinct valley-Hall phases," *Adv. Opt. Mater.* (in preparation)

List of Conference Publications

1. Yupei Wang, Jian Wei You, Zhihao Lan, Nicolae C. Panoiu, "Topological valley plasmon transport in graphene bi-layer metasurfaces: applications to sensing nanodevices," *Proc. SPIE* **11344**, Metamaterials XII, 113441E (2020).

2. Jian Wei You, Yupei Wang and Nicolae C. Panoiu, "Valley-Hall Topological Transport in Graphene Plasmonic Crystal Waveguides," *14th International Congress on Artificial Materials for Novel Wave Phenomena (Metamaterials) 2020*, 28 September-3 October 2020, New York, USA.

3. Yupei Wang, Jian Wei You and Nicolae C. Panoiu, "All-optically Control of Light Propagation in Valley-Hall Topological Waveguides of Graphene Metasurfaces," *15th International Congress on Artificial Materials for Novel Wave Phenomena (Metamaterials) 2021*, 20-24 September 2021, New York, USA.

4. Yupei Wang, Jian Wei You, Zhihao Lan and Nicolae C. Panoiu, "Optically and Chemically Controllable Light Flow in Topological Plasmonic Waveguides Based on Graphene Metasurfaces," *Photonics and Electromagnetics Research Symposium (PIERS) 2022*, 25-29 April 2022, Hangzhou, China.

5. Yupei Wang and Nicolae C. Panoiu, "Optically controllable coupling between edge and topological waveguide modes of certain graphene metasurfaces," *Proc. SPIE* **12130**, Metamaterials XIII, 1213004 (2022).

List of notations and acronyms

1D, 2D, 3D	one-dimensional, two-dimensional, three-dimensional
A_k^n	Berry connection of nth band
C	Chern number
C_L	layer Chern number
CMT	coupled-mode theory
C_V	valley Chern number
ε_0	electric permittivity of vacuum ($8.854 \times 10^{-12} F \cdot m^{-1}$)
ε	electric permittivity
ε_r	relative electric permittivity
EBL	electron-beam lithography
FBZ	first Brillouin zone
FEM	finite-element method
FWM	four-wave mixing
GV	group velocity
HOMO	highest occupied molecular orbital
LCP	left-circularly-polarized
LUMO	lowest unoccupied molecular orbital
μ_0	magnetic permeability of vacuum ($1.257 \times 10^{-6} H \cdot m^{-1}$)
μ	magnetic permeability
μ_r	relative magnetic permeability
Ω	Berry curvature
PhCs	photonic crystals
POMO	partially occupied molecular orbital
QHE	quantum-Hall effect
QHI	quantum-Hall insulator
QSHE	quantum spin-Hall effect
QVHE	quantum valley-Hall effect
RCP	right-circularly-polarized
SL	slow light

SHG	second-harmonic generation
SPPs	surface plasmon polaritons
STM	scanning tunneling microscope
TE	transverse electrical
TM	transverse magnetic
TH	third-harmonic
THG	third-harmonic generation
TPA	two photon absorption
UV	ultraviolet
ZGV	zero group velocity

Contents

List of Figures

Chapter 1

Introduction

The recent realization of photonic topological insulators has led to the discovery of entirely new optical states and revolutionary applications. The meaning of topology in topological photonics arises from the topological invariant, Chern number in integer quantum Hall effect (QHE) of condensed matter [1]. Topology is a branch of mathematics that studies the unchanged properties of geometric figures after continuous changes in shape, which only considers the positional relationship between objects without considering their shapes and sizes [2]. For example, in Fig. 1.1(a), without cutting or gluing but only with stretching and twisting, an object in the shape of a ring can be deformed into the shape of a mug with a hole in the handle, but cannot be deformed into a shape without holes. Although the shapes of ring and mug are different, they are topologically equivalent. In topology, this important topological property is expressed by the defined genus.

Based on the concepts from topology, topological insulators were explored and quantitatively defined in solid state physics, which are electronic materials that have a bulk bandgap like ordinary insulators but contain protected conducting states localized at their edges or surfaces [3, 4, 5]. Electrons traveling along the edges or surfaces of topological insulators are strongly resistant to any dissipation or backscattering, just as holes in deforming rings are resistant to any continuous changes in shape. Hence, this unchanging feature of an electron traveling in the topological insulator is quantitatively explained by Chern number (genus) [4]. The first example of a topological insulator with QHE was two-dimensional (2D) electrons in a

(a)

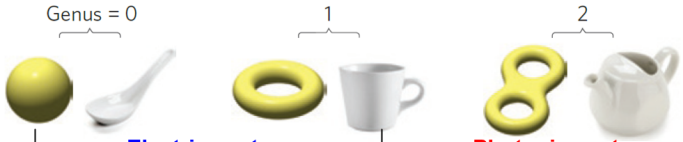

(b)

	Electric system	Photonic system
particle	electrons	photons
equations	Dirac equation	Maxwell's equations
platform	crystalline material with inversion symmetry breaking	photonic crystals with inversion symmetry breaking
Chern number	number of topological edge state	number of topological edge mode
band	energy band structure 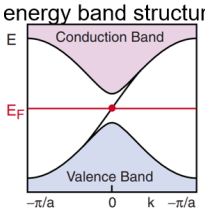	photonic band diagram 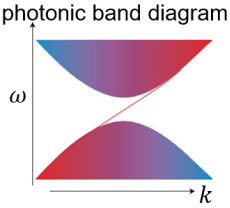
interface	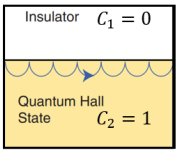	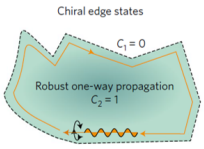

Figure 1.1: (a) Objects of six different geometries can be grouped into three pairs of topologies with different topological invariants. (b) Comparison between quantum Hall effect in condensed matter and analog quantum Hall effect in photonic crystals.

uniform magnetic field discovered in 1980, in which the variation of Hall resistance with respect to the applied magnetic field is a quantized value and remains constant regardless of size, composition, and purity of the sample [6]. Besides, the quantized value of Hall resistance is proportional to the number of scattering-free edge states with induced disorders, which is called Chern number. When the Chern number is zero, it is proved that there is no topologically protected edge state, which is topologically trivial, otherwise it is topologically non-trivial for a nonzero Chern number. In 1988, Haldane proposed a theoretical model that the necessary condition to achieve such phenomenon is the inversion symmetry breaking rather than an external magnetic field [7]. The discovery of topological properties of materials provides a new degree of freedom for us to understand materials, discover materials and even create materials.

Since back-scattering is a major reason of unwanted feedback and losses in or-

dinary photonic waveguides, transferring the scattering-free feature of topologically protected edge states in solid state physics into photonic waveguides is a natural choice. A detailed comparison between QHE in the solid state physics and analog QHE of photonic crystals is presented in Fig. 1.1(b). To analogize the periodic distribution of atoms in crystalline materials, the photonic crystal as an optical periodic structure, is introduced into the topological photonics [8, 9]. The periodical change of the dielectric constant artificially creates a lattice for light, which shows great potential in the development of the QHE in photonic systems. By solving Maxwell's equations of photonic crystals with inversion symmetry breaking, one can realize the topological photonic mode inside the nontrivial frequency bandgap, whose optical field is localized at the domain-wall interface. Research in topological photonics has been attracting increasing attention, especially due to the novel and unique properties, like unidirectional propagation and its robustness against disorder-induced backscattering [10, 11], which have the potential to contribute to the development of robust on-chip ultra-compact nanophotonic devices.

Topological photonic modes could be achieved by gapping out symmetry-protected Dirac cones, for example, an analogy of the time-reversal symmetry breaking feature of the quantum Hall effect is induced by magneto-optical effects under an external static magnetic field [10, 11, 12]. However, magneto-optic photonic crystals only have a strong response to an applied magnetic field at microwave frequencies, so that extending these phenomena to the optical domain requires alternative solutions. To this end, spatial-inversion symmetry breaking is induced in time-reversal invariant photonic systems by spatially asymmetric perturbations [13, 14]. The topological nontrivial characteristics could be theoretically described by the integer topological index, Chern number. When the Chen number is zero, it is proved that there is no nontrivial topologically protected edge mode, otherwise, the number of topological edge modes inside the nontrivial bandgap is exactly the difference of Chern number across the domain wall interface [see Fig. 1.1(b)] [15, 16]. Currently, a variety of experimental platforms are available for topological photonics, including metamaterials, photonic crystals, and evanescently coupled waveg-

uides [17]. Importantly, topologically-protected edge modes have been explored not only in the context of fundamental science, but also with the aim to fulfill their potential for new applications, such as robust light-transmission devices [18, 19], optical signal processing devices [20], time-delay lines [21, 22], and sensors [23].

In addition to the linear optical response of topological photonic systems, nonlinear topological photonics has also been studied, leading to the development of active and tunable applications implemented in robust topological photonic systems. Key functionalities of active photonic devices, such as tunability, optical frequency generation, and sensing, can most effectively be implemented by employing the nonlinear optical response of the topological photonic system [24]. Besides, the unique characteristics of topological insulators, like the strongly localized topological edge mode and the co-existence of bulk, trivial and nontrivial edge modes with different spatial profiles, offer potential advantages to enhance pump intensity and filter different beams in nonlinear processes, respectively. To this end, active topological photonic devices relying on nonlinear optical effects, including Kerr effect [25], second-harmonic generation (SHG) [26], third-harmonic generation (THG) [27], and four-wave mixing (FWM) [28], have been successfully demonstrated. Moreover, the unique properties of graphene-based topological system and nonlinear effects can be considered for developing photonic platforms and nonlinear systems, which can tune a topologically-protected defect-immune light by a change of light intensity. Key factors, such as large, tunable carrier densities [29, 30] and long intrinsic relaxation times up to the picosecond range [31, 32], make graphene an ideal platform to achieve passive and active topological plasmonics with high frequency, low loss and large topological bandgaps. Due to the large optical near-field enhancement and large life-time of plasmons in graphene metasurfaces, the THG interaction of plasmonic edge states can be achieved in graphene metasurfaces at an ultralow pump power based on a relatively large nonlinear coefficient. In the next section, the main objectives of this thesis will be introduced.

1.1 Main Objective of The Thesis

In this thesis, two main objectives have been formulated and specified: i) designing topologically protected waveguides with required symmetry breaking, ii) applying such topological waveguide into tunable and robust plasmonic nanodevices based on the fact that light propagation of topological edge modes shows unidirectional and scattering-free characteristics against induced disorders.

The necessary condition to achieve a topologically protected edge mode is to break the time-reversal or spatial inversion symmetry of the system. To meet this challenge, for the first objective of designing a topological photonic waveguide, I will start from the periodic hexagonal array of holes in a monolayer graphene plasmonic waveguide. The honeycomb lattice of graphene waveguide exhibits the gapless Dirac cone at the corner of the Brillouin zone, which is protected by C_{6v} point-group symmetry. To gap out the symmetry-protected Dirac cone and open a nontrivial bandgap, the reduction of C_{6v} point-group symmetry is achieved by introducing extra nanoholes. Based on the wave optics module of COMSOL, I will numerically calculate the band diagram of the unit cell of the graphene nanohole crystal with spatial-inversion symmetry breaking along the high-symmetry points of the Brillouin zone. Specifically, the valley Chern number of bulk valley modes below the bandgap at K and K' valleys is computational evaluated based on the Wilson-loop method. Furthermore, since the difference of the valley Chern number across the domain-wall can be nonzero by a π rotation of a graphene nanohole crystal, I will numerically compute the projected band diagram of a finite supercell with a mirror-symmetric domain-wall interface. Additionally, the unidirectional characteristics of the light propagation of topological valley edge mode will be computed by the full-wave simulations.

In addition to the monolayer graphene plasmonic waveguide with spatial-inversion symmetry breaking, we generalize the concept of layer degree of freedom for a multilayer graphene system to reveal three important properties. First, the lattice of different layers can belong to various point symmetry groups, which plays a significant role in breaking the spatial-inversion symmetry of the whole multi-

layer system. Second, the layer degree of freedom introduces an additional mirror symmetry breaking between different graphene layers. Third, due to the additional layer degree of freedom, topological modes with new layer-polarized characteristics have been proposed in layered photonic crystals. As a result, the bilayer graphene nanohole waveguide with a new layer degree of freedom will be systematically studied and designed. First, the mirror symmetry breaking between the top and bottom freestanding layers of graphene circular nanohole metasurfaces, is introduced into the D_{6h} point-group-symmetry protected double Dirac cones. Aiming to properly define the nontrivial bandgap, I will calculate the frequency band diagram of bilayer graphene crystals over the entire Brillouin zone, which will clearly illustrate the transition between two Dirac cones of bilayer graphene metasurfaces from weak to strong interlayer coupling. Following the same procedure of the monolayer graphene system, I will present the projected band diagram of the bilayer graphene waveguide with a mirror-symmetric domain-wall interface in which the topological valley mode appears, and will show its chirality and unidirectional light propagation under a circularly-polarized source.

Second, layered graphene metasurfaces with triangular nanoholes have been proposed, which can introduce a new rotation degree of freedom compared with bilayer metasurfaces composed of circular nanoholes. Starting from the monolayer graphene triangular nanohole waveguide, I will analyze its band diagram with a nontrivial frequency bandgap when the inversion symmetry of the graphene system is reduced, which can be theoretically explained by solving the eigenvalue functions based on a 2×2 effective Hamiltonian. Significantly, I will derive the effective Hamiltonian of bilayer and three-layer graphene triangular nanohole metasurfaces by taking the interlayer coupling between any two layers into account. The comparison of the frequency dispersion curves near the K point calculated by the effective Hamiltonian and COMSOL simulations will be present. Subsequently, I will quantitatively define and distinguish two quantized topological invariants of the layered graphene metasurfaces, valley and layer Chern numbers, which are the linear combinations of valley Chern numbers of the bands below the bandgap around K valley.

It will further be utilized to describe topological modes with valley-chirality-locked and layer-polarized characteristics.

Taking advantages of the strong Kerr nonlinearity and tunable chemical potential of graphene, the second objective of tunable topological applications is fulfilled on the proposed graphene nanohole metasurfaces. I will first describe the Kerr effect in the monolayer graphene nanohole metasurface excited by a bulk mode, which can uniformly change the refractive index of the whole graphene metasurface. To quantitatively investigate the change of topological valley mode in response to the applied bulk mode, the projected band diagram under different pump powers will be computed, and I will demonstrate an active all-optical switch based on the fact that the frequency change of bandgap via Kerr effect can switch a topological interface mode into a leaky bulk mode. Besides, since the Kerr effect can lead to a frequency shift of the bandgap, I will quantitatively identify the wavevector mismatch between topological mode and trivial edge mode inside the bandgap under an increasing pump power, which can be extracted via three methods, the projected band diagram, Fourier transform, and coupled-mode theory. Then, I will show an efficient coupling between topological and trivial edge modes when the phase-matching condition is fulfilled. Moreover, I will design a molecular gas sensor on the proposed bilayer graphene metasurfaces, in which the frequency bandgap can be tuned via the gas concentration absorbed onto the graphene metasurfaces. When the topological mode is switched into a scattered bulk mode, the transmission of the topological interface mode will be rapidly reduced, and the quantitative relation between the transmission and gas concentration in the environment will be estimated.

1.2 Outline

In Chapter 2, I will present the background theory of photonic crystals, optical properties of graphene, physical background and reviews of remarkable works about topological photonics. Starting from Maxwell's equations, I will introduce the band structure of photonic crystals with periodic electric permittivity. To illustrate graphene as an ideal platform to possess topological edge mode, graphene will be

systematically described by introducing its gapless electric band structure and optical properties. Specifically, the linear and nonlinear optical response of graphene will be demonstrated and summarized by its linear and nonlinear surface conductivity. Subsequently, I will describe the basic background of topological photonics based on the discovery of the quantum Hall effect in solid state physics, especially, I will introduce the quantized topological invariant and topological nontrivial bandgap. Finally, I will review the literature on time-reversal variant and invariant topological insulators under the time-reversal and spatial-inversion symmetry breaking, respectively.

Chapter 3 describes the proposed monolayer graphene nanohole plasmonic crystal waveguide, which is designed by controlling the size of nanoholes in a hexagonal unit cell to achieve the unidirectional light propagation of a topologically-protected valley mode. Since the spatial-inversion symmetry breaking in graphene is easier to be realized than the time-reversal symmetry breaking in graphene with an external magnetic field, the C_{6v} point group symmetry of the graphene plasmonic waveguide can be reduced by tuning the size of extra nanoholes. As a consequence, the symmetry-protected Dirac cone is gapped out, which will be presented in the band diagram of the proposed graphene metasurface. Significantly, the topologically protected edge mode will appear inside the nontrivial bandgap and its corresponding light propagation will show unidirectional features.

The proposed monolayer graphene nanohole waveguide is further applied to an active all-optical switch and a nonlinear mode coupler in Chapters 4 and 5, respectively. By taking advantage of the large Kerr nonlinearity of graphene, the device can be operated using low optical power and in a tunable manner in response to an applied electric field. In Chapter 4, an active all-optical switch is achieved by using a pump-probe configuration, in which a pump field injected in a bulk mode of the metasurface is used to tune the photonic structure based on the fact that the refractive index of graphene is uniformly tuned via Kerr effect. Under the excitation source with a fixed frequency, the light propagation along the domain-wall interface

can be switched from a topological interface mode into a leaky bulk mode, which will be quantitatively described by the power-dependent transmission of the signal mode. Importantly, I will show the change of required switching pump power if the device is operated in the slow-light (SL) regime.

Chapter 5 further studies the influence of Kerr effect on the valley-Hall topological transport in the proposed graphene nanohole metasurface. Topological interface modes and trivial edge modes of a specially designed graphene metasurface can be coupled in a tunable and optically controllable manner, thus providing an efficient approach to transfer optical power to topologically protected modes. When an optical pump propagating in a bulk mode of the metasurface is employed to tune the band structure of the photonic system, consequently, the coupling coefficient and wave-vector mismatch between edge and topological interface modes vary with the pump power. This tunable coupling mechanism is particularly efficient due to the large Kerr coefficient of graphene. Importantly, I will perform phase-mismatch analysis using both *ab initio* full-wave simulations and a coupled-mode theory that captures the main physics of this active coupler and observe a good agreement between the two approaches.

Chapter 6 studies and discusses the bilayer graphene system that possesses plasmonic topological valley interface modes when the mirror symmetry of the metasurface is broken by horizontally shifting the lattice of holes of the top layer of the two freestanding graphene layers in opposite directions. I will first present the symmetry-protected Dirac cone for the monolayer graphene metasurface. By introducing an additional graphene layer, the new degree of freedom like mirror symmetry breaking between two layers, can be utilized to achieve nontrivial bandgap in the momentum space. In this configuration, the unidirectional characteristics of light propagation of topological valley mode will be investigated in the domain-wall interface of the bilayer graphene metasurface by the full-wave simulations in COMSOL.

Chapter 7 applies the bilayer graphene metasurface into a chemically controllable molecular gas sensor, which is based on the topological unidirectional proper-

ties of this metasurface using the fact that the Fermi energy of graphene varies upon chemical doping. This effect induces a strong variation of the transmission of the topological guided modes under the increasing gas concentrations absorbed onto the graphene sheet, which can be employed as the underlying working principle of gas sensing devices.

Chapter 8 proposes the layered graphene metasurfaces with triangular nanoholes, and demonstrates a simple rotation of the triangular holes could make a great contribution to the nontrivial frequency bandgap. Under specific rotation angles of triangular holes in layered graphene metasurfaces, the topological valley modes are distinguished by two different confinement characteristics, i.e. chirality-momentum-locked and layer-polarized features. It is further quantitatively proved by the defined layer Chern number and valley Chern number of the layered graphene metasurfaces, which are computed by solving the eigenvalue problem with the effective Hamiltonian.

The main conclusions of this thesis will be summarized in Chapter 9. Future perspectives for extending this work are also included in this chapter.

Bibliography

[1] J. E. Avron, R. Seiler, and B. Simon, "Homotopy and quantization in condensed matter physics," Phys. Rev. Lett. **51**, 51-53 (1983).

[2] C. C. Adams, *The Knot Book: An Elementary Introduction to the Mathematical Theory of Knots* (American Mathematical Society, 1994).

[3] M. Z. Hasan and C. L. Kane, "Colloquium: topological insulators," Rev. Mod. Phys. **82**, 3045 (2010).

[4] J. E. Moore, "The birth of topological insulators," Nature **464**, 194-198 (2010).

[5] Y. Ando, "Topological insulator materials," J. Phys. Soc. Jpn. **82**, 102001 (2013).

[6] K. V. Klitzing, G. Dorda, and M. Pepper, "New method for high-accuracy determination of the fine-structure constant based on quantized Hall resistance," Phys. Rev. Lett. **45**, 494 (1980).

[7] F. D. M. Haldane, "Model for a quantum Hall effect without Landau levels: Condensed-matter realization of the "parity anomaly"," Phys. Rev. Lett. **61**, 2015 (1988).

[8] F. D. M. Haldane and S. Raghu, "Possible realization of directional optical waveguides in photonic crystals with broken time-reversal symmetry," Phys. Rev. Lett. **100**, 013904 (2008).

[9] S. Raghu and F. D. M. Haldane, "Analogs of quantum-Hall-effect edge states in photonic crystals," Phys. Rev. A **78**, 033834 (2008).

[10] Z. Wang, Y. D. Chong, J. D. Joannopoulos, and M. Soljacic, "Reflection-free one-way edge modes in a gyromagnetic photonic crystal," Phys. Rev. Lett. **100**, 013905 (2008).

[11] Z. Wang, Y. D. Chong, J. D. Joannopoulos, and M. Soljacic, "Observation of unidirectional backscattering-immune topological electromagnetic states," Nature **461**, 772-775 (2009).

[12] Y. Poo, R. X. Wu, Z. Lin, Y. Yang, and C. T. Chan, "Experimental realization of self-guiding unidirectional electromagnetic edge states," Phys. Rev. Lett. **106**, 093903 (2011).

[13] T. Ma and G. Shvets, "All-Si valley-Hall photonic topological insulator," New J. Phys. **18**, 025012 (2016).

[14] X. T. He, E. T. Liang, J. J. Yuan, H. Y. Qiu, X. D. Chen, F. L. Zhao and J. W. Dong, "A silicon-on-insulator slab for topological valley transport," Nat. Commun. **10**, 872 (2019).

[15] D. Xiao, W. Yao, and Q. Niu, "Valley-contrasting physics in graphene: magnetic moment and topological transport," Phys. Rev. Lett. **99**, 236809 (2007).

[16] L. Lu, J. D. Joannopoulos, and M. Soljacic, "Topological photonics," Nat. Photonics **8**, 821 (2014).

[17] T. Ozawa, H. M. Price, A. Amo, N. Goldman, M. Hafezi, L. Lu, M. C. Rechtsman, D. Schuster, J. Simon, O. Zilberberg, and I. Carusotto, "Topological photonics," Rev. Mod. Phys. **91**, 015006 (2019).

[18] Y. Yang, Y. Poo, R. X. Wu, Y. Gu, and P. Chen, "Experimental demonstration of one-way slow wave in waveguide involving gyromagnetic photonic crystals," Appl. Phys. Lett. **102**, 231113 (2013).

[19] S. Mittal, J. Fan, S. Faez, A. Migdall, J. M. Taylor, and M. Hafezi, "Topologically robust transport of photons in a synthetic gauge field," Phys. Rev. Lett. **113**, 087403 (2014).

[20] X. Zang and C. Jiang, "Edge mode in nonreciprocal photonic crystal waveguide: Manipulating the unidirectional electromagnetic pulse dynamically," J. Opt. Soc. Am. B **28**, 554-557 (2011).

[21] M. Hafezi, E. A. Demler, M. D. Lukin, and J. M. Taylor, "Robust optical delay lines with topological protection," Nat. Phys. **7**, 907–912 (2011).

[22] X. Cheng, C. Jouvaud, X. Ni, S. H. Mousavi, A. Z. Genack, and A. B. Khanikaev, "Robust reconfigurable electromagnetic pathways within a photonic topological insulator," Nat. Mater. **15**, 542-548 (2016).

[23] Y. Wang, J. W. You, Z. Lan and N. C. Panoiu, "Topological valley plasmon transport in bilayer graphene metasurfaces for sensing applications," Opt. Lett. **45**, 3151-3154 (2020).

[24] R. W. Boyd, *Nonlinear Optics* (Academic Press, 2008).

[25] D. Leykam and Y. D. Chong, "Edge solitons in nonlinear-photonic topological insulators," Phys. Rev. Lett. **117**, 143901 (2016).

[26] Z. Lan, J. W. You, Q. Ren, W. E. I. Sha, and N. C. Panoiu, "Second-harmonic generation via double topological valley-Hall kink modes in all-dielectric photonic crystals," Phys. Rev. A **103**, L041502 (2021).

[27] D. Smirnova, S. Kruk, D. Leykam, E. Melik-Gaykazyan, D. Y. Choi, and Y. Kivshar, "Third-harmonic generation in photonic topological metasurfaces," Phys. Rev. Lett. **123**, 103901 (2019).

[28] J. W. You, Z. Lan, and N. C. Panoiu, "Four-wave mixing of topological edge plasmons in graphene metasurfaces," Sci. Adv. **6**, eaaz3910 (2020).

[29] F. Leonard, C. D. Spataru, M. Goldflam, D. W. Peters, and T. E. Beechem, "Dynamic Wavelength-Tunable Photodetector Using Subwavelength Graphene Field-Effect Transistors," Sci. Rep. **8**, 45873 (2017).

[30] D. K. Efetov and P. Kim, "Controlling electron-phonon interactions in graphene at ultrahigh carrier densities," Phys. Rev. Lett. **105**, 256805 (2010).

[31] T. Low and P. Avouris, "Graphene plasmonics for terahertz to mid-infrared applications," ACS Nano **8**, 1086–1101, (2014).

[32] H. Yan, *et al.* "Infrared spectroscopy of tunable Dirac terahertz magnetoplasmons in graphene," Nano Lett. **12**, 3766–3771 (2012).

Chapter 2

Background

In this chapter, I will review the physical background of photonic crystals (PhCs), graphene, and topological photonics. In Sec. 2.1, starting from Maxwell's equations, an introduction of the band structure of PhCs will be presented. Then, in Sec. 2.2, the electric band structure and optical properties of graphene, which is mainly utilized as the underlying material in my thesis, will be illustrated. Finally, in Sec. 2.3, the basic concepts of topological photonics, such as Berry connection, Berry curvature, and Chern number, will be described by extending the background theory of the quantum Hall effect (QHE) in solid-state physics. The main types of topological photonic insulators under different symmetry-reversal breaking will be classified and characterized. Specifically, the advances in time-reversal variant and invariant topological insulators will be reviewed under the induced time-reversal and spatial-inversion symmetry breaking, respectively.

2.1 Overview of Photonic Crystals

PhCs are artificial optical nanostructures formed by periodic arrangement of media with different refractive indices [1]. Due to the periodicity of high and low permittivity, PhCs may allow light to propagate or may forbid it depending on the periodicity of the PhCs and the wavelength of light waves. The dispersion relationship of light waves has a band-like structure, which is called photonic band structure [2]. The forbidden frequency ranges are called photonic bandgaps, and light or electromagnetic waves whose frequencies fall in the forbidden band cannot propagate

[3].

2.1.1 Maxwell's Equations

As light is a kind of electromagnetic field, the physical principle of optics and electromagnetic field dynamics can be described by four Maxwell's equations. The time-dependent macroscopic forms of Maxwell's equations can be written as [4],

$$\begin{aligned} \nabla \cdot \boldsymbol{D}(\boldsymbol{r},t) &= \rho(\boldsymbol{r},t), \\ \nabla \cdot \boldsymbol{B}(\boldsymbol{r},t) &= 0, \\ \nabla \times \boldsymbol{E}(\boldsymbol{r},t) &= -\frac{\partial \boldsymbol{B}(\boldsymbol{r},t)}{\partial t}, \\ \nabla \times \boldsymbol{H}(\boldsymbol{r},t) &= \boldsymbol{J}(\boldsymbol{r},t) + \frac{\partial \boldsymbol{D}(\boldsymbol{r},t)}{\partial t}, \end{aligned} \tag{2.1}$$

where $\boldsymbol{E}$ and $\boldsymbol{H}$ are electric and magnetic fields, respectively. $\boldsymbol{D}$ is electric displacement, $\boldsymbol{B}$ is magnetic induction, ρ is charge density and $\boldsymbol{J}$ is current density. Maxwell's equations consist of four laws in differential form, Gauss's law, solenoidality of the magnetic induction, Maxwell-Faraday's law, and Ampere's law in Eq. (2.1), respectively. In an electromagnetic material, the four macroscopic field vectors, $\boldsymbol{E}$, $\boldsymbol{D}$, $\boldsymbol{B}$, $\boldsymbol{H}$, are related by the electric polarisation $\boldsymbol{P}$ and magnetisation $\boldsymbol{M}$. The relations are given as [4],

$$\begin{aligned} \boldsymbol{D}(\boldsymbol{r},t) &= \varepsilon_0 \boldsymbol{E}(\boldsymbol{r},t) + \boldsymbol{P}(\boldsymbol{r},t), \\ \boldsymbol{H}(\boldsymbol{r},t) &= \frac{1}{\mu_0}\boldsymbol{B}(\boldsymbol{r},t) - \boldsymbol{M}(\boldsymbol{r},t), \end{aligned} \tag{2.2}$$

where ε_0 and μ_0 are the vacuum electric permittivity and the vacuum magnetic permeability, respectively. Moreover, the electric polarization $\boldsymbol{P}$ and magnetization $\boldsymbol{M}$ are the vector fields that express induced electric dipole moments in a dielectric material and induced magnetic dipole moments in a magnetic material, respectively. In an isotropic medium, the electric polarization $\boldsymbol{P}$ and magnetization $\boldsymbol{M}$ are proportional to the electric field $\boldsymbol{E}$ and magnetic field $\boldsymbol{H}$, respectively, which can be

expressed by,

$$\begin{aligned} \boldsymbol{P}(\boldsymbol{r},t) &= \varepsilon_0 \chi_e \boldsymbol{E}(\boldsymbol{r},t), \\ \boldsymbol{M}(\boldsymbol{r},t) &= \mu_0 \chi_m \boldsymbol{H}(\boldsymbol{r},t), \end{aligned} \tag{2.3}$$

where χ_e and χ_m are the electric and magnetic susceptibilities of the medium, respectively. Taking into account these relations, the electric displacement $\boldsymbol{D}$ and magnetic induction $\boldsymbol{B}$ can be represented in terms of electric and magnetic fields,

$$\begin{aligned} \boldsymbol{D}(\boldsymbol{r},t) &= \varepsilon_0 \varepsilon_r \boldsymbol{E}(\boldsymbol{r},t) = \varepsilon \boldsymbol{E}(\boldsymbol{r},t), \\ \boldsymbol{B}(\boldsymbol{r},t) &= \mu_0 \mu_r \boldsymbol{H}(\boldsymbol{r},t) = \mu \boldsymbol{H}(\boldsymbol{r},t), \end{aligned} \tag{2.4}$$

where linear parameter $\varepsilon = \varepsilon_0 \varepsilon_r$ is the electric permittivity and $\mu = \mu_0 \mu_r$ is the magnetic permeability of the medium, with the relative permittivity $\varepsilon_r = 1 + \chi_e$ and relative permeability $\mu_r = 1 + \chi_m$.

Based on Maxwell's equations, an important solution is formed to be transverse plane waves propagating in an isotropic medium without sources. When $\rho = 0$ and $\boldsymbol{J} = 0$, the curl of third equation Eq. (2.1) can be written as,

$$\nabla \times \nabla \times \boldsymbol{E}(\boldsymbol{r},t) = -\mu \frac{\partial}{\partial t} \nabla \times \boldsymbol{H}(\boldsymbol{r},t), \tag{2.5}$$

Inserting the fourth equation of Eq. (2.1) into Eq. (2.5), it can be expressed as,

$$\nabla \times \nabla \times \boldsymbol{E}(\boldsymbol{r},t) = -\mu \varepsilon \frac{\partial^2 \boldsymbol{E}(\boldsymbol{r},t)}{\partial t^2}, \tag{2.6}$$

Utilizing Laplace operator relation $\nabla^2 \boldsymbol{E} = \nabla(\nabla \cdot \boldsymbol{E}) - \nabla \times (\nabla \times \boldsymbol{E}) = -\nabla \times (\nabla \times \boldsymbol{E})$ without a source ($\nabla \cdot \boldsymbol{E} = 0$), Eq. (2.6) can be rewritten in the form of Helmholtz equation,

$$\nabla^2 \boldsymbol{E}(\boldsymbol{r},t) - \mu \varepsilon \frac{\partial^2 \boldsymbol{E}(\boldsymbol{r},t)}{\partial t^2} = 0, \tag{2.7}$$

Considering a harmonic time-dependent transverse plane wave, the electric field for a fixed frequency ω is given as,

$$\boldsymbol{E}(\boldsymbol{r},t) = \boldsymbol{E}(\boldsymbol{r},\omega) e^{-i\omega t} = \boldsymbol{E}(\omega) e^{i(\boldsymbol{k}\cdot\boldsymbol{r} - \omega t)}, \tag{2.8}$$

with $\boldsymbol{k}$ being the wave vector. Taking Eq. (2.8) into Eq. (2.7), one can obtain the time-dependent Eq. (2.7) in frequency domain,

$$\nabla^2 \boldsymbol{E}(\boldsymbol{r},\omega) + \mu\varepsilon\omega^2 \boldsymbol{E}(\boldsymbol{r},\omega) = 0, \tag{2.9}$$

and then simplify it,

$$-k^2 \boldsymbol{E}(\boldsymbol{r},\omega) + \mu\varepsilon\omega^2 \boldsymbol{E}(\boldsymbol{r},\omega) = 0, \tag{2.10}$$

hence, the wave number can be expressed as $k = \sqrt{\mu\varepsilon}\omega = \sqrt{\mu_0\varepsilon_0}n\omega = n\omega/c = \omega/v_p$, where n is refractive index of the medium and v_p is phase velocity.

2.1.2 Electrodynamic Theory of Photonic Crystals

In classical electromagnetism, the study of electromagnetic wave propagation is based on Maxwell's equations. As for periodic media, Bloch in 1928 [5] extended the wave propagation analysis from one-dimensional (1D) to three-dimensional (3D) PhCs. Bloch further studied the wave propagation and proved that the wave could propagate without scattering in a periodic media, and only the imperfections of the periodic structure cause scattering [6].

Considering a harmonic time-dependent transverse plane wave, the electric field and magnetic field for a fixed frequency ω can be written as mode profiles times complex exponential,

$$\begin{aligned} \boldsymbol{E}(\boldsymbol{r},t) &= \boldsymbol{E}(\boldsymbol{r},\omega)e^{-i\omega t}, \\ \boldsymbol{H}(\boldsymbol{r},t) &= \boldsymbol{H}(\boldsymbol{r},\omega)e^{-i\omega t}, \end{aligned} \tag{2.11}$$

The optical periodicity of PhCs is defined by the periodic dielectric function, $\varepsilon(\boldsymbol{r}) = \varepsilon(\boldsymbol{r}+\boldsymbol{R})$, where the primitive lattice vector $\boldsymbol{R}$ indicates periodicity in three dimensions. With the assumption of the source-free system at a fixed frequency ω, inserting Eq. (2.11) into Eq. (2.1), Maxwell's equations in frequency domain

become [7],

$$\begin{aligned}
&\nabla \cdot [\varepsilon(\boldsymbol{r})\boldsymbol{E}(\boldsymbol{r},\omega)] = 0,\\
&\nabla \cdot \boldsymbol{H}(\boldsymbol{r},\omega) = 0,\\
&\nabla \times \boldsymbol{E}(\boldsymbol{r},\omega) - i\omega\mu_0 \boldsymbol{H}(\boldsymbol{r},\omega) = 0,\\
&\nabla \times \boldsymbol{H}(\boldsymbol{r},\omega) + i\omega\varepsilon_0\varepsilon(\boldsymbol{r})\boldsymbol{E}(\boldsymbol{r},\omega) = 0,
\end{aligned} \tag{2.12}$$

Simplifying Eq. 2.12, we obtain a propagation equation entirely for the magnetic field,

$$\nabla \times \left(\frac{1}{\varepsilon(\boldsymbol{r})} \nabla \times \boldsymbol{H}(\boldsymbol{r},\omega) \right) = \left(\frac{\omega}{c} \right)^2 \boldsymbol{H}(\boldsymbol{r},\omega), \tag{2.13}$$

By solving Eq. (2.13) together with $\nabla \cdot \boldsymbol{H} = 0$, it gives the magnetic field $\boldsymbol{H}(\boldsymbol{r},\omega)$, which then can be utilized to solve for the electric field,

$$\boldsymbol{E}(\boldsymbol{r},\omega) = \frac{i}{\omega\varepsilon_0\varepsilon(\boldsymbol{r})} \nabla \times \boldsymbol{H}(\boldsymbol{r},\omega), \tag{2.14}$$

Eq. (2.13) entirely in magnetic field can be regarded as a eigenvalue equation where $\boldsymbol{H}$ and $\left(\frac{\omega}{c}\right)^2$ are eigenfunctions and eigenvalues, respectively. Based on the periodic arrangement of atoms in the crystal, the concepts in solid state physics, like reciprocal space, Brillouin zone, and dispersion relation, are introduced to PhCs. Since the lattice of a crystal can be represented in the real and reciprocal spaces, the periodicity of permittivity $\boldsymbol{R}$ in PhCs can be related to the periodicity of wave vector $\boldsymbol{k}$ in the reciprocal space. Based on the Bloch's theorem, the Bloch function can be used to express eigenfunction $\boldsymbol{H}$ by a periodic function,

$$\boldsymbol{H}(\boldsymbol{r},\omega) = e^{i\boldsymbol{k}\cdot\boldsymbol{r}} \boldsymbol{u}_{\boldsymbol{k}}(\boldsymbol{r},\omega), \tag{2.15}$$

where $e^{i\boldsymbol{k}\cdot\boldsymbol{r}}$ is a plane wave phase shift term and $\boldsymbol{u}_{\boldsymbol{k}}(\boldsymbol{r},\omega) = \boldsymbol{u}_{\boldsymbol{k}}(\boldsymbol{r}+\boldsymbol{R},\omega)$ is a periodic function and has the same periodicity as the crystal structure, which is a key function defining the wave propagation by multiplying a plane wave phase term. Wave vector $\boldsymbol{k}$ is periodic, $\boldsymbol{k} = \boldsymbol{k} + \boldsymbol{G}$, in the reciprocal space, where the primitive reciprocal lattice vector $\boldsymbol{G}$ is related to the primitive lattice vector $\boldsymbol{R}$ and the relation satisfies $\boldsymbol{R}_i \cdot \boldsymbol{G}_j = 2\pi\delta_{i,j}$ $(i,j = 1,2,3)$. Consequently, the $\boldsymbol{k}$ in the primitive cell

could represent all the eigensolutions in the reciprocal space.

The first Brillouin zone (FBZ) is defined in a reciprocal region of the primitive cell. Hence, band structures outside the FBZ are repeated bands in FBZ so that the dispersion relation in FBZ fully provides all the band information and generates the band diagram. Interestingly, if the periodic structure has a certain symmetry, like mirror- or inversion-symmetry, the FBZ can be simplified to an irreducible Brillouin zone. The Bloch state in Eq. (2.15) satisfies Maxwell's equations, and Eq. (2.13) now changes,

$$(\nabla + i\boldsymbol{k}) \times \frac{1}{\varepsilon(\boldsymbol{r})} (\nabla + i\boldsymbol{k}) \times \boldsymbol{u}_{\boldsymbol{k}}(\boldsymbol{r}, \omega) = \left(\frac{\omega(\boldsymbol{k})}{c} \right)^2 \boldsymbol{u}_{\boldsymbol{k}}(\boldsymbol{r}, \omega), \tag{2.16}$$

At different Bloch wave vector $\boldsymbol{k}$, Eq. (2.16) generates different and discrete set of eigenvalues $\omega_n(\boldsymbol{k})$. Importantly, the relation in eigenvalue function $\omega_n(\boldsymbol{k})$ indicates the band structure of the nth band. In addition, based on the periodic boundary conditions of Eq. (2.16), the eigenvalue functions can be simplified and solved in a unit cell of the PhC. The region where there is no eigensolution for any wave vector $\boldsymbol{k}$, is called a photonic bandgap of the PhC, so that the corresponding frequency shows the cut-off frequency domains. If the periodic permittivity in PhCs is regarded as a periodic crystal potential in this eigenvalue function, the photonic bandgap can appear due to the influence of the periodic potential.

2.1.3 Band Diagrams of Photonic Crystals

The propagation of electromagnetic waves and the emerged bandgap in a periodic structure is a significant and fundamental theoretical concept used in our project. In photonics, periodic media could possess frequency bandgaps, where the light inside the bandgap cannot propagate through the periodic structure. Rayleigh firstly studied the electromagnetic field propagation in one-dimensional PhCs in 1887, the periodic planes show an angle-dependent bandgap where the light propagation is blocked [8]. After that, periodically structured PhCs that are periodic in one, two, and three directions were introduced by Yablonovitch in 1987 [9]. Such one-, two- and three-dimensional (1-, 2-, and 3-D) PhCs have been widely studied in relation

to electromagnetism and solid state physics, fabrication, and applications.

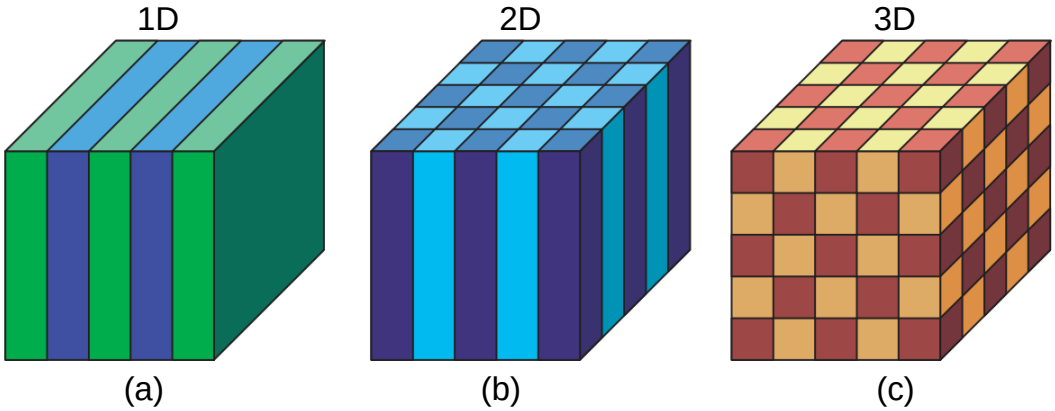

Figure 2.1: Schematic of PhCs with a periodic arrangement of permittivity along different directions. From (a) to (c), one-, two-, and three-dimensional PhCs show the periodicity of permittivity along one, two, and three directions, respectively. Reproduced from Ref. [10]

As schematically shown in Fig. 2.1, 1D, 2D, and 3D PhCs are defined by the direction of the periodic arrangement of permittivity, and different colors indicate different permittivity of the medium. For 1D PhCs, the multilayer film composed of alternating layers with different permittivity has been widely studied, and the band diagrams of the multilayer film consisting of three different permittivities are shown in Fig. 2.2. The Brillouin zone is from $-\pi/a$ to π/a and the diagram of a uniform film is given in Fig. 2.2(b). When the permittivity difference between two alternating layers is introduced (see Fig. 2.2(c)), no mode is allowed inside the yellow region, so that a photonic bandgap separating the top and bottom frequency domains appears at the edge of the Brillouin zone ($k = \pm\pi/a$). Figure 2.2(d) indicates a wider photonic bandgap when the difference in permittivity between two alternating layers is increased.

Two-dimensional PhCs are composed of the periodic arrangement of media with two different permittivities in two directions. The lattice constant has the same order of magnitude as light wavelength; e.g., the lattice constant of PhCs operating in the microwave regime is typically in the millimeter range, which makes fabrication easier. Figures 2.3(a)(b) illustrate the band diagrams of two common types of 2D periodic PhCs with a square lattice of dielectric-rods and air-holes with the

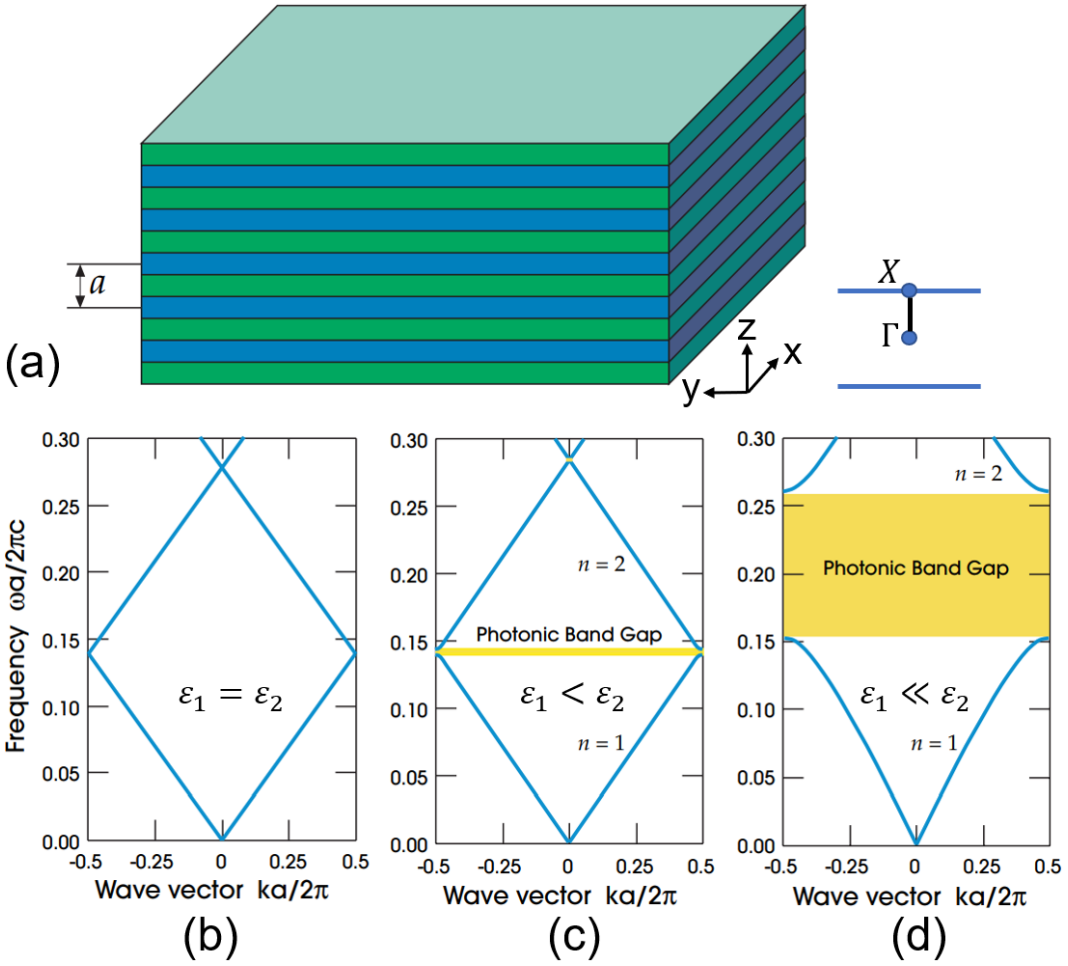

Figure 2.2: (a) Schematic of one-dimensional multilayer film with periodic permittivity arrangement along the z direction. The permittivity of alternating blue and green layers is ε_1 and ε_2, respectively. Band diagrams of 1D multilayer film (b) with uniform permittivity ($\varepsilon_1 = \varepsilon_2$), (c) with slightly permittivity difference between alternating layers, and (d) with increasing permittivity difference between two alternating layers. Reproduced from Ref. [10]

same lattice constant a and permittivity of the dielectric medium, respectively. The right insets show that the 2D PhCs are aligned along the x-axis and y-axis, while it is homogeneous along the z-axis. The frequency is expressed as a dimensionless ratio, and the TE and TM bands are marked by red and blue curves, respectively. The band diagram of the square array of dielectric cylinders only has a complete bandgap [blue domain in Fig. 2.3(a)] for TM modes, while the band diagram of the square array of air square holes only has a complete bandgap [red domain in Fig. 2.3(b)] for TE modes. To obtain a complete bandgap overlap between TE and TM modes, the 2D PhCs with a hexagonal array of holes in a dielectric medium has

been introduced, and the corresponding irreducible Brillouin zone contains three high symmetric points (Γ, M and K). For example, in Fig. 2.3(c), the bandgap between the first and second TE bands overlaps with the gap between the second and third TM bands, resulting in a relatively large complete bandgap for all polarization.

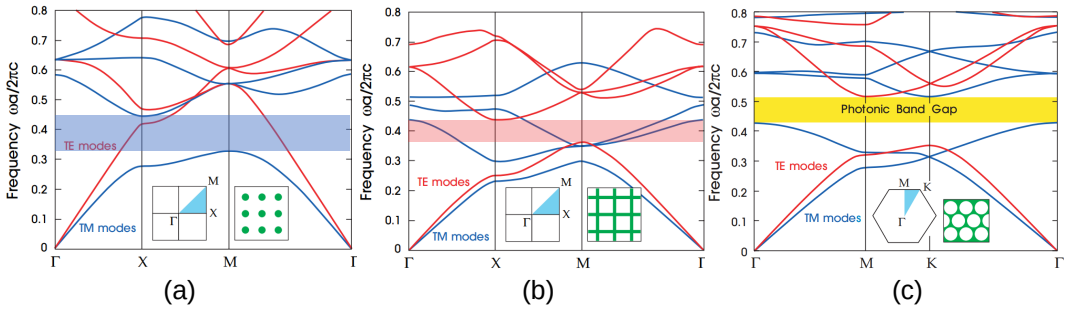

Figure 2.3: (a) Band structure of a two-dimensional square array of cylinders with radius $r = 0.2a$ and permittivity $\varepsilon = 8.9$ (right inset) along high-symmetric points Γ, X and M in the square Brillouin zone (left inset). The blue curves represent TM modes and the red curves represent TE modes. (b) Band structure of a two-dimensional square array of air square holes in dielectric slab with thickness $0.165a$ and permittivity $\varepsilon = 8.9$ (right inset). (c) Band structure of a two-dimensional hexagonal array of circular holes in dielectric slab with the radius of holes $r = 0.48a$ and permittivity $\varepsilon = 13$ (right inset) along high-symmetric points Γ, M, and K in the hexagonal Brillouin zone (left inset). Reproduced from Ref. [10]

The emergence of a photonic bandgap is highly dependent on the parameters, like the permittivity difference between two media, lattice structure, and the filling ratio between different media in the lattice. To be more specific, it is easier to achieve a photonic bandgap if the permittivity difference between two different electric media is larger. For 2D PhCs, the lattice with a hexagonal array of air holes may perform better than a square lattice, and 2D PhCs exhibit different band structures for TE and TM modes [11, 12]. Due to the difficulty in fabrication, the research on three-dimensional PhCs is somewhat behind that on two-dimensional PhCs. Even in the semiconductor industry, there is no reliable method for manufacturing three-dimensional PhCs. Taking advantage of light transmission features in PhCs, like low loss, total internal reflection, and low group velocity at the edge of the bandgap, PhCs have been broadly applied in photonic crystal mirrors [13], optical sensors [14], and photonic crystal fibers with better transmission characteristics

[15].

2.2 Introduction to Graphene

Graphene is a one-atom-thick allotrope of carbon with sp^2 hybridization consisting of a single layer of atoms arranged in a two-dimensional honeycomb lattice nanostructure, which was experimentally discovered and isolated by Geim and Novoselov [16]. The remarkable properties of graphene have made it a valuable nanomaterial and have attracted increasing attention, as it has the thinnest thickness, exceptional tensile strength, high electrical conductivity, high thermal conductivity, and optical transparency.

2.2.1 Band Structure of Graphene

Since carbon has four valence electrons, in the case of a superposition of the $2s$ and two $2p$ orbitals, three valence electrons are used for the sp^2 bonds in graphene. The orbitals form a trigonal planar structure with a formation of a σ bond between carbon atoms, which leads to carbon atoms in graphene as a honeycomb lattice, as shown in Fig. 2.4(a). The two inversion-symmetric triangular sublattices (A and B) are marked by black and white circles, respectively. Due to the opposite directions of nearest neighbours of sublattices A and B, the honeycomb lattice is not a Bravais lattice because two neighbouring sites are not equivalent, and can

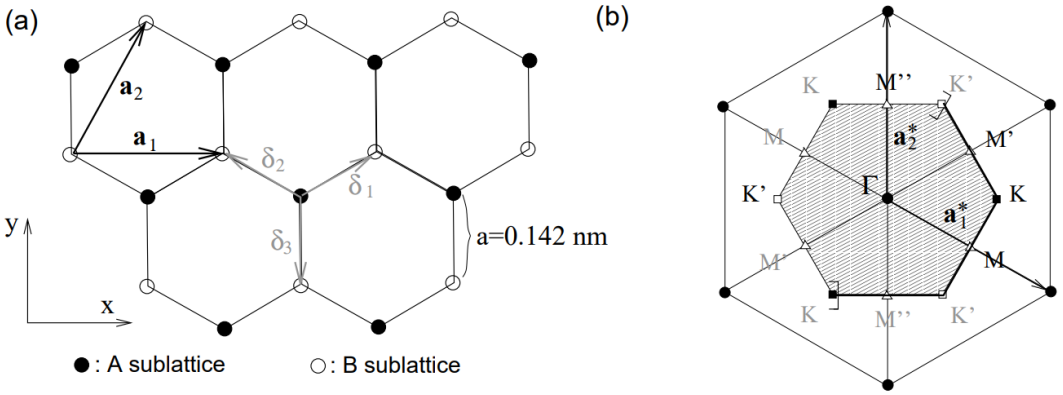

Figure 2.4: (a) Honeycomb lattice of graphene. $\boldsymbol{a}_1$ and $\boldsymbol{a}_2$ are basis vectors of the primitive unit cell. The vectors $\boldsymbol{\delta_1}$, $\boldsymbol{\delta_2}$, and $\boldsymbol{\delta_3}$ connect carbon atoms with a lattice constant a. (b) Graphene reciprocal lattice and the first Brillouin zone (FBZ) within it. $\boldsymbol{a}_1^*$ and $\boldsymbol{a}_2^*$ are basis vectors of the reciprocal lattice. The center, corners, and centers of edges in the FBZ are indicated by Γ, K and M, respectively.

be viewed as a triangular Bravais lattice with a two-atom basis (A and B). The reciprocal honeycomb lattice with respect to the triangular Bravais lattice, which is defined with basis vectors $\boldsymbol{a}_1^*$ and $\boldsymbol{a}_2^*$ satisfying $\boldsymbol{a}_i \cdot \boldsymbol{a}_j^* = 2\pi\delta_{i,j}$ $(i,j = 1,2)$, is depicted in Fig. 2.4(b). The FBZ represents a set of inequivalent points in the reciprocal space, where Γ, K, and M are the center, corner, and edge center of the FBZ, respectively. Specifically, among six corners, only two corners K and K' are inequivalent based on the fact that other corners can be obtained from K and K' by adding $2\boldsymbol{a}_1^*$ or $2\boldsymbol{a}_2^*$.

Due to the unaffected $2p_z$ orbital hosting the fourth valence electron, the π band between neighboring carbon atoms is half filled. In this way, the band structure of graphene corresponds to the dispersion of bonding and antibonding molecular orbitals, namely π and π^* bands. The tight-binding Hamiltonian for π electrons

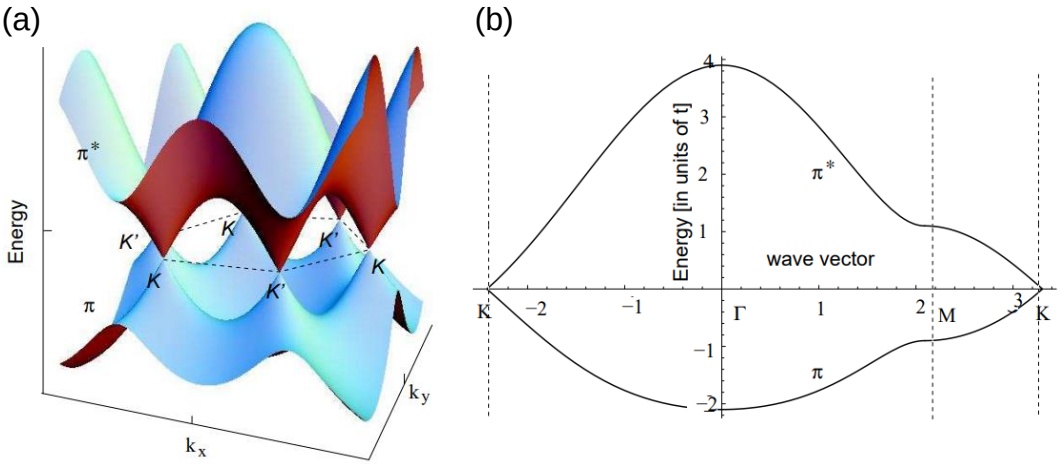

Figure 2.5: (a) Energy dispersion over the whole Brillouin zone for π (lower surface or valence band) and (upper surface or conduction band) π^* bands of graphene. (b) Electric band structure of graphene along the high-symmetry points of FBZ. Reproduced from Ref. [17].

in graphene is considered by t nearest-neighbor hopping energy (hopping between different sublattices) and t' next nearest-neighbor hopping energy (hopping in the same sublattice). The eigenenergies dispersion derived from tight-binding Hamiltonian are,

$$E_{\pm}(\boldsymbol{k}) = \pm t\sqrt{3+f(\boldsymbol{k})} - t'f(\boldsymbol{k}), \tag{2.17}$$

with $f(\boldsymbol{k}) = 2\cos\left(\sqrt{3}k_y a\right) + 4\cos\left(\frac{\sqrt{3}}{2}k_y a\right)\cos\left(\frac{3}{2}k_x a\right)$. Because each π electron

may occupy either a spin-up or a spin-down state, the plus sign applies to the conduction band and the minus sign indicates the lower valence band. The energy dispersion in the whole FBZ and along the high-symmetry points is shown in Figs. 2.5(a) and 2.5(b), respectively. The π band touches the π^* band at the corners of the FBZ (K and K'), and this unusual electronic band structure is called Dirac cone where the energy of the valence and conduction bands are not equal anywhere in the k-space, except at the zero-dimensional Dirac points (K and K'). Therefore, the Fermi level is situated at the Dirac points. To gain a deeper insight into the energy dispersion around the Dirac points, the energy dispersion around the K or K' was obtained by Wallace [18],

$$E_{\pm}(\boldsymbol{q}) \approx \pm v_F |\boldsymbol{q}| + O\left[(q/K)^2\right], \tag{2.18}$$

where $\boldsymbol{q}$ is the small momentum measured relatively to the Dirac points with $|\boldsymbol{K}| >> |\boldsymbol{q}|$ and $v_F = -\frac{3ta}{2\hbar}$ is the Fermi velocity with a value of $v_F \approx 1 \times 10^6 \mathrm{m/s}$. As indicated in Fig. 2.5(b), the linear energy dispersion around the Dirac points K and K' can be described by the massless Dirac equation. In this way, within the semiclassical approximation, the cyclotron mass m^* is defined as [17],

$$m^* = \frac{1}{2\pi}\left[\frac{\partial A(E)}{\partial E}\right]_{E=E_F}, \tag{2.19}$$

where $A(E) = \pi q^2(E) = \pi \frac{E^2}{v_F^2}$. Combining Eq. (2.18) and Eq. (2.19), the cyclotron mass of graphene is rewritten as,

$$m^* = \frac{E_F}{v_F^2} = \frac{k_F}{v_F}, \tag{2.20}$$

Based on the energy dispersion of graphene at Dirac points, it is useful to define an effective tight-binding Hamiltonian of graphene. The Schrödinger equation is $H(\boldsymbol{k})|\Psi_{\boldsymbol{k}}\rangle = E(\boldsymbol{k})|\Psi_{\boldsymbol{k}}\rangle$. Due to the two opposite signs of eigenvalues $E(\boldsymbol{k})$ in Eq. (2.18), the effective Hamiltonian of graphene is described by a 2 by 2 Hamiltonian

matrix,

$$H(\boldsymbol{k}) = -\frac{3ta}{2\hbar}\begin{pmatrix} 0 & k_x - ik_y \\ k_x + ik_y & 0 \end{pmatrix} = v_F \boldsymbol{\sigma}\cdot\boldsymbol{q} \tag{2.21}$$

where the wavevector $\boldsymbol{q}$ is measured from the Dirac points and Pauli matrix $\boldsymbol{\sigma} = (\sigma_x, \sigma_y)$ describes "spin up" and "spin down" states of two sublattices of the honeycomb lattice.

2.2.2 Optical Properties of Graphene

Optical Absorption

In addition to the linear dispersion relation of quasiparticles in graphene, graphene has remarkable optical properties as well. For example, the optical absorption in graphene depends only on the fine-structure constant $\alpha = \frac{e^2}{\hbar c} = 1/137$, with an absorptivity of about $\pi\alpha = 2.3\%$ over a wide wavelength range, making it almost transparent [19]. In the thickness range of several layers of graphene, the absorption rate increases by 2.3% for each additional layer of graphene. Large-area graphene films also have excellent optical properties, which usually vary with the thickness of graphene. This is the unusual low-energy electronic structure of monolayer graphene. Applying an external magnetic field, one can tune the optical response of graphene up to the terahertz range [20].

To control the optical properties of graphene, the use of doping is considered to be one of the most practical methods, which can tune the Fermi level or even open a bandgap. Specifically, common methods of doping are achieved by heteroatom doping, chemical modification strategy, and the method of electrostatic field tuning. For example, by applying a voltage to a dual-gate bilayer graphene field-effect transistor at room temperature, Zhang *et al.* [21] demonstrated gate-controlled tunable electronic bandgap of bilayer graphene between 0 and 0.25 eV. Schedin *et al.* [22] showed a linear relation between chemically induced carrier concentration in graphene and gas molecules (NO_2) attaching to graphene's surface, as a method of chemical doping. The tunability of graphene makes it a promising material not only for sensing applications but also for other tunable integrated optical applications where its sensitivity upon external electric or magnetic field is required.

When the intensity of the incident light exceeds a certain critical value, the optical absorption of gapless graphene will reach saturation. This nonlinear optical behavior is called saturable absorption, and the threshold is called saturable fluency. Due to Pauli blocking, the energy of photons less than two times the Fermi energy ($2E_F$) cannot be absorbed. With increasing input light, carriers accumulated in the conduction band are increasing, which can inhibit the excitation of carriers in return. Given strong visible or near-infrared excitation, graphene can easily become saturated because of its wideband optical absorption and gapless properties. This property allows graphene to be utilized in passively mode-locked lasers for the generation of ultrafast pulses with high peak power, which was proposed in the telecommunication band by Bao *et al.* [23].

Permittivity of Graphene

The optical properties of graphene are best described by its permittivity. As a 2D material, the optical properties of graphene can be characterized by conductivity σ as a function of frequency, temperature and chemical potential [24]. If we assume graphene is in the *xy* plane as a 2D material, the components of conductivity that contain *z*-axis cancel. As a result, the surface conductivity tensor of graphene is a 2×2 tensor that only contains four *xx*, *xy*, *yx*, *yy* conductivity components. Therefore, the surface conductivity tensor which incorporates the graphene magneto-optical effects is given by [25, 24],

$$\sigma = \begin{bmatrix} \sigma_L & \sigma_H \\ -\sigma_H & \sigma_L \end{bmatrix}, \tag{2.22}$$

where σ_L and σ_H are the longitudinal conductivity and the Hall conductivity, respectively. Based on the Drude model at room temperature and for frequency below the mid-infrared region, the longitudinal and Hall conductivity can be written as [26],

$$\sigma_L = \overline{\sigma} \frac{1 - i\omega\tau}{(\omega_c\tau)^2 + (1 - i\omega\tau)^2}, \tag{2.23}$$

$$\sigma_H = \overline{\sigma} \frac{\omega_c\tau}{(\omega_c\tau)^2 + (1 - i\omega\tau)^2}, \tag{2.24}$$

where frequency-independent $\overline{\sigma}$ part is given by,

$$\overline{\sigma} = \frac{2e^2\tau k_B T}{\pi\hbar^2} ln\left[2cosh\left(\frac{\mu_c}{2k_B T}\right)\right], \tag{2.25}$$

where T is the temperature, τ is relaxation time, e is the electron charge, k_B is the Boltzmann constant, and $\hbar$ is the reduced Planck's constant. A basic optical parameter of graphene, chemical potential $\mu_c = \hbar v_F\sqrt{n_0\pi} = E_F$ is determined by the Fermi velocity v_F and carrier density n_0. The chemical potential of ideal pure graphene at any temperature is at the crossing of the bands. With the help of the gate voltage or chemical doping, one can control the carrier density n_0 varying their chemical potential. Moreover, $\omega_c \approx eB_z v_F^2/\mu_c$ is the cyclotron frequency which is generated by the z-axis magnetic field B_z and will vanish if there is no external magnetic field. Note that Hall conductivity is induced by an external magnetic field.

For the case when the frequency is above the mid-infrared region, within the random-phase approximation [27], the general conductivity formula of graphene without an external magnetic field can be expressed as the sum of intraband and interband contributions, namely $\sigma_L = \sigma_{intra} + \sigma_{inter}$. The intraband conductivity is given by electron-photon scattering processes [28, 29],

$$\sigma_{intra}(\omega) = \frac{e^2 k_B T\tau}{\pi\hbar^2(1-i\omega\tau)}\left[\frac{\mu_c}{k_B T} + 2\ln\left(e^{-\frac{\mu_c}{k_B T}} + 1\right)\right], \tag{2.26}$$

For interband conductivity, direct interband electron transitions generate interband conductivity, which is much smaller than the intraband term at room temperature and for frequency below the mid-infrared region. The interband conductivity at room temperature ($\mu_c >> k_B T$) can be approximated as [28, 29],

$$\sigma_{inter}(\omega) = \frac{ie^2}{4\pi\hbar}\ln\left[\frac{2|\mu_c| - (\omega + i\tau^{-1})\hbar}{2|\mu_c| + (\omega + i\tau^{-1})\hbar}\right], \tag{2.27}$$

In computational modeling, the material permittivity is usually related to the bulk conductivity rather than effective surface parameters in 3D simulation. Therefore, the effective thickness of graphene is considered to calculate the bulk conductiv-

ity σ_b, which can be simply described as $\sigma_b = \sigma_L / h_{eff}$ and h_{eff} is the effective thickness of graphene. The permittivity of graphene could be described in terms of conductivity, and the relation is given as follows,

$$\varepsilon_g = 1 + \frac{i\sigma_b}{\varepsilon_0 \omega} = 1 + \frac{i\sigma_L}{\varepsilon_0 \omega h_{eff}}, \tag{2.28}$$

In consequence, the graphene permittivity is simplified and in dependence on the frequency ω, which defines the dispersion properties of graphene. Hence, the optical properties of graphene are described by its electric permittivity ε_g, which can be evaluated by inserting the surface conductivity Eq. (2.27) and (2.26) into Eq. (2.28) [30],

$$\varepsilon_g = 1 - \frac{e^2}{4\varepsilon_0 \pi \hbar \omega h_g} \ln\left(\frac{\xi - i\overline{\omega}}{\xi + i\overline{\omega}}\right) + \frac{ie^2 k_B T \tau}{\varepsilon_0 \pi \hbar^2 \omega \overline{\omega} h_g} \left[\frac{\mu_c}{k_B T} + 2\ln\left(e^{-\frac{\mu_c}{k_B T}} + 1\right)\right], \tag{2.29}$$

where ω is the frequency, $\overline{\omega} = 1 - i\omega\tau$, and $\xi = 2\tau|\mu_c|/\hbar$.

Graphene Plasmonics

Graphene physics and plasmonics have many common areas. Surface plasmon polaritons (SPPs) are electromagnetic surface waves, which are generated by the oscillation of free electrons in metal and propagate in the form of electromagnetic waves along the interface between a metal and dielectric medium configuration. The unique properties of SPPs, like sensitivity to the local interface and subwavelength localization, break the diffraction limit and lead to potential applications of new integrated photonics devices [31]. Plasmonics in graphene are attracting increasing attention, chiefly due to graphene tunable and adjustable intrinsic plasmons at different frequency ranges, based on the fact that electrically tunable plasmonic resonance can be easily achieved by varying the carrier density of graphene [32]. In addition, the combination of graphene with traditional noble-metal nanostructures can realize novel plasmonic applications with tunable characteristics.

By solving Maxwell's equations for electromagnetic waves at graphene interface, and selecting appropriate continuity boundary conditions for the fields, we

obtain the plasmon dispersion of graphene in terms of its conductivity [33],

$$-2\pi iq\sigma(\omega) = \omega, \tag{2.30}$$

where wave vector $q = \sqrt{k_x^2 - (\omega/c)^2}$. Based on Eq. (2.26) and (2.27), under the condition of $\omega >> \tau^{-1}$, this equation gives the dispersion solution when the intraband conductivity is dominant. Considering only the intraband surface conductivity of graphene, the resonance frequency of graphene is given by [34],

$$\omega_r^2 = \frac{8e^2 k_B T q}{\hbar} \ln\left[2\cosh(\mu_c/2k_B T)\right], \tag{2.31}$$

Based on the definition of chemical potential $\mu_c \propto n_0^{1/2}$ at low temperatures, the plasmon frequency is peculiarly dependent on the carrier density, and scales like $\omega_r \propto n_0^{1/4}$.

Now, we review the experimental observations and research of tunable intrinsic plasmons in graphene metasurfaces.

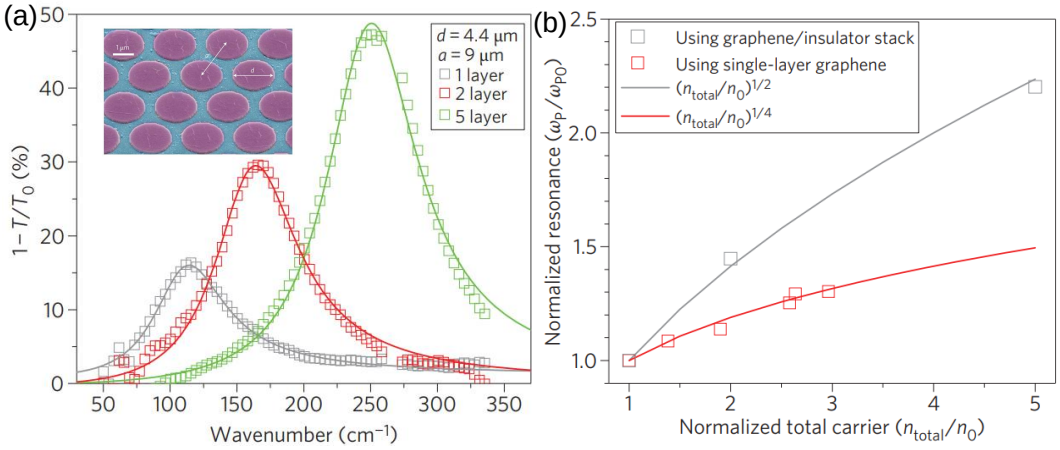

Figure 2.6: Tunable infrared plasmonic graphene-based devices. (a) Plasmon extinction in transmission of the stacked graphene/insulator microdisk array with one, two, and five graphene layers, marked by grey, red and green rectangles, respectively. The left inset indicates the SEM image of the proposed stacked graphene/insulator microdisk array arranged in a triangular lattice. (b) Normalized carrier density dependence of the normalized plasmonic resonance frequency, determined for graphene/insulator microdisk array (grey) and single-layer graphene (red), respectively. Reproduced from Ref. [32]

As indicated in Fig. 2.6, Yan *et al.* [32] experimentally demonstrated direct in-

teraction of localized graphene plasmons with infrared light. This was demonstrated using transparent photonic devices composed of a stack of graphene/insulator microdisk array arranged in a triangular lattice, which can be tuned by parameters like the diameter d of the microdisk, the lattice constant a of triangular lattice, the number of graphene layers. Specifically, Figure 2.6(a) indicates that the resonance frequency shifts upwards as the number of graphene layers in the patterned graphene/insulator stacks increases, in the meantime, the peak intensity increases significantly with the increment of the graphene layer. Moreover, the total carrier density of the plasmonic devices can be tuned by increasing the number of graphene layers in stacked graphene/insulator microdisk, and its relation with a plasmonic resonance frequency determined for single graphene layer and graphene/insulator stack is given in Fig. 2.6(b). The plasmonic resonance of a single graphene layer follows the $\omega_r \propto n_0^{1/4}$ dependence, while the enhanced plasmonic resonance of the patterned graphene/insulator stack indicates $n_0^{1/2}$ carrier density dependence. In addition, they showed the potential applications of graphene/insulator stack as a widely tunable far-infrared notch filter with 8.2 dB rejection ratio and Terahertz linear polarizer with 9.5 dB extinction ratio.

Nonlinear Optical Properties of Graphene

Nonlinear optics refers to the nonlinear response properties of light in a nonlinear media, such as frequency, polarization, and phase of incident lights [36]. Nonlinear optical properties are typically observed under the interaction with strong coherent light such as lasers. The electric polarization generated by the medium depends on the incident electric field. Under a low light and matter interaction, the high-order terms of electric polarization can be ignored because the high-order coefficients are extremely small compared with linear coefficient, so the linear relationship between electric polarization and electric field can be approximated. However, under the interaction with a strong laser field with high intensity, the high-order term of the electric polarization cannot be ignored, and nonlinear effects appear. These nonlinear interactions give rise to a number of optical phenomena, such as frequency-mixing processes, optical Kerr effect, cross-phase modulation, and multi-

photon absorption [36, 37].

The standard semiclassical description of nonlinear optical response is based on Maxwell's equations in Eq. (2.1), including nonlinear dependence of the electric polarization, $\boldsymbol{P}$, on the applied electric field with nonlinear electric susceptibilities. The nonlinear electric polarization can be described by a Taylor series [36],

$$\boldsymbol{P}(\boldsymbol{r},t) = \varepsilon_0\chi^{(1)}\boldsymbol{E}(\boldsymbol{r},t) + \varepsilon_0\chi^{(2)}\boldsymbol{E}^2(\boldsymbol{r},t) + \varepsilon_0\chi^{(3)}\boldsymbol{E}^3(\boldsymbol{r},t) + \cdots \tag{2.32}$$

where $\chi^{(1)}$ is the linear electric susceptibilities, and the quantities $\chi^{(2)}$ and $\chi^{(3)}$ are the second- and third-order nonlinear electric susceptibilities, respectively. To be more specific, the linear susceptibility $\chi^{(1)}$ is responsible for the common refractive index of the medium; the second-order nonlinear susceptibility $\chi^{(2)}$ could generate second-order effects such as the SHG process; and the third-order nonlinear susceptibility $\chi^{(3)}$ could describe phenomena, like third-harmonic generation (THG) process, four-wave mixing (FWM) process and an intensity-dependent optical Kerr effect.

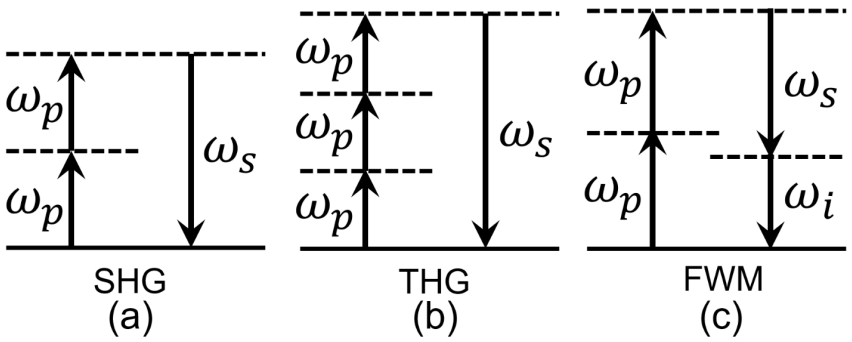

Figure 2.7: From leftmost to the rightmost panels, energy level scheme of SHG, THG, and FWM processes.

We show in Fig. 2.7 the photon energy level of three different harmonic generation processes. The applied field frequency is called the pump frequency ω_p, the desired output frequency is called the signal frequency ω_s, and the other, unwanted, output frequency is called the idler frequency ω_i. Specifically, the SHG process contains two photons in the nonlinear interaction with applied pump ω_p and generated signal ω_s. Similarly, the interaction between three photons of energy ω_p leads

to an output signal ω_s in the THG process. If two different optical frequency components (pump and signal) propagate together in a nonlinear medium with a $\chi^{(3)}$ coefficient, pump ω_p provides amplification for a signal frequency component ω_s and generates an idler frequency component ω_i as well, which is called degenerate FWM [see Fig. 2.7(c)].

Based on the tunable photonic properties of graphene, the nonlinear processes in graphene including nonlinear absorption [38], nonlinear refraction [39], THG, FWM process [40], and optical Kerr effect [41] have also been widely studied, especially the aspects of excitation methods of various lasers, broad frequency domain, and multiple graphene layers. For two-dimensional materials, similarly to the linear optical properties of graphene which can be described by its permittivity in terms of surface conductivity, the nonlinear optical response of graphene can generally be described by nonlinear surface conductivity tensors. Since the second-order nonlinear optical process can occur only in noncentrosymmetric crystals, graphene as a centrosymmetric material, exhibits THG and a strong optical Kerr effect with large third-order nonlinear susceptibility. The third-harmonic (TH) surface conductivity tensor of graphene can be expressed by [42],

$$\sigma_s^{(3)} = \frac{i\sigma_0 \left(\hbar v_F e\right)^2}{48\pi \left(\hbar\omega\right)^4} T\left(\frac{\hbar\omega}{2E_F}\right), \tag{2.33}$$

In this way, the bulk nonlinear conductivity of graphene can be evaluated in terms of surface conductivity and effective thickness as $\sigma_b^{(3)} = \sigma_s^{(3)}/h_{eff}$, which is closely related to the bulk third-order nonlinear susceptibility $\chi^{(3)}$ of graphene. Since the nonlinear susceptibility is usually measured in experiments, we define the nth-order nonlinear susceptibility [42],

$$\chi^{(n)} = \frac{i}{\varepsilon_0 n\omega_f}\sigma_b^{(n)}, \tag{2.34}$$

where $\sigma_b^{(n)}$ is nth-order nonlinear bulk conductivity, the ω_f is the fundamental frequency, and $n\omega_f$ represents the frequency at nth-order harmonic. The nonlinear susceptibility is a complex valued physical quantity, and it can be measured by ex-

perimental techniques, like Z-scan [43], FWM [40], harmonic generation [44], and pump-probe [45]. The nonlinear absorption, like saturable absorption, is related to the imaginary part of the third-order nonlinear susceptibility, while the real part of the third-order nonlinear susceptibility of graphene plays a significant role in nonlinear optical processes such as THG and optical Kerr effect.

Due to large optical near-field enhancement and large life-time of plasmons in graphene metasurfaces, strong nonlinear interactions can be achieved in graphene metasurfaces at an ultralow pump power in a wide range of wavelengths based on a relatively large nonlinear coefficient. The real part of $\chi^{(3)}$ is responsible for nonlinear changes in the refractive index, and it causes a variation in the refractive index of graphene which is proportional to the intensity of the applied light, namely, Kerr effect. Zhang *et al.* [39] measured a giant nonlinear refractive index $n_2 = 10^{-7}\mathrm{cm}^2/\mathrm{W}$ of graphene by Z-scan technique at 1.55 μm, which is almost 9 orders of magnitude larger than bulk dielectrics.

To summarize, the optical properties of graphene make it as an ideal 2D platform to achieve plasmonic and other optical modes. Firstly, the tunable and large chemical potential (Fermi energy) $\mu_c = \hbar v_F \sqrt{n_0 \pi}$ with Fermi velocity $v_F = 9.1 \times 10^5 \mathrm{m/s}$ [46], is determined by tunable and large carrier densities $n_0 \approx 10^{11} - 10^{14}$ cm^{-2} [47], which can be electrically and chemically tuned by gate voltage and chemical doping, respectively. Since graphene is a tunable optical material, the terahertz to the mid-infrared frequency range of graphene plasmon polaritons is more widely applied than the noble metal plasmons at low-frequency range. This property makes graphene a promising material for precise and tunable plasmonic devices and sensing applications.

Secondly, electrons in graphene have tunable and small Drude mass, $m^* = E_F/v_F^2$. Under an external magnetic field, it contributes to an ultrahigh cyclotron frequency $\omega_c = eB/cm^* = eB_z v_F^2/cE_F$ up to Terahertz range.

Thirdly, due to a relatively large nonlinear coefficient, THG and optical Kerr effect can be realized in graphene metasurfaces at an ultralow pump power, which can lead to tunable nonlinear optical processes in graphene-based materials by con-

trolling the light intensity.

Fourthly, graphene has an extremely large relaxation time τ which can be achieved via high-quality graphene fabrication [48]. It has been demonstrated that the lifetime of graphene plasmons can be increased to 50 ps if graphene is under a strong static magnetic field [49]. The large relaxation time significantly reduces the imaginary part of permittivity of graphene, which leads to long light propagation length in graphene with low energy loss.

2.3 Topological Photonics

Research in topological photonics, inspired by the theory of QHE in solid-state physics, has led to the discovery of novel and unique phenomena, such as unidirectional, defect-immune, and scattering-free propagation of light [50, 51, 52], which have the potential to contribute to the development of robust on-chip ultracompact nanophotonic devices. Currently, a variety of experimental platforms are available for topological photonics, including metamaterials, PhCs, evanescently coupled waveguides, and optical-ring resonators [52].

Photonic topological phases are the classical electromagnetic wave analogs of electron topological phases studied in condensed matter physics. Klitzing *et al.* firstly proposed the integer QHE in 1980 [53]. When an external magnetic field is applied and perpendicular to the current flow of an electrical conductor, the Hall effect is the generation of a voltage difference (Hall voltage) across the electrical conductor transverse to the current flow due to the Lorentz force, and the Hall conductance (ratio between channel current and Hall voltage) is proportional to the strength of applied magnetic field. Differently, Klitzing *et al.* demonstrated that two-dimensional electron gas under a strong external magnetic field shows the corresponding Hall conductance being independent on the external magnetic field, which exactly equals to e^2/hC_n with C_n being an integer [54]. Moreover, under the action of the driving force provided by the confining potential, strong magnetic fields lead to a suppression of both elastic and inelastic backscattering of the unidirectional movement of electrons along the edge of the electric system, and the

unidirectional propagation direction is dependent on the incident direction of external magnetic field. Significantly, the integer quantity of Hall conductance is exactly equal to the number of scattering-free states propagating along the edges.

By referring to the concept of topological invariant under a continuous change in topology, the number of scattering-free edge states is defined by a topological invariant, Chern number C_n. In other words, if the Chern number of a system is nonzero, which is topological nontrivial, the corresponding number of edge states with unidirectional and scattering-free characteristics is called topological edge states. In contrast, the system with a zero Chern number is topologically trivial. To realize a topologically nontrivial system, the breaking of inversion symmetry is an inevitable requirement. In the system with QHE, an external magnetic field is the key factor to break the time-reversal symmetry of the system.

Moreover, another interesting effect of a new 2D topological phase, the quantum spin-Hall effect (QSHE) in the presence of time-reversal symmetry, was proposed by Kane and Mele in 2005 [55, 56]. They demonstrated the spin-Hall effect with zero Chern number by introducing the binary topological invariant Z_2. In this case, the binary topological invariant represents the Chern number and characterizes the wave function. Each topological invariant is nonzero but the sum of them can lead to zero Chern number. The simulation results show that the topological spin-Hall states are robust against disorders without an external magnetic field. Moreover, Raghu and Haldane firstly studied the QHE edge states in periodic PhCs [57, 58]. Through the time-reversal symmetry breaking via an external magnetic field, two-dimensional Faraday-effect media exhibits a nontrivial photonic bandgap. As a result, a topological edge mode at a frequency inside the bandgap shows unidirectional propagation properties and is immune to backscattering and disorder [58].

2.3.1 General Concepts of Topological Phases

In topology, the Gauss-Bonnet theorem expresses a relationship between surfaces in differential geometry, which is the integral of a Gaussian curvature K_c over the entire surface S_c of the continuum. Then, it is proved that the integral product of a

closed surface is an integer multiplying 2π, namely $\int K_c dS_c = 2\pi\chi_c$. The integer χ_c called topological invariant is related to the genus of the surface, which makes it possible to define different topologies. In an electronic system, we can naturally introduce similar integrals to calculate the topological invariants of different systems. Before introducing such integrals, the object of the integral and the interval of the integration should be defined. Firstly, based on the periodicity of the crystal lattice, the first Brillouin zone is topologically equivalent to a torus. The basic geometrical and topological properties of a single-particle Hamiltonian $H_{\boldsymbol{k}}$ in the momentum space, such as the Berry connection, Berry curvature, Berry phase, and the Chern number, are introduced. The Bloch's theorem describes the eigenstates $u_{n,\boldsymbol{k}}(\boldsymbol{r})$ in the momentum space obey periodicity condition and satisfy,

$$H_{\boldsymbol{k}} u_{n,\boldsymbol{k}}(\boldsymbol{r}) = E_n(\boldsymbol{k}) u_{n,\boldsymbol{k}}(\boldsymbol{r}), \tag{2.35}$$

where $E_n(\boldsymbol{k})$ is the energy dispersion of nth band, and the geometrical properties of the nth band are described by how the eigenstate $u_{n,\boldsymbol{k}}$ varies with $\boldsymbol{k}$ vector in the first Brillouin zone [59]. This geometrical property can be quantitatively defined by the Berry phase γ [60].

$$\gamma = \oint \boldsymbol{A}_k^n \cdot d\boldsymbol{k}, \tag{2.36}$$

where $\boldsymbol{A}_k^n$ is the Berry connection, which is defined as,

$$\boldsymbol{A}_k^n = i\langle \boldsymbol{u}_{n,\boldsymbol{k}} | \boldsymbol{\nabla}_{\boldsymbol{k}} | \boldsymbol{u}_{n,\boldsymbol{k}} \rangle, \tag{2.37}$$

Note that the Berry connection is not gauge invariant under a gauge transformation of $|\boldsymbol{u}_{n,\boldsymbol{k}}\rangle \rightarrow e^{i\zeta(\boldsymbol{k})} |\boldsymbol{u}_{n,\boldsymbol{k}}\rangle$, so that a gauge invariant Berry curvature is given by,

$$\boldsymbol{\Omega}_k^n = \boldsymbol{\nabla}_{\boldsymbol{k}} \times \boldsymbol{A}_k^n, \tag{2.38}$$

Berry phase in Eq. (2.36) for a given closed path is gauge invariant modulo 2π, so that Chern number is defined as the integral of Berry curvature over the whole FBZ,

$$C^n = \frac{1}{2\pi}\int_{BZ} \boldsymbol{\Omega}^n_{\boldsymbol{k}} dS_{\boldsymbol{k}},, \tag{2.39}$$

From this integral, if Berry connection $\boldsymbol{A}^n_k$ is continuous in the FBZ, the Chern number must be zero, which can be changed if Berry connection $\boldsymbol{A}^n_k$ is not continuous. Moreover, the FBZ can be divided into two regions S and S', with the common boundary as $\partial S = -\partial S'$. Equation (2.39) becomes,

$$\begin{aligned} C^n &= \frac{1}{2\pi}\oint_{\partial S} \boldsymbol{A}^n_k d\boldsymbol{k} - \frac{1}{2\pi}\oint_{\partial S'} \boldsymbol{A}^n_k d\boldsymbol{k} \\ &= \frac{1}{2\pi}\left(\gamma - \gamma'\right) \end{aligned} \tag{2.40}$$

where γ and γ' are the Berry phases along the contour of ∂S and $\partial S'$, respectively. Since Berry phases are calculated along the same path, the difference between them will be multiples of 2π, which indeed proves that the Chen number is an integer [61]. Avron *et al.* [62] demonstrated that the Chern number must be strictly constant under smooth perturbations, which preserves the bandgap separating *n*th band from adjacent bands. Chen number is an important numerical value characterizing the quantized collective behavior of the wave function, and it is the topological invariant of quantum Hall insulators (QHI). Furthermore, Chern number can also characterize the topological properties of a photonic system.

The Haldane model [63] was the first 2D condensed-matter lattice model that proved to exhibit a nonzero quantization of the Hall conductance in the absence of an external magnetic field. The model proved that breaking the time-reversal symmetry is necessary to obtain the QHE. For a honeycomb lattice like graphene, possessing Dirac cones in the electric band structure (see Fig. 2.5), the cone-like electric band structure is generated by the linear crossing between the valence and conduction bands at the Fermi level, and can be theoretically described by massless fermions in the relativistic Dirac equation. Massless fermions lead to various QHE in topological materials based on the fact that the additional mass term will open

the nontrivial bandgap at the Dirac point.

For example, a Pauli matrix term σ_z can be introduced into the effective Hamiltonian of graphene [Eq. (2.21)], so that an energy gap will be opened at the Dirac points and a nonzero Chern number of the band below the bandgap is obtained. This σ_z perturbation term can be achieved by breaking time-reversal symmetry or spatial-inversion symmetry, based on the fact that the gapless Dirac cones are protected by the inversion symmetry of the crystal lattice [64]. It can also be explained by the zero Chern number of the system without inversion symmetry breaking. Then, when the time-reversal symmetry is present, the Berry curvature obeys $\boldsymbol{\Omega^n}(-\boldsymbol{k}) = -\boldsymbol{\Omega^n}(\boldsymbol{k})$ in the FBZ, leading to the integral of Berry curvature (Chern number) over the FBZ necessarily being zero. A new QSHE in a time-reversal invariant system with an energy gap that is generated by the spin-orbit interaction was introduced by Kane and Mele in 2005 [55]. When an external magnetic field is applied, the magnetic fields acting on the two spins are opposite, which causes the Chern numbers of spin-polarized electrons for spin-up and spin-down to have opposite signs. Therefore, the Chern numbers for each spin are nonzero while the total Chern number of the system remains zero with the preserved time-reversal symmetry.

To introduce these topological phases in a photonic system, PhCs play a significant role. PhCs periodically change the refractive index (or the dielectric constant ε), which is analog to the periodic distribution of atoms in crystalline materials with an artificially created lattice. In this way, periodic structures and the Brillouin zone of PhCs can be achieved. Similar to the formula for electronic systems, the electric field in the photonic system is utilized to calculate the Berry connection and the Berry curvature, which are integrated over the FBZ to obtain the Chen number. The inversion symmetry breaking can be introduced to make the photonic crystal topologically nontrivial. By referring to Bloch's theorem, an effective periodic photonic potential $V(\boldsymbol{r})$ is added to the system, which can gap out a trivial bandgap due to Bragg diffraction [51]. In topological systems, the symmetry breaking generates the gauge-dependent Berry connection $\boldsymbol{A}_k^n$ acting as a kind of vector potential in the

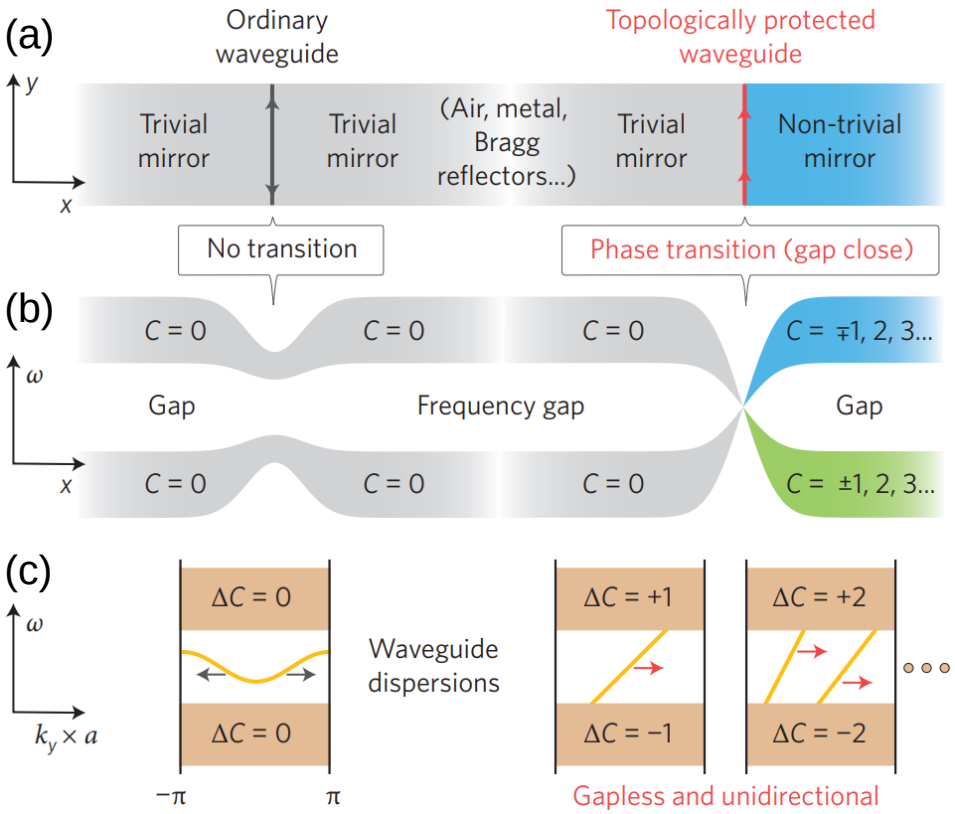

Figure 2.8: Topological phase transition. (a) Comparison between trivial and nontrivial periodic photonic waveguides formed by mirrors. (b) Transition between frequency bands of trivial and nontrivial waveguides. (c) Band diagram of trivial and nontrivial topological waveguide with interfacial states. ΔC represents the Chern number difference between the mirror shown in Fig. 2.8(a). Reproduced from Ref. [50]

wave function. Consequently, the gauge-invariant Berry curvature and Chern number can be explained as the magnetic field and the number of magnetic monopoles of the Berry flux, respectively. Similarly, in the time-reversal invariant systems with QSHE, the corresponding Berry connection, Berry curvature, and Chern number appear in pairs with pseudospin up and pseudospin down. When the Chen number is zero, it is proved that there is no Berry monopole in the FBZ when the inversion symmetry is preserved, which is topologically trivial. Otherwise, nonzero Chern numbers are topologically non-trivial [50].

Figure 2.8 summarizes the main types of topological phase transition in trivial and nontrivial photonic waveguides. The bandgap of an insulator is similar to the frequency gap of an optical mirror which reflects and can not transmit light in a

given frequency range. As shown in Figs. 2.8(a) and 2.8(b), for a trivial waveguide (left) with an interface formed by two mirrors with same topologies, both frequency bands have zero Chen numbers, so they can be connected directly across the interface with a topologically trivial frequency bandgap in which light cannot propagate. For topologically nontrivial waveguide (right) formed by two different topologies, their frequency bands cannot be directly connected, so that the frequency bandgap is closed and the Chen number of the topologically nontrivial mirror becomes zero. Meanwhile, the topological phase transition occurs at the interface where the gap is opened again. Since the topological phase transition takes place at the interface, there will be gapless edge modes at the interface, which are topologically protected. In general, the number of gapless edge modes is equal to the difference of the Chern numbers across the interface [51].

The property of edge modes inside trivial and nontrivial bandgaps is illustrated in Fig. 2.8(c). In a trivial waveguide (left), there is no edge mode inside the gap that traverses through the entire bandgap, so the bandgap still exists in the trivial waveguide even if there is a certain edge mode. Moreover, the light of a trivial edge mode at a fixed frequency is allowed to propagate in two directions with opposite group velocities, and the phenomenon of backscattering can exist during the light propagation. For the topologically protected waveguide, as shown on the right of Fig. 2.8(c), propagating edge modes appear when a nontrivial frequency bandgap opens. The frequency dispersion of the topologically protected edge mode inside the bandgap traverses through the entire bandgap, which only allows light propagating in opposite directions (positive or negative) along opposite edges (top or bottom) of the system. Since the frequency dispersion of edge modes is spatially separated, the scattering processes from one edge mode to the other edge mode can be suppressed during the unidirectional propagation of these edge modes [52]. Specifically, the Chen number represents the number of unidirectional topologically protected edge modes inside the bandgap. This remarkable property creates a range of new opportunities throughout topological photonics, which makes it possible to design and fabricate waveguides guiding scattering-free unidirectional light in a ro-

bust manner.

Topological photonic modes could be achieved by gapping out symmetry-protected Dirac cones. For example, time-reversal symmetry can be broken through temporal modulation or magneto-optical effects under an external static magnetic field, which is an analogue QHE. For time-reversal invariant photonic systems, field symmetry or spatial-inversion symmetry breaking can be induced by spatial asymmetric perturbations, which emulates QSHE or quantum valley-Hall effect (QVHE) [65]. We will present and discuss in more detail the concepts of time-reversal symmetry and invariant time-reversal symmetry breaking.

2.3.2 Time-reversal Symmetry Systems in Photonics

Time-reversal symmetry breaking in photonic systems could be achieved in the presence of an external magnetic field, and this effect can be considered as the integer QHE in an electron gas. Hence, the topology of band structure can be quantified by the integer-valued Chern number. Most of the experiments studied topologically protected unidirectional propagation against back-scattering in magneto-optical platforms.

In photonic systems, the magnetic permeability of the material can be changed by introducing ferrite rods under an external magnetic field, which can realize the analog QHE of photons. Wang *et al*. firstly conducted the experiment on a magneto-optical photonic crystal at microwave frequencies and successfully realized the QHE of the topological one-way edge waveguide in 2009 [66]. The sketch of the experimental setup is shown in Fig.2.9(a). The array of ferrite rods is sandwiched between two parallel metallic plates under a uniform magnetic field, which forms a gyromagnetic photonic crystal with confined 2D TM modes. By breaking the time-reversal symmetry with a magnetic field related to the interface between topologically protected waveguides and topologically trivial mirrors (air), a nontrivial topological bandgap is opened and an edge mode emerges inside the bandgap, as shown in Fig.2.9(b). Specifically, the number of edge modes in each bandgap and their propagation direction are determined by the sum of the Chern numbers of all bands below the edge mode. Figure 2.9(c) demonstrates that the corresponding light

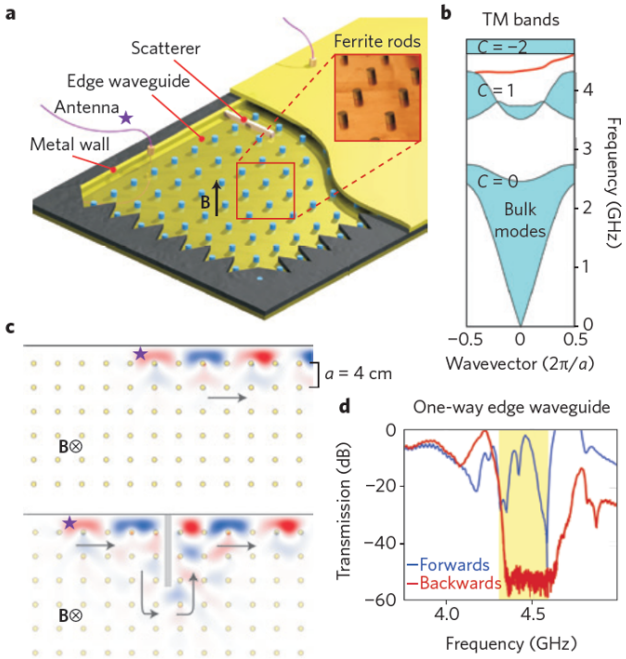

Figure 2.9: Two-dimensional magneto-optical photonic crystal generating a one-way edge waveguide in the microwave domain. (a) Experiment setup of the magneto-optical waveguide under a 0.2T magnetic field. The blue dots indicate the Ferrite rods that are sandwiched between two parallel copper plates. The metal wall prevents the radiation loss into the air so that the 2D TM mode is confined in the edge waveguide. (b) Projected dispersion of the TM mode band (blue region), a topologically protected one-way edge mode (red line) appears between the second and third bands. (c) One-way topological edge mode propagation in the waveguide under a static magnetic field B. The unidirectional light propagation is against a long metallic scatterer. (d) Transmissions of forward and backward modes show non-reciprocal and robust properties of the one-way topological edge mode. Reproduced from Ref. [66]

propagation is unidirectional and without back-scattering, which is independent on the nature and strength of scatters or defects. In Fig. 2.9(d), the transmission of the forward and backward propagating lights is measured. It is found that the intensity of the backward propagating light was orders of magnitude less than the forward propagating light, indicating that the light of topological mode is indeed propagating in one direction.

Graphene is an attractive 2D plasmonic platform to realize relatively unexploited topological propagation and integrated photonic devices from terahertz to the mid-infrared regime, due to its tunable Fermi energy (chemical potential), ultra-high cyclotron frequencies up to the terahertz range and long relaxation times [68].

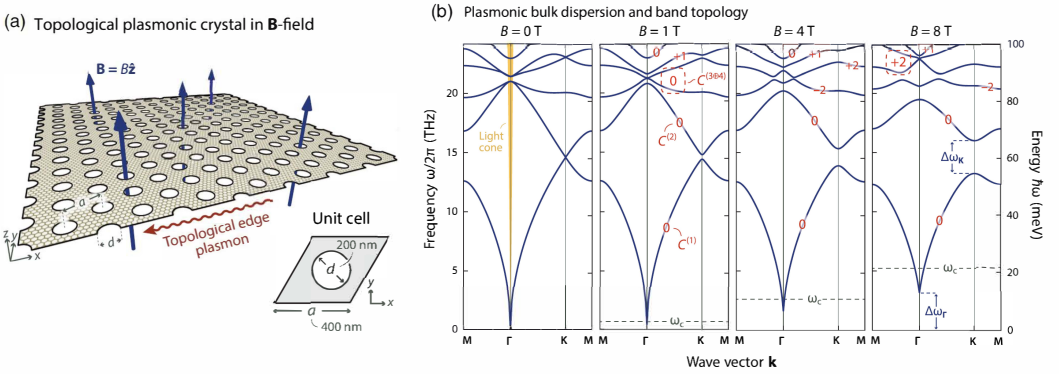

Figure 2.10: Band topology of the periodically patterned monolayer graphene under a static magnetic field. (a) Schematic of the monolayer graphene metasurface, which consists of a rhombic unit cell with a hole. (b) Band diagram along the high-symmetry points of the first Brillouin zone (FBZ) under different magnetic fields ($B = 0, 1, 4, 8$ T). Reproduced from Ref. [67]

Additionally, advances in nanofabrication techniques like electron-beam lithography (EBL), scanning tunneling microscope (STM) lithography, or ultraviolet (UV) lithography method, also make it possible to fabricate precise periodic topologically protected graphene structures [69]. All these advantages can lead to a graphene-based topological structure with high frequency, relatively large bandgap, long propagation, and low loss [70]. Taking advantage of these remarkable properties, the time-reversal symmetry breaking in 2D graphene platform, was theoretically proposed via a static magnetic field by Jin *et al.* in 2017 [67]. The proposed 2D monolayer graphene metasurfaces consist of a periodic hexagonal array of holes, as indicated in Fig.2.10(a). A perpendicular static magnetic field is applied and breaks the time-reversal symmetry. Therefore, the symmetry-protected Dirac cones are gapped out so that a nontrivial bandgap emerges at the frequency of a few tens of terahertz. Figure 2.10(b) demonstrates that the nontrivial bandgap size increases with the increasing magnetic field B. Consequently, a topological plasmonic edge state emerges inside the gap and the light propagation of topological edge state is immune to a structural defect.

Because magneto-optic PhCs have a strong reaction on the magnetic field in the microwave domain, most experiments were conducted on gyromagnetic PhCs. How to extend the microwave domain towards optical frequencies is another hot topic.

At optical frequencies, the weak magneto-optical effect could be strengthened by enhanced in man-made metamaterials [71]. The resulting bandgap is narrower than the bandgap in the microwave domain but is still wide enough to achieve topological edge states. Another efficient solution is to break the time-reversal invariant symmetries of a photonic system at optical frequencies rather than adding an external magnetic field in the microwave region.

2.3.3 Analog Quantum Spin-Hall Systems in Photonics

In a time-reversal invariant system as indicated in Fig. 2.11, the additional nonzero Berry curvature occurs in two time-reversal partner domains, called pseudo-spin-up and pseudo-spin-down, respectively. In each time-reversal partner domain, additional Berry curvature generates nonzero spin-Chern numbers with opposite signs ($\pm$ or $\mp$) for two mixing bands. In this way, the sum of spin-Chern numbers for two time-reversal partner domains remains zero while the nonzero spin-Chern number can be assigned to each pseudo-spin with a spin Chern number as $C_{spin} = (C_{\downarrow} - C_{\uparrow})/2$, which removes the requirement of time-reversal symmetry breaking by an external magnetic field. When a domain-wall interface is created by combining two domains with opposite signs of the spin-Chern number of each pseudo-spin, the nonzero spin-Chern number difference across the domain-wall interface could possess topologically protected edge modes with pseudo-spin-up or pseudo-spin-down, called helical edge states.

In the presence of time-reversal symmetry, other symmetries, like field symmetry and spatial-inversion symmetry can be broken in condensed matter, and achieve a kind of QSHE or QVHE. Starting from analog quantum spin-Hall systems, various methods have been utilized to introduce a synthetic magnetic field into PhCs, such as coupled resonators [72, 73], controlling the phase of dynamic modulation in the time domain [74], in which pseudo-spins are represented by clockwise and anticlockwise modes. Since the synthetic magnetic field is analogous to the external magnetic field in quantum Hall topological photonic insulators, one can achieve the equivalence between the QHE and the QSHE in PhCs. Hafezi *et al.* firstly proposed the spin-Hall optical systems with linear optical elements in 2011 [72], and then

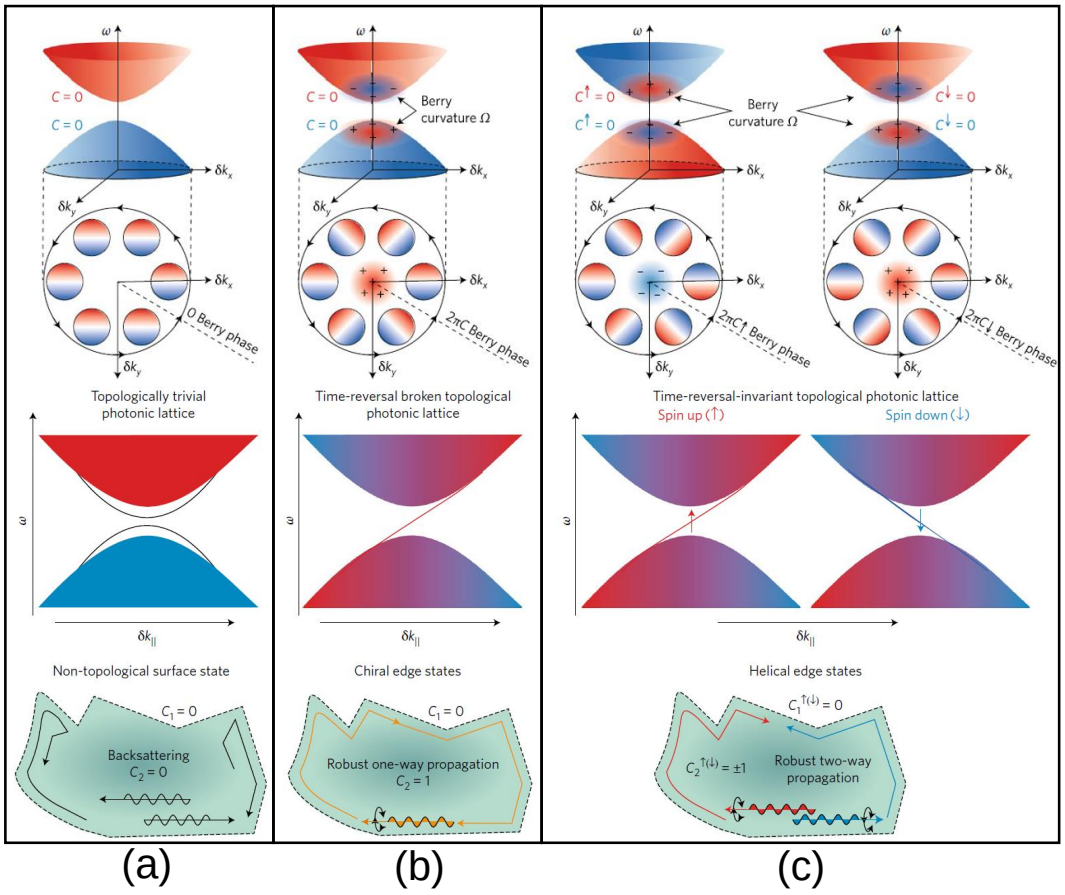

Figure 2.11: Comparison between (a) trivial photonic lattice, (b) nontrivial QHI, and (c) nontrivial quantum spin-Hall topological photonic insulators. Top: band structure with a frequency bandgap. Middle: band structure with edge states inside the bandgap. Bottom: transport of trivial, topological one-way, and helical edge states along the interface. Reproduced from Ref. [51]

carried out the experiments on silicon ring resonator arrays in 2013 [73].

Figure 2.12(c) indicates the sketch of the silicon optical ring micro-resonator array used in this experiment. The coupling between two neighboring resonators is via an off-resonant link ring. By controlling differential optical paths, photons can be made to hop between neighboring resonators in opposite directions to create a synthetic magnetic field. In this system, nonzero hopping coupling phases of two neighboring resonators change linearly in two opposite directions. This phenomenon is similar to the cyclotron motions of electrons under a static magnetic field with the increasing or decreasing ($\pm$) vector potentials. Consequently, two pseudospins are degenerate as two components of the modes of ring resonators pre-

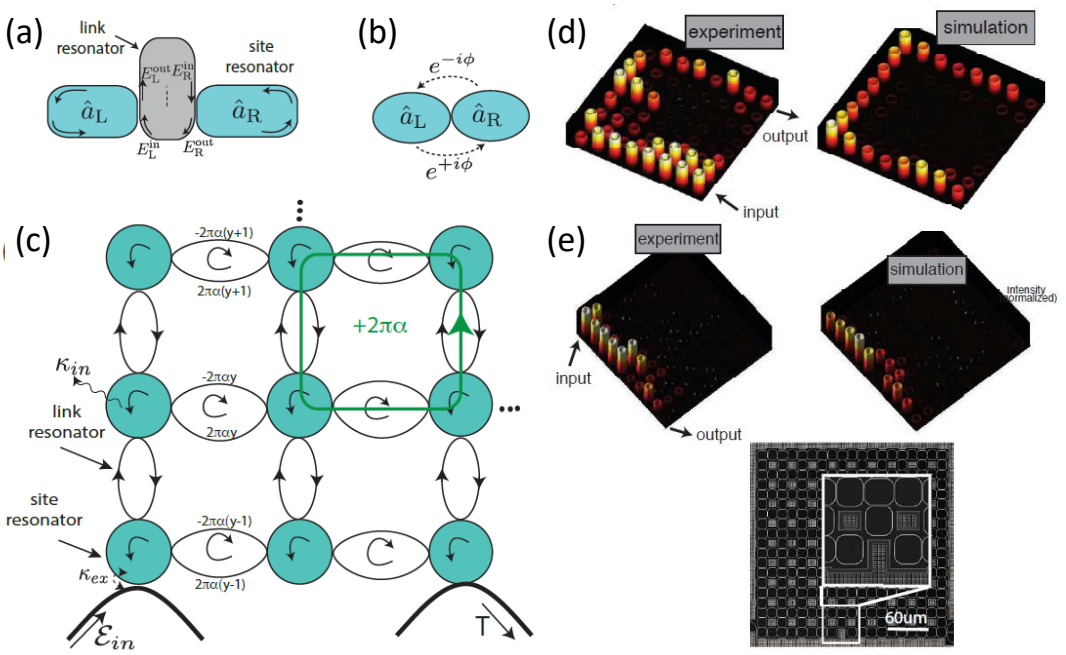

Figure 2.12: Topological features and structure design of a spin-Hall optical system with a synthetic magnetic field. (a) Schematic of the dynamic coupling between the two site resonators, which is governed by a link resonator. (b) The integral of the upper and lower off-resonant link resonators can be viewed as the hopping phase difference between two neighboring site resonators. (c) Sketch of the 2D coupled ring resonator array. The hopping phase difference leads to optical paths in opposite directions. (d) Spatial intensity profile of the edge state showing light propagation along the boundary of the system. (e) Spatial intensity profile of the edge mode showing routing of light around a defect. (a), (b), and (c) are reproduced from Ref. [72], and (d) and (e) are reproduced from Ref. [73]

serving time-reversal symmetry in the synthetic magnetic field, and the optical path of a pair whispering gallery-like modes has two opposite propagation directions, clock-wise and counter-clock-wise directions, corresponding to psuedospin down and psuedospin up, respectively.

The 2D coupled-resonator optical waveguides show robustness against defects, as indicated in Figs. 2.12(d) and 2.12(e). The silicon ring resonator array setup operates in the telecom range. When an edge mode is excited by an input laser, the edge mode propagates along the edge of the spin-Hall system in a specific clockwise direction [see Fig. 2.12(d)]. If a resonator part is removed [see Fig. 2.12(e)], the topological edge mode still propagates along the edge without back-scattering. As a result, photonic devices based on the spin-Hall effect system can improve

the topological performance and achieve the two spin edge states robust against perturbations. In these systems, the Chern number is zero but the nonzero binary topological invariant provides two robust spin edge states with opposite chiralities under opposite synthetic magnetic fields.

Bianisotropy-induced magneto-electric coupling phenomena have been widely studied in electromagnetic metamaterials possessing the bianisotropy coupling, which serves as a synthetic gauge field leading to a topological transition across the edge. Cheng *et al.* [75] and Lai *et al.* [76] experimentally studied robust propagation of topological edge modes along reconfigurable domain walls by combining two hexagonal arrays of metallic cylinders attaching top and bottom metacrystal plates, respectively. By moving cylinders up or down between the parallel plates, the inversion symmetry is reduced and a nontrivial bandgap is opened with a nonzero spin-Chern number for psuedospins at lower and upper bands. When the domain-wall interface is created by switching cylinders up and down (change of the synthetic gauge field), the psuedospin up and down edge modes appear inside the bandgap with opposite group velocities, whose robust properties against induced disorder were demonstrated in the experiments. Moreover, spin-locked topological edge modes were further applied as an ultrafast topological switch based on the fact that the topological edge mode only propagates along the reconfigurable domain-wall interface.

There are several key differences between the edge modes generated on the domain-wall interface of quantum Hall and quantum spin-Hall topological photonic insulators. For example, the edge of the quantum Hall topological photonic insulators only supports one-way propagation of the topological edge mode based on the fact that only one topologically protected edge mode corresponds to one edge termination. By contrast, topological edge modes at the domain-wall interface of quantum spin-Hall topological photonic insulators are spin-polarized and propagate along the direction corresponding to their spins as indicated in Fig. 2.11. Therefore, in the case of quantum spin-Hall topological photonic insulators, spin-polarized edge modes propagate in the opposite directions when the time-reversal symmetry

is preserved.

2.3.4 Analog Quantum Valley-Hall Systems in Photonics

Electrons in two-dimensional crystals with a honeycomb lattice structure possess a valley degree of freedom. These systems exhibit a QVHE whose sign depends on the valley index. It is very similar to the QSHE, in which spin-polarized electrons are replaced by valley-polarized carriers associated to two valleys [77]. Valley degree of freedom, which is associated to the conduction-band minima (or valence-band maxima) in graphene-like two-dimensional (2D) materials with honeycomb lattice [78, 79], has recently been introduced to photonics [80, 81], too, whereby it behaves like a spin-like binary degree of freedom at high-symmetry corner points $K = (4\pi/3a, 0)$ and $K' = (-4\pi/3a, 0)$ of the FBZ with the lattice constant a.

Each valley has intrinsic chiral vorticity with specific angular momentum, which is opposite around K and K' with either left-circular or right-circular polarization. Under the valley-conservation assumption, the topological invariant of photons (valley Chern number) is defined by integrating the Berry curvature over one of the two valleys rather than the whole FBZ. Specifically, when the spatial-inversion symmetry of the system is broken, valley Chern numbers corresponding to two valleys K and K' are half-integer and have opposite signs, namely $C_K = \pm 1/2$ and $C_{K'} = \mp 1/2$.

Through a rotation of π of two honeycomb semi-infinite topological waveguides with spatial-inversion symmetry breaking, a mirror-symmetric domain-wall interface is generated, in which topologically protected valley modes can form based on the fact that the difference of valley Chern number ($\Delta C = \pm 1$) across the interface is nonzero. Since the topological valley mode exhibits valley-chirality-locking property at two valleys, circularly polarized edge modes can be selectively excited by selecting the specific angular momentum of the excitation source, and the corresponding light propagation of each circularly polarized edge mode shows a unidirectional property.

This new topological invariant, valley degree of freedom, was introduced in PhCs. Ma and Shvets [82] studied a topological valley system with a hexagonal

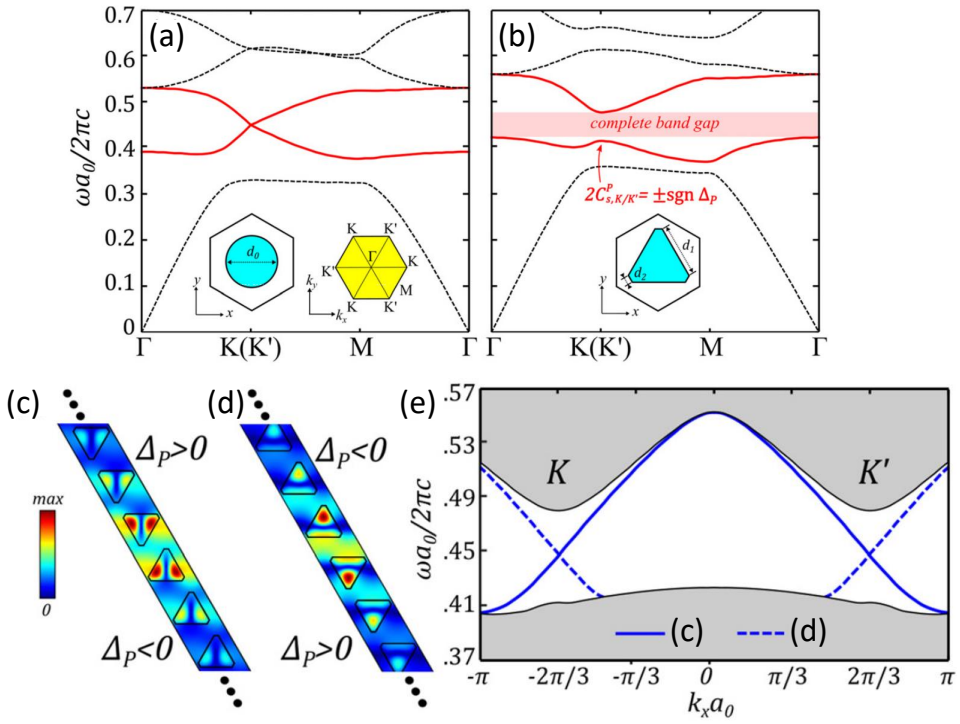

Figure 2.13: Photonic band diagrams of unperturbed and perturbed Si photonic structures. (a) Band diagram of the unperturbed Si rob structure. Degenerate bands form a Dirac cone at $K(K')$ symmetric points, marked by red lines. Insets show the hexagonal unit cell with a Si rob and its corresponding FBZ. (b) Band diagram of the perturbed Si rob structure. The symmetry-protected Dirac cone is gapped out at $K(K')$ point. Inset shows the perturbed unit cell with a triangular Si rob. (c) Finite supercell with a mirror-symmetric domain-wall interface. (d) Finite supercell with a domain-wall interface formed by flipping unit cell of (c) with π. (e) Projected band diagram of the finite supercell with a domain-wall interface. Two frequency dispersion curves of topological valley modes corresponds to configurations in (c) and (d). Reproduced from Ref. [82]

lattice, as shown in Fig. 2.13(a). A symmetry-protected Dirac cone appears at the two nonequivalent K and K' valleys of the FBZ. Then, the spatial geometric perturbations on the hexagonal lattices break the spatial-inversion symmetry and the symmetry-protected Dirac cones are gapped out at nonequivalent K and K' points [see Fig. 2.13(b)]. This hexagonal lattice with spatial-inversion symmetry breaking exhibits nontrivial Berry curvature distribution in the momentum space around each valley, which gives rise to a valley-dependent topological index associated to the integral of Berry curvature around a valley [83]. By integrating the Berry curvature around each Dirac point, one can find out that the signs of valley Chern number at K and K' symmetry points are opposite [82], $C_{K,K'} = \pm 1/2$, but the total Chern

number of the FBZ is still zero. Therefore, the domain-wall interface can be formed *via* rotations of the supercell by $\pi/3$, or π in order to connect the K and K' points. Figures 2.13(c) and 2.13(d) illustrate the domain-wall interface via a rotation of π. Since the difference of two valley Chern numbers across the domain-wall interface can be $+1$ or -1, a topologically protected edge mode appears inside the bandgap. As indicated in Fig. 2.13(e), a pair of valley-momentum-locked modes appears inside the bandgap, corresponding to configurations of the domain-wall interface in Fig. 2.13(c) and 2.13(d). Each topological valley mode has opposite group velocities at K and K' points, resulting in unidirectional light propagation along the domain-wall interface in opposite directions.

As the bandgap can emerge at the K and K' valleys with opposite valley-Chern numbers, two supercells can be generated by combining two semi-infinite waveguides with a $\pi/3$, or π rotation. It leads to a restricted condition for bending domain-wall interfaces, like zigzag interfaces, that only a $2\pi/3$ bended zigzag interface can preserve the unidirectional and backscattering-immune light propagation of a topological valley chiral mode [84]. For the armchair domain-wall interface, the breaking of translational symmetry perpendicular to the domain-wall interface mixes the K and K' points of two honeycomb lattices, so that the valley Chen number difference across the domain-wall interface cannot be well defined [85]. Similarly, when the bandgap of the projected band structure with the zigzag domain-wall interface is larger than a cutoff value, the Berry curvatures associated to two nonequivalent valleys spread significantly and overlap with each other in the FBZ. Hence, the valley Chern numbers of K and K' valleys are not well defined [85].

Until now, valley-Hall photonic modes have been mostly studied in bulk materials, such as PhCs [50, 51, 52], which have been less explored in 2D photonic platforms, including graphene. Key factors, such as large, tunable carrier densities and long intrinsic relaxation times up to the picosecond range, make graphene an ideal platform for topological plasmonics at high frequency with low loss.

2.3.5 Chern Number Calculation

The topological invariant, Chern number, is an important integer that can indicate the number of topological edge states inside a nontrivial bandgap. For a non-degenerate nth band that is separated from other bands, the Chern number of this single nth band can be defined as the integral over the momentum-space path:

$$C^n = \frac{1}{2\pi}\oint_{\partial BZ} \boldsymbol{A}_k^n d\boldsymbol{k} = \frac{i}{2\pi}\oint_{\partial BZ} \langle \boldsymbol{u}_{n,\boldsymbol{k}} | \boldsymbol{\nabla}_{\boldsymbol{k}} | \boldsymbol{u}_{n,\boldsymbol{k}} \rangle \, d\boldsymbol{k} \tag{2.41}$$

with $|\boldsymbol{u}_{n,\boldsymbol{k}}\rangle = |e^{i\boldsymbol{k}\cdot\boldsymbol{r}}\boldsymbol{E}_{n,\boldsymbol{k}}(\boldsymbol{r})\rangle$ being the normalized eigenstate of the nth band at $\boldsymbol{k}$ point, and $\boldsymbol{A}_k^n = i\langle \boldsymbol{u}_{n,\boldsymbol{k}} | \boldsymbol{\nabla}_{\boldsymbol{k}} | \boldsymbol{u}_{n,\boldsymbol{k}} \rangle$ defined as the corresponding Berry connection. Moreover, the Chern number can be recast from the line integral of the Berry connection to the integral of the curl of $\boldsymbol{A}_k^n$ over the Brillouin zone by using the Stokes theorem applied to Eq. (2.41),

$$C^n = \frac{1}{2\pi}\int_{BZ} \boldsymbol{\Omega}_{\boldsymbol{k}}^n dS_{\boldsymbol{k}} = \frac{i}{2\pi}\int_{BZ} \boldsymbol{\nabla}_{\boldsymbol{k}} \times \langle \boldsymbol{u}_{n,\boldsymbol{k}} | \boldsymbol{\nabla}_{\boldsymbol{k}} | \boldsymbol{u}_{n,\boldsymbol{k}} \rangle \, dS_{\boldsymbol{k}} \tag{2.42}$$

with $\boldsymbol{\Omega}_k^n = \boldsymbol{\nabla}_{\boldsymbol{k}} \times \boldsymbol{A}_k^n = i\boldsymbol{\nabla}_{\boldsymbol{k}} \times \langle \boldsymbol{u}_{n,\boldsymbol{k}} | \boldsymbol{\nabla}_{\boldsymbol{k}} | \boldsymbol{u}_{n,\boldsymbol{k}} \rangle$ being the Berry curvature of the nth band at point $\boldsymbol{k}$.

In the numerical calculation of the Chern number, the Brillouin zone is discretized into $N \times N$ plaquettes as shown in Fig. 2.14. Based on the Wilson-loop method, the integral of Berry curvature in each small discretized plaquette can be expressed in the form of a Wilson loop connecting four corner points from k_1 to k_4 (see red arrows in Fig. 2.14) [86]. In this way, the Chern number, as the integral of Berry curvature over the entire FBZ, becomes the sum of all Wilson loops of each small discretized plaquette. It should be noted that a similar discretization scheme can be used for the first Brillouin zone of different shapes, and the refining of the discretization mesh improves the evaluation accuracy of the Chern number [87]. If the shape of the Brillouin zone is not a square, e.g. it is a hexagonal lattice, the Brillouin zone can be reshaped into an equivalent rhombic zone due to its periodicity in the momentum space, which will be further discussed in Sec. 3.4.

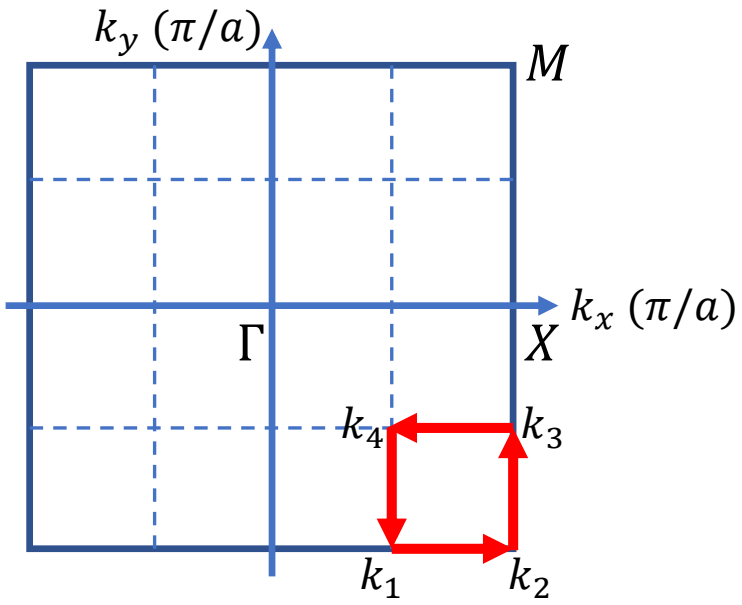

Figure 2.14: Schematic of a computational simulation zone over a square Brillouin, which is discretized into 4×4 plaquettes along the k_x and k_y directions. In particular, the red small loop from k_1 to k_4 is utilized to calculate discretized Berry curvature of each plaquette.

$$\begin{aligned} C^n &= \frac{1}{2\pi}\int_{BZ} \boldsymbol{\Omega}_{\boldsymbol{k}}^n dS_{\boldsymbol{k}} = \frac{1}{2\pi}\sum_{BZ} \Omega_{\boldsymbol{k}}^n \Delta S_{\boldsymbol{k}} \\ &= \frac{1}{2\pi}\sum_{BZ} \mathrm{Im}\ln\left[U^n_{\boldsymbol{k_1}\to\boldsymbol{k_2}} U^n_{\boldsymbol{k_2}\to\boldsymbol{k_3}} U^n_{\boldsymbol{k_3}\to\boldsymbol{k_4}} U^n_{\boldsymbol{k_4}\to\boldsymbol{k_1}}\right] \end{aligned} \tag{2.43}$$

where $U^n_{\boldsymbol{k_\alpha}\to\boldsymbol{k_\beta}}$ is normalized as $\frac{\left\langle \boldsymbol{u}_{n,\boldsymbol{k_\alpha}} | \boldsymbol{u}_{n,\boldsymbol{k_\beta}} \right\rangle}{\left|\left\langle \boldsymbol{u}_{n,\boldsymbol{k_\alpha}} | \boldsymbol{u}_{n,\boldsymbol{k_\beta}} \right\rangle\right|}$ with $\alpha,\beta = 1,2,3,4$ indicating the four corner points of each plaquette, and $\left\langle \boldsymbol{u}_{n,\boldsymbol{k_\alpha}} | \boldsymbol{u}_{n,\boldsymbol{k_\beta}} \right\rangle = \int \varepsilon(\boldsymbol{r}) \boldsymbol{u}_{n,\boldsymbol{k_\alpha}}(\boldsymbol{r})^* \cdot \boldsymbol{u}_{n,\boldsymbol{k_\beta}}(\boldsymbol{r}) d^2\boldsymbol{r}$. Note that if the material is dispersive, $\varepsilon(\boldsymbol{r})$ will also depend on the frequency of the nth band at $\boldsymbol{k}$ point, $\omega_n(\boldsymbol{k})$.

If the bands are degenerate, the Chern number for a single band is not unambiguously defined. Therefore, a composite Chern number is introduced based on the degenerate bands. Then, if there are N degenerate bands, the composite Chern number $C^{(n\oplus n+1\oplus\ldots\oplus n+N-1)}$ calculated using eigenstates from $\boldsymbol{u}_{n,\boldsymbol{k}}$ to $\boldsymbol{u}_{n+N-1,\boldsymbol{k}}$

can be expressed as,

$$
\begin{aligned}
C^{(n\bigoplus n+1\bigoplus ...\bigoplus n+N-1)} &= \frac{1}{2\pi}\mathrm{Tr}\oint_{\partial BZ}\boldsymbol{A}_k^{(n\bigoplus n+1\bigoplus ...\bigoplus n+N-1)}d\boldsymbol{k} \\
&= \frac{i}{2\pi}\mathrm{Tr}\oint_{\partial BZ}\begin{pmatrix} \ddots & \vdots & \iddots \\ \cdots & \left\langle \boldsymbol{u}_{n_i,\boldsymbol{k}}|\boldsymbol{\nabla}_{\boldsymbol{k}}|\boldsymbol{u}_{n_j,\boldsymbol{k}}\right\rangle & \cdots \\ \iddots & \vdots & \ddots \end{pmatrix} d\boldsymbol{k}
\end{aligned}
\tag{2.44}
$$

where $\boldsymbol{A}_k^{(n\bigoplus n+1\bigoplus ...\bigoplus n+N-1)}$ is a $N\times N$ matrix with each element being the Berry connection between every two degenerate eigenstates, namely $i\left\langle \boldsymbol{u}_{n_i,\boldsymbol{k}}|\boldsymbol{\nabla}_{\boldsymbol{k}}|\boldsymbol{u}_{n_j,\boldsymbol{k}}\right\rangle$ with $i,j=n,n+1,\ldots,n+N-1$. By applying Stokes theorem to Eq. (2.44), the Berry curvature defining composite Chern number can be expressed by [88],

$$
\begin{aligned}
C^{(n\bigoplus n+1\bigoplus ...\bigoplus n+N-1)} &= \frac{1}{2\pi}\int_{BZ}\boldsymbol{\Omega}_{\boldsymbol{k}}^{(n\bigoplus n+1\bigoplus ...\bigoplus n+N-1)}dS_{\boldsymbol{k}} \\
&= \frac{1}{2\pi}\sum_{BZ}\Omega_{\boldsymbol{k}}^{(n\bigoplus n+1\bigoplus ...\bigoplus n+N-1)}\Delta S_{\boldsymbol{k}} \\
&= \frac{1}{2\pi}\int_{BZ}Tr\boldsymbol{\nabla}_{\boldsymbol{k}}\times\boldsymbol{A}_k^{(n\bigoplus n+1\bigoplus ...\bigoplus n+N-1)}dS_{\boldsymbol{k}} \\
&= \frac{1}{2\pi}\sum_{BZ}\mathrm{Im}\mathrm{Tr}[\ln[U_{\boldsymbol{k_1}\to\boldsymbol{k_2}}^{(n\bigoplus n+1\bigoplus ...\bigoplus n+N-1)}U_{\boldsymbol{k_2}\to\boldsymbol{k_3}}^{(n\bigoplus n+1\bigoplus ...\bigoplus n+N-1)} \\
&\quad U_{\boldsymbol{k_3}\to\boldsymbol{k_4}}^{(n\bigoplus n+1\bigoplus ...\bigoplus n+N-1)}U_{\boldsymbol{k_4}\to\boldsymbol{k_1}}^{(n\bigoplus n+1\bigoplus ...\bigoplus n+N-1)}]] \\
&= \frac{1}{2\pi}\sum_{BZ}\mathrm{Im}\ln[\det[U_{\boldsymbol{k_1}\to\boldsymbol{k_2}}^{(n\bigoplus n+1\bigoplus ...\bigoplus n+N-1)}U_{\boldsymbol{k_2}\to\boldsymbol{k_3}}^{(n\bigoplus n+1\bigoplus ...\bigoplus n+N-1)} \\
&\quad U_{\boldsymbol{k_3}\to\boldsymbol{k_4}}^{(n\bigoplus n+1\bigoplus ...\bigoplus n+N-1)}U_{\boldsymbol{k_4}\to\boldsymbol{k_1}}^{(n\bigoplus n+1\bigoplus ...\bigoplus n+N-1)}]]
\end{aligned}
\tag{2.45}
$$

where $U_{\boldsymbol{k_\alpha}\to\boldsymbol{k_\beta}}^{(n\bigoplus n+1\bigoplus ...\bigoplus n+N-1)}$ is the normalized $N\times N$ link matrix between each degenerate states, and is defined as,

$$
U_{\boldsymbol{k_\alpha}\to\boldsymbol{k_\beta}}^{(n\bigoplus n+1\bigoplus ...\bigoplus n+N-1)}(i,j)=\frac{\left\langle \boldsymbol{u}_{n_i,\boldsymbol{k_\alpha}}|\boldsymbol{u}_{n_j,\boldsymbol{k_\beta}}\right\rangle}{|\left\langle \boldsymbol{u}_{n_i,\boldsymbol{k_\alpha}}|\boldsymbol{u}_{n_j,\boldsymbol{k_\beta}}\right\rangle|}
\tag{2.46}
$$

The composite Chern number in the discretized Brillouin zone can be finally computed via Eq. (2.45). Moreover, valley Chern number which is defined around the corner of the Brillouin zone can also be computed via Eqs. (2.43) and (2.45).

The only difference between the Chern number and valley Chern number is that the integral over the first Brillouin zone should be performed in the momentum space around each nonequivalent valley. The detailed computational analysis of the valley Chern number of photonic structures investigated in our work will be discussed in Sec. 3.4.

Bibliography

[1] J. D. Joannopoulos, P. R. Villeneuve, and S. Fan, "Photonic crystals," Solid State Commun. **102**, 165-173 (1997).

[2] J. B. Pendry, "Photonic band structures," J. Mod. Opt. **41**, 209-229 (1994).

[3] E. Yablonovitch, "Photonic band-gap structures," J. Opt. Soc. Am. B **10**, 283-295 (1993).

[4] J. D. Jackson, *Classical electrodynamics* (John Wiley, 2007).

[5] F. Bloch, "Quantum mechanics of electrons in crystal lattices," Z. Phys **52**, 555-600 (1928).

[6] K. Sakoda, *Optical properties of photonic crystals* (Springer Science & Business Media, 2004).

[7] J. D. Joannopoulos, P. R. Villeneuve, and S. Fan, "Photonic crystals: putting a new twist on light," Nature **386**, 143-149 (1997).

[8] L. Rayleigh, "XVII. On the maintenance of vibrations by forces of double frequency, and on the propagation of waves through a medium endowed with a periodic structure," Lond. Edinb. Dublin philos. mag. j. sci. **24**, 145-159 (1887).

[9] E. Yablonovitch, "Inhibited spontaneous emission in solid-state physics and electronics," Phys. Rev. Lett. **58**, 2059 (1987).

[10] J. D. Joannopoulos, *et al. Photonic crystals: molding the flow of light* (Princeton university press, 2011).

[11] S. G. Johnson, A. Mekis, S. Fan, and J. D. Joannopoulos, "Molding the flow of light," Comput. Sci. Eng. **3**, 38-47 (2001).

[12] K. Sakoda, *Optical properties of photonic crystals* (Springer Science, 2004).

[13] B. Semnani, J. Flannery, R. Al Maruf, and M. Bajcsy, "Spin-preserving chiral photonic crystal mirror," Light Sci. Appl. **9**, 1-12 (2000).

[14] R. V. Nair and R. Vijaya, "Photonic crystal sensors: An overview," Prog. Quantum Electron. **34**, 89-134 (2010).

[15] T. A. Birks, J. C. Knight, and P. S. J. Russell, "Endlessly single-mode photonic crystal fiber," Opt. Lett. **22**, 961-963 (1997).

[16] K. S. Novoselov, *et al.* "Electric field effect in atomically thin carbon films," Science **306**, 666-669 (2004).

[17] A. C. Neto, F. Guinea, N. M. Peres, K. S. Novoselov, and A. K. Geim, "The electronic properties of graphene," Rev. Mod. Phys. **81**, 109 (2009).

[18] P. R. Wallace, "The band theory of graphite," Phys. Rev. **71**, 622 (1947).

[19] R. R. Nair, *et al.* "Fine structure constant defines visual transparency of graphene," Science **320**, 1308-1308 (2008).

[20] J. Liu, A. R. Wright, C. Zhang, and Z. Ma, "Strong terahertz conductance of graphene nanoribbons under a magnetic field," Appl. Phys. Lett. **93**, 041106 (2008).

[21] Y. Zhang, *et al.* "Direct observation of a widely tunable bandgap in bilayer graphene," Nature **459**, 820-823 (2009).

[22] F. Schedin, A. K. Geim, S. V. Morozov, E. W. Hill, P. Blake, M. I. Katsnelson, and K. S. Novoselov, "Detection of individual gas molecules adsorbed on graphene," Nat. Mater. **6**, 652-655 (2007).

[23] Q. Bao, *et al.* "Atomic-layer graphene as a saturable absorber for ultrafast pulsed lasers," Adv. Funct. Mater. **19**, 3077-3083 (2009).

[24] V. P. Gusynin, S. G. Sharapov, and J. P. Carbotte, "On the universal ac optical background in graphene," New J. Phys. **11**, 095013 (2009).

[25] V. P. Gusynin, S. G. Sharapov, and J. P. Carbotte, "Magneto-optical conductivity in graphene," J. Phys.: Condens. Matter **19**, 026222 (2006).

[26] D. L. Sounas and C. Caloz, "Gyrotropy and nonreciprocity of graphene for microwave applications," IEEE Trans. Microwave Theory Tech. **60**, 901-914 (2012).

[27] L. A. Falkovsky and A. A. Varlamov, "Space-time dispersion of graphene conductivity," Eur. Phys. J. B **56**, 281-284 (2007).

[28] L. A. Falkovsky, "Optical properties of graphene," J. Phys. Conf. Ser. **129** 012004 (2008).

[29] L. A. Falkovsky, and S. S. Pershoguba, "Optical far-infrared properties of a graphene monolayer and multilayer," Phys. Rev. B, **76**, 153410 (2007).

[30] P. A. D. Gonçalves and N. M. Peres, *An introduction to graphene plasmonics* (World Scientific,2016).

[31] D. K. Gramotnev and S. I. Bozhevolnyi, "Plasmonics beyond the diffraction limit," Nat. Photonics **4**, 83-91 (2010).

[32] H. Yan, *et al.* "Tunable infrared plasmonic devices using graphene/insulator stacks," Nat. Nanotechnol. **7**, 330-334 (2012).

[33] A. N. Grigorenko, M. Polini, and K. S. Novoselov, "Graphene plasmonics," Nat. Photonics **6**, 749-758 (2012).

[34] L. A. Falkovsky, "Optical properties of graphene," J. Phys. Conf. Ser. **129**, 012004 (2008).

[35] J. Chen, *et al.* "Optical nano-imaging of gate-tunable graphene plasmons," Nature **487**, 77-81 (2012).

[36] R. W. Boyd, *Nonlinear Optics* (Academic Press, 2008).

[37] Y. R. Shen, *Principles of nonlinear optics* (United States, 1984).

[38] J. Ren, X. Zheng, Z. Tian, D. Li, P. Wang, and B. Jia, "Giant third-order nonlinearity from low-loss electrochemical graphene oxide film with a high power stability," Appl. Phys. Lett. **109**, 221105 (2016).

[39] H. Zhang, S. Virally, Q. Bao, L. K. Ping, S. Massar, N. Godbout, and P. Kockaert, "Z-scan measurement of the nonlinear refractive index of graphene," Opt. Lett. **37**,1856-1858 (2012).

[40] E. Hendry, P. J. Hale, J. Moger, A. K. Savchenko, and S. A. Mikhailov, "Coherent nonlinear optical response of graphene," Phys. Rev. Lett. **105**, 097401 (2010).

[41] D. B. Soh, R. Hamerly, and H. Mabuchi, "Comprehensive analysis of the optical Kerr coefficient of graphene," Phys. Rev. A, **94**, 023845 (2016).

[42] V. Kumar, "Linear and nonlinear optical properties of graphene: a review," J. Electron. Mater. **50**, 3773-3799 (2021).

[43] C. B. De Araújo, A. S. Gomes, and G. Boudebs, "Techniques for nonlinear optical characterization of materials: a review," Rep. Prog. Phys. **79**, 036401 (2016).

[44] A. Saynatjoki, *et al.* "Rapid large-area multiphoton microscopy for characterization of graphene," ACS nano, **7**, 8441-8446 (2013).

[45] R. Wang, B. A. Ruzicka, N. Kumar, M. Z. Bellus, H. Y. Chiu, and H. Zhao, "Optical pump-probe studies of carrier dynamics in few-layer MoS2," Bull. Am. Phys. Soc. **2012**, 57 (2012).

[46] Z. Fang, *et al.* "Active tunable absorption enhancement with graphene nanodisk arrays," Nano Lett. **14**, 299-304 (2014).

[47] D. K. Efetov and P. Kim, "Controlling electron-phonon interactions in graphene at ultrahigh carrier densities," Phys. Rev. Lett. **105**, 256805 (2010).

[48] X. Du, I. Skachko, A. Barker, and E. Andrei, "Approaching ballistic transport in suspended graphene," Nat. Nanotechnol. **3**, 491 (2008).

[49] I. Petković, F. I. B. Williams, K. Bennaceur, F. Portier, P. Roche, and D. C. Glattli, "Carrier drift velocity and edge magnetoplasmons in graphene," Phys. Rev. Lett. **110**, 016801 (2013).

[50] L. Lu, J. Joannopoulos, and M. Soljačić, "Topological photonics," Nat. Photonics **8**, 821 (2014).

[51] A. Khanikaev and G. Shvets, "Two-dimensional topological photonics," Nat. Photonics **11**, 763-773 (2017).

[52] T. Ozawa, *et al.* "Topological photonics," Rev. Mod. Phys. **91**, 015006 (2019).

[53] K. Klitzing, G. Dorda, and M. Pepper, "New method for high-accuracy determination of the fine-structure constant based on quantized Hall resistance,"Phys. Rev. Lett. **45**, 494 (1980).

[54] K. Von Klitzing, "The quantized Hall effect," Rev. Mod. Phys. **58**, 519 (1986).

[55] C. L. Kane and E. J. Mele, "Quantum spin Hall effect in graphene," Phys. Rev. Lett. **95**, 226801 (2005).

[56] C. Kane and E. Mele, "Z_2 topological order and the quantum spin Hall effect," Phys. Rev. Lett. **95**, 146802 (2005).

[57] F. Haldane and S. Raghu, "Possible realization of directional optical waveguides in photonic crystals with broken time-reversal symmetry," Phys. Rev. Lett. **100**, 013904 (2008).

[58] S. Raghu and F. Haldane, "Analogs of quantum-Hall-effect edge states in photonic crystals," Phys. Rev. A **78**, 033834 (2008).

[59] N. Nagaosa, J. Sinova, S. Onoda, A. H. MacDonald, and N. P. Ong, "Anomalous hall effect. Reviews of modern physics," **82**, 1539 (2010).

[60] D. Xiao, M. C. Chang, and Q. Niu, "Berry phase effects on electronic properties," Rev. Mod. Phys. **82**, 1959 (2010).

[61] M. Kohmoto, "Topological invariant and the quantization of the Hall conductance," Ann. Phys. **160**, 343-354 (1985).

[62] J. E. Avron, R. Seiler, and B. Simon, "Homotopy and quantization in condensed matter physics," Phys. Rev. Lett. **51**, 51 (1983).

[63] F. D. M. Haldane, "Model for a quantum Hall effect without Landau levels: Condensed-matter realization of the "parity anomaly"," Phys. Rev. Lett. **61**, 2015 (1988).

[64] B. A. Bernevig, T. L. Hughes, S. Raghu, and D. P. Arovas, "Theory of the three-dimensional quantum Hall effect in graphite," Phys. Rev. Lett. **99**, 146804(2007).

[65] Z. Qiao, S. A. Yang, W. Feng, W. K. Tse, J. Ding, Y. Yao, J. Wang, and Q. Niu, "Quantum anomalous Hall effect in graphene from Rashba and exchange effects," Phys. Rev. B **82**, 161414 (2010).

[66] Z. Wang, Y. Chong, J. Joannopoulos, and M. Soljačić, "Observation of unidirectional backscattering-immune topological electromagnetic states," Nature **461**, 772-775 (2009).

[67] D. Jin, T. Christensen, M. Soljačić, N. Fang, L. Lu, and X. Zhang, "Infrared topological plasmons in graphene," Phys. Rev. Lett. **118**, 245301 (2017).

[68] V. P. Gusynin, S. G. Sharapov, and J. P. Carbotte, "Sum rules for the optical and Hall conductivity in graphene," Phys. Rev. B **75**, 165407 (2007).

[69] V. Singh, D. Joung, L. Zhai, S. Das, S. Khondaker, and S. Seal, "Graphene based materials: past, present and future," Prog. Mater Sci. **56**, 1178-1271 (2011).

[70] T. Low and P. Avouris, "Graphene plasmonics for terahertz to mid-infrared applications," ACS Nano **8**, 1086-1101 (2014).

[71] X. Luo, M. Zhou, J. Liu, T. Qiu, and Z. Yu, "Magneto-optical metamaterials with extraordinarily strong magneto-optical effect," Appl. Phys. Lett. **108**, 131104 (2016).

[72] M. Hafezi, E. Demler, M. Lukin, and J. Taylor, "Robust optical delay lines with topological protection," Nat. Phys. **7**, 907-912 (2011).

[73] M. Hafezi, S. Mittal, J. Fan, A. Migdall, and J. Taylor, "Imaging topological edge states in silicon photonics," Nat. Photonics **7**, 1001-1005 (2013).

[74] K. Fang, Z. Yu, and S. Fan, "Realizing effective magnetic field for photons by controlling the phase of dynamic modulation," Nat. Photonics **6**, 782-787 (2012).

[75] X. Cheng, C. Jouvaud, X. Ni, S. H. Mousavi, A. Z. Genack, and A. B. Khanikaev, "Robust reconfigurable electromagnetic pathways within a photonic topological insulator," Nat. Mater. **15**, 542-548 (2016).

[76] K. Lai, T. Ma, X. Bo, S. Anlage, and G. Shvets, "Experimental realization of a reflections-free compact delay line based on a photonic topological insulator," Scientific reports **6**, 1-7 (2016).

[77] K. F. Mak, K. L. McGill, J. Park, and P. L. McEuen, "The valley Hall effect in MoS2 transistors," Science **344**, 1489-1492 (2014).

[78] W. Yao, D. Xiao, and Q. Niu, "Valley-dependent optoelectronics from inversion symmetry breaking," Phys. Rev. B **77**, 235406 (2008).

[79] Y. Zhang, *et al.* "Direct observation of a widely tunable bandgap in bilayer graphene," Nature **459**, 820-823 (2009).

[80] Y. Kim, K. Choi, J. Ihm, and H. Jin, "Topological domain walls and quantum valley Hall effects in silicene," Phys. Rev. B **89**, 085429 (2014).

[81] D. Malterre, B. Kierren, Y. Fagot-Revurat, C. Didiot, F. De Abajo, F. Schiller, J. Cordón, and J. Ortega, "Symmetry breaking and gap opening in two-dimensional hexagonal lattices," New J. Phys. **13**, 013026 (2011).

[82] T. Ma and G. Shvets, "All-Si valley-Hall photonic topological insulator," New J. Phys. **18**, 025012 (2016).

[83] D. Xiao, W. Yao, and Q. Niu, "Valley-contrasting physics in graphene: magnetic moment and topological transport," Phys. Rev. Lett. **99**, 236809 (2007).

[84] Y. Yang, Y. Xu, T. Xu, H. Wang, J. Jiang, X. Hu, and Z. Hang, "Visualization of a unidirectional electromagnetic waveguide using topological photonic crystals made of dielectric materials," Phys. Rev. Lett. **120**, 217401 (2018).

[85] J. Noh, S. Huang, K. P. Chen, and M. C. Rechtsman, "Observation of photonic topological valley Hall edge states," Phys. Rev. Lett. **120**, 063902 (2018).

[86] W. H. Xang, G. Y. Guo, and J. H. Jiang, "Band topology in classical waves: Wilson-loop approach to topological numbers and fragile topology," New J. Phys. **21**, 093029 (2019).

[87] R. Zhao, G. D. Xie, M. L. Chen, Z. Lan, Z. Huang, and E. I. Wei, "First-principle calculation of Chern number in gyrotropic photonic crystals," Opt. Express **28**, 4638-4649 (2020).

[88] T. Fukui, H. Suzuki, and Y. Hatsugai, "Chern numbers in a discretized Brillouin zone: Efficient method to compute (spin) Hall conductances," J. Phys. Soc. Jpn. **74**, 1674–1677 (2005).

Chapter 3

Optically controllable light flow in topological plasmonic waveguides based on graphene metasurfaces

3.1 Introduction

The discovery and impact of the quantum Hall effect and other phenomena of topological nature in condensed matter physics have spurred the extension of these ideas to photonics, resulting in the emergence of topological photonics [1, 2, 3, 4, 5]. New phenomena and applications, such as unidirectional, topologically protected light propagation in which disorder-induced backscattering is suppressed, have been demonstrated [6, 7]. By analogy with the time-reversal symmetry breaking feature of the quantum Hall effect [8, 9], early research efforts have focused on the generation of topologically-protected edge states in magneto-optical photonic crystals (PhCs) under an external magnetic field [10, 11, 12, 13]. However, magneto-optic PhCs only have a strong response to an applied magnetic field at microwave frequencies, so that extending these phenomena to the optical domain requires alternative solutions. To this end, in time-reversal invariant photonic systems, phenomena analog to quantum spin-Hall [14, 15, 16, 17] and quantum valley-Hall [18, 19, 20, 21] effects have been demonstrated upon breaking the spin-conservation and spatial-inversion symmetries, respectively.

Valley degree of freedom in condensed-matter physics, which is associated to the conduction-band minima (or valence-band maxima) in graphene-like two-dimensional (2D) materials [22, 23], has recently been introduced to photonics [24], too. These materials exhibit nontrivial Berry curvature distribution in the momentum space around each valley, which gives rise to a valley-dependent topological index associated to the integral of Berry curvature around a valley [22]. Furthermore, a domain-wall interface separating two topologically distinct valley PhCs can support valley-momentum-locked modes localized at the interface, similar to the quantum-valley Hall effect [24]. Until now, valley-Hall photonic modes have been mostly studied in bulk materials, such as photonic crystals [25, 16], being less explored in 2D photonic platforms, including graphene. As the thinnest material known, graphene consists only of a single layer of carbon atoms arranged in a hexagonal pattern. This 2D material is becoming a promising platform to achieve passive and active topologically protected plasmonic modes [26, 27], due to its high carrier mobility and long relaxation time [28, 29, 30]. Equally importantly, recent advances in nanofabrication techniques, like electron-beam lithography (EBL), STM lithography, and ultraviolet (UV) lithography method, make it possible to achieve graphene-based plasmonic nanostructures with particularly complex geometrical configurations[31, 32].

Most of the research in topological photonic structures has primarily been focused on the investigation of the linear optical response of such photonic systems. However, key functionalities of active photonic devices, such as tunability, optical frequency generation, and sensing, can most effectively be implemented by employing the nonlinear optical response of the underlying materials [33, 34, 35, 36]. The idea of applying optical nonlinear effects to topological systems can realize active applications with valuable phenomena, including ultra-short pulsed lasers, optical signal processing, and ultra-fast all-optical switches [37, 38]. To this end, active topological photonic devices relying on nonlinear optical effects, including Kerr effect [39], second-harmonic generation (SHG) [40, 41], third-harmonic generation (THG) [41, 42], and four-wave mixing (FWM) [43], have been successfully demon-

strated. In particular, frequency-mixing processes between phase-matched topological edge modes, including SHG [40, 41, 44], FWM [43] and third-harmonic generation (THG) [41, 44], have been recently studied in PhCs and two-dimensional (2D) materials. In addition, applications of these nonlinear optical effects to imaging of topological edge states *via* THG [42], lattice edge solitons [45, 46], traveling-wave amplifiers [47], topological sources of quantum light [48], and topological insulator lasers [49, 50] have been proposed theoretically [45, 47, 49] and in some cases demonstrated experimentally [42, 46, 48, 50].

Unique properties of graphene-based topological systems, in conjunction with strong nonlinear optical interactions occurring in graphene, can be employed to develop nonlinear photonic devices and systems, which can optically control topologically-protected defect-immune light propagation at the nanoscale. Key factors, such as large, tunable carrier densities [51, 52] and long intrinsic relaxation times up to the picosecond range [53, 54], make graphene an ideal platform for topological plasmonics at high frequency, low loss, and large topological bandgaps. In particular, due to the large optical near-field enhancement and extended life-time of plasmons in graphene metasurfaces, SHG, THG, and other nonlinear optical interactions of plasmonic edge states can be achieved in graphene metasurfaces at ultralow optical pump power [55, 56].

A research topic of considerable practical importance is the development of efficient schemes for coupling light to optical modes of topological nature. The fact that this is by no means a trivial challenge, can be understood from the following example. Thus, by employing photonic valley-Hall effects, one can design optical waveguiding structures supporting valley-momentum-locked modes localized at the interface between two domains characterized by different valley Chern numbers [57, 58]. To excite these topological modes, one usually places a point-like source near the interface between two domains so that the interface mode is excited and subsequently measured [59, 60]. In practice, however, this approach can be very ineffective, chiefly for two reasons. First, in addition to the topological mode, the interface can support regular modes, too, and these regular modes are generally

excited together with the topological mode. Second, using a point-like source to excite an optical mode can be a rather inefficient approach, as the spatial overlap between the source field and the optical mode can be rather limited.

This example illustrates the importance of the development of efficient excitation techniques that would allow one to couple optical power from external sources to topological modes of photonic structures. Moreover, if such coupling techniques would permit a certain degree of tunability their functionality would be further enhanced. With these goals in mind, adopting graphene as the material platform to use for the implementation of these ideas is a natural choice, as it possesses ultra-fast response time [61, 62] and strong optical nonlinearity [63, 64], which are optimal features when seeking to achieve device operation at low optical power and ultrafast tunability.

In this chapter, we study the unidirectional light propagation of a topologically-protected valley mode on a single graphene nanohole plasmonic crystal waveguide. The topological work on graphene has been studied previously by Ref. [26], in which the time-reversal symmetry breaking of the graphene layer is achieved by adding an external magnetic field. However, a strong magnetic field up to 8 T is required to generate the magneto-optical effect in graphene, which is difficult to achieve in practice. Therefore, a time-reversal invariant photonic system with spatial symmetry breaking is considered. By introducing and tuning the size of extra nanoholes to break and reduce the spatial-inversion symmetry of graphene nanohole metasurface, the symmetry-protected Dirac cones are gapped out. As a result, a unidirectional topological valley mode can emerge inside a nontrivial bandgap. Since the Kerr coefficient of graphene is more than 9 orders of magnitude larger than that of bulk dielectrics [65, 66], graphene-based topological systems show great potential to develop ultra-fast active photonic nanodevices. We demonstrate that the influence of Kerr effect on valley-Hall topological transport in the proposed graphene nanohole metasurfaces can be used to implement an all-optical switch and an efficient mode coupler, by tuning the refractive index of graphene via a pump beam injected in bulk modes. The variation of refractive index can result in

a frequency shift of bandgap, and such effect can be employed to control the signal propagation and wave-vector mismatch between different modes in the graphene nanohole waveguide. Our computational results show that the required pump power is strongly dependent on the group velocity (GV) of pump bulk mode, especially in the slow-light (SL) regime.

This chapter is organized as follows. In Sec. 3.2, we demonstrate the design of a single graphene nanohole plasmonic waveguide with the spatial-inversion symmetry breaking. In particular, a quantitative analysis of the valley Chern number is given based on the Wilson loop approach, which corresponds to the number of topologically protected valley modes inside the nontrivial bandgap with unidirectional feature. This is followed in Sec. 3.3 by the design of an all-optical switch based on the proposed graphene nanohole waveguide. Starting from the optical properties of the pump beam injected by chosen bulk modes, we computationally describe the power dependence of the nontrivial bandgap. In particular, we discuss the optically controllable signal propagation in the proposed nanoswitch, and its dependence on the pump power injected by a bulk mode with reduced GV. Then, in Sec. 3.4, we describe theoretically and computationally the optically controllable nonlinear coupling between edge and topological modes of the graphene metasurface and its dependence on the mode parameters, such as frequency, wave vector mismatch, and pump power. Specifically, a quantitative analysis of the phase-matching condition has been presented based on the wave-vector difference between topological and edge modes extracted from three different methods. Finally, in Sec. 3.5, we summarize the main conclusions of this chapter.

3.2 Valley-Hall Topological Transport in Graphene Nanohole Waveguide

The topological waveguide investigated in this thesis is implemented by using a composite graphene metasurface, as schematically illustrated in Fig. 3.1 [67]. The waveguide is created by adjoining together two semi-infinite graphene metasurfaces in a mirror-symmetric manner, thus generating a domain-wall interface oriented

along the y-axis, as highlighted yellow region in Fig. 3.1(a). Two mirror-symmetric graphene metasurfaces consist of a periodic hexagonal array of holes in a uniform graphene sheet. The unit cell and the FBZ are shown in Figs. 3.1(b) and 3.1(c), respectively. The unit cell of the metasurface contains two holes, such that the spatial-inversion symmetry of the system is broken when two holes have different radii, denoted here by R and r. In this chapter, we fix the lattice constant $a = 400\sqrt{3}$nm and the radius of the big hole $R = 140$ nm. The optical dispersion relation

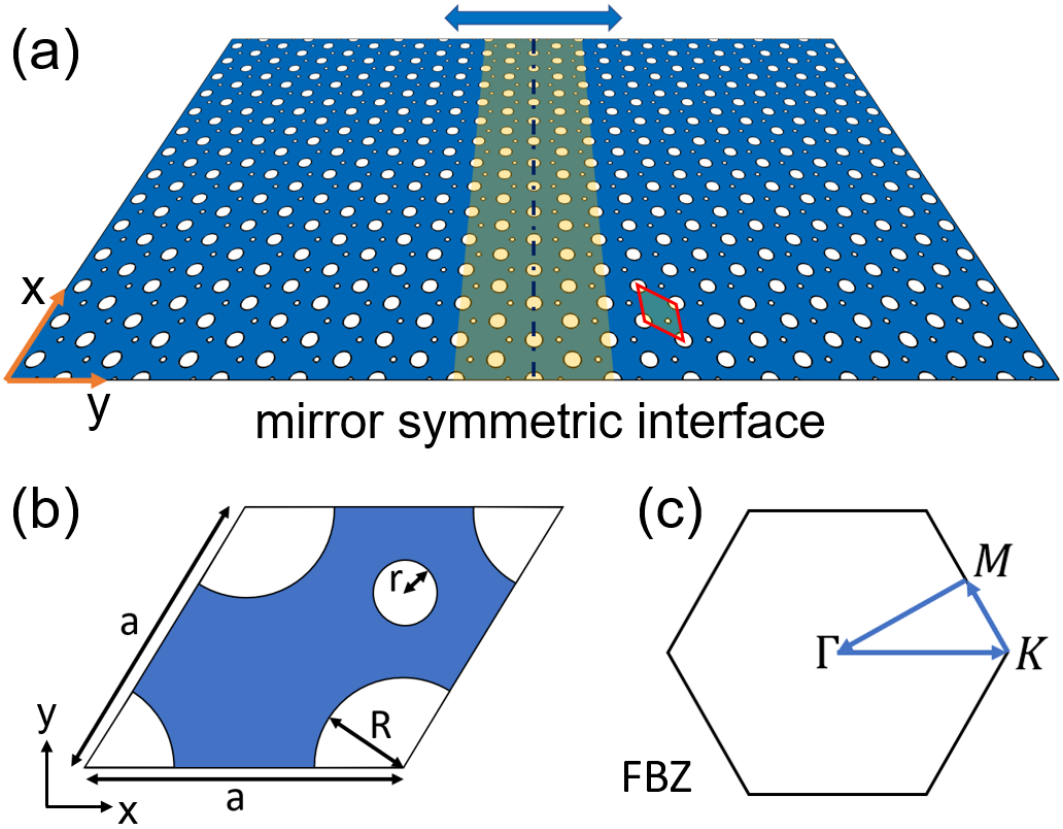

Figure 3.1: (a) Schematic of the graphene plasmonic nanohole crystal with a domain-wall interface oriented along the y-axis. The left- and right-hand side domains with mirror symmetry are composed of the same unit cell. (b) Primitive unit cell of the graphene crystal with a lattice constant, a, containing two nanoholes with radii R and r. (c) First Brillouin zone (FBZ) of the graphene plasmonic nanohole crystal with three high-symmetry points Γ, M and K.

of graphene is described by its electric permittivity ε_g, which is given by Kubo's formula [68, 69],

$$\varepsilon_g = 1 - \frac{e^2}{4\varepsilon_0 \pi \hbar \omega h_g} \ln\left(\frac{\xi - i\overline{\omega}}{\xi + i\overline{\omega}}\right) + \frac{ie^2 k_B T \tau}{\varepsilon_0 \pi \hbar^2 \omega \overline{\omega} h_g}\left[\frac{\mu_c}{k_B T} + 2\ln\left(e^{-\frac{\mu_c}{k_B T}} + 1\right)\right], \quad (3.1)$$

where ω is the frequency, T is the temperature, h_g is the effective thickness of graphene, μ_c is the chemical potential, $\bar{\omega} = 1 - i\omega\tau$, and $\xi = 2\tau|\mu_c|/\hbar$, with τ being the relaxation time. In our analysis, we set $T = 300\,\mathrm{K}$, $\tau = 50\,\mathrm{ps}$, $h_g = 0.5\,\mathrm{nm}$, and $\mu_c = 0.2\,\mathrm{eV}$. Note that dispersive and dissipative effects are incorporated in our simulations via the frequency-dependent complex surface conductivity of graphene, defined as $\sigma_s = -i\varepsilon_0\omega h_g(\varepsilon_g - 1)$. In this way, the optical properties of 2D graphene can be directly expressed by its surface current density, namely $\boldsymbol{J_s} = \sigma_s \boldsymbol{E}$.

3.2.1 Band Diagram of Infinite Graphene Nanohole Crystal

In this section, band diagrams of the proposed graphene nanohole metasurface with a nontrivial bandgap will be presented, in which the topological nontrivial property will be quantitatively described by the valley Chern number below the bandgap.

To demonstrate the existence of topological modes in our structured graphene metasurface, we have computed the photonic band structure of an infinite graphene nanohole crystal. The finite-element method (FEM) computations were performed with COMSOL Multiphysics®, a commercially available software package [70].

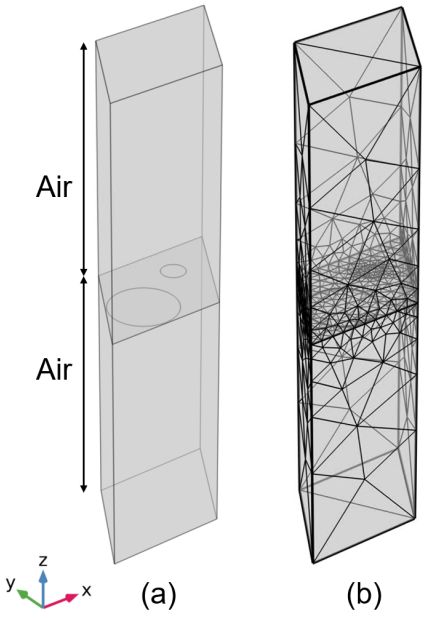

Figure 3.2: Simulation setting for the graphene nanohole plasmonic crystal. (a) Periodic boundary conditions are added along the x-axis and y-axis while scattering boundary conditions are added on the air boundary along the z-axis. (b) Mesh distribution of the unit cell of a graphene nanohole crystal with a minimum mesh size of 5 nm.

In order to build an infinite 2D nanostructured graphene crystal, periodic boundary conditions are set on edges of the unit cell along the x-axis and y-axis, as demonstrated in Fig. 3.2(a). In this three-dimensional (3D) simulation, the scattering boundary conditions are set on the top and bottom boundaries. In particular, the height of two air domains along the z-axis is as large as $2a$, which is large enough to model the light radiation and scattering. Figure 3.2(b) shows the mesh distribution on the designed unit cell with a minimum mesh size of 5 nm, which enables the accuracy of the FEM simulation.

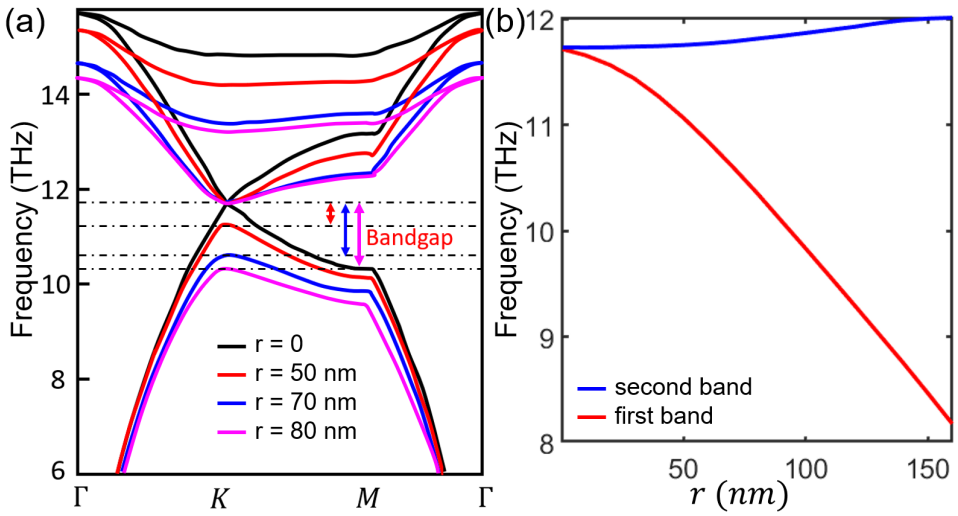

Figure 3.3: (a) Band diagram of the graphene metasurface, determined for different radii of extra nanohole r. When $r = 0$, a Dirac cone is formed at the crossing point of the first and second bands (black lines). By introducing an extra nanohole with an increasing radius from r =50 nm (red lines), r =70 nm (blue lines), to 80 nm (magenta lines) in the primitive cell of the graphene crystal, nontrivial bandgaps emerge with an increasing gap size. (b) Variation of frequency of the photonic bandgap at K point with respect to the size of extra nanohole r. The frequency maxima of the first band and the frequency minima of the second band are marked by red and blue lines, respectively.

To properly identify the frequency bandgap, plasmonic bands of this graphene nanohole crystal have been evaluated through the high-symmetry points Γ, K and M in the FBZ [as shown in Fig. 3.1(c)], and the result is given in Fig. 3.3. In Fig. 3.3(a), the photonic band diagram of an infinite graphene nanohole crystal, determined in the case when the metasurface has inversion symmetry without extra nanohole $r = 0$, and for a noncentrosymmetric metasurface containing extra

nanoholes with radii $r = 50\,\text{nm}$, $r = 70\,\text{nm}$, and $r = 80\,\text{nm}$, are plotted by black, red, blue, and magenta curves, respectively.

As shown by the black curves in Fig. 3.3(a), when the small nanohole $r = 0$, there is a Dirac cone at K point, which is protected by the C_{6v} symmetry of big nanoholes. The first and second bands indeed linearly transit each other at Dirac point located at the frequency of 11.8 THz. In order to open up the inversion-symmetry-protected Dirac cone, extra air nanoholes ($r \neq 0$) are introduced into graphene plasmonic crystal, which reduces the spatial symmetry to C_{3v} symmetry group. As a consequence, the C_{6v}-symmetry-protected Dirac cone is gapped out, resulting in the formation of a nontrivial frequency bandgap, as illustrated by red, blue, and magenta curves in Fig. 3.3(a). This bandgap, which opens upon breaking the spatial-inversion symmetry of the lattice, is topologically nontrivial [21]. In addition, the variation of the size of bandgap indicates its dependence on the radius of extra nanohole r, and the computational result of this relationship is presented in Fig. 3.3(b). The frequency maximum of the first band at K point is represented by a red line while the blue line indicates the frequency minima of the second band at K point. The size of the bandgap increases with the radius r of extra nanoholes, based on the fact that the perturbation of spatial-inversion symmetry breaking is increasing. When the radius of extra nanohole increases from 50 nm to 80 nm, the width of bandgap approximately increases by 1 THz due to a remarkable frequency shift of the first band. Note that the size of bandgap larger than 1 THz is not a good choice, based on the fact that the frequency dispersion curve at K point spreads significantly, resulting in the corresponding valley Chern number at K point cannot be properly defined. Hence, the topologically-protected property inside a relatively large bandgap is hard to be realized. For our subsequent analysis in this chapter, the radius of the smaller holes is fixed to $r = 50\,\text{nm}$, which possesses a relatively suitable nontrivial bandgap from 11.1 THz to 11.8 THz.

3.2.2 Valley Chern Number of Graphene Nanohole Crystal

To quantitatively evaluate the nontrivial topological protection of the photonic system, Chern number and valley Chern number are defined based on the integral of

the Berry curvature over the momentum space, which can be computationally evaluated by Eq. (2.43) in a discretized Brillouin zone. For a system with time-reversal symmetry breaking under an external magnetic field, the Chern number is the integral of the Berry curvature over the whole FBZ. Similarly but differently, in time-reversal invariant valley-Hall systems with a spatial-inversion symmetry breaking, the Chern number calculated over the whole FBZ is zero, while the integrals of the Berry curvature have opposite signs around two nonequivalent valleys, which leads to a valley-dependent nontrivial property. As a result, a new topological index, valley Chern number $C_v^n = \pm 1/2$, is defined by the integral of a Berry curvature of the nth band in the momentum space around each valley [71, 72].

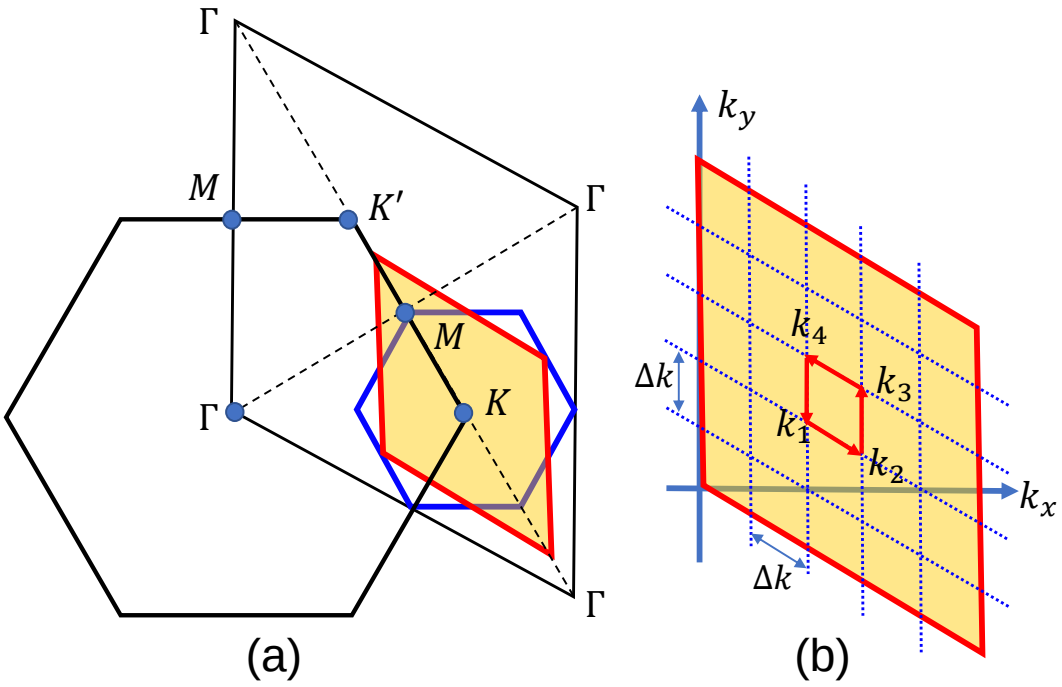

Figure 3.4: Schematic of the valley Chern number calculation. (a) Hexagonal (blue) computational domain around the high-symmetric point K and the reshaped but equivalent rhombic (red) computational domain for the convenience of calculation. (b) Example of a 5×5 discretization of the chosen rhombic domain in the momentum space.

Based on the clarification of the Chern number calculation in Eqs. (2.43) and (2.45), Chern number of the individual band and composite Chern number of degenerate bands can be evaluated in the discretized Brillouin zone by the Wilson-loop approach. To gain deeper insight into the valley Chern number of the pro-

posed graphene nanohole plasmonic crystal, valley Chern number of the first band in Fig. 3.3(a) is computationally calculated around the K and K' valleys. Composed by a honeycomb lattice, the proposed graphene nanohole crystal has a hexagonal FBZ as shown in Fig. 3.1(c). To simplify the discretization of the FBZ, as indicated in Fig. 3.4(a), the hexagonal FBZ in black is reshaped into a rhombic FBZ centered at the M point, which is more convenient to discrete the FBZ along two axes. Due to the periodicity of the FBZ in reciprocal space, two Brillouin zones with different shapes are equivalent. In this way, a similar transformation can be applied to a domain around the K (K') point to calculate the valley Chern number. In Fig. 3.4(a), a small hexagonal blue domain centered at the K point with a sidelength from K to M is chosen to calculate the valley Chern number, which is reshaped into a small rhombic domain for calculation convenience as highlighted yellow region. It should be noted that the selection of a integral domain in the momentum space depends on the spread of the Berry curvature around K point in the FBZ, so that the integral domain should be large enough to cover the spread of Berry curvature. To be more specific, the chosen integral domain is extended around the K valley till the Berry curvature approaches zero, namely, the computed valley Chern number remains unchanged. In our calculations, the chosen hexagonal (rhombic) domain is suitable for the valley Chern number evaluation of each band in Fig. 3.3(a).

Utilizing the Wilson-loop approach in Eq. (2.43), one can obtain the discretized Berry curvature in each small plaquette calculated by the normalized eigenstates at four corner points (k_1, k_2, k_3, and k_4) of the plaquette. Specifically, the discretization of the chosen rhombic domain along two directions with an example of 5×5 meshed small plaquettes is shown in Fig. 3.4(b). The Wilson loop is indicated by the red arrowed line in each plaquette, and the mesh size of each plaquette is $\Delta k = \frac{\sqrt{3}k_{K\to M}}{5}$. Note that, in addition to the selection of a domain around a valley, the convergence to an accurate valley Chern number requires an effective sampling in the chosen domain. We find that in all cases considered in our later discussion, a 18×18 k-sampling is sufficient to achieve convergence to the correct valley Chern number.

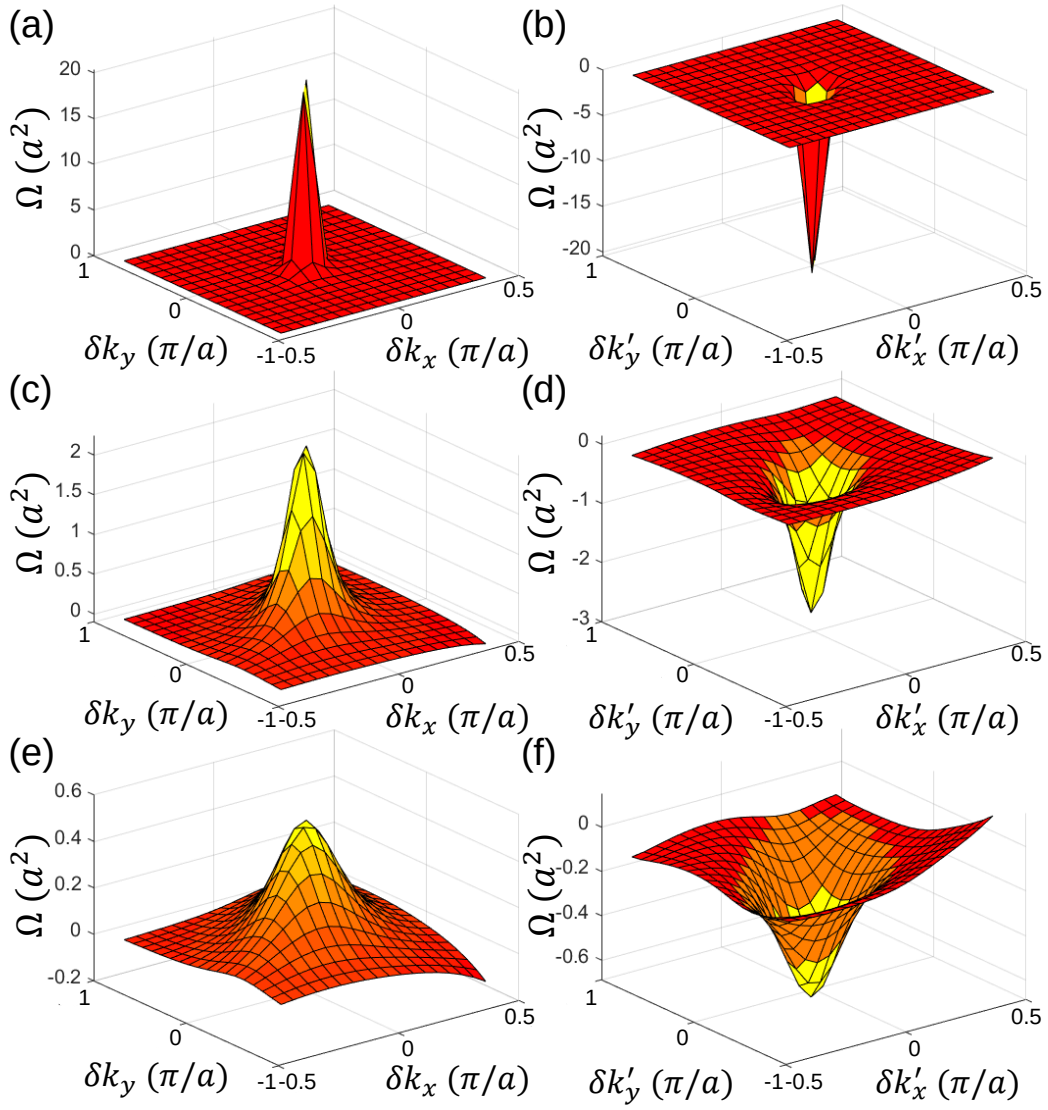

Figure 3.5: Computed Berry curvature distribution of the first band over K and K' valleys, determined for different values of the radius of holes r. (a) and (b) Berry curvatures of the first band when $r = 20\,\text{nm}$ over K and K' valleys, respectively. (c) and (d) same as (a) and (b) but for $r = 50\,\text{nm}$. (e) and (f) same as (a) and (b) but for $r = 70\,\text{nm}$.

Since the band diagram of graphene nanohole plasmonic crystal possesses a nontrivial bandgap between the first and second bands, valley Chern numbers of the first band over the discretized K and K' valleys are computational calculated based on FEM simulation in COMSOL, and the results computed in a 18×18 discretization of K valley are shown in Fig. 3.5. First, the frequency dispersion relation of the first band in the discreted k space, is solved by the eigenfrequency solver in COMSOL. Since the proposed graphene nanohole metasurface is a dispersive pho-

tonic system, the permittivity of graphene crystal $\varepsilon_g(\boldsymbol{r})$ at the frequency of the first band is estimated based on Eq. 3.1. Then, the Berry curvature of each small plaquette is calculated by the link variable $U^n_{\boldsymbol{k}_\alpha \to \boldsymbol{k}_\beta} = \frac{\langle \boldsymbol{u}_{n,\boldsymbol{k}_\alpha} | \boldsymbol{u}_{n,\boldsymbol{k}_\beta} \rangle}{|\langle \boldsymbol{u}_{n,\boldsymbol{k}_\alpha} | \boldsymbol{u}_{n,\boldsymbol{k}_\beta} \rangle|}$ $(\alpha, \beta = 1,2,3,4)$ between two adjacent k points, and the normalized eigenstate $|\boldsymbol{u}_{n,\boldsymbol{k}}\rangle = |e^{i\boldsymbol{k}\cdot\boldsymbol{r}}\boldsymbol{E}_{n,\boldsymbol{k}}(\boldsymbol{r})\rangle$ $(n = 1,2)$ at each k point is obtained by the FEM simulation of COMSOL. Finally, the valley Chern number is the sum of the Berry curvature of each small plaquette over the discretized k space.

In the proposed graphene nanohole crystal with different values of the radius of holes r, the size of bandgap increases with the increment of the radius of nanoholes r. Thus, valley Chern numbers of the first band over the K and K' valleys for three cases when $r = 20\,\text{nm}$, $50\,\text{nm}$, and $70\,\text{nm}$ are considered, and corresponding Berry curvature distributions in a 18×18 discretized k space are given in Figs. 3.5(a)(b), 3.5(c)(d), and 3.5(e)(f), respectively. In all cases, the Berry curvature distribution in a unit of a^2 shows a remarkable peak at K and K' points, and the Berry curvature of the first band over the K valley (right column) is exactly opposite to the Berry curvature of the first band over the K' valley (left column).

For the case of $r = 20\,\text{nm}$ in Fig. 3.5(a) and 3.5(b), the Berry curvature is the largest among three cases, and computed valley Chern numbers of the first band over K and K' valleys are 0.48 and -0.48, respectively. A 0.02 difference compared to the theoretical value $C_v = \pm 1/2$ proves the accuracy of Wilson loop computational method. For other two cases ($r = 50\,\text{nm}$ and $r = 70\,\text{nm}$) with wider nontrivial bandgaps, computed valley Chern numbers of the first band over K and K' valleys when $r = 50\,\text{nm}$ slightly decrease to 0.34 and -0.34 as indicated in Fig. 3.5(c) and 3.5(d), respectively. Moreover, valley Chern numbers of the first band over K and K' valleys when $r = 70\,\text{nm}$ are further reduced to 0.29 and -0.29 as shown in Fig. 3.5(e) and 3.5(f), respectively. The computational accuracy of the valley Chern number slightly drops with an increasing size of the nontrivial bandgap between the first two bands. This is attributable to a spread of the Berry curvature over the valley, resulting in a rapid drop of the peak of Berry curvature. Since the Berry curvature over the K valley spreads significantly and overlaps with adjacent Berry curvatures

over K' valleys, the computed valley Chern number when $r > 50\,\text{nm}$ cannot be properly defined, so that we will use the valley Chern number with a theoretical value $\pm 1/2$ for the later discussion.

3.2.3 Band Diagram of Finite Graphene Nanohole Crystal Waveguide

The proposed graphene metasurface with spatial-inversion symmetry breaking exhibits a nontrivial Berry curvature distribution in the momentum space around two nonequivalent K and K' valleys, and the sign of valley Chern numbers with the absolute value $1/2$ of the first band is opposite at K and K' points. In order to obtain a nonzero valley-dependent topological index, the K and K' points can be connected by rotating the proposed graphene crystal with spatial-inversion breaking by $\pi/3$, π, or $5\pi/3$ rotation angles.

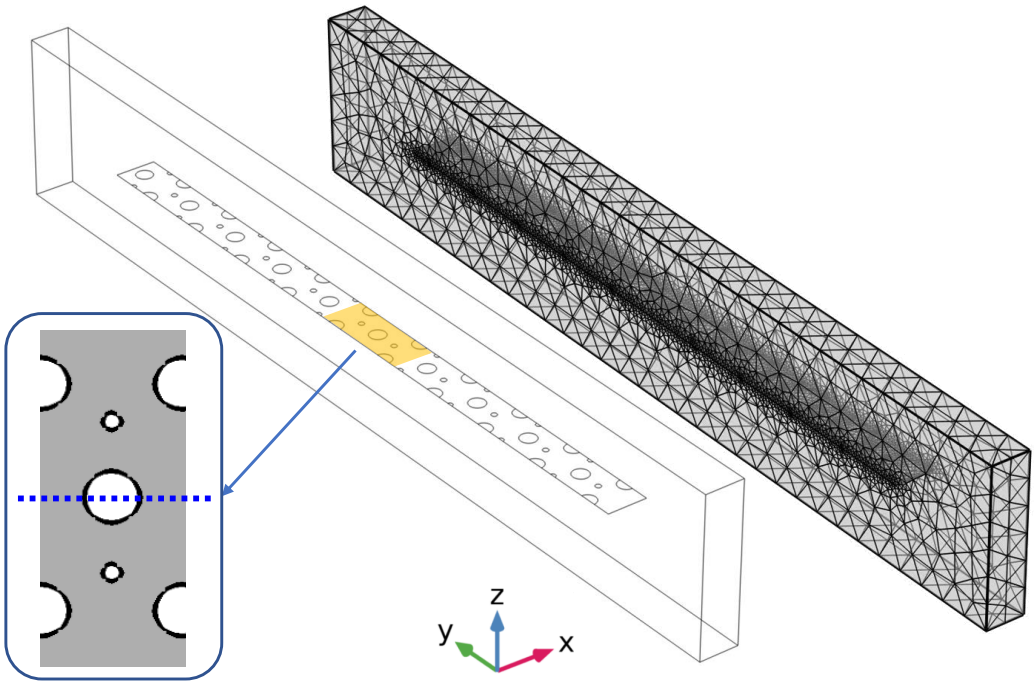

Figure 3.6: Schematic and mesh setting of the supercell of finite graphene nanohole plasmonic waveguide with a mirror-symmetric domain-wall interface (highlighted in the yellow region).

As a result, a domain-wall interface can be constructed by placing together two graphene metasurfaces in a mirror-symmetric manner, i.e., rotated by π w.r.t. each

other, as per Fig. 3.1(a), which connects K ($C_v = \pm 1/2$) and K' ($C_v = \mp 1/2$) valleys. Consequently, the difference of the valley Chern number across the domain-wall at each valley is $\Delta C_v = \pm 1$. As a result, valley-Hall topological modes appear inside the nontrivial bandgap of this composite graphene metasurface with a domain-wall interface.

The schematic of the supercell is shown in Fig. 3.6, which is mirror-symmetric with respect to the highlighted domain-wall interface. We used a supercell with a number of 20 unit cells along the y-axis and periodic boundary conditions along x-axis. This means that the metasurface is finite along the transverse direction (y-axis) and infinite along the longitudinal one (x-axis). To simulate the light scattering, all air boundaries are set with absorption boundary conditions. In particular, the minimum mesh size of the graphene simulation domain is smaller than 7 nm to ensure high accuracy of our FEM analysis in COMSOL.

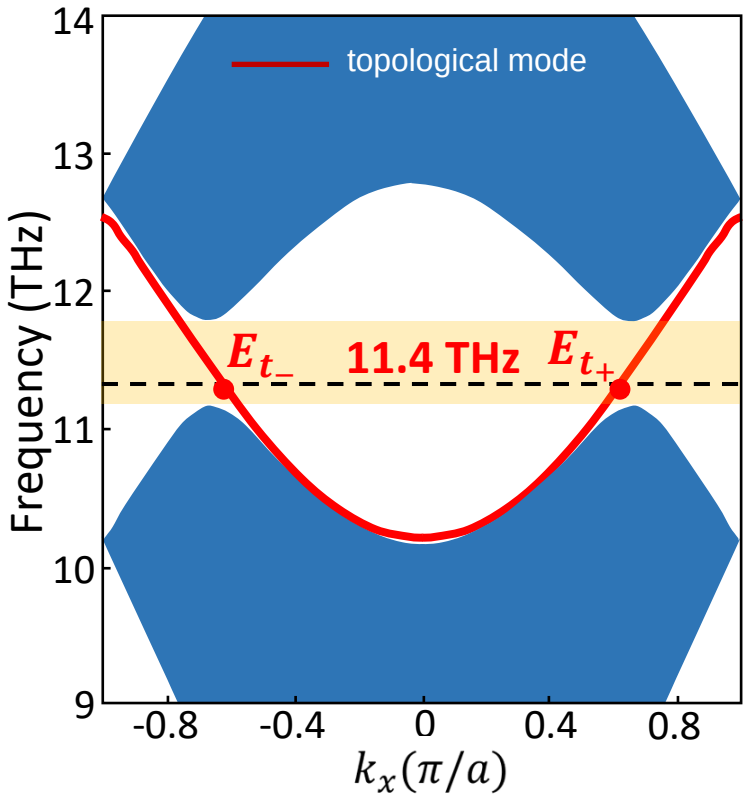

Figure 3.7: Projected band diagram (blue region) of the interface graphene nanohole plasmonic waveguide with extra nanoholes $r = 50$ nm. A topologically protected interface mode (red line) emerges inside the nontrivial bandgap.

The nonzero valley Chern number difference across the domain-wall interface makes it possible to generate valley-momentum-locked interfacial modes, and the projected band diagram is illustrated in Fig. 3.7. Since the metasurface is only periodic along the x-axis with a period a, the wave vector k_x of the projected band diagram varies from $-\pi/a$ to π/a. The blue regions represent the projected bulk modes and the yellow strip shows the nontrivial bandgap in which a topological interface mode appears marked by a red line. Interestingly, the topological valley mode is continuous and does not connect with bulk bands, whereas the topological edge mode induced by the time-inversion symmetry breaking connects bulk bands.

3.2.4 Topological Features of The Interface Modes

In order to gain deeper physical insights into the topological interface mode, the corresponding field distribution is calculated at the frequency 11.4 THz, which is in the bandgap and only crosses the topological band at two points E_{t_-} and E_{t_+}. As indicated in Fig. 3.8, both topological modes propagate along the domain-wall interface with a highly confined field distribution. Furthermore, the unidirectional feature of valley-momentum-locked interface mode is further investigated. Due to group velocities (the slope of frequency dispersion curve of the topological band) of topological modes at E_{t_-} and E_{t_+} points being opposite, it leads to the light propagation of these topological modes along opposite directions. To this end, six electric dipoles with increasing or decreasing phase differences ($\pm\pi/3$) are placed together on the corners of a small hexagon, which can generate Poynting vector distributions in opposite directions, namely opposite polarization. Under the excitation of a left-circularly-polarized (LCP) source at the frequency of 11.4 THz, see Fig. 3.8(a), the topologically protected interfacial mode propagates along the domain-wall interface in the positive x-axis direction with positive group velocity, whereas the topological mode propagates in the negative x-axis with negative group velocity under a right-circular-polarized (RCP) excitation source at the frequency of 11.4 THz, as shown in Fig. 3.8(b).

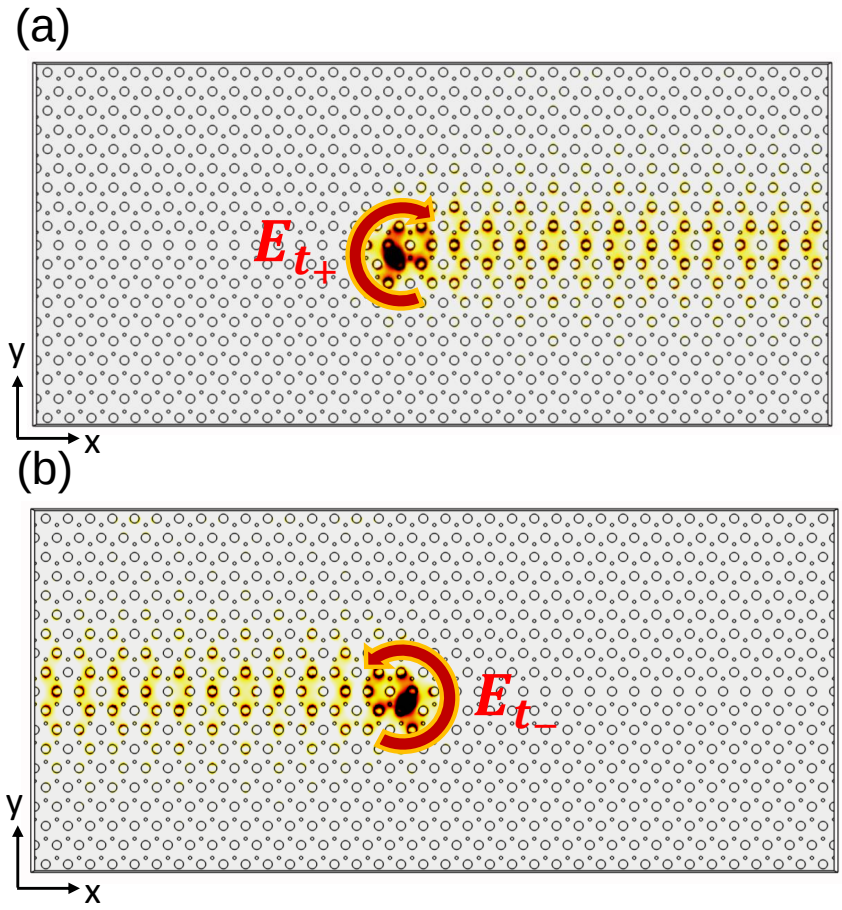

Figure 3.8: (a) Unidirectional propagation of topological interfacial mode along the positive direction of x-axis, when the finite graphene waveguide is excited by a LCP source at 11.4 THz. (b) Unidirectional propagation of topological interfacial mode along the negative direction of x-axis, under a RCP source excitation at 11.4 THz.

3.3 Graphene-based All-optical Switch

In this section, taking advantage of the unidirectional feature of the topological interface mode along with the strong nonlinear optical properties of graphene, an active graphene-based all-optical nanoswitch implemented on the proposed graphene nanohole waveguide is designed. By tuning the refractive index of graphene through the Kerr effect via a pump beam, one can achieve a power-dependent frequency bandgap, which will result in the light transmission of topological interface mode in a tunable manner.

3.3.1 Blue-shifted Nontrivial Bandgap *via* Kerr Effect

Kerr effect is a nonlinear optical process ideal to use for tuning the optical properties of graphene, chiefly due to its extremely large second-order nonlinear refractive index, n_2. In particular, Kerr coefficient n_2 of graphene is more than 9 orders of magnitude larger than that of most optical materials customarily used in nonlinear optics. Additionally, other features of graphene, such as chemically and electrically tunable optical properties and strong nonlinear optical response in a broad frequency domain spanning from terahertz to mid-infrared frequencies [73, 74], are particularly attractive for nonlinear optics applications.

The change of the refractive index of graphene in response to an applied (pump) electric field $\mathbf{E}_p(\mathbf{r})$ is described by:

$$\Delta n(\mathbf{r}) = \frac{1}{2} c\varepsilon_0 n n_2 \left|\mathbf{E}_p(\mathbf{r})\right|^2, \tag{3.2}$$

where n is the index of refraction of graphene in the absence of the applied electric field and $n_2 = 7.5 \times 10^{-7}\,\mathrm{cm}^2/\mathrm{W}$ is the second-order nonlinear refractive index of graphene at the frequency of 11.4 THz [75, 76]. Moreover, the pump power propagating in an optical mode with field distribution, $\mathbf{E}_p(\mathbf{r})$, can be expressed as follows [77, 78]:

$$P_p = \frac{v_g}{4a} \int_{V_{cell}} \frac{\partial}{\partial \omega} \left[\omega \varepsilon_m(\mathbf{r};\omega)\right] \left|\mathbf{E}_p(\mathbf{r})\right|^2 d\mathbf{r}, \tag{3.3}$$

where $v_g = d\omega/dk_x$ is the GV, V_{cell} is the volume of the unit cell, and $\varepsilon_m(\mathbf{r};\omega)$ is the spatial distribution of the frequency-dependent permittivity of the metasurface (or PhC), that is $\varepsilon_m(\mathbf{r};\omega) = \varepsilon_0$ [$\varepsilon_m(\mathbf{r};\omega) = \varepsilon_g(\omega)$] if $\mathbf{r}$ corresponds to a point in air (graphene). Note that for our graphene structure the waveguide dispersion is much larger than the material dispersion of graphene, so that the latter one can be discarded by setting $\varepsilon_m(\mathbf{r};\omega) \equiv \varepsilon_m(\mathbf{r})$. In the later discussion, the amplification coefficient, α, between a pump field E_p and an electric field of chosen bulk mode E_b is introduced in order to quantitatively indicate the increase of pump power P_p, namely $\alpha = E_p/E_b$.

Since the Kerr coefficient of graphene is particularly large, one can induce a significant variation of the refractive index of the metasurface even at moderate values of the applied local electric field, $\mathbf{E}_p(\mathbf{r})$. This in turn will lead to a sizeable frequency shift of the mode dispersion curves. To quantify this effect, we have determined numerically the projected band structure of the composite graphene metasurface and, implicitly, the frequency dispersion curves of the edge and topological waveguide modes. Importantly, in our calculations we have incorporated the contribution of the pump beam to the calculated projected band structure of the composite metasurface. Specifically, we have implemented using COMSOL an algorithm consisting of three main steps [79, 80, 81]. First, for a given optical pump power and the corresponding distribution of the electric permittivity of the metasurface, $\varepsilon'_m(\mathbf{r})$, we determined the field profile corresponding to the bulk mode used as the pump beam. Then, we used (3.2) to compute the local variation of the refraction index, $\Delta n(\mathbf{r})$, and subsequently the updated spatial distribution of the electric permittivity of the metasurface, $\varepsilon''_m(\mathbf{r}) = \varepsilon_0[n_0(\mathbf{r}) + \Delta n(\mathbf{r})]^2$, with $n_0(\mathbf{r}) = \sqrt{\varepsilon_m(\mathbf{r})/\varepsilon_0}$ being the spatial distribution of the index of refraction of the unperturbed metasurface. In the last step, the projected band structure was determined using the new permittivity distribution, $\varepsilon''_m(\mathbf{r})$. These steps were repeated until the difference $|\varepsilon'_m(\mathbf{r}) - \varepsilon''_m(\mathbf{r})|_{\mathbf{r}\in V_{cell}}$ was smaller than a certain threshold. Note that, due to the very small relative change of the electric permittivity induced by the pump, one iteration sufficed.

To investigate the influence of refractive index of graphene nanohole plasmonic waveguide on the light propagation of topological mode, several high-power bulk modes are employed as pump modes to tune the refractive index of the entire graphene waveguide. Since the power of the signal light is low that the signal-induced variation of refractive index of graphene waveguide is negligible, the light propagation of a topological interface mode is only controlled by the pump-induced variation of refractive index n of graphene nanohole metasurfaces. The optical characteristics of pump modes applied to the proposed graphene nanohole plasmonic waveguide (see Fig. 3.1) with extra nanoholes $r = 50\,\text{nm}$ are demonstrated in Fig. 3.9. In Fig. 3.9(a), blue regions represent bulk modes and a topological band

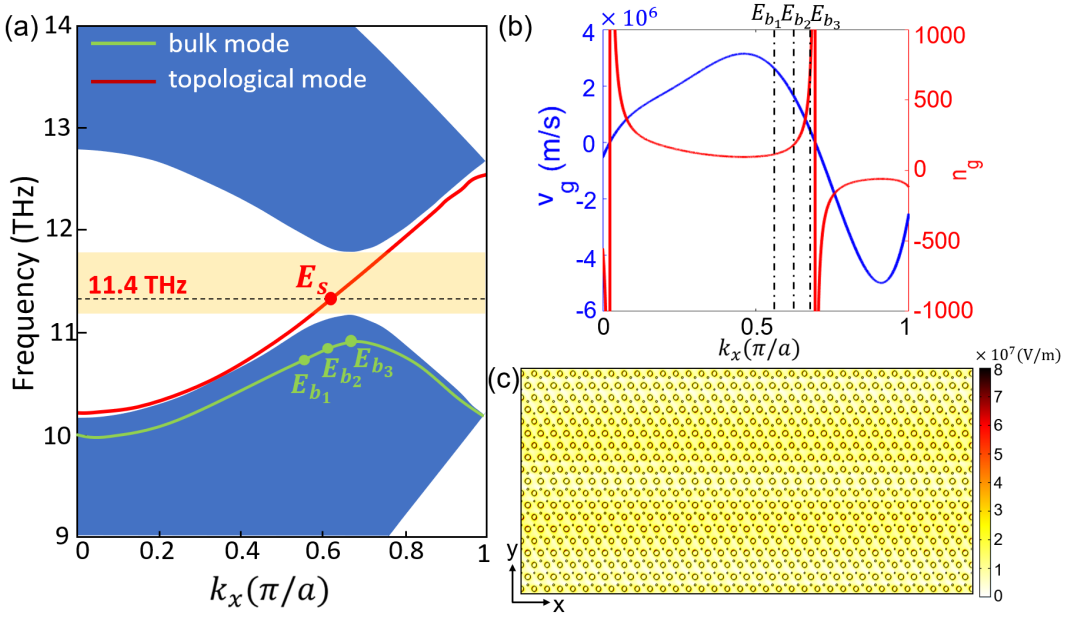

Figure 3.9: (a) Projected band diagram (blue region) of the graphene nanohole plasmonic waveguide with extra nanoholes $r = 50$ nm. A topologically protected band (red line) emerges inside the nontrivial bandgap. (b) Variation of group velocity v_g and group index $n_g = c/v_g$ with respect to k_x, corresponding to the bulk band [green line in (a)] in which three bulk modes E_{b_1}, E_{b_2} and E_{b_3} are selected. (c) Field distribution corresponding to the bulk mode E_{b_1} in (a).

inside the nontrivial bandgap is marked by a red line. For a chosen bulk-mode band indicated by the green curve, the frequency dispersion curve of the bulk band shows a peak when wave vector k_x approaches $0.7\pi/a$. To quantitatively identify the SL regime, the group velocity v_g and group index $n_g = c/v_g$ of the bulk band are shown in Fig. 3.9(b). Specifically, for three chosen bulk modes E_{b_1} ($k_x = 0.55\pi/a$), E_{b_2} ($k_x = 0.61\pi/a$) and E_{b_3} ($k_x = 0.67\pi/a$), the GV of these bulk modes is reduced from 2.7×10^6m/s to 1.8×10^6m/s, and then sharply decreases to 5.3×10^5m/s. As a result, GV of the bulk mode is close to zero with group index n_g of the bulk mode approaching 1000, namely into the SL regime [82]. Slow light can generally provide strong field enhancement for the nonlinear interaction, which is potential to be applied on novel photonic nanodevices. More specifically, the field distribution of bulk mode E_{b_1} with the largest group velocity among three chosen bulk modes is presented in Fig. 3.9(c). The corresponding light propagation of bulk mode shows a uniformly extended field distribution on the entire graphene nanohole metasurface. If the pump beam is injected by an extended bulk mode, this would lead to a signif-

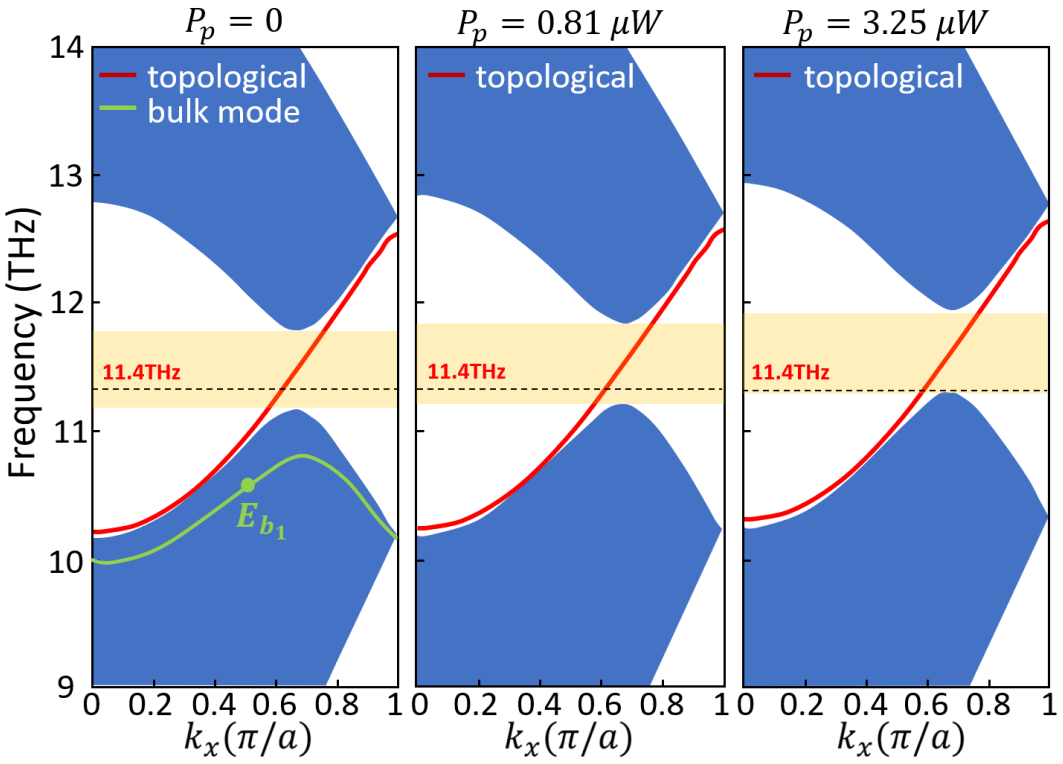

Figure 3.10: Projected band diagram of graphene nanohole plasmonic waveguide under the pump injected by bulk mode E_{b_1} determined for increasing pump powers $P_p = 0$, $P_p = 0.81\,\mu\text{W}$ and $P_p = 3.25\,\mu\text{W}$, respectively.

icant variation of refractive index in the whole graphene metasurface based on the optical Kerr effect. Note that our simulation results show similar electric fields of other two bulk modes E_{b_2} and E_{b_3} in Fig. 3.9(a) with different group velocities.

Since the optical Kerr effect on graphene nanohole plasmonic waveguide is performed by introducing the pump power injected by a relatively uniform bulk mode, the variation of band diagram of graphene nanohole metasurface as the increment of P_p is investigated in Fig. 3.10. Based on the strong Kerr effect in graphene, the whole graphene nanohole platform is uniformly pumped by a bulk mode, which can optically change the index of refraction of the graphene system. In this case, the electric field of bulk mode E_{b_1} is chosen as the pump field. When the pump field is amplified with electric field amplification coefficient $\alpha = 0, 0.006, 0.012$ with respect to the electric field of E_{b_1}, P_p is increased from 0, $0.81\,\mu\text{W}$ to $3.25\,\mu\text{W}$, respectively. Interestingly, computational results show that the frequency of nontrivial bandgap shifts up with the increasing pump power, which shows a relatively large

shift of 0.3 THz comparing with the size of topological bandgap 0.7 THz. To be more specific, if the frequency of signal mode is fixed at 11.4 THz, by increasing P_p, we can switch the topological interface mode (inside the bandgap) to a leaky bulk mode (outside the bandgap) at the threshold switching pump power $P_p = 3.25\,\mu W$ ($\alpha = 0.012$). Here, we should note that the relative position of each band would not change as the increment of pump power, although their frequency would shift up consistently.

3.3.2 Design of Active All-optical Switch

Based on the blue-shifted band diagram of the graphene waveguide with an increasing pump power, the proposed graphene nanohole plasmonic metasurface is employed to realize an active graphene-based all-optical switch.

As schematically shown in Fig. 3.11(a), a pump beam E_p (yellow region) is injected into the graphene nanohole plasmonic waveguide with a bulk mode E_b, while a LCP source at the frequency of 11.4 THz generates an optical signal E_s. Note that the LCP source is chosen as an extremely weak signal seed, so that the refractive index change of graphene induced by the LCP source can be ignored. The length of the graphene plasmonic metasurface is $L = 35a$ in order to achieve a stable signal propagation in the domain-wall interface along the x-axis. We used absorbing boundary conditions, and placed the boundaries of the computational domain in such a way that they are slightly separated from the graphene metasurface by a thin layer of air, which is utilized to model the radiation of light close to the edges. By increasing the length of graphene metasurface, one improves the accuracy and stability of the simulations of light propagation. In addition, the length can be as large as possible, however, with this choice of $L = 35a$ the simulation time decreases. Based on the fact that the signal beam can be switched from a topological interface mode into a leaky bulk mode by tuning the pump power, the optical signal at 11.4 THz can be turned ON/OFF near a certain pump power threshold. To validate these ideas, the transmission of signal beam is defined by the ratio between the input power $P_{s_{in}}$ measured near the LCP source, and the output power $P_{s_{out}}$ measured at the end of graphene waveguide, namely $\eta = P_{s_{out}}/P_{s_{in}}$. Moreover, the field distribution

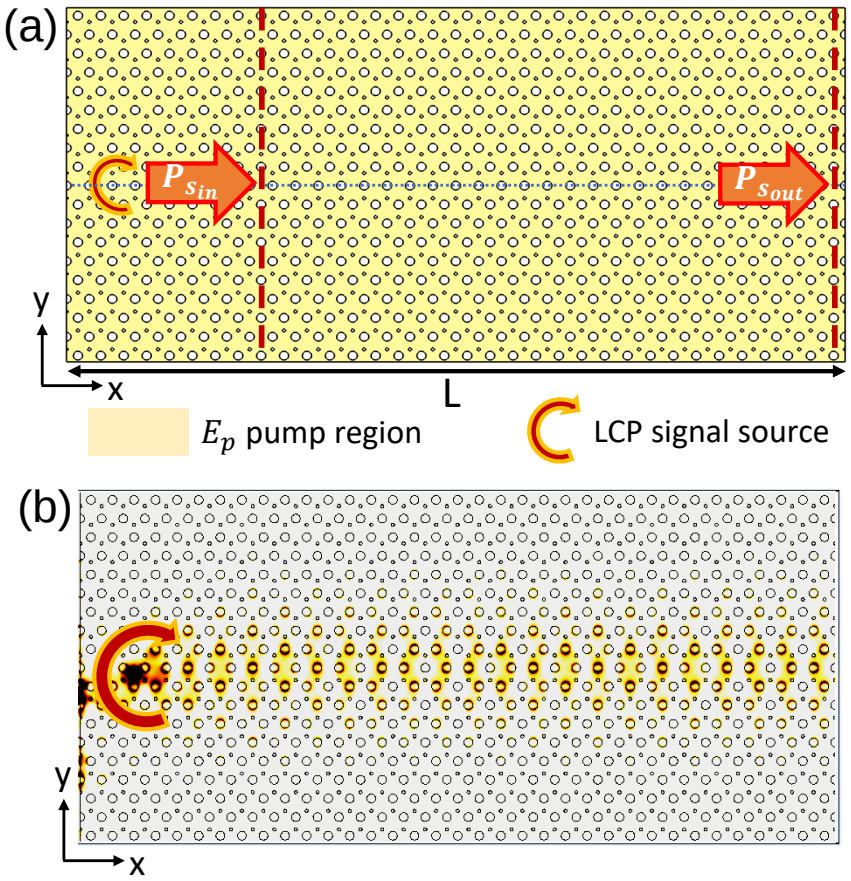

Figure 3.11: (a) Schematic of the active all-optical switch based on the graphene nanohole plasmonic waveguide. Light is pumped in the pump field E_p (yellow region), whereas the signal E_s is generated by a LCP source at 11.4 THz and carries an input power $P_{s_{in}}$ and output power $P_{s_{out}}$. The length of the simulated graphene nanohole waveguide is $L = 35a$. (b) Light propagation of a signal mode excited by a LCP at 11.4 THz without applied pump field, corresponding to the topological interface mode E_s in Fig. 3.9(a).

of the signal mode E_s excited by a LCP source at 11.4 THz is given in Fig. 3.11(b), it shows the light propagation of topological mode along the domain-wall interface without applied pump beam $P_p = 0$.

3.3.3 Result and Discussion

Variations of the signal transmission with respect to the electric field amplification coefficient α and pump power P_p are shown in Fig. 3.12(a) and 3.12(b), respectively. Red dotted circles, blue triangles, and black stars correspond to pump beams injected by three bulk modes, E_{b_1}, E_{b_2} and E_{b_3}, respectively. By employing three bulk modes with group velocities approaching the SL regime, transmissions of the

signal under different pump modes show a similar trend. The signal mode begins to couple with the bulk mode when the amplification coefficient $\alpha \geq 0.012$ in all cases and then shows slightly different variation trends as expected in Fig. 3.10. Then, with the increment of electric field amplification coefficient α over 0.022, transmissions of the signal under different pump modes sharply decrease to less than 0.1.

Such switching-off functionality is achieved based on the fact that the propagating signal beam is turned from a topological mode into a radiation bulk mode, which can also result in a dramatically reduced output power. Moreover, the transmission of the signal with respect to the pump power is studied, and the result is given in Fig. 3.12(b). Under the pump power injected by three bulk modes, the transmission of the signal beam shows a dramatic decrement when the pump power increases beyond a certain threshold value for all cases, which indeed achieves optical ON/OFF functionality to switch a signal beam. Moreover, the required switching pump power varies with pump beams of different GV. It can be seen that the smaller GV of the pump mode is the lower threshold pump power is. In particular, more than a $5\times$ reduction of the switching optical pump power between E_{b_1} and E_{b_3} bulk modes is observed in our investigations.

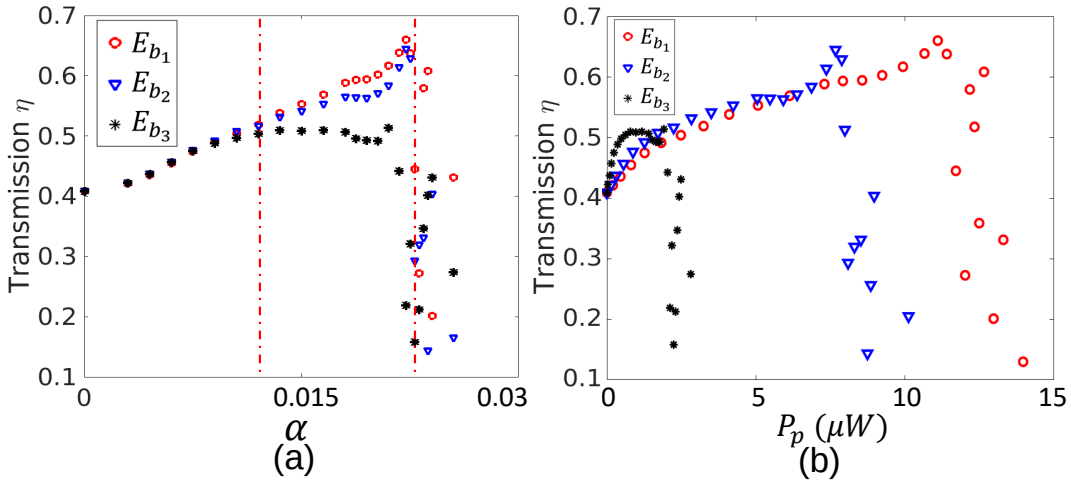

Figure 3.12: (a)(b) Signal transmission, defined as $\eta = P_{s_{out}}/P_{s_{in}}$, with respect to electric field amplification coefficient $\alpha = E_p/E_b$ and pump power P_p, respectively, determined for three bulk modes with different GV shown in Fig. 3.9(a).

3.4 Optically Controllable Nonlinear Mode Coupling *via* Kerr Effect

In this section, we design and theoretically analyze an effective scheme to couple light into an interface topological mode of a graphene metasurface. We demonstrate that, by taking advantage of the large Kerr nonlinearity of graphene, the device can be operated using low optical power and in a tunable manner. This functionality is achieved by using a pump-probe configuration, in which a pump field propagating in a bulk mode of the metasurface is used to tune its photonic structure and thus control the nonlinear optical coupling between a trivial edge mode and an interface topological mode in which a signal beam propagates. Importantly, we also show that the required pump power can be significantly reduced if the device is operated in the slow-light (SL) regime. The conclusions of our rigorous computational investigation of the coupling mechanisms are supported by a coupled-mode theory (CMT) describing the dynamics of the amplitudes of the two coupled modes.

3.4.1 Kerr Tunability of Edge and Topological Waveguide Modes

To demonstrate the existence of waveguide topological modes in our proposed graphene nanohole metasurface, we have determined the photonic band structure of an infinite crystal of the proposed graphene nanohole metasurface (see Fig. 3.1), as well as the projected band structure of the interface waveguide obtained by joining together in a mirror-symmetric manner two semi-infinite metasurfaces. Aiming to achieve efficient coupling between topological and edge modes inside the nontrivial bandgap, we consider a certain graphene nanohole waveguide with a relatively wide bandgap, which allows more flexibility in tuning the mode coupling. Therefore, for our later analysis in this chapter, we fix the lattice constant of the graphene nanohole metasurface $a = 500\,\text{nm}$. Since the unit of frequency in the photonic band diagram is $2\pi c/a$, the size of the unit cell determines the response optical frequency of the system. If the size of lattice constant a is increased by 30%, the Dirac frequency of the photonic band diagram at K point would be reduced by 6%. Note that the con-

clusions of this study remain qualitatively valid if one increases (or decreases) the lattice constant, and only the whole band diagram will be compressed (or stretched). In the first step of our analysis we determined the linear optical response of the system by neglecting the optical nonlinearity of graphene. The photonic band diagram of an infinite metasurface, determined in the case when the metasurface has inversion symmetry, *i.e.*, $R = 140\,\text{nm}$ and $r = 0$, and for a noncentrosymmetric metasurface with $R = 140\,\text{nm}$ and $r = 70\,\text{nm}$, are plotted in Fig. 3.13(a) using blue and red curves, respectively. It should be noted that graphene metasurfaces with such geometrical parameters can be readily fabricated using widely available fabrication techniques, such as *e*-beam lithography

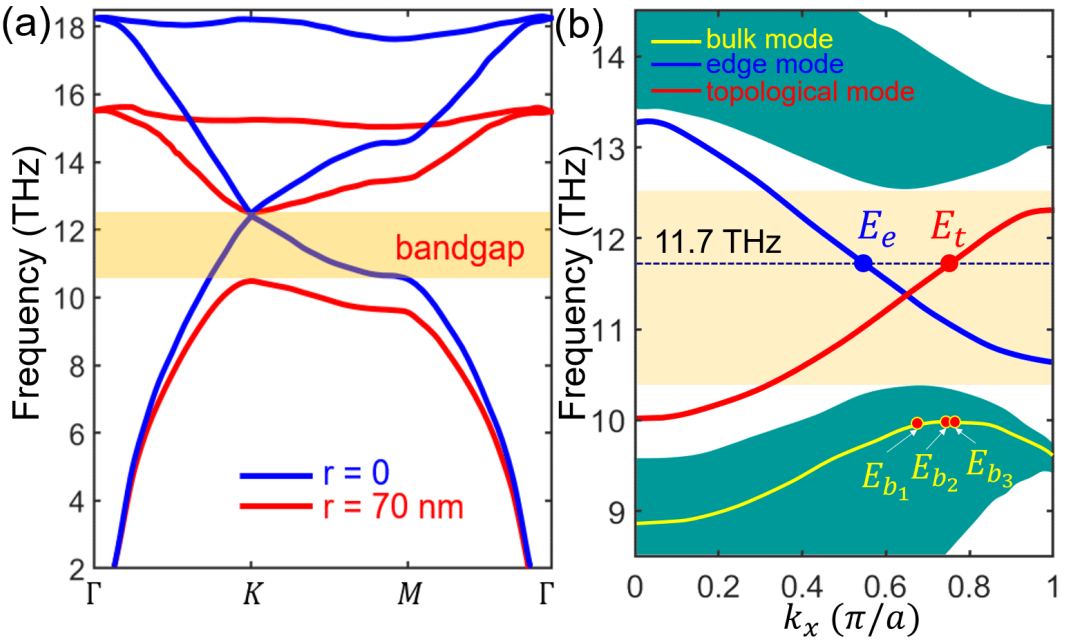

Figure 3.13: (a) Band diagram of the graphene metasurface with a lattice constant $a = 500\,\text{nm}$, determined for different radii of extra nanohole r. When $r = 0$, a Dirac cone is formed at the crossing point of the first and second bands (blue lines). By introducing a second nanohole with $r = 70\,\text{nm}$ in the primitive cell of the metasurface, a nontrivial bandgap (yellow band) from 10.4 THz to 12.5 THz is created. (b) Projected band structure of the composite metasurface, showing bulk bands (green) forming a continuum, nontrivial topological mode (red) of the graphene plasmonic waveguide, and a trivial edge mode (blue). The smaller and larger holes have radius of $r = 70\,\text{nm}$ and $R = 140\,\text{nm}$, respectively. The frequency dispersion curve of a bulk mode, depicted in yellow, together with three points indicating photonic states with different group velocities that were used as pump modes, are also shown.

The calculated band diagrams show that in the case when the graphene metasurface has inversion symmetry ($r = 0$, blue lines), that is when the lattice of holes belongs to the C_{6v} point symmetry group, there exists a symmetry-protected Dirac cone at the K-symmetry point. To be more specific, the first and second bands cross each other forming a Dirac point with frequency of 12.5 THz, with the frequency dispersion nearby this Dirac point being linear. Moreover, the C_{6v} point symmetry group is reduced to C_{3v} symmetry group when holes with finite radius, $r \neq 0$, are introduced in the unit cell of the graphene metasurface. One consequence of this change in symmetry is that a band gap opens at the frequency of the Dirac point. For a radius of $r = 70$ nm [red lines in Fig. 3.13(a)], the frequency minimum of the second band remains practically unchanged whereas the frequency maximum of the first band decreases by about 2.1 THz. This bandgap, which opens upon breaking the inversion symmetry of the lattice, is topologically nontrivial and is indicated in Fig. 3.13(a) by the yellow strip. All these results remain qualitatively unchanged if the hole radius r is varied, with the frequency bandgap becoming wider (narrower) when the radius r increases (decreases). In our subsequent analysis, the radius of the smaller holes is fixed to $r = 70$ nm.

The projected band structure of the composite metasurface that contains the 1D interfacial waveguide has been computed numerically and is presented in Fig. 3.13(b). In these calculations we used a supercell with a number of 20 unit cells along the y-axis and periodic boundary conditions along the x-axis. Since the metasurface is periodic along the x-axis with period a, the wave vector component k_x varies from 0 to π/a. The green regions in Fig. 3.13(b) represent the projected bulk bands, with one such mode being indicated by the yellow curve, whereas the blue and red lines represent the frequency dispersion curves of a trivial edge mode propagating at the edges of the metasurface and a topological valley waveguide mode located at the domain-wall interface between two metasurfaces, respectively. Also, the yellow band shows the nontrivial bandgap. Moreover, the dispersion curves of the trivial edge mode and waveguide topological mode cross each other, suggesting that, near the crossing frequency, optical power can be efficiently transferred

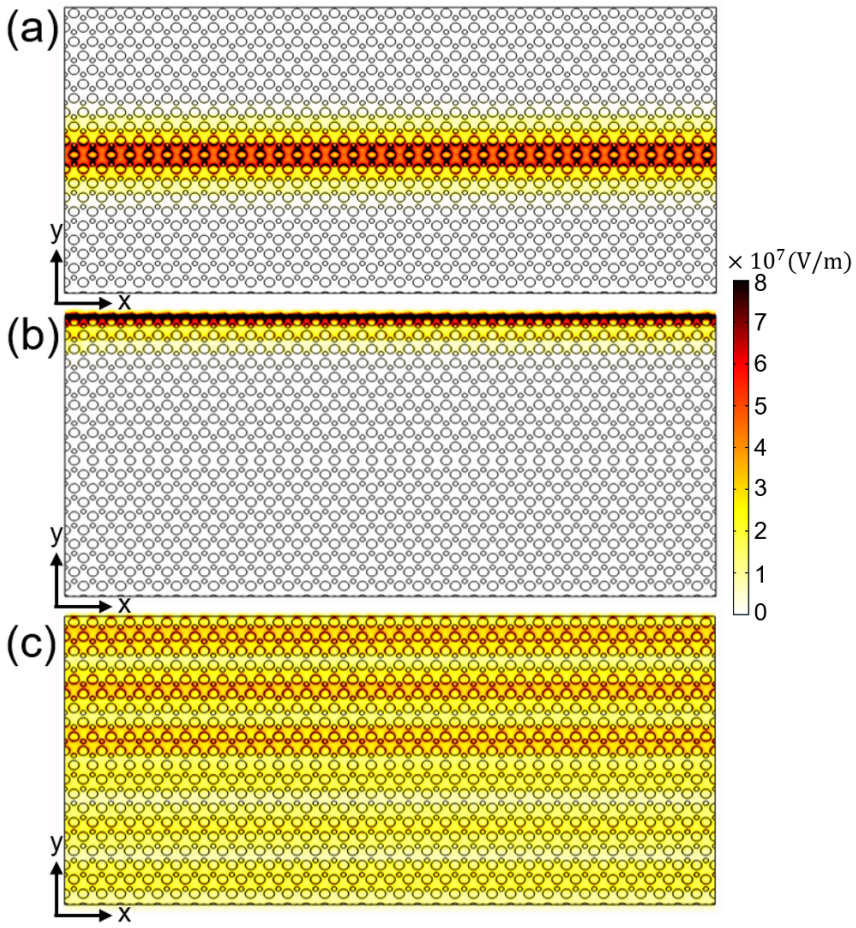

Figure 3.14: From the top to bottom panel, field distribution of the topological interface mode corresponding to 11.7 THz, trivial edge mode determined at the same frequency [labelled E_t and E_e in Fig. 3.13(b), respectively], and the bulk mode labelled E_{b_1} in Fig. 3.13(b), respectively.

between the two modes.

To further explore the optical properties of the modes of the finite, composite graphene metasurface (bulk, edge, and topological modes) we have determined their optical field profiles. In the case of the topological valley mode and trivial edge mode, we chose a frequency inside the bandgap, of 11.7 THz; the corresponding field distributions are depicted in Figs. 3.14(a) and 3.14(b), respectively. The optical field of the topological interfacial mode propagates along the waveguide formed by the two metasurfaces, whereas the optical field of the edge mode is located at the boundary of the metasurface. Note that the field distribution of both modes is highly localized, which is primarily due to the large electric permittivity

of graphene. Moreover, we also plot in Fig. 3.14(c) the optical field profile of the bulk mode indicated in Fig. 3.13(b) by the yellow curve, determined at wave vector and frequency marked with the red dot labelled "E_{b_1}". As expected, the optical field of the bulk mode spreads throughout the graphene metasurface, but the corresponding field intensity is markedly stronger in the upper half of the metasurface. Our simulation results show similar electric field profiles for the bulk mode determined at the other two points labelled by "E_{b_2}" and "E_{b_3}". However, despite the fact that field profiles of the bulk mode do not change much among the points E_{b_1}, E_{b_2}, and E_{b_3}, the group velocity (GV) determined at these points has significantly different values. As it will become apparent later on, this has important consequences regarding the operation of our device, especially vis-à-vis its optical tunability.

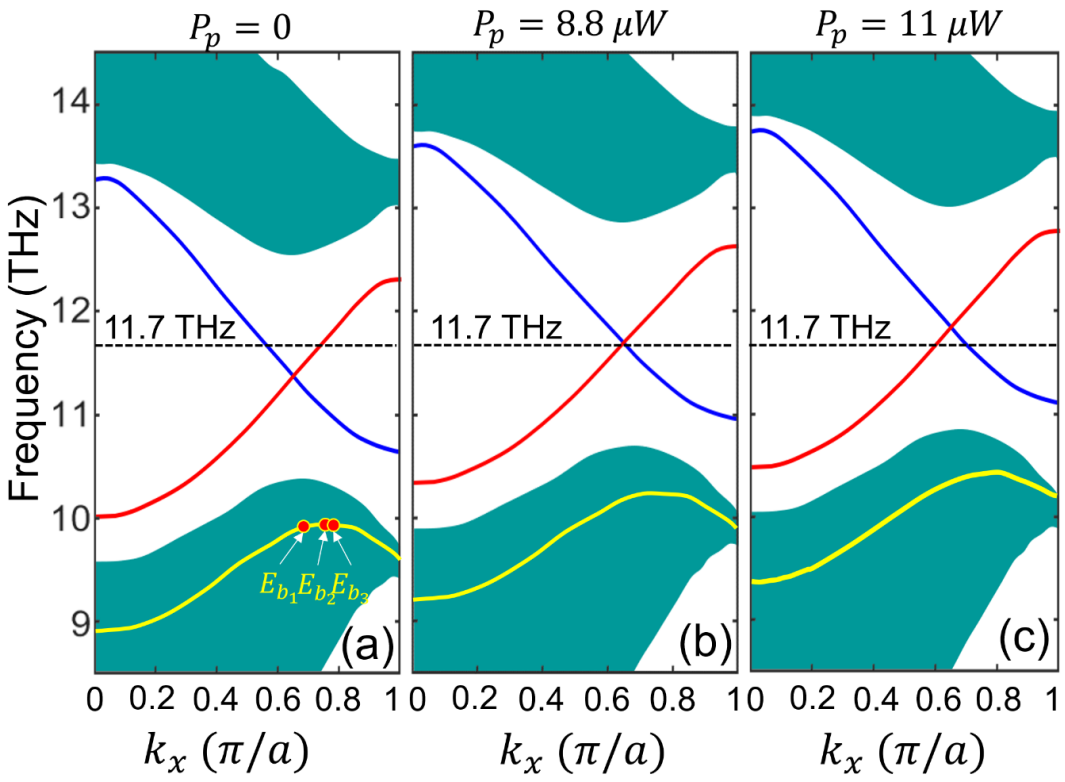

Figure 3.15: From leftmost to the rightmost panels, projected band diagrams of the composite graphene metasurface, calculated for the unperturbed photonic system ($P_p = 0$), as well as for a photonic system in which the pump power is $P_p = 8.8\,\mu$W and $P_p = 11\,\mu$W, respectively. The pump power is inserted in the mode labelled E_{b_1}. The horizontal dashed line indicates the frequency of an optical signal to be transferred from the edge mode into the topological waveguide mode.

The field distribution of the pump mode plotted in Fig. 3.14(c) suggests that the coupling between the edge and topological interfacial modes could be tuned by dint of the Kerr effect to vary the electrical permittivity of graphene in the region between the edge of the metasurface and the interface. Therefore, we investigate the influence of the optical power propagating in the bulk pump mode on the dispersion characteristics of the edge and topological modes. The results pertaining to the calculation of the projected band structure of the metasurface under the influence of Kerr effect are presented in Fig. 3.15. The projected band structures plotted in this figure have been determined for increasing values of the pump power, P_p. However, in all these calculations we used the same (bulk) pump mode, namely the mode E_{b_1} at frequency of 9.9 THz in Fig. 3.13(b). These results show that, when injecting in the mode E_{b_1} pump power with increasing values of $P_p = 8.8\,\mu\text{W}$ and $P_p = 11\,\mu\text{W}$, the projected band structure of the composite metasurface is blue-shifted by about 0.4 THz and 0.5 THz, respectively, as compared to the projected band structure of the unperturbed metasurface ($P_p = 0$).

A consequence of this blue shift of the projected band diagram is that, for a given frequency inside the nontrivial bandgap, the mismatch between wave-vectors of the topological and edge modes, $\Delta k_x = k_{x,t} - k_{x,e}$, varies with the inserted pump power. Consequently, for a given frequency of the signal, the phase-matching condition defined by $\Delta k_x = 0$ can be satisfied by properly tuning the pump power. In other words, the optical coupling between the edge and topological modes can be effectively controlled by tuning the pump power coupled into the bulk mode.

Apart from this blue shift of the projected band diagram, the overall characteristics of the frequency dispersion of the system are practically unchanged. This is demonstrated by the fact that the main dispersion coefficients of the modes depend only weakly on the pump power. This conclusion is illustrated by the results presented in Fig. 3.16, where we plot the GV, v_g, of the pump mode and its group index, n_g, defined as $n_g = c/v_g$. These physical quantities have been determined for an unperturbed composite metasurface ($P_p = 0$) and for a metasurface for which $P_p = 11\,\mu\text{W}$. Note that we chose to focus on the influence of the pump power in

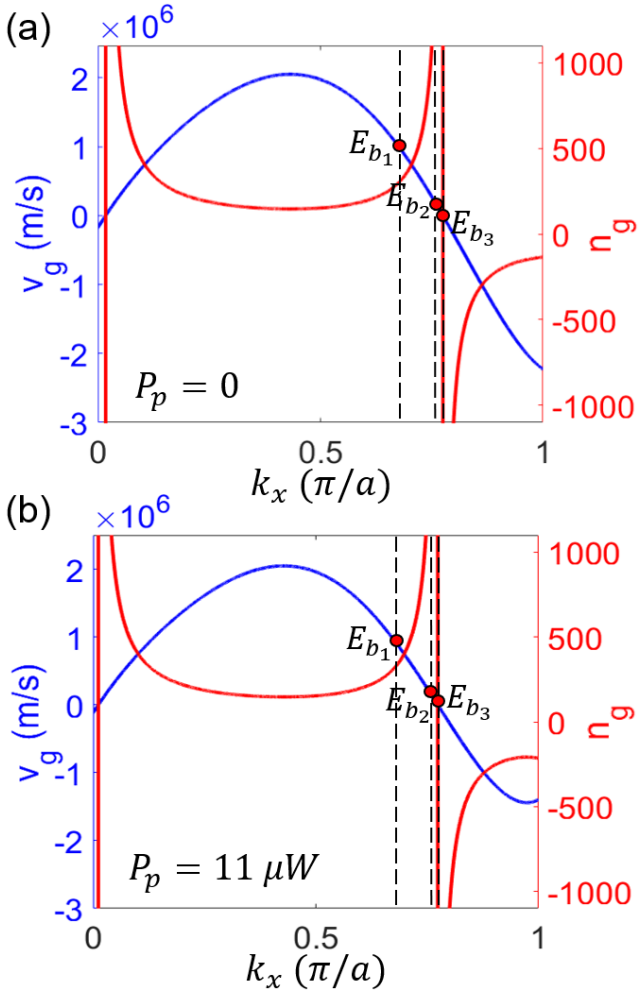

Figure 3.16: (a), (b) Dependence on the wave vector k_x of the group velocity v_g (blue curves) and group index n_g (red curves) of the bulk mode indicated by the yellow curve in Figs. 3.15(a) and 3.15(c), determined for a pump power of $P_p = 0$ and $P_p = 11\,\mu$W, respectively. The pump propagates in the mode labelled E_{b_1}.

the bulk modes on the optical response of the metasurface because, as it is apparent from Eq. (3.3), the pump power employed to optically tune the system depends on the GV of the bulk mode.

In the case when $P_p = 0$, which corresponds to Fig. 3.16(a), the dispersion curve of the GV shows two zero-group-velocity (ZGV) points defined as $v_g(k_x) = 0$, at $k_x \approx 0$ and $k_x \approx 0.775(\pi/a)$. These ZGV points define two SL regions where the group index has particularly large values. Specifically, as k_x is tuned from the bulk mode E_{b_1} [$k_x = 0.68(\pi/a)$] to the bulk mode E_{b_3} [$k_x = 0.774(\pi/a)$], v_g decreases and approaches zero, resulting in an increase of the group index to over 1000. This

physical picture changes only slightly when $P_p \neq 0$. The main difference in the case when a pump power is applied is that the values of the optical dispersion coefficients change with the pump power, especially near the edge of the first Brillouin zone, namely near $k_x = \pi/a$.

The property of extremely small group velocity of the bulk modes can be employed to optimize the operation of the nonlinear optical coupler. To be more specific, it can be seen from Eq. (3.3) that for a given pump power P_p, the smaller the GV of the mode (that is, the deeper in the SL regime the device is operated), the larger an optical field is generated and consequently a larger variation of the index of refraction of the metasurface is achieved. Therefore, for a given operating pump power, the smaller the GV is, the larger is the induced frequency shift of the projected band structure. As a design principle, it becomes apparent that in order to attain an optimum operation of our nonlinear optical coupler, namely to achieve a minimum operating pump power, the system parameters must be chosen in such a way that the phase-matching condition $\Delta k_x = 0$ is fulfilled in the SL region.

3.4.2 Analysis of The Phase-matching Condition

To control optically the frequency dispersion of the topological waveguide mode and its coupling to the edge modes, we use a pump beam that propagates in a bulk mode of the metasurface, illustrated by an orange arrow in Fig. 3.17. Specifically, the electrical permittivity of the metasurface can be controlled using the pump beam *via* the Kerr effect in the graphene. The input red arrow in Fig. 3.17 indicates the excitation of the edge mode that carries the optical signal. Upon coupling to the topological waveguide mode, the signal propagates to the output of the waveguide where it is collected. Since the difference between the wave-vectors of the topological and edge modes is the key physical parameter that governs the efficiency of the optical coupling between the two modes, in what follows we focus our attention on the dependence of this physical quantity on the pump power, P_p.

To begin with, we assume that the pump power is inserted in the graphene metasurface using the bulk mode E_{b_1}. For this configuration, using full-wave numerical simulations based on the finite-element method, we determined the spatial

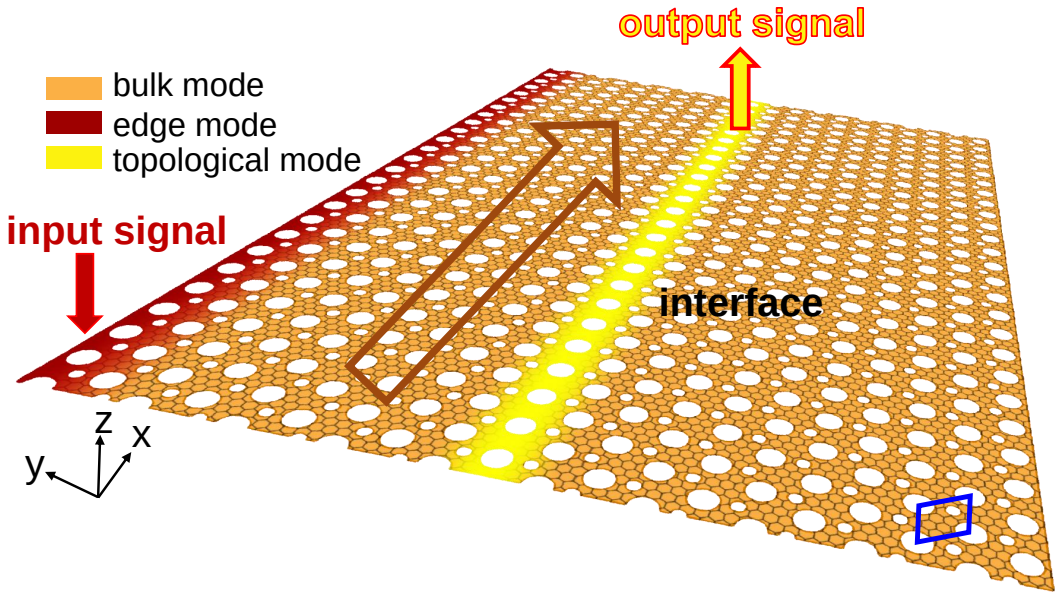

Figure 3.17: Schematic of the graphene metasurface plasmonic waveguide showing the coupling between the edge and topological interfacial modes. The graphene waveguide is created by adjoining together in a mirror-symmetric way two semi-infinite graphene metasurfaces consisting of a hexagonal periodic distribution of holes with primitive unit cell marked by blue rhombus. The red and yellow arrows indicate the optical signal coupled to the trivial edge mode (red) and the output signal collected from the topological mode (yellow), after it propagated along the domain-wall interface. The orange arrow indicates the pump beam propagating in the bulk mode, and is used to control the optical coupling between the edge and interface modes.

field profile in the nonlinear optical coupler for pump power values of $P_p = 0$ (unperturbed metasurface) and $P_p = 10\,\mu\text{W}$, the corresponding results being presented in Fig. 3.18(a) and 3.18(b), respectively.

We used absorbing boundary conditions, and placed the boundaries of the computational domain in such a way that they are slightly separated from the graphene metasurface by a thin layer of air. By avoiding the graphene metasurface to reach the boundaries of the computational domain one improves the accuracy and stability of the simulations. Moreover, the transverse width of the upper domain of the graphene structure has width of 10 unit cells and was chosen to be larger than that of the lower domain, which has width of 3 unit cells, because both the overlap between the optical fields of the two modes and the field distribution of the bulk pump mode are primarily localized in the upper domain of the graphene metasurface. In

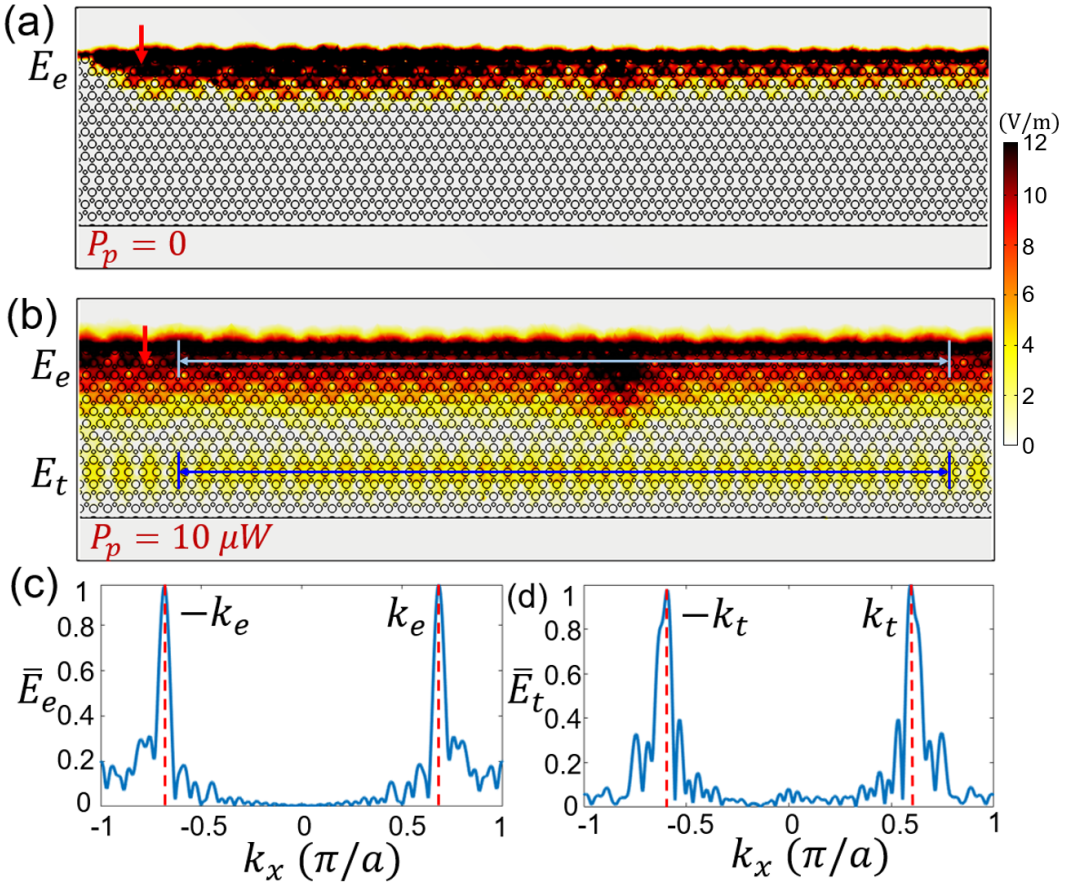

Figure 3.18: (a), (b) Spatial field profile in the nonlinear coupler, determined for $P_p = 0$ and $P_p = 10\,\mu\text{W}$, respectively. The input pump power is injected in the bulk mode E_{b_1} at frequency of 11.7 THz, *via* a dipole source indicated by the red arrow. (c), (d) Fourier transform of normalized electric fields of the trivial edge mode, $\bar{E}_e$, and topological mode, $\bar{E}_t$, shown in Fig. 3.18(b), respectively. The spatial intervals of the Fourier-transform calculations of the edge and topological modes are marked by light and dark blue lines in Fig. 3.18(b), respectively.

addition, with this choice the simulation time decreases. Finally, the edge mode is excited *via* a dipole source (red arrow) with frequency of 11.7 THz, placed in the vicinity of the top boundary of the graphene metasurface with length of 65 unit cells along the longitudinal direction.

Our calculations show that when $P_p = 0$, the wave-vector mismatch is relatively large, $\Delta k_x = 0.28\pi/a$. As expected, because of this significant wave-vector mismatch only a small amount of optical power couples into the topological mode, a fact illustrated by Fig. 3.18(a), too. By contrast, when the pump power injected in the bulk mode E_{b_1} increases to $P_p = 10\,\mu\text{W}$, the spatial field distribution presented in

Fig. 3.18(b) reveals an efficient optical coupling between the topological and edge modes. This conclusion is also supported by the significantly reduced value of the wave-vector mismatch, which in this case is $\Delta k_x = 0.032\pi/a$. This demonstrates that the amount of optical power transferred from the edge mode to the topological waveguide mode can be effectively tuned by optically tuning the wave-vector mismatch between the two modes *via* the pump power P_p propagating in the bulk mode.

The wave-vector mismatch can also be extracted from the spatial field profiles presented in Figs. 3.18(a) and 3.18(b), which provides an alternative approach to quantitatively analyzing the operation of the proposed nonlinear optical coupler. This approach consists in Fourier transforming the field profiles, $\mathbf{E}(\mathbf{r})$, to the momentum space, $\bar{\mathbf{E}}(\mathbf{k})$, and subsequently extracting the value of the wave-vectors corresponding to the peaks of the field spectra. This procedure is illustrated by the spectra plotted in Figs. 3.18(c) and 3.18(d), which correspond to the edge and topological modes observed in Fig. 3.18(b), respectively. These spectra, corresponding to a pumped metasurface, display two symmetrically located peaks pertaining to forward- (k_e, k_t) and backward-propagating $(-k_e, -k_t)$ modes.

To gain deeper insights into the physics of the optical coupling between the edge and topological modes, we developed a coupled-mode theory (CMT) that describes the dynamics of the mode amplitudes upon their propagation in the graphene metasurface. To this end, consider the x-dependent amplitudes of the edge and topological mode, $E_e(x)$ and $E_t(x)$, respectively, in a case characterized by the wave-vector mismatch, Δk_x. Then, their dependence on the propagation distance, x, is governed by the following system of coupled ordinary differential equations [83, 84]:

$$\frac{dE_e(x)}{dx} = i\kappa E_t(x) e^{-i\Delta k_x x} - \frac{\alpha_l}{2} E_e(x), \tag{3.4}$$

$$\frac{dE_t(x)}{dx} = i\kappa E_e(x) e^{i\Delta k_x x} - \frac{\alpha_l}{2} E_t(x), \tag{3.5}$$

where α_l is the loss coefficient due to intrinsic and radiative losses and κ is the coupling coefficient between the modes. Note that, for the sake of simplicity, we

assumed that the loss coefficients of the two modes are equal.

After simple mathematical manipulations, one can derive from Eqs. (3.4) and (3.5) the dependence on the propagation distance of the physical quantities of interest, namely the mode powers $P_e(x) = |E_e(x)|^2$ and $P_t(x) = |E_t(x)|^2$. Subject to the initial conditions $E_e(0) = E_0$ and $E_t(0) = 0$, the optical power of edge and topological interface modes can be expressed as:

$$P_e(x) = \frac{P_0}{\xi^2} e^{-\alpha_l x} \left[\xi^2 \cos^2(\xi \kappa x) + \rho^2 \sin^2(\xi \kappa x)\right], \tag{3.6}$$

$$P_t(x) = \frac{P_0}{\xi^2} e^{-\alpha_l x} \sin^2(\xi \kappa x), \tag{3.7}$$

where $P_0 = |E_0|^2$ is the initial power inserted in the edge mode, $\rho = \Delta k_x/(2\kappa)$ is a parameter that measures the relative coupling strength, and $\xi = \sqrt{1+\rho^2}$ is a wave-vector scaling factor. It can be easily verified using Eqs. (3.6) and (3.7) that the total power in the two modes satisfies the power decay relation, $P_e(x) + P_t(x) = P_0 e^{-\alpha_l x}$.

The CMT provides us an alternative approach to determine the wave-vector mismatch between the edge and topological modes, and consequently the means to validate the physical assumptions on which the CMT is based. In particular, by fitting the powers $P_e(x)$ and $P_t(x)$ determined using full-wave simulations with the analytic solutions Eqs. (3.6) and (3.7), one can extract the parameters κ and Δk_x of the nonlinear optical coupler. This procedure and the corresponding results are summarized in Fig. 3.19. Thus, we present in Figs. 3.19(a) and 3.19(b) the dependence on the propagation distance of the optical power in the topological mode, $P_t(x)$, determined in the regime of weak coupling ($P_p = 12.3\,\mu\text{W}$) and optimum coupling ($P_p = 15.4\,\mu\text{W}$), respectively, when the pump power is inserted in the bulk mode E_{b_1}. In the full-wave simulations the power P_t is computed by integrating the longitudinal component of the Poynting vector, S_x, across the transverse extent of the interface region.

The top two panels of Fig. 3.19 show that the CMT solution of Eqs. (3.4) and (3.5) provides a good fit for the variation of the envelope of the full-wave solution obtained numerically, suggesting that it properly captures the main physics of the optical structure. The full-wave simulations, on the other hand, describe the power

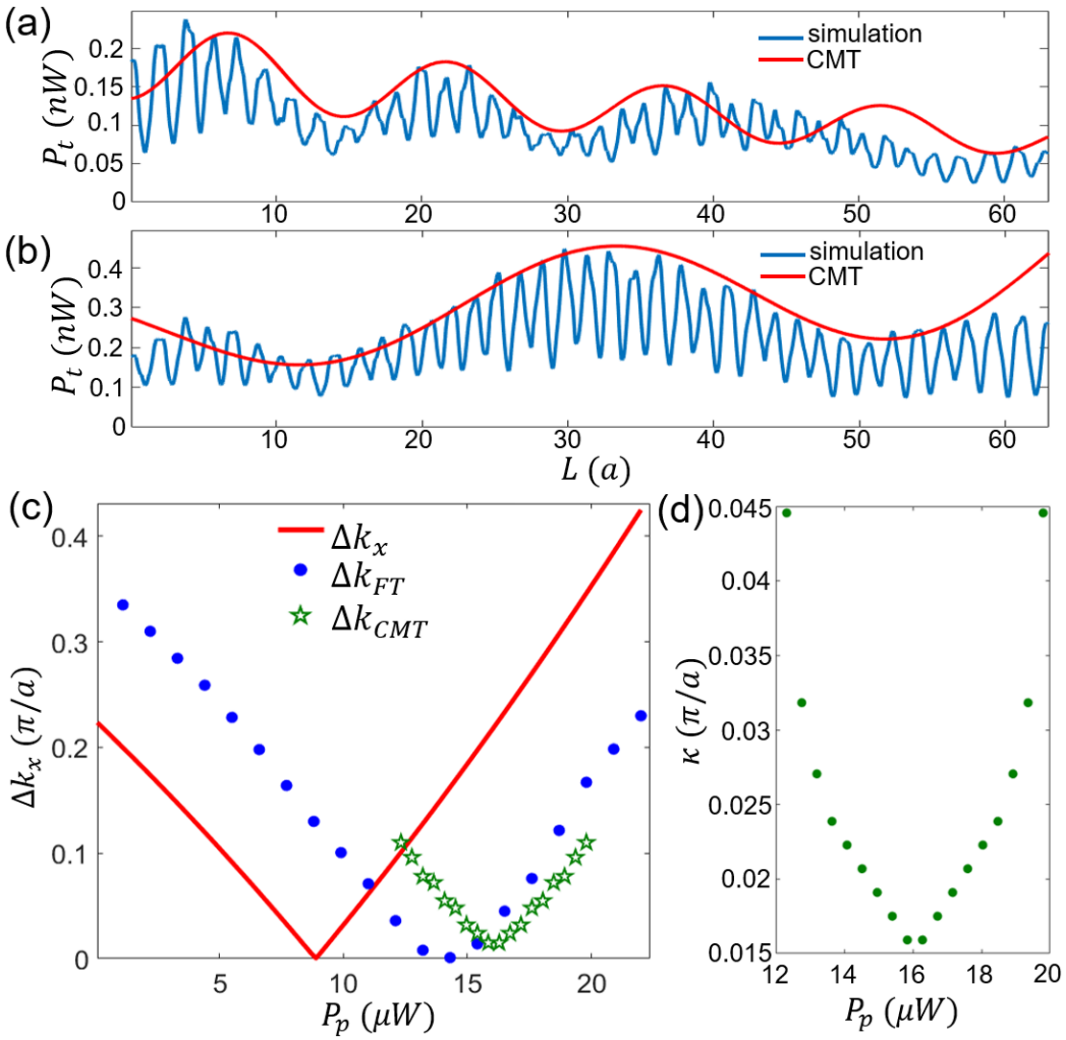

Figure 3.19: (a), (b) Power of the topological interfacial mode, P_t, vs. the propagation length L, determined in the regimes of weak coupling ($P_p = 12.3\,\mu$W) and optimum coupling ($P_p = 15.4\,\mu$W), respectively, as predicted by the CMT. Blue and red curves correspond to full-wave simulations and fitted solutions of the CMT, respectively. (c) Dependence of wave-vector mismatch, Δk_x, on the pump power P_p injected in the bulk mode E_{b_1}. The wave-vector Δk_x is extracted from the projected band diagram (red line), Fourier transform of the spatial distribution of the propagating fields (dots), and CMT (stars). (d) Coupling coefficient κ *vs.* pump power P_p, predicted by the CMT.

dynamics at the lattice constant scale. Moreover, it can be seen in Fig. 3.19(a) that if the pump power $P_p = 12.3\,\mu$W, the power P_t determined using the CMT oscillates with period of about $15a$, the wave-vector mismatch and coupling constant being $\Delta k_x = 0.11\pi/a$ and $\kappa = 0.045\pi/a$, respectively. When the pump power is increased to $P_p = 15.4\,\mu$W, which corresponds to the data in Fig. 3.19(b), the period of the

power oscillations increases to $40a$, whereas $\Delta k_x = 0.024\pi/a$ and $\kappa = 0.006\pi/a$. It can be said that an optimum coupling regime has been reached as the wave-vector mismatch between the two modes has decreased to a vanishingly small value.

To quantify more completely the influence of the pump power on the efficiency of the mode coupling, we determined the wave-vector mismatch for different values of the pump power using the three methods we just described. The results of these calculations, presented in Fig. 3.19(c), demonstrate that the wave-vector mismatch determined using the projected band diagram (Δk_x), the Fourier transform of the spatial distribution of the field (Δk_{FT}), and the CMT (Δk_{CMT}) depends on the pump power in a similar way, the only difference being a slight shift of a few μW's among the corresponding curves. Specifically, in all three cases, the wave-vector mismatch vanishes for the pump power P_p injected in the bulk mode E_{b_1} approaching a certain value, so that all three methods predict that efficient mode matching can be achieved by tuning P_p.

The CMT allows one to extract from the power dynamics not only the wave-vector mismatch but also the coupling constant κ. The relevant data, plotted in Fig. 3.19(d), show that κ reaches a minimum value for the same pump power for which $\Delta k_{CMT} \approx 0$, that is when the two modes are phase-matched.

3.4.3 Optically Controllable Mode Coupling in the Slow-light Regime

As we have previously alluded to, SL effects can potentially be used to reduce the operating pump power of the nonlinear optical coupler. To quantitatively analyze these nonlinear optical effects, we tuned the frequency of the pump beam in such a way that the corresponding GV of the bulk pump mode is significantly reduced and repeated the analysis performed in the case when the pump power is inserted in the bulk mode E_{b_1}. In what follows, we discuss the conclusions of these computational investigations.

To vary the GV of the pump beam we chose its frequency in such a way that the bulk pump mode is tuned from E_{b_1} to E_{b_2} and finally to E_{b_3}. In the first part of our analysis, in all these three cases we used the Fourier transform based approach

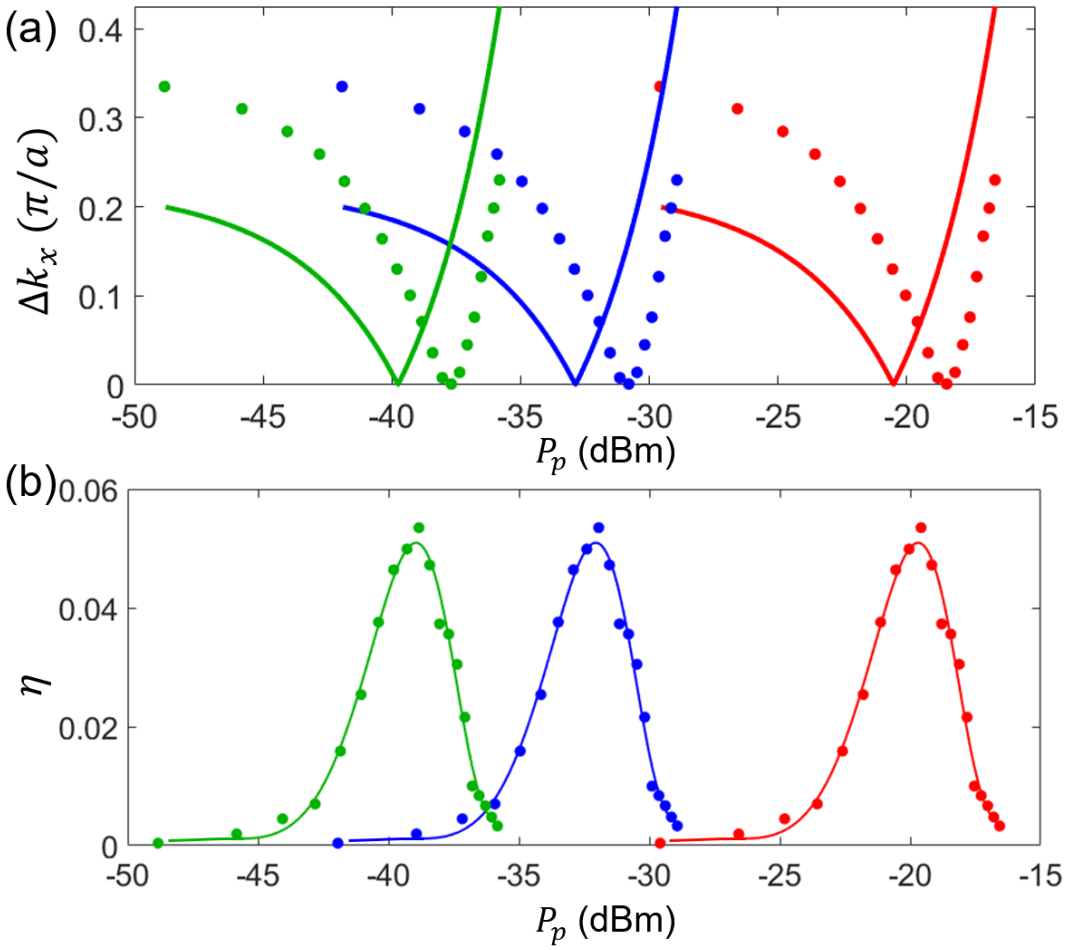

Figure 3.20: (a) Wave-vector mismatch Δk_x *vs.* pump power P_p, when the pump beam propagates in mode E_{b_1} (red), E_{b_2} (blue), and E_{b_3} (green). The solid and dotted curves correspond to Δk_x extracted from the projected band diagram and calculated by Fourier transforming the spatial distribution of the field, respectively. (b) Ratio η_t between the output power in the topological mode and the input power in the edge mode *vs.* the pump power, determined for the pump modes E_{b_1} (red), E_{b_2} (blue), and E_{b_3} (green). The solid curves are a guide to the eye.

to compute the pump power dependence of the wave-vector mismatch, Δk_x, the outcome of these calculations being depicted with dotted symbols in Fig. 3.20(a). In addition to this analysis based on the Fourier transform of the spatial field profiles, we also used the pump power dependent projected band diagrams to extract the value of Δk_x and summarize the results of these calculations in Fig. 3.20(a) using solid curves.

In all three cases the two methods agree in their prediction of the pump power

at which the two modes are phase-matched ($\Delta k = 0$). When the phase-matching condition is fulfilled by tuning the pump power to a certain value, the topological and edge modes are most efficiently coupled, meaning that a maximum amount of power can be transferred between the two modes. Note that this critical pump power value depends strongly on the GV of the pump beam. In particular, this pump power decreases by more than $100\times$ when the pump mode is pushed deep into the SL domain, namely when it is tuned from mode E_{b_1} (red curve) to E_{b_3} (green curve).

The most important parameter that characterizes our nonlinear optical coupler is the transmission coefficient, η_t, defined as the ratio between the output power in the topological mode and the input power of the edge mode, as it quantifies the efficiency of the optical coupler. Therefore, in the second part of our analysis of the nonlinear optical coupler we have determined the dependence of η_t on the pump power. These computations, whose conclusions are presented in Fig. 3.20(b), have been performed for the pump modes E_{b_1} (red), E_{b_2} (blue), and E_{b_3} (green). The pump power dependence of the transmission η_t shows that, as expected, in all cases there is a certain value of the pump power for which maximum transmission is achieved. This pump power at which maximum transmission corresponds to $\Delta k = 0$ [Fig. 3.20(a) and 3.20(b)] which demonstrates that the optical power is transferred between the two modes through evanescent mode coupling. Importantly, the pump power required to achieve maximum power transfer decreases as the GV of the pump mode, v_g, decreases; however, it is noteworthy to point out that the maximum transferred power does not depend on v_g.

3.5 Conclusion

In summary, we demonstrated the graphene nanohole plasmonic metasurface whose spatial-inversion symmetry is broken by introducing extra nanoholes. The spatial-inversion symmetry breaking of graphene metasurface opens up a symmetry-protected Dirac cone, which leads to the emergence of a nontrivial bandgap. Based on the Wilson loop computational method, the non-vanishing valley Chern numbers calculated inside discretized domains around K and K' valleys, quantitatively define

the topological nontrivial property of the proposed graphene metasurface. Our results show that the computational accuracy of valley Chern number for the first band is strongly dependent on the size of bandgap. Specifically, since the Berry curvature distribution of the first band with a narrower bandgap is less spread around each valley, the calculated valley Chern number is more closed to $\pm 1/2$. By placing two halves of graphene nanohole metasurfaces together in a mirror-symmetric manner, a ± 1 valley Chern number difference across the domain-wall interface is achieved. As a result, a topological interface mode appears inside the bandgap and its corresponding light propagation along the domain-wall interface shows a unidirectional feature.

Based on the linear optical response of the proposed graphene nanohole metasurface, an active optically-tunable switch has been proposed based on the Kerr effect in the proposed topologically protected valley-Hall graphene nanohole plasmonic metasurface. Taking advantage of the graphene platform with a large nonlinear refractive index, the Kerr effect of graphene is used to shift the frequency of nontrivial bandgap due to the variation of refractive index of the system, so that we can optically control the signal propagation in the graphene nanohole waveguide. Under the pump injected by bulk modes with reduced GV, our computational results show and prove that the transmission of the optical signal steeply decreases as the increment of the pump power, which indeed realizes an active all-optical switch. Specifically, the switching power is strongly dependent on the GV of pump mode, and the required switching pump power is significantly reduced when the all-optical switch works in the SL regime. This design of optically controllable switch may contribute to the development of active photonic nanodevice implemented in integrated graphene-based topological systems.

Moreover, we have investigated an optically controllable nonlinear coupler that can be used to transfer optical power between a trivial edge mode and a topological interface mode of the proposed graphene nanohole plasmonic metasurface. The nonlinear optical coupler is controlled *via* the Kerr effect in graphene induced by a pump beam. Specifically, the pump beam is employed to tune the band structure

of the photonic system and, consequently, the key parameter that defines the efficiency of the nonlinear optical coupler, namely the wave-vector mismatch between the edge and topological interface modes. Importantly, we have also demonstrated that the required pump power can be significantly reduced if the optical device is operated in the slow-light regime. We performed our analysis using both *ab initio* full-wave simulations and a CMT that captures the main physics of this active coupler and observed a good agreement between the two approaches. Practical technological implications of this work have been discussed, too. Our work proposed a new way to excite topological interface mode via optically-controllable coupling between topological and trivial edge modes with high efficiency, which can facilitate and spur the development of new or improved active photonic devices that combine the advantages provided by topological photonics and nonlinear optics.

In addition to the proposed graphene nanohole plasmonic crystal metasurfaces with reduced spatial-inversion symmetry, in the next chapter, we design a bilayer graphene metasurface to realize valley topological plasmonic modes by utilizing a novel mechanism of mirror symmetry breaking between the top and bottom graphene layers by horizontally shifting two layers, and the topological properties of the bilayer graphene metasurfaces will also be discussed.

Bibliography

[1] L. Lu, J. D. Joannopoulos, and M. Soljacic, "Topological photonics," Nat. Photon. **8**, 821-829 (2014).

[2] A. B. Khanikaev and G. Shvets, "Two-dimensional topological photonics," Nat. Photon. **11**, 763-773 (2017).

[3] T. Ozawa, *et al.* "Topological photonics," Rev. Mod. Phys. **91**, 015006 (2019).

[4] B. Y. Xie, H. F. Wang, X. Y. Zhu, M. H. Lu, Z. D. Wang, and Y. F. Chen, "Photonics meets topology," Opt. Express **26**, 24531-24550 (2018).

[5] X. C. Sun, C. He, X. P. Liu, M. H. Lu, S. N. Zhuand, and Y. F. Chen, "Two-dimensional topological photonic systems," Prog. Quantum Electron. **55**, 52-73 (2017).

[6] Y. Wu, C. Li, X. Hu, Y. Ao, Y. Zhao, and Q. Gong, "Applications of topological photonics in integrated photonic devices," Adv. Opt. Mater. **5**, 1700357 (2017).

[7] M. S. Rider, S. J. Palmer, S. R. Pocock, X. Xiao , P. Arroyo Huidobro, and V. Giannini, "A perspective on topological nanophotonics: Current status and future challenges," J. Appl. Phys. **125**, 120901 (2019).

[8] M. Z. Hasan and C. L. Kane, "Colloquium: Topological insulators," Rev. Mod. Phys. **82**, 3045-3067 (2010).

[9] X. L. Qi and S. C. Zhang, "Topological insulators and superconductors," Rev. Mod. Phys. **83**, 1057 (2011).

[10] F. D. M. Haldane and S. Raghu, "Possible realization of directional optical waveguides in photonic crystals with broken time-reversal symmetry," Phys. Rev. Lett. **100**, 013904 (2008).

[11] Z. Wang, Y. D. Chong, J. D. Joannopoulos, and M. Soljacic, "Reflection-free one-way edge modes in a gyromagnetic photonic crystal," Phys. Rev. Lett. **100**, 013905 (2008).

[12] Z. Wang, Y. D. Chong, J. D. Joannopoulos, and M. Soljacic, "Observation of unidirectional backscattering-immune topological electromagnetic states," Nature **461**, 772-775 (2009).

[13] Y. Poo, R. X. Wu, Z. Lin, Y. Yang, and C. T. Chan, "Experimental realization of self-guiding unidirectional electromagnetic edge states," Phys. Rev. Lett. **106**, 093903 (2011).

[14] A. B. Khanikaev, S. Hossein Mousavi, W. K. Tse, M. Kargarian, A. H. MacDonaldand, and G, Shvets, "Photonic topological insulators," Nat. Mater. **12**, 233-239 (2013).

[15] T. Ma, A. B. Khanikaev, S. H. Mousavi and G. Shvets, "Guiding electromagnetic waves around sharp corners: topologically protected photonic transport in metawaveguides," Phys. Rev. Lett. **114**, 127401 (2015).

[16] L. H. Wu and X. Hu, "Scheme for achieving a topological photonic crystal by using dielectric material," Phys. Rev. Lett. **114**, 223901 (2015).

[17] K. Y. Bliokh, D. Smirnova, and F. Nori, "Quantum spin Hall effect of light," Science **348**, 1448-1451 (2015).

[18] T. Ma and G. Shvets, "All-Si valley-Hall photonic topological insulator," New J. Phys. **18**, 025012 (2016).

[19] X. T. He, E. T. Liang, J. J. Yuan, H. Y. Qiu, X. D. Chen, F. L. Zhao, and J. W. Dong, "A silicon-on-insulator slab for topological valley transport," Nat. Commun. **10**, 872 (2019).

[20] M. I. Shalaev, W. Walasik, A. Tsukernik, Y. Xu, and N. M. Litchinitser, "Robust topologically protected transport in photonic crystals at telecommunication wavelengths," Nat. Nanotechnol. **14**, 31-34 (2019).

[21] J. W. You, Z. Lan, Q. Bao, and N. C. Panoiu, 2020 "Valley-Hall topological plasmons in a graphene nanohole plasmonic crystal waveguide," IEEE J. Sel. Top. Quantum Electron. **26**, 4600308 (2020).

[22] D. Xiao, W. Yao, and Q. Niu, "Valley-contrasting physics in graphene: magnetic moment and topological transport," Phys. Rev. Lett. **99**, 236809 (2007).

[23] A. Rycerz, J. Tworzydło, and C. W. J. Beenakker, "Valley filter and valley valve in graphene," Nat. Photon. **3**, 172-175 (2007).

[24] T. Ma and G. Shvets, "All-Si valley-Hall photonic topological insulator," New J. Phys. **18**, 025012 (2016).

[25] Y. Kang, X. Ni, X. Cheng, A. B. Khanikaev, and A. Z. Genack, "Pseudo-spin–valley coupled edge states in a photonic topological insulator," Nat. Commun. **9**, 1-7 (2018).

[26] D. Jin, T. Christensen, M. Soljacic, N. X. Fang, L. Lu, and X. Zhang, "Infrared Topological Plasmons in Graphene," Phys. Rev. Lett. **118**, 245301 (2017).

[27] J. W. You, Z. Lan, and N. C. Panoiu, "Four-wave mixing of topological edge plasmons in graphene metasurfaces," Sci. Adv. **6**, eaaz3910 (2020).

[28] J. W. You, S. Bongu, Q. Bao, and N. C. Panoiu, Nanophotonics, "Nonlinear optical properties and applications of 2D materials: theoretical and experimental aspects," **8**, 63-97 (2018).

[29] P. A. D. Goncalves and N. M. Peres, *An Introduction to Graphene Plasmonics* (World Scientific, 2016).

[30] X. Du, I. Skachko, A. Barker, and E. Y. Andrei, "Approaching ballistic transport in suspended graphene," Nat. Nanotechnol. **3**, 491-495 (2008).

[31] V. Singh, D. Joung, L. Zhai, S. Das, S. I. Khondaker, and S. Seal, "Graphene Based Materials: Past, Present and Future," Prog. Mater. Sci. **56**, 1178-1271 (2011).

[32] Y. Zhang, L. Zhang, and C. Zhou, "Review of chemical vapor deposition of graphene and related applications," Acc. Chem. Res. **46**, 2329-2339 (2013).

[33] D. Smirnova, D. Leykam, Y. Chong, and Y. Kivshar, "Nonlinear topological photonics," Appl. Phys. Rev. **7**, 021306 (2020).

[34] X. Zhou, Y. Wang, D. Leykam, and Y. D. Chong, "Optical isolation with nonlinear topological photonics," New J. Phys. **19**, 095002 (2017).

[35] S. Kruk, *et al.* "Nonlinear light generation in topological nanostructures," Nat. Nanotechnol. **14**, 126-130 (2019).

[36] Y. Hadad, A. B. Khanikaev, and A. Alu, "Self-induced topological transitions and edge states supported by nonlinear staggered potentials," Phys. Rev. B **93**, 155112 (2016).

[37] C. Monat, M. De Sterke, and B. J. Eggleton, "Slow light enhanced nonlinear optics in periodic structures," J. Opt. **12**, 104003 (2010).

[38] N. C. Panoiu, M. Bahl, and R. M. Osgood Jr, "Optically tunable superprism effect in nonlinear photonic crystals," Opt. Lett. **28**, 2503-2505 (2003).

[39] Y. Lumer, Y. Plotnik, M. C. Rechtsman, and M. Segev, "Self-localized states in photonic topological insulators," Phys. Rev. Lett. **111**, 243905 (2013).

[40] Z. Lan, J. W. You, Q. Ren, W. E. I. Sha, and N. C. Panoiu, "Second-harmonic generation via double topological valley-Hall kink modes in all-dielectric photonic crystals," Phys. Rev. A **103**, L041502 (2021).

[41] Z. Lan, J. W. You, and N. C. Panoiu, "Nonlinear one-way edge-mode interactions for frequency mixing in topological photonic crystals," Phys. Rev. B **101**, 155422 (2020).

[42] D. Smirnova, S. Kruk, D. Leykam, E. Melik-Gaykazyan, D. Y. Choi, and Y. Kivshar, "Third-harmonic generation in photonic topological metasurfaces," Phys. Rev. Lett. **123**, 103901 (2019).

[43] J. W. You, Z. Lan, and N. C. Panoiu, "Four-wave mixing of topological edge plasmons in graphene metasurfaces," Sci. Adv. **6**, eaaz3910 (2020).

[44] J. W. You and N. C. Panoiu, "Tunable and dual-broadband giant enhancement of second-harmonic and third-harmonic generation in an optimized graphene-insulator-graphene metasurface," Phys. Rev. B **102**, 121403 (2020).

[45] D. Leykam and Y. D. Chong, "Edge solitons in nonlinear-photonic topological insulators," Phys. Rev. Lett. **117**, 143901 (2016).

[46] S. Mukherjee and M. C. Rechtsman, "Observation of Floquet solitons in a topological bandgap," Science **368**, 856-859 (2020).

[47] V. Peano, M. Houde, F. Marquardt, and A. A. Clerk, "Topological quantum fluctuations and traveling wave amplifiers," Phys. Rev. X **6**, 041026n (2016).

[48] S. Mittal, E. A. Goldschmidt, and M. Hafezi, "A topological source of quantum light," Nature **561**, 502-506 (2018).

[49] G. Harari, *et al.* "Topological insulator laser: Theory," Science **359**, eaar4003 (2018).

[50] M. A. Bandres, *et al.* "Topological insulator laser: Experiments," Science **359**, eaar4005 (2018).

[51] B. Huard, J.A. Sulpizio, N. Stander, K. Todd, B. Yang, and D. Goldhaber-Gordon, "Transport measurements across a tunable potential barrier in graphene," Phys. Rev. Lett. **98**, 236803 (2007).

[52] M. F. Craciun, S. Russo, M. Yamamoto, and S. Tarucha, "Tuneable electronic properties in graphene," Nano Today **6**, 42-60 (2011).

[53] W. Li, *et al.* "Ultrafast all-optical graphene modulator," Nano lett. **14**, 955-959 (2014).

[54] C. R. Dean, *et al.* "Boron nitride substrates for high-quality graphene electronics," Nat. Nanotechnol. **5**, 722-726 (2010).

[55] E. Hendry, P. J. Hale, J. Moger, A. K. Savchenko, and S. A. Mikhailov, "Coherent nonlinear optical response of graphene," Phys. Rev. Lett. **105**, 097401 (2010).

[56] X. Yao and A. Belyanin, "Giant optical nonlinearity of graphene in a strong magnetic field," Phys. Rev. Lett. **108**, 255503 (2012).

[57] J. W. Dong, X. D. Chen, H. Zhu, Y. Wang, and X. Zhang, "Valley photonic crystals for control of spin and topology," Nat. Mater. **16**, 298-302 (2017).

[58] F. Gao, *et al.* "Topologically protected refraction of robust kink states in valley photonic crystals," Nat. Phys. **14**, 140-144 (2018).

[59] A. B. Khanikaev, S. Hossein Mousavi, W. K. Tse, M. Kargarian, A. H. MacDonald, and G. Shvets, "Photonic topological insulators. Nature materials," **12**, 233-239 (2013).

[60] Y. Gong, S. Wong, A. J. Bennett, D. L. Huffaker, and S. S. Oh, "Topological insulator laser using valley-Hall photonic crystals," Acs Photonics **7**, 2089-2097 (2020).

[61] H. Yan, Z. Li, X. Li, W. Zhu, P. Avouris, and F. Xia, "Infrared spectroscopy of tunable Dirac terahertz magneto-plasmons in graphene," Nano Lett. **12**, 3766-3771 (2012).

[62] D. Jin, T. Christensen, M. Soljacic, N. X. Fang, L. Lu, and X. Zhang, "Infrared topological plasmons in graphene," Phys. Rev. Lett. **118**, 245301 (2017).

[63] X. Yao and A. Belyanin, "Giant optical nonlinearity of graphene in a strong magnetic field," Phys. Rev. Lett. **108**, 255503 (2012).

[64] J. W. You, S. R. Bongu, Q. Bao, and N. C. Panoiu, "Nonlinear optical properties and applications of 2D materials: theoretical and experimental aspects," Nanophotonics **8**, 63-97 (2019).

[65] E. Dremetsika, *et al.* "Measuring the nonlinear refractive index of graphene using the optical Kerr effect method," Opt. Lett. **41**, 3281-3284 (2016).

[66] J. L. Cheng, N. Vermeulen, and J. E. Sipe, "Third order optical nonlinearity of graphene," New J. Phys. **16**, 053014 (2014).

[67] Y. Wang and N. C. Panoiu, "Optically controllable coupling between edge and topological interface modes of graphene metasurfaces," J. Opt. **24**, 104002 (2022).

[68] L. A. Falkovsky, "Optical properties of graphene," J. Phys. Conf. Ser. **129**, 012004 (2008).

[69] M. Weismann and N. C. Panoiu, "Theoretical and computational analysis of second-and third-harmonic generation in periodically patterned graphene and transition-metal dichalcogenide monolayers," Phys. Rev. B **94**, 035435 (2016).

[70] COMSOL Multiphysics®, www.comsol.com.

[71] M. Blanco de Paz, *et al.* "Tutorial: computing topological invariants in 2D photonic crystals," Adv. Quantum Technol. **3**, 1900117 (2020).

[72] X. D. Chen, X. T. He, and J. W. Dong, "All-Dielectric Layered Photonic Topological Insulators," Laser Photonics Rev. **13**, 1900091 (2019).

[73] H. Liu , Y. Liu, and D. Zhu, "Chemical doping of graphene," J. Mater. Chem. **21**, 3335-2245 (2011).

[74] Z. Fang, *et al.* "Active tunable absorption enhancement with graphene nanodisk arrays," Nano Lett. **14**, 299-304 (2014).

[75] S. Thakur, B. Semnani, S. Safavi-Naeini, and A. H. Majedi, “Experimental characterization of the ultrafast, tunable and broadband optical Kerr nonlinearity in graphene," Sci. Rep. **9**, 1-10 (2019).

[76] H. Zhang, S. Virally, Q. Bao, L. K. Ping, S. Massar, N. Godbout, and P. Kockaert, “Z-scan measurement of the nonlinear refractive index of graphene,” Opt. lett. **37**, 1856-1858 (2012).

[77] K. Sakoda, *Optical Properties of Photonic Crystals* (Springer, 2005).

[78] S. Lavdas and N. C. Panoiu, “Theory of pulsed four-wave mixing in one-dimensional silicon photonic crystal slab waveguides,” Phys. Rev. B **93**, 115435 (2016).

[79] N. C. Panoiu, M. Bahl, and R. M. Osgood, “ Optically tunable superprism effect in nonlinear photonic crystals,” Opt. Lett. **28**. 2503-2505 (2003).

[80] N. C. Panoiu, M. Bahl, and R. M. Osgood, “Ultrafast optical tuning of a superprism effect in nonlinear photonic crystals,” J. Opt. Soc. Am. B **21**, 1500-1508 (2004).

[81] N. C. Panoiu, M. Bahl, and R. M. Osgood, “All-optical tunability of a nonlinear photonic crystal channel drop filter,” Opt. Express **12**, 1605-1610 (2004).

[82] S. E. Harris and L. V. Hau, “Nonlinear optics at low light levels," Phys. Rev. Lett. **82**, 4611-4614 (1999).

[83] A. Yariv, “Coupled-mode theory for guided-wave optics,” IEEE J. Quantum Electron. **9**, 919-933 (1973).

[84] W. P. Huang, “Coupled-mode theory for optical waveguides: an overview,” JOSA A, **11**, 963-983 (1994).

Chapter 4

Topological valley plasmon transport in bilayer graphene metasurfaces for sensing applications

4.1 Introduction

Previous chapters present the monolayer topologically-protected graphene plasmonic metasurface with nanoholes of different sizes, which is further applied to an active optically-controllable nanoswitch and a nonlinear mode coupler. However, the new inversion symmetry breaking, like mirror-symmetry, can be introduced when an additional layer is added and coupled to a single-layer graphene system. Hence, in this chapter, we design a bilayer graphene metasurface to realize, to the best of our knowledge, for the first time, valley topological plasmonic modes by utilizing a novel mechanism of mirror-symmetry breaking between the top and bottom freestanding layers of a graphene metasurface, by horizontally shifting in opposite directions the lattice of holes of the top layer. Although the spatial-inversion symmetry of each individual graphene layer is unperturbed, the proposed bilayer system provides a new mirror-symmetry breaking between the top and bottom layers when the interlayer coupling is enhanced. As such, the symmetry-protected Dirac cones are gapped out at the K point and, consequently, a topological nontrivial frequency bandgap emerges. Furthermore, topologically guided valley modes are observed

along a domain-wall interface with respect to which the composite metasurface is mirror symmetric. Our full-wave numerical simulations verify that the light propagation along the domain-wall interface shows indeed a unidirectional feature.

Based on the unidirectional propagation feature of the topological interface mode in the bilayer graphene metasurface, an efficient sensing application has been proposed in this chapter. As a single layer of carbon atoms arranged in a two-dimensional (2D) honeycomb lattice, graphene is a particularly promising 2D material for sensing applications, chiefly due to its distinct advantages, such as, large surface area [1, 2, 3], tunable optical properties [4, 5, 6], high carrier mobility [7, 8], and high electrical and thermal conductivity at room temperature [9, 10, 11]. A large number of graphene-based sensors in electrochemical [12, 13], strain [14, 15] and electrical areas [16, 17] has been proposed. For instance, for electrochemical sensors, the large surface area of graphene contributes to the loading of the desired molecules with effective interaction. Based on Kubo's formula, the optical characteristic (surface conductivity σ_s) of graphene is highly dependent on its chemical potential, which can be tuned by electrostatic biasing [18, 19] or chemical doping [20, 21]. Therefore, graphene is particularly suitable for chemical sensing because the chemical tunability of graphene can significantly influence its optical response to an applied electric field.

To illustrate the applicability of graphene for chemical sensing, in what follows we demonstrate how a topological interfacial mode in the bilayer graphene plasmonic metasurface can be used to design a molecular gas sensor using the fact that the Fermi energy of graphene varies upon chemical doping. This effect induces a strong variation of the frequency of bandgap and the transmission of the topological interface modes, which can be employed as the underlying working principle of gas sensing devices. Specifically, the sensitivity of the proposed graphene-based molecular sensor is defined and evaluated. Our work may open up new ways of developing robust integrated plasmonic devices for molecular sensing and gas detection.

This chapter is organized as follows. In Sec. 4.2, the bilayer graphene nanohole

plasmonic metasurfaces with a novel mirror symmetry-breaking are designed and introduced. In addition, the unidirectional light propagation of the topologically-protected interface mode excited by a circular-polarized source is discussed. Section 4.3 introduces a molecular gas sensor based on the proposed bilayer graphene metasurfaces, taking advantage of the chemical potential tunability of graphene when the system is under the exposure of NO_2 gas molecules. In particular, the transmission that can indicate the NO_2 concentration of the environment and corresponding sensitivity of the molecular sensor are quantitatively estimated. Final conclusions about the proposed bilayer graphene waveguide and the designed graphene-based molecular sensor will be given in Sec. 4.4.

4.2 Bilayer Graphene Nanohole Metasurfaces with Mirror-symmetry Breaking

We will introduce in this section a well-designed bilayer graphene metasurface that possesses plasmonic topological valley interface modes when the mirror-symmetry of the metasurface is broken by horizontally shifting in opposite directions the lattice of holes of the top layer of the two freestanding graphene layers. In this configuration, the light propagation of the topological valley mode along the domain-wall interface of the bilayer graphene metasurface shows unidirectional features.

The schematic of the proposed graphene bilayer metasurface is shown in Fig. 4.1. The bilayer metasurface consists of two freestanding, optically coupled graphene plasmonic crystals with the same unit cell. Note that the conclusions of this study remain qualitatively valid if one assumes that the two graphene layers are separated by a certain dielectric material instead of air, the only changes being of quantitative nature. Moreover, the hole lattice of the left- and right-hand side domains of the top graphene layer is horizontally shifted, in opposite directions and normally onto an interface lying along the x-axis, by a certain distance, s. As indicated in Fig. 4.1(a), it leads to the formation of a mirror-symmetric domain-wall interface along the x-axis. As we will demonstrate in what follows, this interface behaves as a plasmonic waveguide that possesses topological plasmonic modes. Each

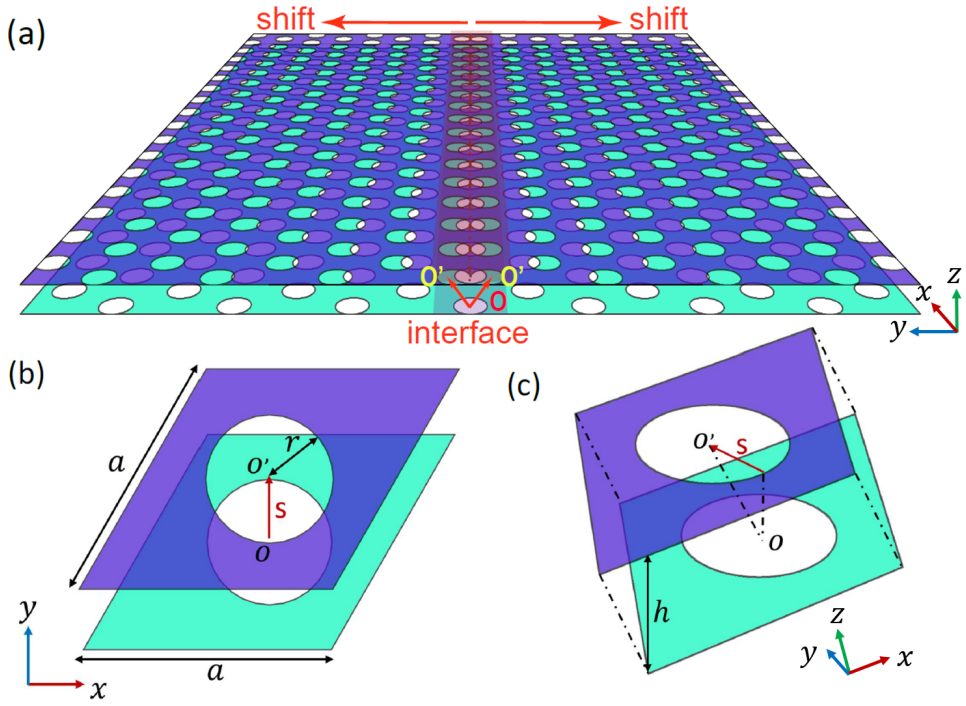

Figure 4.1: Schematic of the bilayer graphene metasurface. (a) The metasurface contains a domain-wall interface oriented along the x-axis, which is constructed by shifting the hole lattices of the two halves of the top graphene layer (purple) w.r.t. the bottom layer (green) along the positive and negative directions of the y-axis. (b) Top view of the unit cell with lattice constant, a, and horizontal shift, s. Hole centers O and O' correspond to the unit cells of the bottom and top layer, respectively. (c) Bird's eye view of the unit cell with a separation distance, h, between the two layers.

domain consists of a hexagonal graphene plasmonic crystal with a hole in the unit cell. The top view and bird's eye view of the unit cell are given in Figs. 4.1(b) and 4.1(c), respectively. Here is the same as the monolayer graphene metasurface, we fix the lattice constant $a = 400\,\text{nm}$, the hole radius $r = 100\,\text{nm}$, and the separation distance between the top and bottom layers, $h = 90\,\text{nm}$.

Unlike the case of the monolayer graphene metasurface protected by the C_{6v} point symmetry group, the bilayer graphene nanohole metasurface is protected by the D_{6h} point symmetry group [22, 23, 24]. Moreover, the frequency maxima and minima located in the momentum space vary. For the monolayer graphene metasurface or the mirror-symmetric bilayer graphene metasurface ($s = 0$), the frequency maxima and minima are located at the high-symmetry points of the FBZ. However, in the case of a bilayer metasurface with $s \neq 0$, the optical interlayer coupling and

the mirror-symmetry breaking between two graphene layers have a strong effect on the frequency maxima and minima. Thus, in order to properly identify the frequency band gap, the plasmonic bands of this bilayer graphene metasurface have been evaluated in the entire FBZ.

4.2.1 Band Diagrams of Bilayer Graphene Metasurfaces

The simulation settings of bilayer graphene nanohole crystals are shown in Fig. 4.2. In order to properly identify the frequency maxima and minima of the bilayer graphene metasurfaces, the plasmonic bands of this bilayer graphene metasurface have been evaluated in the entire FBZ and the hexagonal FBZ is discretized along the k_x and k_y directions. As shown in Fig. 4.2(c), the k vector in the FBZ is discretized into 500 points in the k_x-axis and k_y-axis, respectively. By sweeping total 500×500 (k_x, k_y) points, the band diagrams of the bilayer graphene metasurfaces throughout the entire FBZ have been determined and the results are shown in Fig. 4.3.

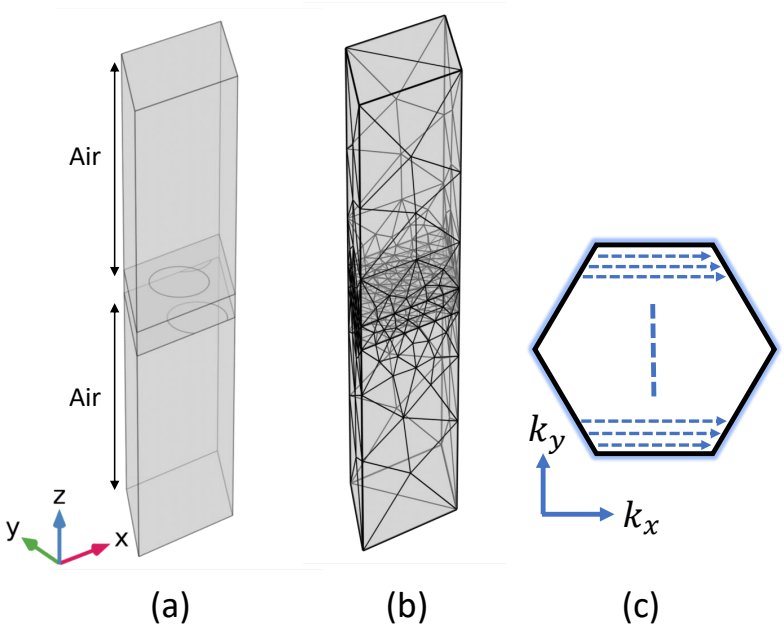

Figure 4.2: Simulation settings on the bilayer graphene nanohole crystal. (a) Periodic boundary conditions are placed along the x-axis and y-axis while absorption boundary conditions are placed on the air interface along the z-axis. (b) Mesh distribution of a unit cell of the bilayer graphene crystal. (c) Discretized entire FBZ along the k_x and k_y directions.

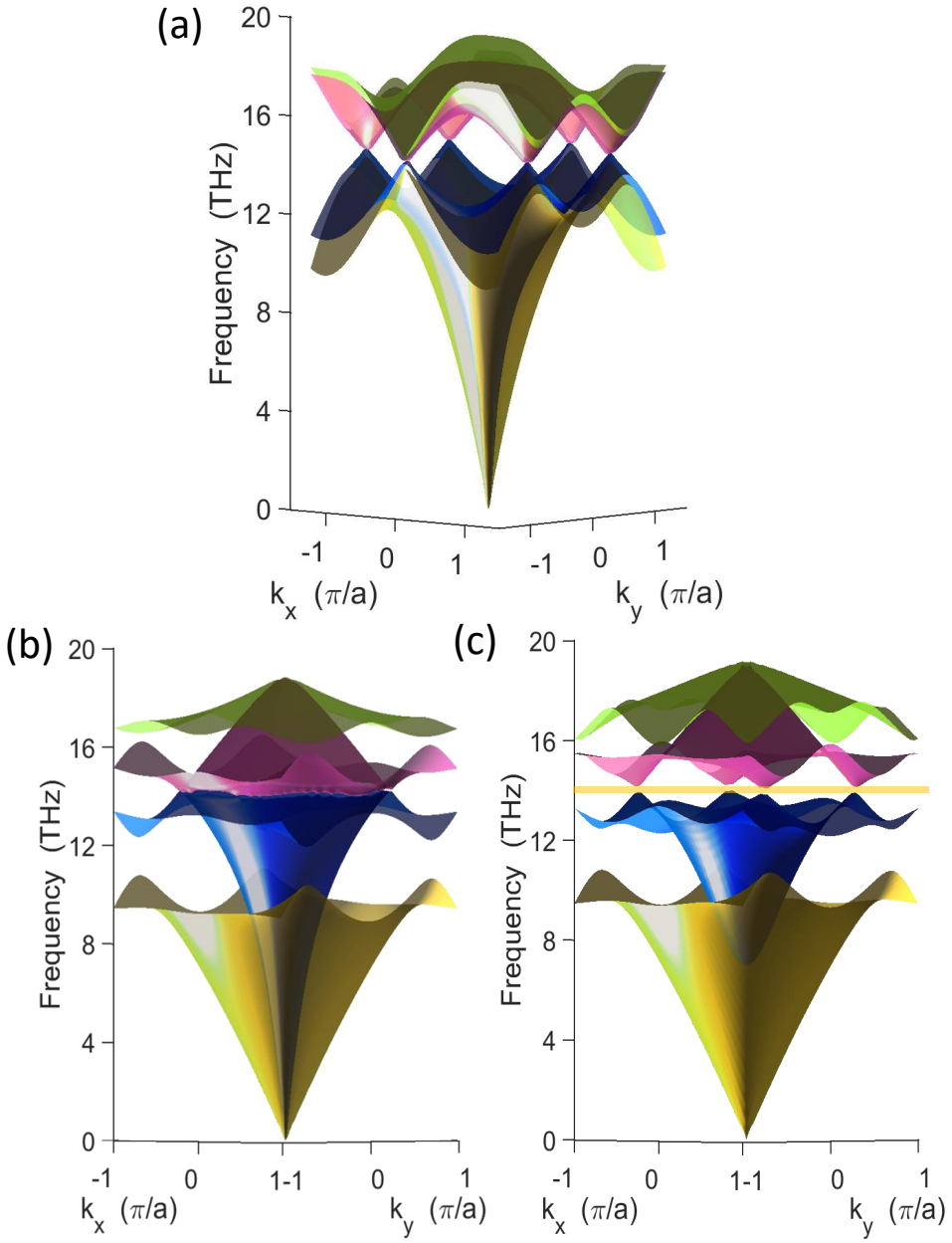

Figure 4.3: Band diagrams of a bilayer graphene metasurface in the FBZ. (a) Band diagram of a bilayer graphene metasurface with $s = 0$, in which the coupling between the top and bottom graphene nanohole crystals is very weak. (b) Band diagram when the optical coupling between top and bottom graphene crystals is enhanced by reducing the separated distance $h = 90\,\text{nm}$. (c) Band diagram of a composite bilayer graphene metasurface in which the coupling between the top and bottom graphene plasmonic crystals is relatively strong, namely $h = 90\,\text{nm}$ and $s = 100\,\text{nm}$, as depicted in Fig. 4.1(c). Since the mirror-symmetry of the composite graphene metasurface is broken in this case, a nontrivial bandgap corresponding to the light yellow region emerges.

When the distance h between the top and bottom graphene layers in Fig. 4.1(c) is large, the optical near-field coupling between the two layers can be neglected. As a consequence, each graphene layer, which is a plasmonic crystal, possesses decoupled Dirac cones protected by D_{6h} point symmetry group [25]. This is indeed verified by the bands presented in Fig. 4.3(a), where the Dirac cones located at 14 THz of each graphene plasmonic crystal perfectly overlap. In order to enhance the optical coupling between the top and bottom graphene layers, the distance h is reduced to $h = 90\,\text{nm}$, which results in a strong interlayer coupling. Figure 4.3(b) shows the effect of this interaction. Thus, due to the strong coupling between the metasurfaces, it is possible to achieve a mirror-symmetry breaking by introducing a horizontal shift of $s = 100\,\text{nm}$, as explained above. As a result, the D_{6h}-symmetry-protected Dirac cones are gapped out, and a frequency band gap emerges. Specifically, the band diagram of the bilayer graphene metasurface exhibits a 0.21 THz topological gap from 13.96 THz to 14.17 THz, as depicted in Fig. 4.3(c). Moreover, the frequency maxima and minima are not necessarily located at the high-symmetry points of the FBZ, which could be clearly obtained by comparing frequency maxima and minima between Figs. 4.3(a) and 4.3(c).

Since the bilayer graphene metasurface has hexagonal symmetry, it possesses six Dirac cones (see Fig. 4.3) with two non-equivalent valleys at K and K' symmetry points. The integral of the Berry curvature around each valley defines the valley Chern number of $C_{K,K'} = \pm 1/2$ [26, 27]. Moreover, the two valleys at K and K' are related to each other *via* rotations of the metasurface by $\pi/3$, π, and $5\pi/3$. Therefore, in order to construct a domain-wall interface that can possess topological interface modes, one can place together two bilayer graphene metasurfaces with $s \neq 0$ in a mirror-symmetric manner, i.e. rotated by π with respect to each other, as per Fig. 4.1(a). Consequently, the difference of the valley Chern number across the domain-wall interface at each valley is $+1$ or -1. In this way, we can obtain a pair of valley-momentum-locked interface states, where the interface state at one valley has a positive group velocity whereas the other has a negative one.

Starting from these ideas, the projected band diagram of a finite bilayer

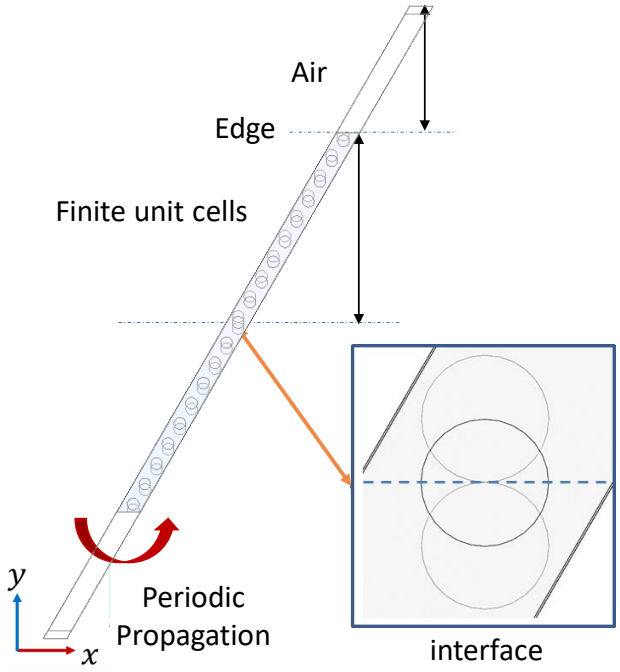

Figure 4.4: Supercell of the finite bilayer graphene crystal with a domain-wall interface constructed by two mirror-symmetric domains. Periodic boundary conditions are placed along the x-axis while absorption boundary conditions are placed along the y-axis and z-axis.

graphene metasurface, consisting of 20 unit cells along the y-axis and periodic along the x-axis is computed, and the detailed simulation settings are given in Fig. 4.4. A mirror-symmetric domain-wall interface is constructed, in which the valley Chern number difference between K and K' valleys could support topologically protected interface modes. Due to the mode scattering being considered in two air domains with placed absorption boundary conditions, there exists other types of trivial edge modes that could emerge inside the nontrivial bandgap and propagate along the boundaries of the finite bilayer graphene metasurface. Since the finite supercell of the bilayer graphene metasurface is periodic along the x-axis with period a, the band diagram is computed with the wave vector component k_x from 0 to π/a, and the results are presented in Fig. 4.5.

The topologically protected edge modes are marked by red lines while the dark red regions represent the projected bulk modes. As a structure with finite width along the y-axis (20 unit cells), the graphene bilayer metasurface embedded air has

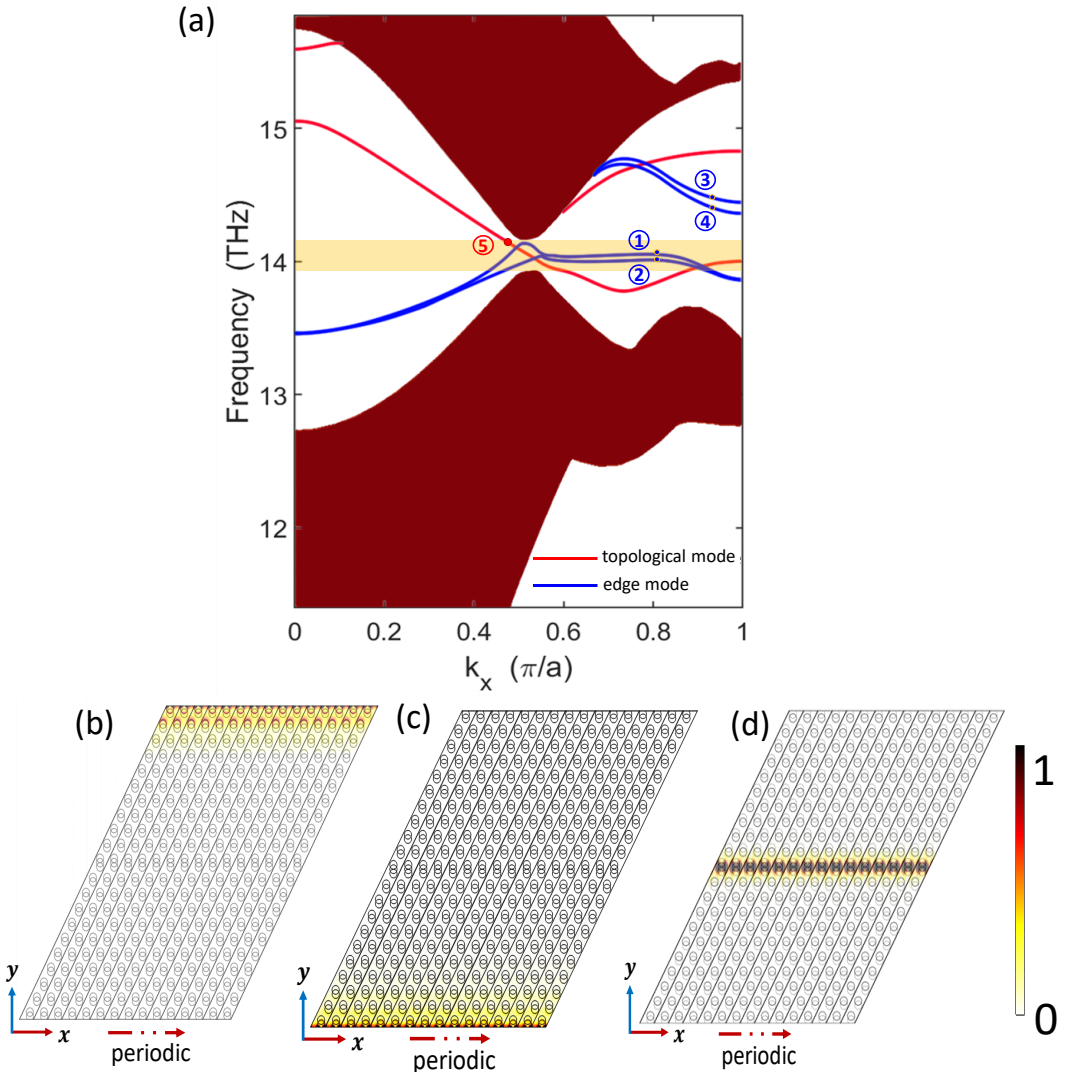

Figure 4.5: (a) Projected band diagram of a finite bilayer graphene metasurface with a width of 20 unit cells and domain-wall interface generated by shifting two halves of the top layer w.r.t the bottom graphene layer ($s = 100\,\text{nm}$). Topological interface modes and trivial edge modes are represented by red and blue lines, respectively, whereas bulk modes correspond to maroon regions. (b) Field distribution of a trivial edge mode located at the upper boundary of the graphene metasurface, which corresponds to ① and ③ in (a). (c) Field distribution of a trivial edge mode located at the lower boundary, which corresponds to ② and ④ in (a). (d) Field distribution of a topological interface mode marked by point ⑤ in (a).

other types of edge modes, too, marked with blue lines in Fig. 4.5(a). These modes are localized at edges of the metasurface and are trivial modes. The trivial edge modes generally appear in pairs inside the gap, e.g. points ① and ② and points ③ and ④ shown in Fig. 4.5(a).

In order to gain deeper physical insights into these two different types of edge modes, we investigated optical field distributions of the edge modes corresponding to points marked in Fig. 4.5(a). Thus, Figures 4.5(b) and 4.5(c) show the highly confined field profiles of the trivial edge modes located at upper and lower boundaries of the metasurface, respectively. The points ① and ② and points ③ and ④ in Fig. 4.5(a) indicate two pairs of edge modes located at opposite boundaries of the metasurface, and can be clearly distinguished from topological interfacial modes. Furthermore, at the frequency of 14.16 THz, located inside the bandgap, there is another edge mode indicated in Fig. 4.5(a) by the red dot ⑤, the corresponding field distribution being presented in Fig. 4.5(d). This field profile clearly shows that the optical field of this topological mode is confined and localized at the domain-wall interface. Specifically, the topological edge modes correspond to pure guided modes whereas the trivial edge mode to leaky guided resonances.

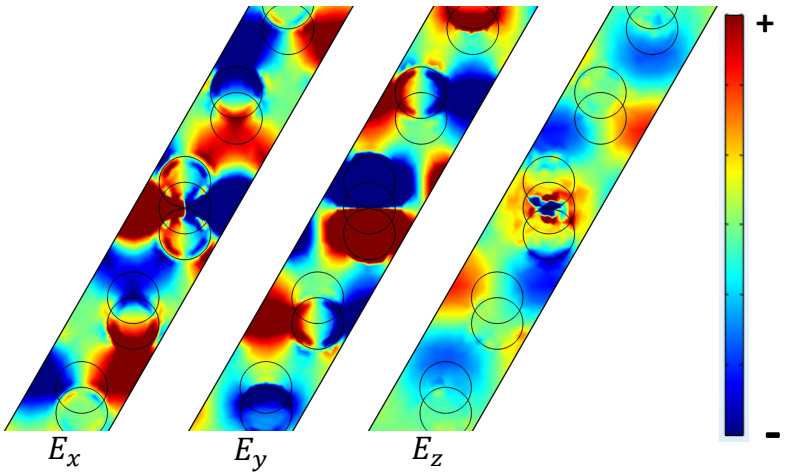

Figure 4.6: Spatial distribution of the E_x, E_y, and E_z components of the topological modes with respect to the domain-wall interface marked by red lines in Fig. 4.5(a).

It should be noted that there are more than one topological interface modes that are marked by red curves. Although some of them are not inside the nontrivial bandgap, it is still necessary to further investigate the mode properties of these topological interface modes, so that the spatial distributions of the E_x, E_y, and E_z components of these topological interfacial modes are shown in Fig. 4.6. All the topological interfacial modes have the same symmetry with respect to the domain-

wall interface. To be more specific, with respect to the interface, the field components E_x and E_z are symmetric whereas the field component E_y is antisymmetric.

4.2.2 Topological Properties of Interfacial Modes

Our computational investigations demonstrate an important property of the interfacial topological modes, namely their unidirectional propagation. Thus, in practice, the topological graphene metasurface is generally a finite system, namely, the graphene metasurface is truncated in the x- and y-direction. In order to break the periodicity along the x-axis, absorption boundary conditions are placed on all the boundaries of the finite bilayer graphene metasurface with length of $35a$ along the x-axis.

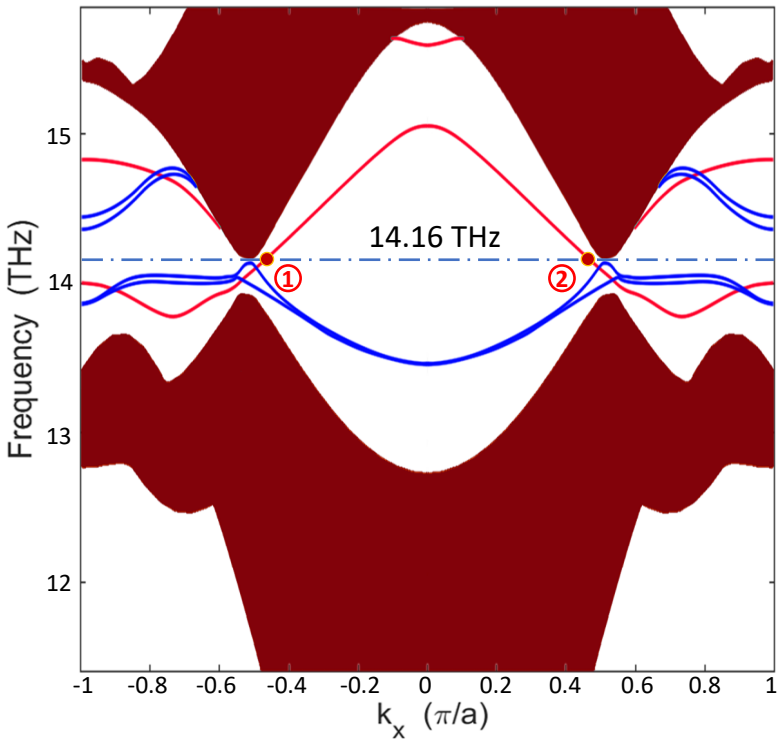

Figure 4.7: Projected band diagram in which there are two topological edge states (points ① and ②) with opposite group velocities at the frequency of 14.16 THz.

We show in Fig. 4.7 the projected band diagram with k_x from $-\pi/a$ to π/a, and the line corresponding to the frequency 14.16 THz is inside the bandgap and only crosses the topological band at two points, i.e. points ① and ②, around K' and K valleys, respectively. When a monochromatic light source with a frequency of

14.16 THz is used to excite the bilayer graphene metasurface, only two topological interfacial modes corresponding to points ① and ② can be excited. These two points have opposite group velocities, which can lead to the light propagation of a topological mode along the domain-wall interface in opposite directions.

In order to study the chirality-momentum-locking property, which arises from the valley-Hall effects induced by the intrinsic chirality associated to each valley [28, 29], the excitation source with a frequency of 14.16 THz was constructed by placing at the corners of a small hexagon six electric dipoles marked by circles in Fig. 4.8. More specifically, six electric dipoles with a phase that increases clockwise are placed at the six corners of a hexagonal unit cell, and the phase difference between neighboring dipoles is set to $\pm\pi/3$ (circles from blue (or red) to red (or blue)), so as to implement right-circularly polarized (RCP) and left-circularly polarized (LCP) sources, respectively.

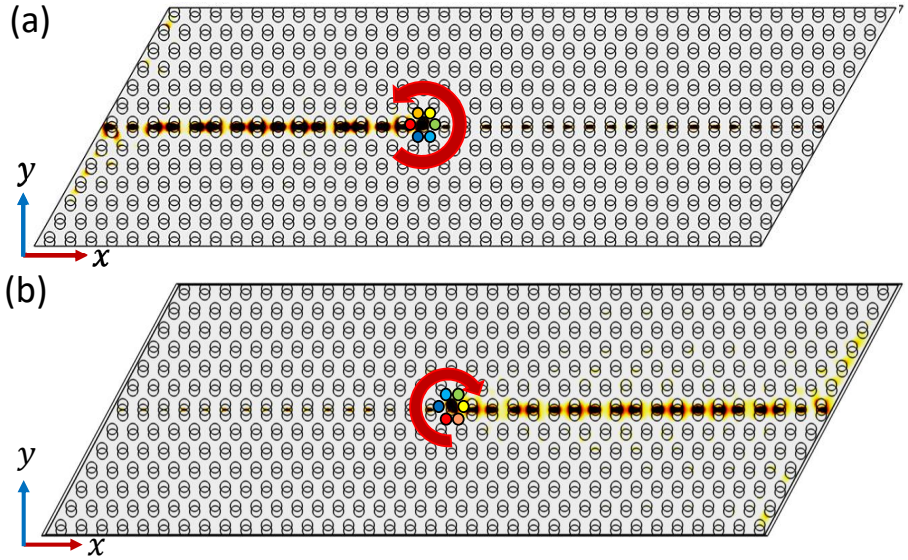

Figure 4.8: (a) Unidirectional propagation along the negative direction of the x-axis, corresponding to point ② in Fig. 4.7, when the finite metasurface is excited by a right-circularly polarized (RCP) source. (b) The same as in (a), but for a left-circularly polarized (LCP) source. In this case, the topological interfacial mode propagates along the positive direction of the x-axis, corresponding to point ① in Fig. 4.7.

As illustrated in Fig. 4.8(a), a RCP light source is placed at the center of the composite bilayer graphene metasurface, and unidirectional topological propagation of light along the negative direction of the x-axis of the domain-wall interface

is observed, which corresponds to point ② in Fig. 4.7 with a negative group velocity. Similarly, as shown in Fig. 4.8(b), a LCP light source located at the center of the metasurface, created by reversing the phase difference between adjacent dipoles, excites at the interface a topological mode that propagates and is focused along the positive direction of the x-axis, corresponding to the point ① in Fig. 4.7 with a positive group velocity. If the dissipative effect of graphene is considered, the complex part of the surface conductivity of graphene contains the relaxation time τ that determines the dissipate effect. The relaxation time is 50 ps in our simulation, and the corresponding propagation distance in bilayer graphene metasurfaces is around 16 µm. The propagation distances are 4 µm, 1.3 µm and 0.6 µm when τ=10 ps, 1 ps and 0.5 ps, respectively.

4.3 molecular gas sensor Based on Bilayer Graphene Metasurfaces

Generally, the chemical potential μ_c of graphene is proportional to the Fermi velocity and the carrier density n_0, which can be tuned via molecular doping as a well-known type of chemical doping [30]. This tunability makes it possible to engineer the chemical potential of graphene with high precision. As such, graphene-based sensors can be used to detect the concentration of specific gases in the environment, by measuring the concentration of the corresponding gas molecules adsorbed onto a graphene sheet in the room temperature. To add specificity to our analysis, we assume that the gas is NO_2.

4.3.1 Tunable Chemical Potential of Graphene

Surface transfer doping occurs via electron transfer between graphene and dopant. The electron transfer is determined by the relative position of the density of states of the highest occupied molecular orbital (HOMO) and lowest unoccupied molecular orbital (LUMO) of the dopant and the Fermi level of graphene. If the HOMO of the dopant is higher than the Fermi level of graphene, the electron will be transferred from the dopant to the graphene layer, and the dopant acts as an electron donor;

if the LUMO of the dopant is lower than the Fermi level of graphene, the electron will be transferred from the graphene to the dopant, and the dopant acts as an electron acceptor. The mechanism of NO_2 doping was investigated theoretically and experimentally by Wehling *et al.* [31]. The Fermi level of NO_2 lies exactly in a partially occupied molecular orbital (POMO), which is about 0.4 eV lower than the Dirac point of graphene and independent of the adsorption configuration. Therefore, the NO_2 molecule is a strong electron acceptor to accept an electron from graphene. In addition, the paramagnetic single NO_2 molecule is a strong acceptor for the monocular doping of graphene, whereas its diamagnetic dimer N_2O_4 causes only weak doping [31]. Other gas molecules, such as NH_3 and CO molecules act as donors, show their potential on the chemical doping of graphene [32]. Since NO_2 gas molecules adsorbed on graphene have been systematically studied, we choose NO_2 gas molecules to tune the Fermi level of graphene based on the relationship between the gas concentration and the carrier density of graphene obtained from experiments.

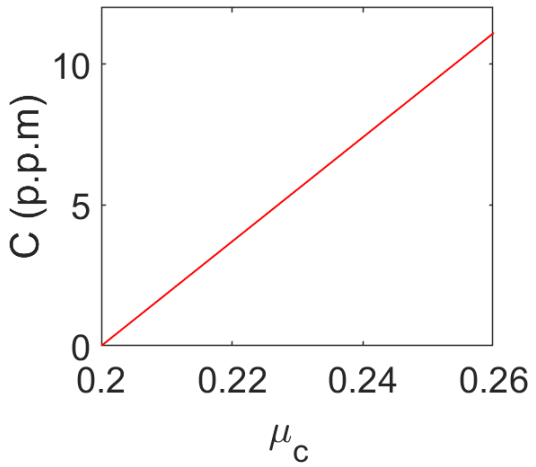

Figure 4.9: Chemical potential, μ_c, of graphene with respect to different NO_2 concentrations C_{NO_2} in the environment.

Schedin *et al.* experimentally studied the variation of the chemically induced charge carrier density with respect to the concentration of NO_2 gas molecules absorbed onto a monolayer graphene [32]. When a monolayer graphene is exposed in an environment with various NO_2 concentrations, a well-fitted linear relation between the induced charge carrier density Δn_0 of graphene and NO_2 gas concentra-

tions C_{NO_2} has been proved. Moreover, by applying positive or negative gate voltage V_g between the graphene, the induced charge carriers Δn_0 in a single graphene layer linearly increases with respect to the increase of the gate voltage V_g. Specifically, the linear relation can be expressed as $n_0 = \beta V_g$, where the linear parameter is experimentally determined as $\beta \approx 7.2 \times 10^{10} cm^{-2} V^{-1}$. Therefore, the gate voltage V_g applied on graphene directly corresponds to the NO_2 gas concentration C_{NO_2} absorbed onto the graphene sheet through an intermediate variable, induced charge carrier density n_0.

Since the chemical potential μ_c of graphene is proportional to the carrier density n_0, the relation between the chemical potential of graphene and the concentration of NO_2 gas molecules can be obtained from experimental results. First, the chemical potential of graphene increases linearly with the increasing applied gate voltage V_g, and the linear relation can be summarized as $\mu_c = \gamma V_g$, where $\gamma \approx 6.6 \times 10^{-3} eV/V$ is extracted from the experiment [33]. Because the applied gate voltage and the gas concentration have a similar effect on the induced carrier density (chemical potential) of graphene, a relationship between the chemical potential and the NO_2 gas concentration can be calculated, which is the basic formula for our designed graphene-based molecular sensor. Specifically, the relation between the variation of the chemical potential induced by NO_2 gas with concentration, C_{NO_2}, is $\Delta\mu_c = \alpha C_{NO_2}$, where the experimentally determined value of α is $\alpha \approx 5.4 \times 10^{-3}$ eV/p.p.m [32, 33, 34]. Figure 4.9 indicates the variation of the chemical potential of graphene from 0.2 eV to 0.26 eV with respect to the increasing concentration of NO_2 gas molecules in the environment. A 0.06 eV small variation of the chemical potential of graphene indicates a relatively large sensitivity of graphene in response to NO_2 gas molecules up to 10 p.p.m. Note that the relationship between the chemical potential of graphene and NO_2 gas concentration is estimated in the room temperature. Since ideal gas law determines the concentration with the given temperature, the higher temperature increases the number of collisions between gas molecules and increases the volumes of total gas and NO_2. In addition, the temperature can be slightly adjusted for finer control of the adsorp-

tion/desorption rates during the molecular doping process [32].

4.3.2 Graphene-based Molecular Sensor Design

The unidirectional propagation feature of the topological interface mode in the bilayer graphene metasurface investigated in this work can be applied to efficient photonic nanodevices. To illustrate this, in what follows we demonstrate how the variation of Fermi energy of graphene upon chemical doping can be utilized to design an efficient molecular sensor.

As shown in Fig. 4.10, the proposed bilayer graphene metasurface is used to design a molecular sensor based on the large variations of its optical properties induced by small changes of its chemical characteristics.

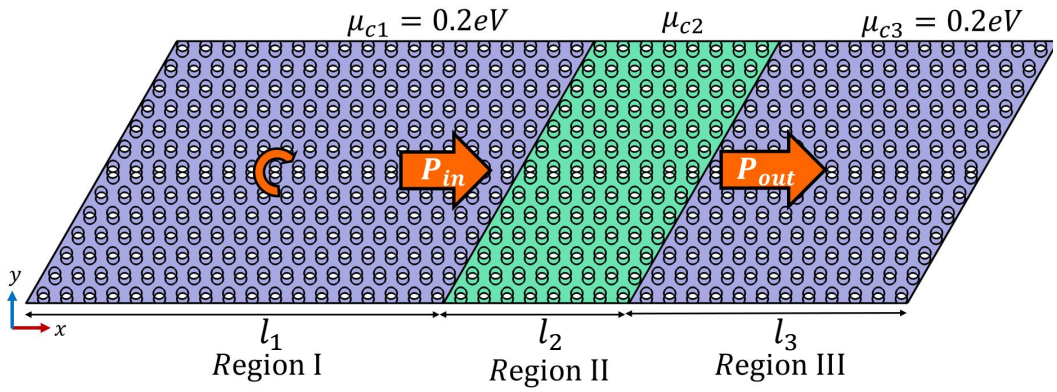

Figure 4.10: Schematic of the proposed molecular sensor. The topological interfacial mode carries an input power and output power in the regions I and III, respectively. An additional bilayer graphene metasurface in the region II is sandwiched in-between the regions I and III, and is used to detect the concentration of adsorbed molecules of a certain gas (NO_2 in our case).

The sensor consists of three bilayer graphene metasurfaces, marked as regions I, II, and III, the lengths of these regions being l_1, l_2, and l_3, respectively, and the corresponding chemical potentials $\mu_{c1} = \mu_{c2} = \mu_{c3} = 0.2\,\text{eV}$. The gas molecules can be adsorbed only in the region II, and upon their adsorption μ_{c2} varies. A LCP excitation source is placed at the center of the region I and the output power is collected in the region III, whereas the region II is exposed to the environment and detects the NO_2 gas molecules.

4.3.3 Principle of The Bandgap Shift

The induced concentration of carriers is increased due to the NO_2 gas molecules adsorbed onto the graphene sheet, which results in the increase of the chemical potential μ_{c2} in the region II. The variation of the chemical potential in the region II, in turn, leads to a variation of the graphene permittivity. As shown in Fig. 4.11(a), when the chemical potential of the bilayer graphene metasurface is slightly increased from 0.2 eV to 0.21 eV with a small 0.01 eV variation, the frequency of the nontrivial bandgap under a 0.21 eV chemical potential shows a relatively large shift about 0.3 THz, compared to the frequency bandgap of the bilayer graphene metasurfaces from 13.96 THz to 14.17 THz with $\mu_c = 0.2$ eV [see Fig. 4.3(c)]. Besides, Figure 4.11(b) indicates that the variation of the chemical potential shifts but does not influence the relative position of each band in the bilayer graphene meta-

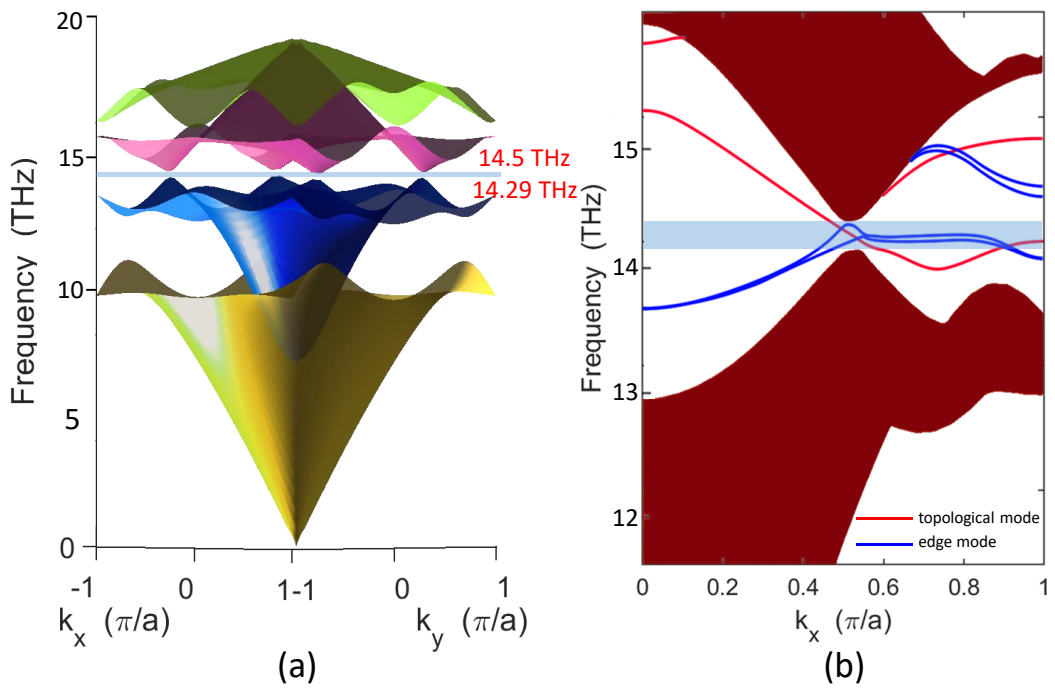

Figure 4.11: Band diagrams of the bilayer graphene metasurface with the chemical potential of 0.21 eV. (a) Band diagram of the infinite bilayer graphene plasmonic crystal. A 0.21 THz nontrivial gap emerges from 14.29 THz to 14.5 THz. (b) Projected band diagram of a finite bilayer graphene metasurface with a 0.21 eV chemical potential. The topological interface and trivial edge modes are represented by red and blue curves, respectively. The nontrivial frequency bandgap marked by a blue strip is shifted upwards compared with Fig. 4.5(a).

surface, especially frequency dispersion curves of topological modes, trivial edge modes, and projected bulk modes. It only shifts up the whole band diagram consistently, which can be easily explained by the increasing Fermi energy of the bilayer graphene metasurface.

The width of the frequency bandgap is only 0.21 THz while the frequency shift of the nontrivial bandgap can be as large as 0.3 THz with only a 0.01 eV increase of the chemical potential. This advantage makes a great contribution on the sensitivity of the designed molecular gas sensor. Consequently, the variation of the chemical potential in the region II, in turn, leads to a variation of the graphene permittivity, and consequently to a shift of the frequency of the topological bandgap associated to region II. This means that, if the frequency of the input light in region I is fixed at 14.16 THz inside the bandgap of this region (see Fig. 4.7), the corresponding topological interfacial mode from the region I can be switched to a leaky bulk mode in the region II, based on the fact that the optical beam at the frequency of 14.16 THz is a bulk mode outside the bandgap in the region II due to the frequency shift of the bandgap. Then, the leaky bulk mode in region II can be recoupled into a topological interfacial mode in region III with $\mu_{c3} = 0.2\,\text{eV}$, which is convenient to detect and collect the output power around the center of the region III. Since the leaky bulk modes are particularly lossy and scattered, the output power P_{out} collected in the region III will sharply decrease.

4.3.4 Transmission and Sensitivity Calculation

In order to validate these ideas, we have studied the light transmission in the proposed graphene-based molecular sensor. To this end, a LCP monochromatic light source with frequency of 14.16 THz is placed in the center of the region I. The lengths of the region I (l_1) and region III (l_3) are $18a$ and $12a$, respectively.

Moreover, we computed the transmission η of the optical power under various NO_2 concentrations in region II, defined as the ratio between the output power, P_{out}, collected in the region III and the input power P_{in} in the region I, namely $\eta = P_{out}/P_{in}$. These calculations were performed for two different values of the length of region II, namely for $l_2 = 8a$ and $l_2 = 14a$, and the results are summarized

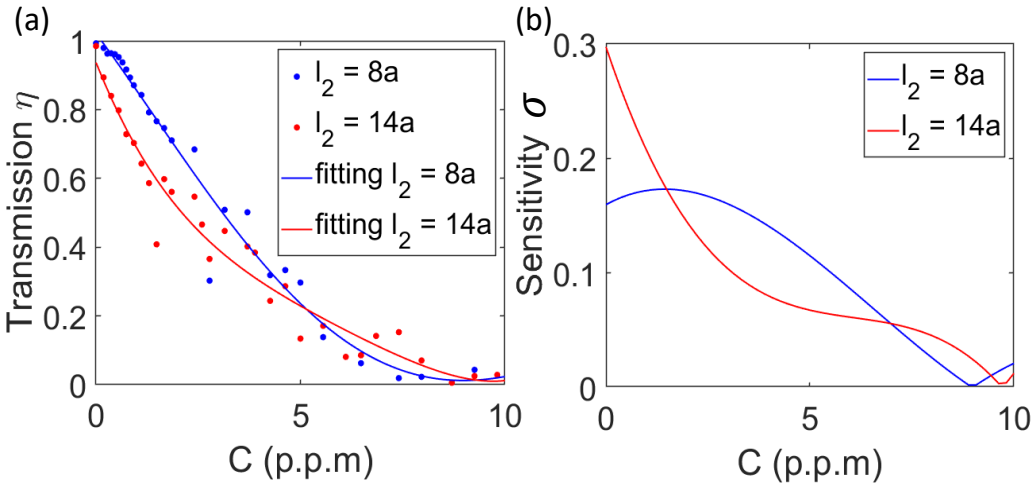

Figure 4.12: Functionality and sensitivity of the graphene-based molecular gas sensor. (a) Light transmission, defined as the ratio between the output and input power, versus the concentration C_{NO_2} of NO_2 gas, determined for $l_2 = 8a$ and $l_2 = 14a$. (b) Dependence of the sensitivity of the molecular sensor on the gas concentration C_{NO_2} of NO_2.

in Fig. 4.12.

It can be seen in Fig. 4.12(a), where we plot the dependence of the transmission on the concentration of molecules adsorbed in region II, that the transmission η decreases steeply when the concentration C_{NO_2} of the NO_2 gas adsorbed in this region increases. In Fig. 4.12(a), the dots represent the numerically computed data, whereas the solid lines indicate the fitting of the results via a third-order polynomial. These results prove that, as expected, the longer the length of the region II is, the larger the slope of the transmission curve is, which means that the radiation loss of the input power in the region II is larger. Note also that when $C > 5$ p.p.m, the transmission in the case when $l_2 = 14a$ is larger than when $l_2 = 8a$, which is attributable to the constructive interference of the mode propagating in region II, and which undergoes multiple reflections at the interfaces between this region and regions I and III. When the concentration C_{NO_2} is larger than about 9 p.p.m, most of the input power is scattered out into radiation modes, so that the transmitted power is almost zero in this case. Moreover, we have also studied the sensitivity of the metasurface sensor, σ, which is defined as the absolute value of the first-order derivative of the transmission with respect to the concentration of NO_2 molecules adsorbed in region

II, that is, $\sigma = |d\eta/dC_{NO_2}|$. As shown in Fig. 4.12(b), our computational results show that the average sensitivity of this graphene-based molecular sensor can be as large as 0.2. The proposed molecular sensor can be used to detect the gas variations in a broad range of molecular concentrations, its sensitivity is particularly large for small concentrations of adsorbed molecules.

4.4 Conclusion

In conclusion, we have proposed a novel mechanism to realize valley-Hall topological plasmon transport in a bilayer graphene metasurface. Starting from the band analysis of a monolayer graphene nanohole metasurface, the enhanced interlayer coupling between two graphene metasurfaces is further considered, and the D_{6h}-symmetry-protected Dirac cones make it possible to achieve a novel mirror-symmetry breaking between the two graphene layers. By horizontally shifting the two halves of the hole lattice of the top layer by a certain distance s with respect to the bottom graphene metasurface, the mirror-symmetry of the bilayer graphene plasmonic crystal is broken, and the band structure over the FBZ exhibits a nontrivial gap which is opened at the frequency of the Dirac point. Moreover, to produce a valley-Hall topological plasmon mode within the nontrivial bandgap, a domain-wall interface is constructed by placing together two bilayer graphene metasurfaces in a way in which the composite metasurface is mirror-symmetric with respect to the domain-wall interface. The results of our numerical computations show that the topologically protected valley mode is highly confined and propagates along the domain-wall interface. Importantly, the proposed waveguide with a mirror-symmetric domain-wall interface supports topological modes that exhibit unidirectional propagation features under a circular-polarized source.

Moreover, we gain further insight into the proposed bilayer graphene metasurface, which is applied as a molecular gas sensor. Based on the fact that the chemical potential of graphene can be sensitively tuned via the gas molecular absorption as a well-known type of chemical doping, we summarized the linear relation between chemical potential and gas concentration in the environment extracted from the ex-

periments. Therefore, a variation of chemical potential (Fermi level) of graphene leads to a frequency shift of the corresponding nontrivial bandgap, which can switch a topological interfacial guided mode into a leaky bulk mode with the power loss. As a result, the transmission of the topological interfacial mode can precisely indicate the chemical potential of graphene, namely the concentration of NO_2 gas molecules in the environment. Our computational results prove that, a tiny variation of chemical potential can significantly change the transmission of a topological interfacial mode and generate high power loss, which improves the sensitivity of the proposed graphene-based molecular sensor. This work could have an important impact on the development of integrated plasmonic devices and key applications pertaining to molecular sensing.

Taking advantage of the new layer degree of freedom in a multilayer system possessing various symmetries (spatial-inversion, mirror), layer pseudospins in distinct valley-Hall phases are attracting increasing attention, due to the discovery of new layer-polarized valley-Hall states. Thus, we will present in the next chapter layered graphene nanohole metasurfaces (monolayer, bilayer, and three-layer), whose mirror-symmetry and inversion symmetry can be broken via the rotation of triangular holes in each layer.

Bibliography

[1] M. D. Stoller, S. Park, Y. Zhu, J. An, and R. S. Ruoff, "Graphene-based ultracapacitors," Nano lett. **8**, 3498-3502 (2008).

[2] A. K. Geim, "Graphene: status and prospects," Science, **324**, 1530-1534 (2009).

[3] J. Zhu, D. Yang, Z. Yin, Q. Yan, and H. Zhang, "Graphene and graphene-based materials for energy storage applications," Small, **10**, 3480-3498 (2014).

[4] M. F. Craciun, S. Russo, M. Yamamoto, and S. Tarucha, "Tuneable electronic properties in graphene," Nano Today **6**, 42-60 (2011).

[5] Y. Zhang, *et al.* "Direct observation of a widely tunable bandgap in bilayer graphene," Nature **459**, 820-823 (2009).

[6] S. K. Patel, M. Ladumor, V. Sorathiya, and T. Guo, "Graphene based tunable grating structure," Mater. Res. Express. **6**, 025602 (2018).

[7] S. Park, and R. S. Ruoff, "Chemical methods for the production of graphenes," Nat. Nanotechnol. **4**, 217-224 (2009).

[8] L. Banszerus, *et al.* "Ultrahigh-mobility graphene devices from chemical vapor deposition on reusable copper," Sci. Adv. **1**, e1500222 (2015).

[9] A. A. Balandin, S. Ghosh, W. Bao, I. Calizo, D. Teweldebrhan, F. Miao, and C. N. Lau, "Superior thermal conductivity of single-layer graphene." Nano lett. **8**, 902-907 (2008).

[10] T. Zhou, Z. Cheng, H. Zhang, M. Le Berre, L. Militaru, and F. Calmon, "Miniaturized tunable terahertz antenna based on graphene," Microw. Opt. Technol. Lett. **56**, 1792-1794 (2014).

[11] S. Guo and S. Dong, "Graphene nanosheet: synthesis, molecular engineering, thin film, hybrids, and energy and analytical applications," Chem. Soc. Rev. **40**, 2644-2672 (2011).

[12] S. Alwarappan, C. Liu, A. Kumar, and C. Z. Li, "Enzyme-doped graphene nanosheets for enhanced glucose biosensing," J. Phys. Chem. C **114**, 12920-12924 (2010).

[13] P. Wu, Q. Shao, Y. Hu, J. Jin, Y. Yin, H. Zhang, and C. Cai, "Direct electrochemistry of glucose oxidase assembled on graphene and application to glucose detection," Electrochim. Acta **55**, 8606-8614 (2010).

[14] J. Zhao, *et al.* "Ultra-sensitive strain sensors based on piezoresistive nanographene films," Appl. Phys. Lett. **101**, 063112 (2012).

[15] Q. Liu, M. Zhang, L. Huang, Y. Li, J. Chen, C. Li, and G. Shi, "High-quality graphene ribbons prepared from graphene oxide hydrogels and their application for strain sensors," ACS nano, **9**, 12320-12326 (2015).

[16] T. Cohen-Karni, Q. Qing, Q. Li, Y. Fang, and C. M. Lieber, "Graphene and nanowire transistors for cellular interfaces and electrical recording," Nano lett. **10**, 1098-1102 (2010).

[17] A. Nag, A. Mitra, and S. C. Mukhopadhyay, "Graphene and its sensor-based applications: A review," Sens. Actuators A: Phys. **270**, 177-194 (2018).

[18] G. W. Hanson, "Dyadic Green's functions for an anisotropic, non-local model of biased graphene," IEEE Trans. Antennas Propag. **56**, 747-757 (2008).

[19] X. He, Z. Y. Zhao, and W. Shi, "Graphene-supported tunable near-IR metamaterials," Opt. Lett. **40**, 178-181 (2015).

[20] H. Liu, Y. Liu, and D. Zhu, "Chemical doping of graphene," J. Mater. Chem. **21**, 3335-3345 (2011).

[21] T. O. Wehling, K. S. Novoselov, S. V. Morozov, E. E. Vdovin, M. I. Katsnelson, A .K. Geim, and A. I. Lichtenstein, "Molecular doping of graphene," Nano lett. **8**, 173-177 (2008).

[22] W. Miller, *Symmetry groups and their applications* (Academic Press, 1973).

[23] F. M. Mahomed, "Symmetry group classification of ordinary differential equations: survey of some results," Math. Methods Appl. Sci. **30**, 1995-2012 (2007).

[24] C. Bradley and A. Cracknell, *The mathematical theory of symmetry in solids: representation theory for point groups and space groups* (Oxford University Press, 2010).

[25] B. Xie, H. Wang, X. Zhu, M. Lu, Z. Wang, and Y. Chen, "Photonics meets topology," Opt. Express **26**, 24531-24550 (2018).

[26] T. Ma and G. Shvets, "All-Si valley-Hall photonic topological insulator," New J. Phys. **18**, 025012 (2016).

[27] H. Pan, Z. Li, C. C. Liu, G. Zhu, Z. Qiao, and Y. Yao, "Valley-polarized quantum anomalous Hall effect in silicene," Phys. Rev. Lett. **112**, 106802 (2014).

[28] J. W. Dong, X. D. Chen, H. Zhu, Y. Wang, and X. Zhang, "Valley photonic crystals for control of spin and topology," Nat. Mater. **16**, 298-302 (2017).

[29] F. Gao, *et al.* "Topologically protected refraction of robust kink states in valley photonic crystals," Nat. Phys. **14**, 140-144 (2018).

[30] D. Rodrigo, O. Limaj, D. Janner, D. Etezadi, F. De Abajo, V. Pruneri, and H. Altug, "Mid-infrared plasmonic biosensing with graphene," Science **349**, 165-168 (2015).

[31] T. O. Wehling, K. S. Novoselov, S. V. Morozov, E. E. Vdovin, M. I. Katsnelson, A. K. Geim, and A. I. Lichtenstein, "Molecular doping of graphene," Nano Lett. **8**, 173–177 (2008).

[32] F. Schedin, A. Geim, S. Morozov, E. W. Hill, P. Blake, M. I. Katsnelson, and K. Novoselov, "Detection of individual gas molecules adsorbed on graphene," Nat. Mater. **6**, 652-655 (2007).

[33] H. Hu, *et al.* "Gas identification with graphene plasmons," Nat. Commun. **10**, 1-7 (2019).

[34] K. S. Novoselov, *et al.* "Two-dimensional gas of massless Dirac fermions in graphene," Nature **438**, 197-200 (2005).

Chapter 5

Interlayer topological supermode transport in layered graphene metasurfaces

5.1 Introduction

Recently, topological valley phases in bilayer structures have been attracting increasing attention due to their flexible interlayer coupling and unusual physical properties [1, 2, 3, 4, 5]. In a photonic system with an additional layer, the new inversion symmetry, like mirror-symmetry between different layers, can be introduced to achieve topological modes with layer-polarized features. Remarkably, layer pseudospins in acoustic and optical valley-Hall phases can generate topological modes with not only valley-chirality-locked but also layer-polarized properties, and they become a new layer degree of freedom [1, 6]. The topological modes confined at the top or bottom layers of bilayer system can be labelled with pseudospin up or pseudospin down, respectively [1, 2, 3, 4, 5]. This topology is described by a quantized topological invariant, layer Chern number, which is defined by the difference between valley Chern numbers of layer pseudospins [1, 3, 4]. Moreover, taking advantage of layer-polarized properties in bilayer systems, various potential applications, such as layer-polarization converters [1] and layer-selected delay lines [4], have been successfully demonstrated. However, layer pseudospins have been

studied less in layered topological photonic systems.

In this chapter, we study the topological layer-polarized and valley-chirality-locked modes of layered graphene metasurfaces. With additional layer degree of freedom, unit cells of different graphene layers are rotated with respect to the lattice in order to break the inversion symmetry and mirror symmetry in the layered graphene metasurfaces. Specifically, the symmetry-protected Dirac cones are gapped out in the proposed bilayer and three-layer graphene metasurfaces, and two kinds of topological valley modes are distinguished inside the nontrivial bandgap with layer-polarized and chirality-momentum-locked characteristics. It is further quantitatively proved and distinguished by two quantized topological invariants, layer Chern number and valley Chern number.

This chapter is organized as follows. In Sec. 5.2, we present the band diagram and effective Hamiltonian of the monolayer graphene metasurface with an inversion symmetry perturbed by rotating the triangular hole with respect to the lattice. This is followed in Sec. 5.3 by the band structure analysis of the bilayer graphene triangular nanohole crystal, which is described well by an effective Hamiltonian of the bilayer graphene system with interlayer coupling. In particular, we present the layer-polarized topological valley modes located at the domain-wall interface with nonzero layer Chern number difference, and the domain-wall interface with nonzero valley Chern number difference supports topological valley modes with chirality-momentum-locked features. Then, in Sec. 5.4, the band diagram of three-layer graphene triangular nanohole system is computational studied, which shows a good agreement with the effective Hamiltonian derived under the assumption of the nonzero interlayer coupling between any two layers. Importantly, by properly choosing a layer operator, the layer Chern number and valley Chern number are defined and calculated based on a set of redefined eigenstates. We prove that the number of layer-polarized topological modes and chirality-momentum-locked topological valley modes matches the layer Chern number and valley Chern number, respectively. Finally, in Sec. 5.5, we summarize the main conclusions of this chapter.

5.2 Monolayer Graphene Triangular Nanohole Metasurface

In this section, I will study the monolayer graphene crystal with triangular nanoholes, which exhibits a nontrivial bandgap due to the fact that the inversion symmetry can be reduced by simply rotating the triangular holes.

5.2.1 Band Analysis with Additional Rotation Degree of Freedom

The graphene-based topological waveguide investigated in this chapter is implemented by introducing additional rotation degree of freedom with respect to the hexagonal lattice. Our previous chapters show that the graphene plasmonic waveguide composed of a hexagonal array of circular nanoholes exhibits a symmetry-

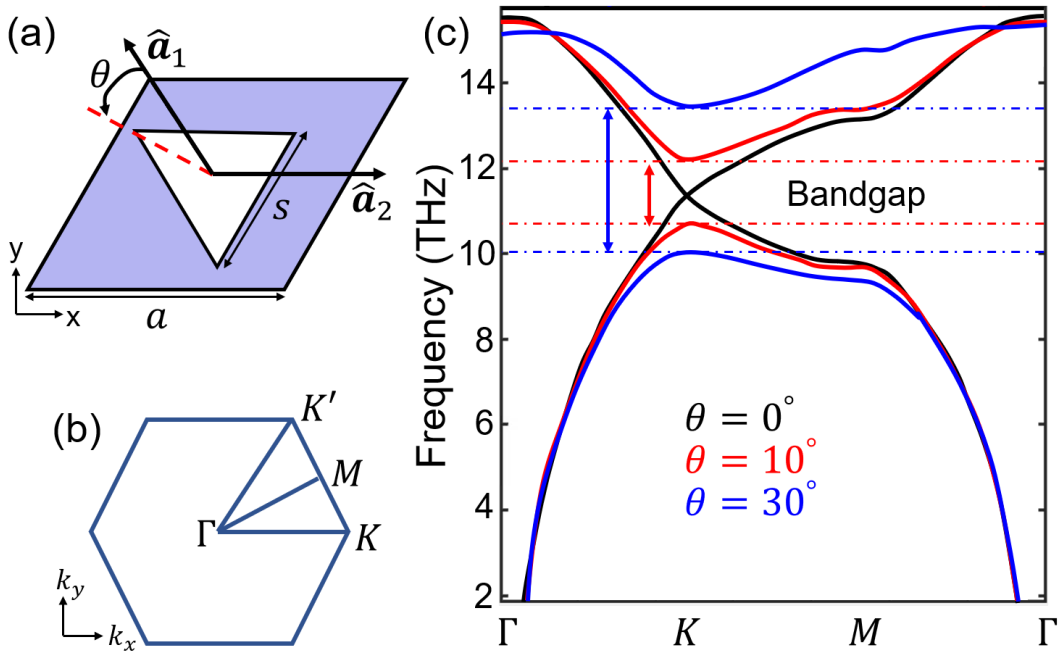

Figure 5.1: (a) Schematic of primitive unit cell of the infinite graphene crystal with a lattice constant, a, containing a triangular nanohole with a sidelength, s. The primitive vectors of hexagonal lattice are $\boldsymbol{a_1}$ and $\boldsymbol{a_2}$, and the rotation angle θ shows the orientation of triangular nanohole with respect to the lattice vector $\boldsymbol{a_1}$. (b) First Brillouin zone (FBZ) of the graphene metasurface composed of a hexagonal lattice. (c) Band diagram of the graphene triangular nanohole metasurface along k vector from Γ to K and then M, determined for different rotation angles θ with respect to the hexagonal lattice.

protected Dirac cone at K point, while the triangular nanohole in a hexagonal lattice can only support C_{3v}-symmetry protected Dirac cone with a specific orientation. To this end, the band diagram of a monolayer graphene plasmonic crystal is investigated, which consists of a hexagonal array of regular triangular holes with specific orientations with respect to the lattice vector, as schematically illustrated in Fig. 5.1(a). The original orientation of triangular nanohole is along the direction of lattice vector $\boldsymbol{a_1}$, and a perturbation is introduced by rotating the triangular hole by an angle θ with respect to $\boldsymbol{a_1}$. Specifically, positive and negative values of θ indicate anticlockwise and clockwise rotations. In our analysis, we considered that the lattice constant was $a = 500\,\text{nm}$ and the sidelength of the regular triangular hole was $s = 200\,\text{nm}$.

In order to properly identify the frequency bandgap of the monolayer graphene triangular nanohole crystal, the band diagram of this graphene metasurface determined for different orientations of triangular hole has been evaluated along the high-symmetric points of the FBZ (see Fig. 5.1(b)), and the results are given in Fig. 5.1(c). The infinite graphene metasurface is investigated by adding the periodic boundary conditions along the edges of unit cell in COMSOL Multiphysics, and the results of photonic band diagrams in the cases with $\theta = 0^\circ$, 10°, and 30° are plotted in black, red and blue curves, respectively. For orientation of triangular hole along $\boldsymbol{a_1}$, the graphene metasurface has C_{3v} point group symmetry, and the first and second frequency dispersion curves linearly cross around 11.4 THz at the K-point, leading to a C_{3v}-symmetry-protected Dirac cone. To open up the Dirac cone, the orientation of the triangular hole is rotated ($\theta \neq 0$) with respect to the hexagonal lattice. Even though the inversion symmetry of the whole system is still C_{3v}, it could reduce the inversion symmetry at the K point, which means that the K point cannot be converted into its equivalent corner by a mirror-symmetry operation on the graphene metasurface. One consequence of this reduced inversion symmetry at K point is that a nontrivial bandgap opens at the frequency of the Dirac point (see Fig. 5.1(c)). To be more specific, the maximum of the first band and the minimum of the second band increases and decreases, respectively. The width of frequency

bandgap increases with the increment of rotation angle θ. When $\theta = 30°$, the frequency bandgap achieves its maximum value of 3.4 THz. Note that all the results will remain qualitatively the same for different values of the sidelength s of the regular triangular hole, but the frequency bandgap would be narrower (wider) for a smaller (larger) s.

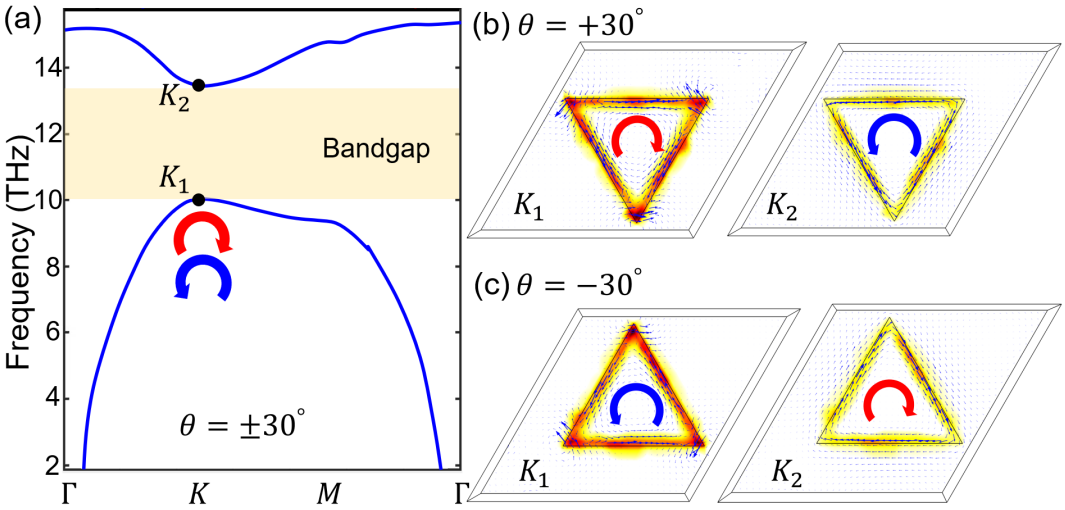

Figure 5.2: (a) First two bands of graphene triangular nanohole crystal, calculated for opposite rotation angles of triangular hole, $\theta = \pm 30°$. The minimum and maximum of two valley bands at K point are marked by K_1 and K_2, respectively. (b) Field distribution of the first two bands at K_1 and K_2 with opposite Poynting vector distributions, with the rotation angle $\theta = +30°$. The red and blue arrows represent left circular-polarized (LCP) and right circular-polarized (RCP) energy flows, respectively. (c) Similar to (b), but for rotation angle $\theta = -30°$.

To gain a deeper insight into the topological properties of the bandgap at K point, the chirality properties of the electric field of the bulk valley mode around two nonequivalent valleys K and K' are investigated. For two cases of triangular hole orientations θ with opposite signs, one could obtain two graphene metasurfaces in a mirror-symmetric manner, so that the change of sign of θ could represent the mirror-symmetry operation of the metasurface and convert K valleys to nonequivalent K' valleys. Hence, we present the band diagram and corresponding electric field of bulk valley modes determined for $\theta = \pm 30°$, and the results are shown in Fig. 5.2. As expected, these two cases exhibit the same band diagram with a relatively large bandgap marked by a yellow strip in Fig. 5.2(a). To study the valley-chirality-locking property of bulk valley modes at K and K' points, the electric field and its

polarization of the first band maximum (K_1) and the second band minimum (K_2) are given in Figs. 5.2(b) and 5.2(c). The distribution of the Poynting vector indicates the flow of the energy of the electromagnetic field in clockwise (LCP) and anticlockwise (RCP) directions marked by red and blue arrows, respectively. For each orientation of the triangular hole, the electric field is tightly localized at the triangular hole, and the vorticities at lower band (K_1) and higher band (K_2) have opposite chiralities. By comparing the chirality between $\theta = \pm 30^\circ$, one can find chiralities of all bands with $\theta = 30^\circ$ are opposite to their chiralities with $\theta = -30^\circ$ at K point. In other words, for any orientation of triangular hole in a hexagonal lattice exhibiting a bandgap, chiralities of bands are opposite between the K and K' valleys. The chirality-locking of bulk valley modes is a significant property to distinguish the sign of valley-dependent topological index, and it can also be used in practical applications to excite topological valley modes by choosing the source with the same chirality [7, 8].

5.2.2 Effective Hamiltonian of Monolayer Graphene Nanohole Crystal

For a single graphene layer composed of triangular holes, due to the C_{3v} symmetry protection, which supports the degeneracy of Dirac cone at K point as shown in Fig. 5.1(c), the 2-fold degeneracy is generated by the existence of a pair of 1D representations. Due to the inversion symmetry reduction occurring when the rotation angle $\theta \neq 0$, the double degeneracy generates a Dirac mass term in the Hamiltonian of a monolayer graphene triangular nanohole crystal. In this way, the perturbed effective 2×2 Hamiltonian spanning two nondegenerate states ψ_{p^-} and ψ_{q^+} based on the $\boldsymbol{k} \cdot \boldsymbol{p}$ perturbation method can be written as [8, 9]:

$$\delta H_s = 2\omega_D v_D \delta k_x \sigma_x + 2\omega_D v_D \delta k_y \sigma_y + 2\omega_D m v_D^2 \sigma_z \tag{5.1}$$

where $\sigma_{x,y,z}$ are the Pauli matrices, $(\delta k_x, \delta k_y)$ is the wavevector around the K point, and ω_D and v_D are the frequency and the slope of frequency dispersion of Dirac cone at K point when the Hamiltonian is unperturbed ($\theta = 0$), respec-

tively. The first two terms are generated based on the C_{3v} symmetry protection in the unperturbed system [9]. The inversion symmetry reduction via rotating triangular holes leads to the third Dirac mass term, which is given by the frequency of two nondegenerated valley states ω_{p^-} and ω_{q^+} at $(\delta k_x, \delta k_y)$ around K point, $2\omega_D m v_D^2 \sigma_z = \begin{pmatrix} \omega_{p^-}^2 - \omega_D^2 & 0 \\ 0 & \omega_{q^+}^2 - \omega_D^2 \end{pmatrix}$. In this way, the perturbed Hamiltonian can be rewritten as,

$$\delta H_s = \begin{pmatrix} \omega_{p^-}^2 - \omega_D^2 & 2\omega_D v_D(\delta k_x - i\delta k_y) \\ 2\omega_D v_D(\delta k_x + i\delta k_y) & \omega_{q^+}^2 - \omega_D^2 \end{pmatrix} \tag{5.2}$$

Due to the rotation angle θ dependence of the frequency of two nondegenerated valley states, the Dirac mass term can be simplified to $\begin{pmatrix} 2\vartheta\omega_D\theta & 0 \\ 0 & -2\vartheta\omega_D\theta \end{pmatrix}$, where the relation coefficient ϑ between the rotation angle and frequency of two valley states can be extracted from the numerical simulations in COMSOL.

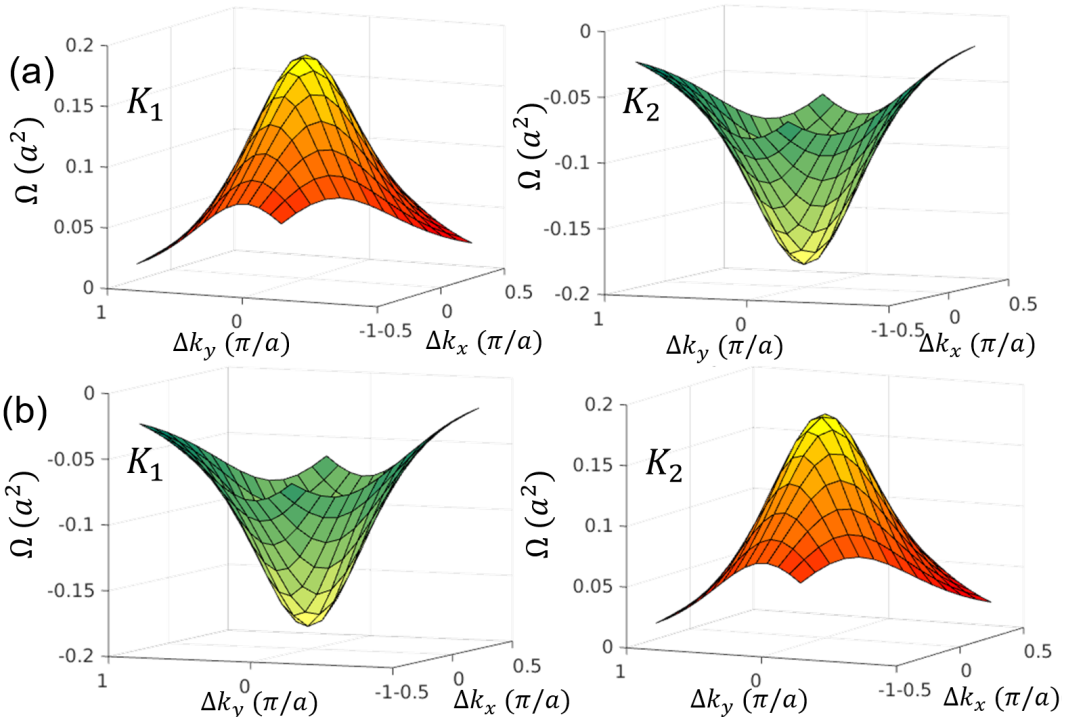

Figure 5.3: Berry curvature Ω distribution of the first two bands over the K valley computed by the effective Hamiltonian, determined for the rotation angle of triangular nanohole (a) $\theta = 30°$ and (b) $\theta = -30°$.

Based on the derived effective perturbed Hamiltonian of monolayer graphene triangular nanohole metasurface, the eigenstates ϕ and eigenvalues (frequency dispersion relation $\delta\omega$) can be found by solving the eigenvalue problem $\delta H_s\phi = \delta\omega\phi$, which provides an alternative way to evaluate a 2×1 eigenstate matrix. This method to calculate valley Chern number could bring a faster simulation time than its in COMSOL (see section 3.2.2 with millions of eigenfield points). In this way, the valley Chern numbers (C_V) of the first two non-degenerate bands can be calculated by the integral of Berry curvature over the K valley. The Wilson-loop method provides a numerical way to calculate the Berry curvature distribution based on the eigenstates in the discretized Brillouin zone, which was explained in Chapter 2 [see Eqs. (2.43) and (2.45)].

Following the same procedure of valley Chern number calculation that is presented in section 3.2.2, the hexagonal domain in the momentum space around the K valley is reshaped into a rhombic domain centered at the K point for the convenience of Brillouin zone discretization, as indicated in Fig. 3.4(a). Based on the Wilson-loop approach in Eq. (2.43), the chosen domain is discretized into 18×18 plaquettes over the K valley, and the discretized Berry curvature Ω in each plaquette is calculated by using the eigenstates ϕ at four k points of the corners of each plaquette, which is obtained from the effective Hamiltonian. Then, the sum of all discretized Berry curvatures over the K valley is the valley Chern number estimated using the effective Hamiltonian.

Since the band diagram of graphene triangular nanohole plasmonic crystal exhibits a frequency bandgap between the first and second bands, the valley Chern number of these two bands determined for graphene metasurfaces with rotation angle of triangular hole $\theta = \pm 30^\circ$ are calculated numerically by effective Hamiltonian, and the corresponding Berry curvature distributions over the 18×18 discretized K valley are shown in Figs. 5.3(a) and 5.3(b). The discretized rhombic Brillouin zone in the momentum space is centered at K point, and the maximum distance $\delta\boldsymbol{k}$ of discretized $\boldsymbol{k}$ point with respect to the K point is $0.5\pi/a$ and π/a along the k_x and k_y directions, respectively. The 2×2 Hamiltonian has two eigen-

values $\delta\omega(\boldsymbol{k})$, which correspond to the frequency dispersion of the first and second bands. For each eigenvalue, there is a 2×1 eigenstate matrix at each $\boldsymbol{k}$ point of the discretized Brillouin zone, which is utilized to calculate the Berry curvature in each plaquette.

In Fig. 5.3(a) with $\theta = 30^\circ$, the Berry curvature distributions of the first (K_1) and second (K_2) bands over the K valley show positive and negative signs, respectively, which is consistent with the chirality property of these two bands. Specifically, the positive sign of Berry curvature corresponds to the LCP energy flow of bulk valley mode while the negative sign indicates the RCP energy flow, as shown in Fig. 5.2(b). In contrast, since the chirality-locking properties of the first two bands when $\theta = -30^\circ$ are opposite with respect to the case $\theta = 30^\circ$, the sign of Berry curvature distribution of the first band when $\theta = -30^\circ$ is negative while the sign of Ω of the second band when $\theta = -30^\circ$ is positive (see Fig. 5.3(b)). The nontrivial Berry curvature distribution shows a peak at the K point, and the valley Chern number is obtained by the integral of Berry curvature over the K valley. In Fig. 5.3(a) with $\theta = 30^\circ$, the valley Chern numbers computed by the Wilson-loop method of the first and second bands are $0.28, -0.28$ while the valley Chern numbers of the first and second bands when $\theta = -30^\circ$ in Fig. 5.3(b) are $-0.28, 0.28$. Note that when the frequency bandgap is relatively large, the distribution of Berry curvature over the corners (K and K' points) of the hexagonal Brillouin zone spreads significantly and overlaps with other Berry curvature at two adjacent corner points. This makes it more difficult to properly define the valley Chern number, as its calculation cannot be extended to the entire FBZ. Therefore, the theoretical valley Chern number $C_v = \pm 0.5$ can only be obtained close to Dirac point with an infinitesimally small perturbation, as reported before [10, 11, 12, 13, 14]. To solve this unavoidable problem, only the sign of computed valley Chern number is preserved and the value of valley Chern number is regarded as 0.5 in our later discussion. Although the total value of Chern number over the FBZ is zero, the inversion symmetry reduction leads to nonzero valley Chern numbers with opposite signs over K and K' valleys. These features have important implications on the topological nature of the valley

modes along the domain-wall interface with ± 1 valley Chern number difference, which is constructed by connecting K and K' points under a π-rotation.

5.3 Bilayer Graphene Triangular Nanohole Metasurfaces with Symmetry Breaking

In this section a graphene bilayer metasurface structure is illustrated to possess two types of topological valley modes in a nontrivial bandgap, i.e., chirality-momentum-locked and layer-polarized topological modes. The method used to create these modes is to reduce the inversion symmetry and break the mirror symmetry of the graphene structure by rotating the triangular nanoholes with specific orientations.

5.3.1 Band Diagram of Bilayer Graphene Crystals

Since the topological features of bandgap with reduced inversion symmetry have been demonstrated in monolayer graphene triangular nanohole crystal by introducing an additional rotation degree of freedom, we investigate bilayer graphene crystals composed of two free-standing, optically coupled graphene triangular nanohole crystals with additional mirror symmetry breaking between the two layers [see Fig. 5.4(a)]. It should be noted that graphene metasurfaces with such geometrical parameters can be readily fabricated using widely available fabrication techniques, such as e-beam lithography. Besides, the topological conclusions of this study remain qualitatively valid if one assumes that the graphene layers are separated by a certain dielectric material (glass with refractive index ≈ 1.52) instead of air, and the calculated band diagram will be slightly compressed along the frequency axis.

By adjoining together two halves of semi-infinite bilayer graphene triangular hole metasurfaces in a mirror-symmetric manner, a domain-wall interface is generated along the x-axis. The top and bird's eye views of the schematic of the proposed bilayer graphene triangular nanohole metasurfaces are shown in Figs. 5.4(b) and 5.4(c), respectively. The two freestanding graphene crystals consist of identical regular triangular nanohole with sidelength s, which are separated along the z-axis by a separation distance h. Same to the monolayer graphene metasurface, we fix the lat-

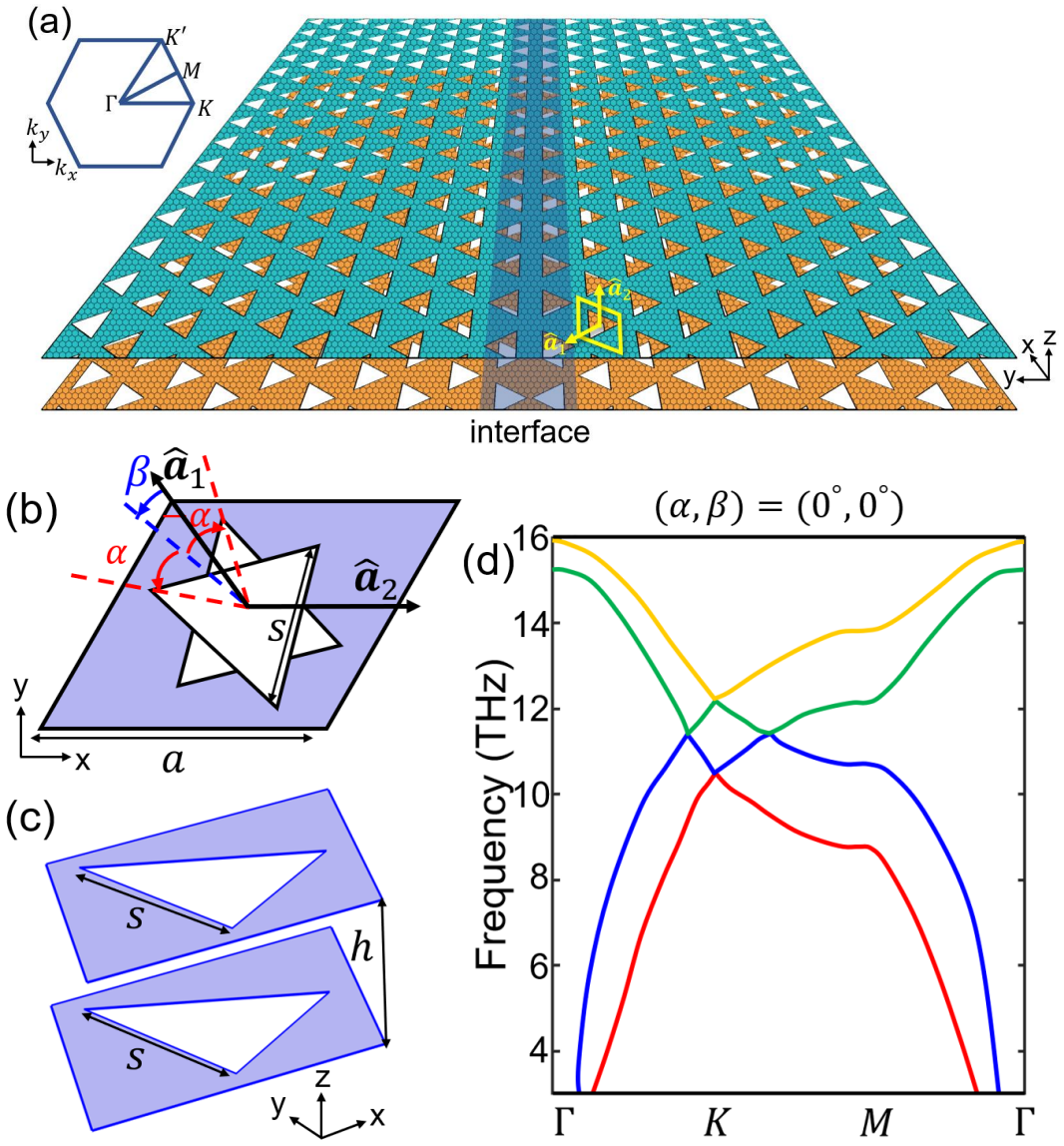

Figure 5.4: (a) Schematic of the bilayer graphene plasmonic waveguide with a mirror-symmetric domain-wall interface oriented along the x-axis. (b) Top view of primitive unit cell of the bilayer graphene metasurface with lattice constant a, of which each layer is composed by triangular nanohole with the same side-length s. The rotation angle of triangular holes in two layers with respect to the hexagonal lattice is determined by external degree of freedom β and internal degree of freedom α, with rotation angle of triangular holes of the top and bottom layers being $\theta_1 = \beta + \alpha$ and $\theta_2 = \beta - \alpha$, respectively. (c) Bird's eye view of the unit cell with a separation distance, h, between the two layers. (d) Band diagram of an infinite bilayer graphene triangular nanohole crystal without perturbation $(\alpha, \beta) = (0^\circ, 0^\circ)$, which exhibits two Dirac cones at the K-point. The first four bands are marked by red, blue, green, and yellow curves, respectively. The Dirac frequencies of two Dirac cones are split depending on the separation distance h due to the interlayer coupling.

tice constant $a = 500\,\text{nm}$, the sidelength of regular triangular holes $s = 200\,\text{nm}$, and the distance between the top and bottom graphene layers $h = 200\,\text{nm}$ to ensure an effective interlayer optical coupling. Note that by decreasing the separation distance h between the two layers, the interlayer optical coupling between two graphene layers increases, so that the corresponding Dirac frequencies of the two Dirac cones are shifted oppositely. Hence, the separation distance ($h = 200\,\text{nm}$) between two layers ensures not only the effective interlayer coupling, but also the appropriate Dirac frequency difference between two Dirac cones. Moreover, the triangular holes in top and bottom layers are rotated with respect to the hexagonal lattice via rotation angles θ_1 and θ_2, respectively. To clarify the relative rotation relationship between the two layers, the external degree of freedom β and internal degree of freedom α are introduced to replace the rotation angle of top (θ_1) and bottom layers (θ_2) in Fig. 5.4(b), which are defined as $\beta = (\theta_1 + \theta_2)/2$ and $\alpha = (\theta_1 - \theta_2)/2$, namely $\theta_1 = \beta + \alpha$ and $\theta_2 = \beta - \alpha$. In other words, the external degree of freedom β represents the common rotation angle of both layers while the internal degree of freedom α represents the relative rotation angle between two graphene layers.

We show in Fig. 5.4(d) the first four bands of the unperturbed graphene bilayer crystal with orientations of triangular holes in both layers along the direction of lattice vector, namely $(\alpha, \beta) = (0^\circ, 0^\circ)$. Due to the existence of interlayer coupling between the two layers, the bilayer graphene triangular nanohole crystal possesses D_{3h}-symmetry-protected double Dirac cones at K points, which are shifted along the frequency axis in opposite directions with respect to the Dirac frequency (11.4 THz) of monolayer graphene crystal. Specifically, one of the Dirac cones emerges between the first (red) and second (blue) bands while another Dirac cone is formed by the linear cross between the third (green) and fourth (yellow) bands.

In order to gap out the D_{3h}-symmetry-protected double Dirac cones, external and internal degrees of freedom are utilized by rotating triangular holes in both layers to reduce the inversion-symmetry of the system. The first four bands calculated for different orientations of triangular holes are shown in Fig. 5.5(a). Starting from the well-understood cases with $\alpha = 0^\circ$, in which the triangular holes in both layers

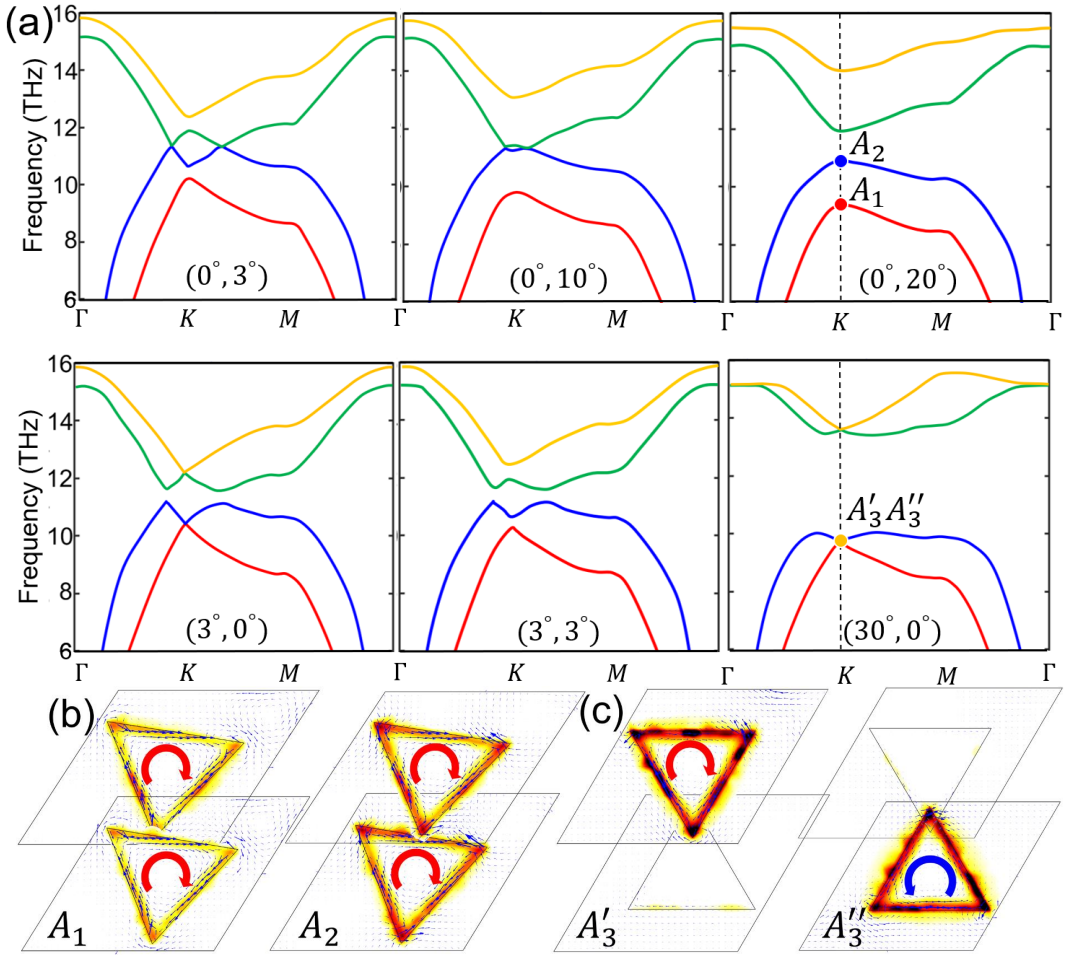

Figure 5.5: (a) First four bulk bands of bilayer graphene triangular nanohole crystals, calculated for various internal degrees of freedom and external degree of freedom (α,β). The nontrivial frequency bandgap can emerge between the second and third bands. (b) Chirality properties of bulk valley modes of the bilayer graphene triangular nanohole crystal with rotation angles $(\alpha,\beta) = (0°,20°)$. From the left to right panel, electric field and Poynting vector distribution of the first two non-degenerate bands at K point correspond to points A_1 and A_2 in (a). (c) Layer-polarized properties of bulk valley modes of the bilayer graphene triangular nanohole crystal with rotation angles $(\alpha,\beta) = (30°,0°)$. From the left to right panel, electric field and Poynting vector distribution of the first two degenerate bands at K point correspond to points A_3' and A_3'' in (a). The red and blue arrows represent LCP and RCP energy flows, respectively.

are mirror-symmetric and are rotated by the same angle β, we show in the top row of Fig. 5.5(a) the band diagrams with increasing common rotation angle β. Due to the rotation of triangular holes in both layers with respect to the hexagonal lattice, the inversion-symmetry of the bilayer graphene crystal at K point is reduced. As a result, each symmetry-protected Dirac cone is gapped out, and two frequency

bandgaps emerge between the first and second bands in the case of one of the Dirac cones and between the third and fourth bands in the case of the other one. With the increase of the common rotation angle β, two frequency bandgaps increase and generate a common nontrivial bandgap of the bilayer graphene metasurface between the second and third bands. Specifically, the nontrivial frequency bandgap cannot emerge until β approaches 10°, and it will reach its maximum value from 10.7 THz to 12.2 THz for $\beta = 30^\circ$.

Unlike the case of inversion-symmetry reduction by simultaneously rotating two triangular nanoholes in both layers with a common rotation angle β ($\alpha = 0^\circ$), the mirror symmetry between the top and bottom layers can be broken by introducing a relative angle $\alpha \neq 0^\circ$, which can result in a nontrivial bandgap as well. We show in the bottom row of Fig. 5.5(a) the band diagrams with the increasing relative rotation angle α. When the mirror-symmetry breaking is introduced in any of the cases with $\alpha \neq 0^\circ$, the D_{3h}-symmetry-protected double Dirac cones are gapped out, and a nontrivial frequency bandgap emerges between the second and third bands. Interestingly, the first two bands linearly cross at K point, which happens to the third and fourth bands as well. In contrast to the cases with $\beta \neq 0^\circ$, there is no threshold rotation angle of α to open a bandgap, based on the fact that mirror-symmetry breaking of the bilayer graphene system can be achieved via a nonzero relative rotation angle ($\alpha \neq 0^\circ$). To be more specific, the size of nontrivial bandgap becomes wider and up to 3.4 THz from 10 THz to 13.4 THz when the angle α increases to 30°.

To gain further insights into the difference between the inversion-symmetry reduction and mirror-symmetry breaking, the polarization of the electric field of two typical cases has been investigated. We first consider the inversion symmetry reduction with only external degree of freedom $(\alpha, \beta) = (0^\circ, 20^\circ)$, and the electric field and Poynting vector distribution of the first two bands at K point are shown in Fig. 5.5(b). For the two bands below the bandgap, the electric field is highly confined and localized around the edges of the triangular nanoholes of both layers, showing a LCP energy flow. Since the valley-chirality-locking property of this bilayer

system is similar to that of monolayer graphene metasurfaces with same rotation angle, we call this bilayer graphene metasurfaces with normal chirality property as *topological valley insulator*. In this configuration, it shows the opposite chirality characteristics at K and K' points, which can be used to construct a domain-wall interface by two graphene metasurfaces with opposite signs of β.

We now consider the bilayer graphene triangular hole crystals with $(\alpha,\beta) = (30^\circ, 0^\circ)$ characterized by mirror-symmetry breaking between the two layers, and energy flows of the corresponding first two degenerate bands at K point are presented in Fig. 5.5(c). Differently but interestingly, the electric field of two degenerate bands is only confined at the triangular hole of one layer. Specifically, the electric field of the first band A_3' is localized at the top layer with a LCP energy flow while the electric field of the second band A_3'' is localized at the bottom layer with a RCP energy flow. Since two degenerate bands at K point exhibit opposite polarization and are localized at different layers, their confinement at different layers can be viewed as being characterized by a pseudospin-up and pseudospin-down, and we denote this bilayer graphene metasurfaces with layer pseudospins as *layered-polarized topological insulator*.

5.3.2 Effective Hamiltonian of Bilayer Graphene Crystals

Following the introduction of the perturbed Hamiltonian of the single graphene layer with triangular holes, the effective Hamiltonian δH^b of a bilayer graphene metasurface is derived by adding a new interlayer coupling term between the two graphene layers. First, the case without interlayer coupling is considered. The bilayer graphene metasurface possesses two Dirac cones at K point with four degenerate states $\{\psi_{p_1^-}, \psi_{q_1^+}, \psi_{p_2^-}, \psi_{q_2^+}\}$. When the first and second graphene layer is rotated by θ_1 and θ_2, respectively, the Hamiltonian of the bilayer system without

considering interlayer coupling is the sum of the Hamiltonian of two layers,

$$\delta H_u^b = \begin{pmatrix} 2\vartheta\omega_D\theta_1 & 2\omega_D v_D(\delta k_x - i\delta k_y) & 0 & 0 \\ 2\omega_D v_D(\delta k_x + i\delta k_y) & -2\vartheta\omega_D\theta_1 & 0 & 0 \\ 0 & 0 & 2\vartheta\omega_D\theta_2 & 2\omega_D v_D(\delta k_x - i\delta k_y) \\ 0 & 0 & 2\omega_D v_D(\delta k_x + i\delta k_y) & -2\vartheta\omega_D\theta_2 \end{pmatrix} \tag{5.3}$$

Then a perturbed Hamiltonian with interlayer coupling is introduced as a diagonal matrix in a new basis [15]. This new basis is defined as a combination of the original four eigenstates,

$$\begin{aligned} \psi_{p,S} &= \frac{1}{\sqrt{2}}\left(\psi_{p_1^-} + \psi_{p_2^-}\right) \\ \psi_{p,A} &= \frac{1}{\sqrt{2}}\left(\psi_{p_1^-} - \psi_{p_2^-}\right) \\ \psi_{q,S} &= \frac{1}{\sqrt{2}}\left(\psi_{q_1^-} + \psi_{q_2^-}\right) \\ \psi_{q,A} &= \frac{1}{\sqrt{2}}\left(\psi_{q_1^-} - \psi_{q_2^-}\right) \end{aligned} \tag{5.4}$$

where subscripts S and A indicate symmetric and antisymmetric eigenstates, respectively. By introducing the new basis, the Hamiltonian with interlayer coupling expressed in the new basis can be written as $\delta H_{b_{inter}} = diag(\omega_S^2, \omega_A^2, \omega_S^2, \omega_A^2)$. As a result, the Hamiltonian with interlayer coupling is rewritten in the original basis as,

$$\delta H_c^b = \begin{pmatrix} 0 & 0 & 2\omega_D\omega_{SA} & 0 \\ 0 & 0 & 0 & 2\omega_D\omega_{SA} \\ 2\omega_D\omega_{SA} & 0 & 0 & 0 \\ 0 & 2\omega_D\omega_{SA} & 0 & 0 \end{pmatrix} \tag{5.5}$$

where the variable $\omega_{SA} = \frac{1}{2}\omega_S^2(\omega_S^2 - \omega_A^2)$, and the interlayer coupling term $2\omega_D\omega_{SA}$ occupies the off-diagonal positions. Therefore, the effective Hamiltonian of the bilayer graphene metasurface can be obtained by combining the Hamiltonian of individual layer and interlayer coupling terms ($\delta H^b = (\delta H_u^b + \delta H_c^b)/2\omega_D$) in the basis of $\{\psi_{p_1^-}, \psi_{q_1^+}, \psi_{p_2^-}, \psi_{q_2^+}\}$,

$$\delta H^b = v_D s_0 \otimes (\delta k_x\sigma_x + \delta k_y\sigma_y) + \vartheta(\alpha s_z + \beta s_0) \otimes \sigma_z + \omega_{SA} s_x \otimes \sigma_0 \tag{5.6}$$

where s_i and σ_i $(i = 0, x, y, z)$ are Pauli matrices indicating the layered pseudospin and orbital degree of freedoms, respectively. The relative and common angles between triangular holes of two layers are defined from the rotation angle of each layer, which are $\alpha = \frac{\theta_1 - \theta_2}{2}$ and $\beta = \frac{\theta_1 + \theta_2}{2}$, respectively. The first term indicates the unperturbed symmetry-protected system with four-fold degeneracy, and the opened nontrivial bandgap via the rotation of each layer is described by the second term, and then the third term shows the interlayer coupling between the two layers. Note that, parameters like slope v_D of the frequency dispersion around Dirac frequency, angular coefficient ϑ, and interlayer coupling strength ω_{SA} can be numerically extracted from the finite element method (FEM) simulation in COMSOL.

Since the frequency dispersion relation of each valley state can be determined by solving the eigenvalue problem $\delta H^b \phi_i = \delta \omega_i \phi_i$, the effective 4×4 Hamiltonian of the bilayer graphene metasurface is used to calculate the first four eigenvalues (frequencies of the first four bands) with four 4×1 eigenstates around the Dirac frequency at K point. To properly obtain the slope v_D, angular coefficient ϑ, and interlayer coupling strength ω_{SA}, the eigenvalues $\delta\omega(\boldsymbol{k})$ calculated from the effective Hamiltonian are fitted to the computed band diagram from COMSOL around K point, and the results determined for different orientations of triangular holes in the bilayer graphene metasurface are shown in Fig. 5.6.

Upon following this fitting procedure, the extracted values of the parameters were $v_D = 4.34$, $\vartheta = 4.3\,\mathrm{deg}^{-1}$, and $\omega_{SA} = -0.8533$. By substituting these values into the effective Hamiltonian Eq. (5.6), one can obtain the frequency dispersion of bands around the K point. In each figure of Fig. 5.6, solid blue curves represent the eigenfrequencies calculated from the effective Hamiltonian while the rigorous results obtained using COMSOL are marked by red dotted curves. For both cases with valley-chirality-locking ($\alpha = 0^\circ$) and layered-polarized ($\alpha \neq 0^\circ$) features, the frequency dispersion relation calculated from the effective Hamiltonian shows a good agreement with COMSOL simulations. It should be noted that some mismatches are observed for the fourth bands at high frequency, because the perturbation brings larger calculation error for higher frequency with shorter wavelength. In addition,

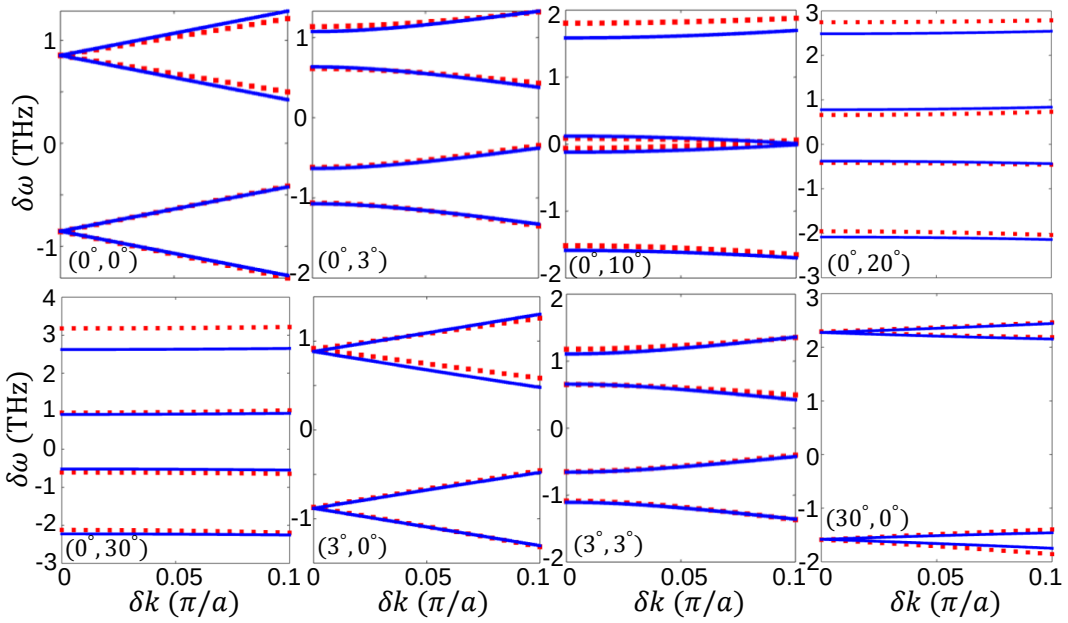

Figure 5.6: Detailed band structure along the k vector difference δk with respect to the K-point, determined for specific rotation angles (α,β) of two triangular holes in bilayer graphene plasmonic crystals. $\delta\omega$ corresponds to the frequency change with respect to the mean value of two Dirac frequencies. The blue solid and red dotted curves indicate band structure calculated by the effective Hamiltonian and COMSOL simulations, respectively.

it is also clearly shown that the lower two bands are degenerate at K point when the mirror symmetry breaking ($\alpha \neq 0°$) is introduced while the bilayer graphene system with inversion symmetry reduction ($\alpha = 0°$) exhibits four non-degenerate bands.

Using the calculated nth eigenfrequency (ω_n) and the corresponding 4×1 eigenstate ($|\boldsymbol{u}_n\rangle$) from the effective perturbed Hamiltonian, one can compute the Berry curvature distribution and valley Chern number of the first four bands based on the Wilson-loop approach. The chosen rhombic domain centered at K point is discretized into 18×18 small plaquettes, and the link variable, $\frac{\langle \boldsymbol{u}_{n,\boldsymbol{k}_1} | \boldsymbol{u}_{n,\boldsymbol{k}_2} \rangle}{|\langle \boldsymbol{u}_{n,\boldsymbol{k}_1} | \boldsymbol{u}_{n,\boldsymbol{k}_2} \rangle|} \frac{\langle \boldsymbol{u}_{n,\boldsymbol{k}_2} | \boldsymbol{u}_{n,\boldsymbol{k}_3} \rangle}{|\langle \boldsymbol{u}_{n,\boldsymbol{k}_2} | \boldsymbol{u}_{n,\boldsymbol{k}_3} \rangle|} \frac{\langle \boldsymbol{u}_{n,\boldsymbol{k}_3} | \boldsymbol{u}_{n,\boldsymbol{k}_4} \rangle}{|\langle \boldsymbol{u}_{n,\boldsymbol{k}_3} | \boldsymbol{u}_{n,\boldsymbol{k}_4} \rangle|} \frac{\langle \boldsymbol{u}_{n,\boldsymbol{k}_4} | \boldsymbol{u}_{n,\boldsymbol{k}_1} \rangle}{|\langle \boldsymbol{u}_{n,\boldsymbol{k}_4} | \boldsymbol{u}_{n,\boldsymbol{k}_1} \rangle|}$, expresses the Berry curvature of the nth band in every small plaquette with four corner points ($\boldsymbol{k}_1, \boldsymbol{k}_2, \boldsymbol{k}_3, \boldsymbol{k}_4$).

We first show in Fig. 5.7(a) the Berry curvature distribution of the first two bands in a topological valley bilayer graphene system. As expected, the distribution of Berry curvature shows a sharp peak at the K point, and the sign of the Berry curvature is consistent with the valley-chirality-locking property for each band in Fig.

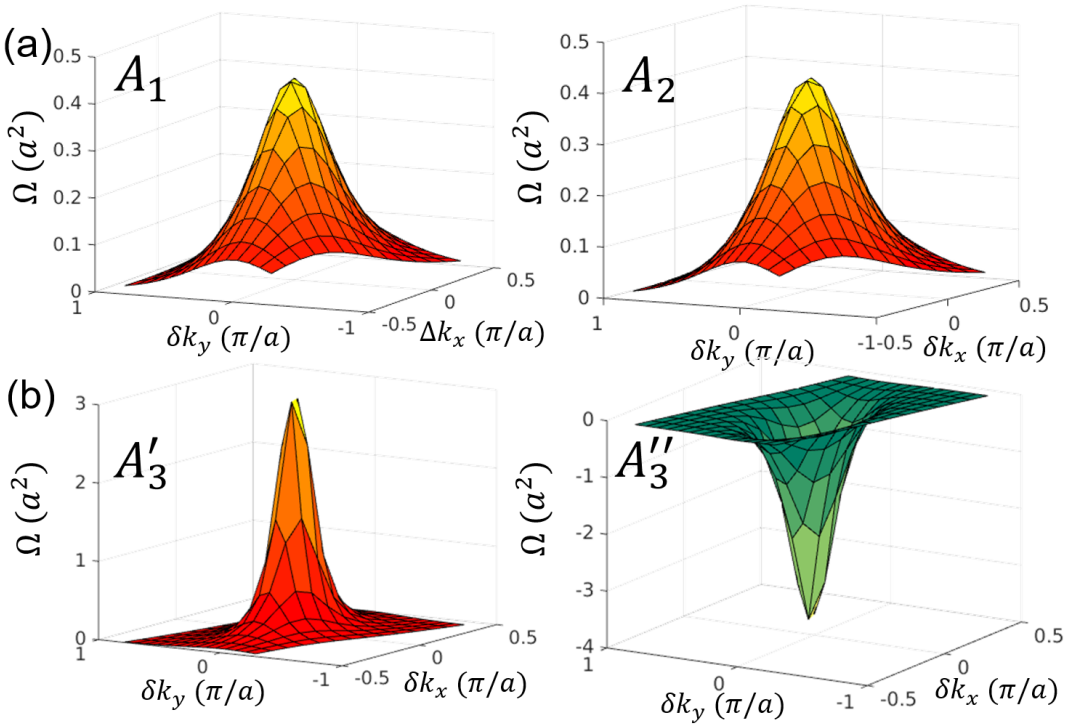

Figure 5.7: (a) Berry curvature Ω distribution of the first two bands (A_1 and A_2 in Fig. 5.5(a)) over the K valley computed by the effective Hamiltonian, determined for rotation angles $(\alpha,\beta) = (0°, 20°)$ with two non-degenerate bands with chirality properties below the bandgap. (b) Similar to (a), but for bilayer graphene crystals with rotation angles $(\alpha,\beta) = (30°, 0°)$ showing two degenerate bands (A_3' and A_3'' in Fig. 5.5(a)) at K point.

5.5(b). Specifically, the positive Berry curvature corresponds to clockwise rotation (LCP) of the energy flux and the valley Chern numbers of these two non-degenerate bands are $(0.5, 0.5)$. Moreover, the valley Chern number and Berry curvature distribution of layered-polarized topological bilayer graphene system with mirror symmetry breaking ($(\alpha,\beta) = (30°, 0°)$) between two layers have been computed, and the results are given in Fig. 5.7(b). Since the lower two bands are degenerate at K points, Berry curvatures of the two degenerate bands are opposite, whose sign agrees with the circular-polarized energy flow in Fig. 5.5(c). In addition, the linear crossing between the two degenerate bands generates an infinitesimally small perturbation, resulting in an extremely sharp peak of the Berry curvature around the K point. As a consequence, the computed valley Chern numbers of two degenerate bands approach 0.5 with $(C_V^1, C_V^2) = (0.5, -0.5)$.

By comparing the lower two bands of topological valley graphene system and

layered-polarized graphene system, the former case shows same valley Chern number ($C_V^1 = C_V^2 = \pm 0.5$) for each non-degenerate band while the latter case has opposite valley Chern number ($C_V^1 = -C_V^2 = \pm 0.5$). As the total valley Chern number is defined by the sum of valley Chern numbers of bands below the nontrivial bandgap ($C_V = C_V^1 + C_V^2$), the total valley Chern number is zero for layer-polarized bilayer graphene metasurfaces. However, it indeed exhibits nontrivial frequency bandgap, so that we can define a new layer Chern number which can indicate the number of layer-polarized modes.

For the layer-polarized graphene system with mirror symmetry breaking, the sign of valley Chern numbers calculated for two degenerate bands cannot properly indicate the layer where the electric field is confined. However, the derived effective Hamiltonian can be projected onto a layer pseudospin subspace with spin operator ($s_z = diag\{1,1,-1,-1\}$), so that eigenstates $\{\phi_1, \phi_2\}$ of the lower two bands can be regrouped into two new eigenstates $\{\psi_+, \psi_-\}$, which represent the field confinement in different layers with eigenvalues of ± 1 for layer pseudospins [16, 17]. To be more specific, by spanning s_z with the basis of eigenstates of lower two bands $\{\phi_1, \phi_2\}$, the 2×2 matrix representation of the spin operator becomes,

$$\langle \phi_i | s_z | \phi_j \rangle = \begin{pmatrix} \langle \phi_1 | s_z | \phi_1 \rangle & \langle \phi_1 | s_z | \phi_2 \rangle \\ \langle \phi_2 | s_z | \phi_1 \rangle & \langle \phi_2 | s_z | \phi_2 \rangle \end{pmatrix} = \begin{pmatrix} m & t \\ t & -m \end{pmatrix} \tag{5.7}$$

where $\langle \phi_1 | s_z | \phi_1 \rangle = -\langle \phi_2 | s_z | \phi_2 \rangle = m$ and $\langle \phi_1 | s_z | \phi_2 \rangle = \langle \phi_2 | s_z | \phi_1 \rangle = t$ are proved by computational results. The eigenvalues of this matrix are $\pm\sqrt{m^2+t^2}$ with eigenstates $(\frac{\sqrt{m^2+t^2}+m}{t}, 1)^T$ and $(\frac{m-\sqrt{m^2+t^2}}{t}, 1)^T$, and the difference between the two eigenvalues indicates the bandgap for the layer-polarized bilayer graphene system. By denoting the upper and lower layer-polarized eigenmodes as $(1,0)^T$ and $(0,1)^T$, the regrouped eigenstates are obtained as,

$$\psi_+ = \frac{\sqrt{m^2+t^2}+m}{t}\phi_1 + \phi_2, \tag{5.8}$$

$$\psi_- = \frac{m-\sqrt{m^2+t^2}}{t}\phi_1 + \phi_2, \tag{5.9}$$

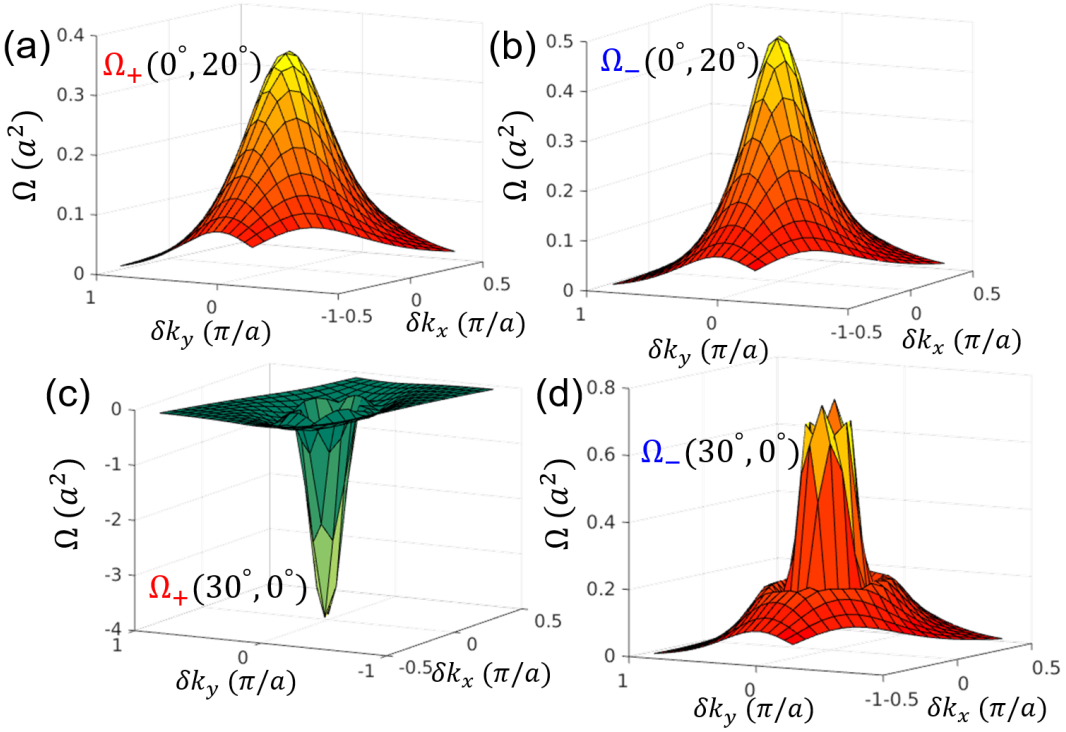

Figure 5.8: Layer-polarized Berry curvature Ω distribution over the K valley computed by the new regrouped eigenstate basis ψ_+ and ψ_-. Notations $+$ and $-$ correspond to eigenstates with layer pseudospins. (a) and (b) for $(\alpha,\beta)=(0^\circ,20^\circ)$. (c) and (d) for $(\alpha,\beta)=(30^\circ,0^\circ)$.

Based on the new basis $\{\psi_+,\psi_-\}$, the Berry curvature distribution $\Omega_\pm$ and layer-polarized valley Chern number $C_V^\pm$ have been computed over the K valley, and the results determined for topological valley and layer-polarized systems are shown in Fig. 5.8. For the topological valley bilayer graphene system with $(0^\circ,20^\circ)$ shown in Figs. 5.8(a) and 5.8(b), Berry curvatures present positive peaks at K point, and the layer-polarized valley Chern numbers computed in the new basis $\{\psi_+,\psi_-\}$ are 0.19 and 0.25, respectively. Since the sign of layer-polarized valley Chern number is same as valley Chern number of lower two bands in Fig. 5.7(a) when $(\alpha,\beta)=(0^\circ,20^\circ)$, the valley Chern number for topological valley system with non-degenerate bands cannot change when it is expressed in different bases of eigenstates. Differently, for layer-polarized topological system with $(30^\circ,0^\circ)$ in Figs. 5.8(c) and 5.8(d), the Berry curvature distributions calculated using $\{\psi_+,\psi_-\}$ around the K point show a peak, and the calculated layer-polarized valley Chern numbers are $C_V^+=-0.5$ and $C_V^-=0.38$. By comparing with valley Chern number

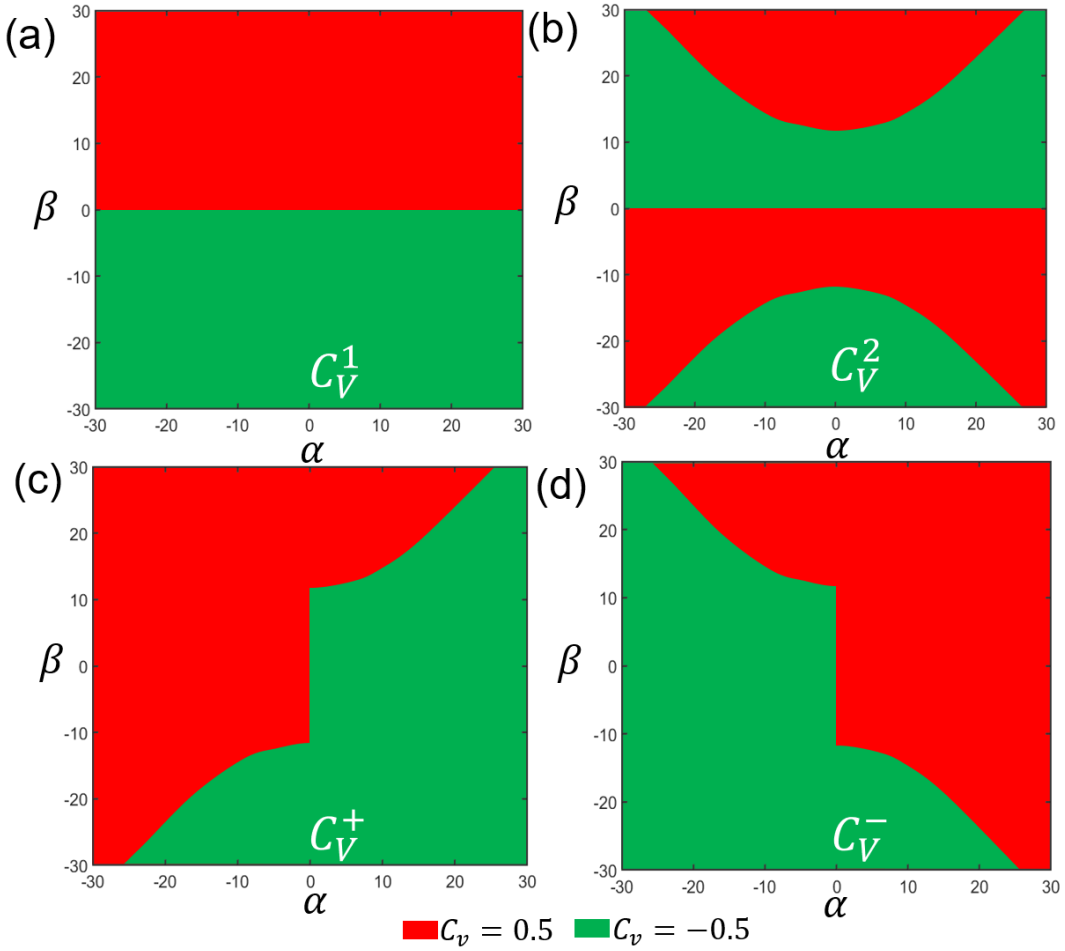

Figure 5.9: (a)(b) Computed valley Chern number distribution of the first C_V^1 and second C_V^2 bands with respect to (α, β), respectively. The red and green domains represent the valley Chern number with positive and negative signs, respectively. (c)(d) same as in (a)(b), but for computed two layer-polarized valley Chern number distribution of layer-polarized eigenstates ψ_+ and ψ_-, respectively.

of lower two degenerate bands in Fig. 5.7(b), the absolute values of layer-polarized valley Chern numbers are no longer the same in the new basis, and signs of the two layer-polarized valley Chern numbers changes with respect to the valley Chern numbers of lower two bands.

To properly identify the valley Chern number for the topological valley and layer-polarized systems, the phase diagram of valley Chern number (C_V^1 and C_V^2) of the lower two bands and layer-polarized valley Chern number ($C_V^{\pm}$) are calculated for different values of rotation angles (α, β), and the computed results are summarized in Fig. 5.9. The sign of computed valley Chern number is extracted at each

(α,β) point from -30° to 30°, in which the red domain represents positive sign of valley Chern number as 0.5 and green region indicates the valley Chern number equals to -0.5. Regarding the phase diagram of valley Chern number of lower two bands in Figs. 5.9(a) and 5.9(b), there is a clear delimitation between the two domains with opposite signs at $\beta = 0$, which explains why the energy flow of two lower bands changes its chirality when the triangular nanoholes have opposite orientations. In addition, there are two semicircular regions at the α axis with $C_V = 0.5$ of the top region and $C_V = -0.5$ of the bottom region. These two regions correspond to the topological valley system with two non-degenerate bands, based on the fact that the value of valley Chern number cannot change in these two regions when it is calculated in different bases, as compared with Figs. 5.9(c) and 5.9(d). Differently, the phase diagram of layer-polarized valley Chern numbers shows its difference in the region other than top and bottom areas (see Figs. 5.9(c) and 5.9(d)). Specifically, a vertical line at $\alpha = 0$ separates the left and right domains with opposite signs. In the region except for top and bottom semicircular areas, the signs of C_V^+ and C_V^- are opposite.

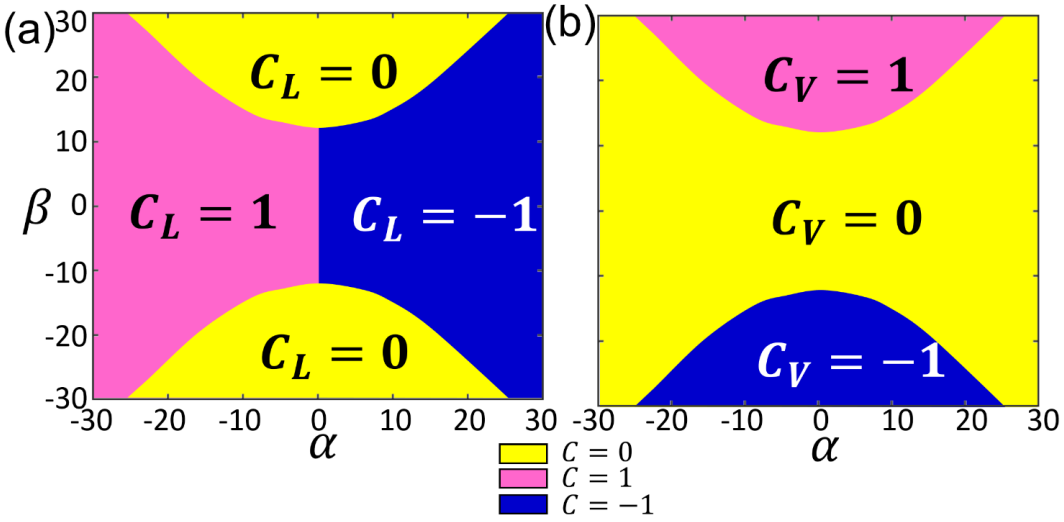

Figure 5.10: (a) Layer Chern number distribution of bilayer graphene crystals with respect to (α,β), defined by the difference between two layer-polarized valley Chern numbers, namely $C_L = C_V^+ - C_V^-$. The regions with 0, 1 and -1 Chern number are depicted in yellow, magenta, and blue, respectively. (b) Valley Chern number distribution of bilayer graphene crystals with respect to (α,β), defined by the sum of two layer-polarized valley Chern numbers ($C_V = C_V^+ + C_V^-$).

Since the valley Chern number has opposite sign in the layer-polarized system, the total layer Chern number in the layer-polarized system can be defined as $C_L = C_V^+ - C_V^-$, whereas the total valley Chern number in the normal topological valley system with chirality features is the sum of valley Chern number below the bandgap, $C_V = C_V^1 + C_V^2 = C_V^+ + C_V^-$. Using these definitions for the valley (CV) and layer-polarized (CL) Chern numbers, the corresponding phase diagrams of the bilayer graphene system with respect to (α, β) are determined and presented in Figs. 5.10(a) and 5.10(b), respectively. The yellow, magenta, and blue regions correspond to Chern numbers with a value of 0, 1, and -1, respectively. First, in the top and bottom areas with layer-polarized valley Chern number ($C_V^{\pm}$) of same sign, the layer Chern number is zero while the valley Chern number is ± 1, leading to a topological valley-chirality-locked system. Moreover, in the remaining region, the total valley Chern number is zero, but two domains with opposite layer Chern numbers ($C_L = \pm 1$) are mirror-symmetric with respect to the vertical line at $\alpha = 0$. Note that for degenerate bands, the composite valley Chern number corresponding to degenerate bands is usually introduced rather than the valley Chern number for each band. However, the composite valley Chern number equals to the sum of valley Chern number of each band in our simulations, so that not only the total valley Chern number but also the layer Chern number can be defined using the linear combination of valley Chern number of each band below the bandgap.

5.3.3 Layer-polarized and Chirality-momentum-locked Topological Interface Modes

From the phase diagram of layer and valley Chern numbers in Fig. 5.10, C_L and C_V can change their signs with respect to orientations of triangular holes in bilayer graphene metasurfaces. By combing bilayer graphene metasurfaces with opposite Chern numbers in a mirror-symmetric manner, the nonzero difference of the Chern number across the interface will lead to the formation of topologically-protected valley modes. To this end, two configurations with nonzero layer Chern number and valley Chern number across the domain-wall interface have been computationally investigated after properly designing a mirror-symmetric domain-wall inter-

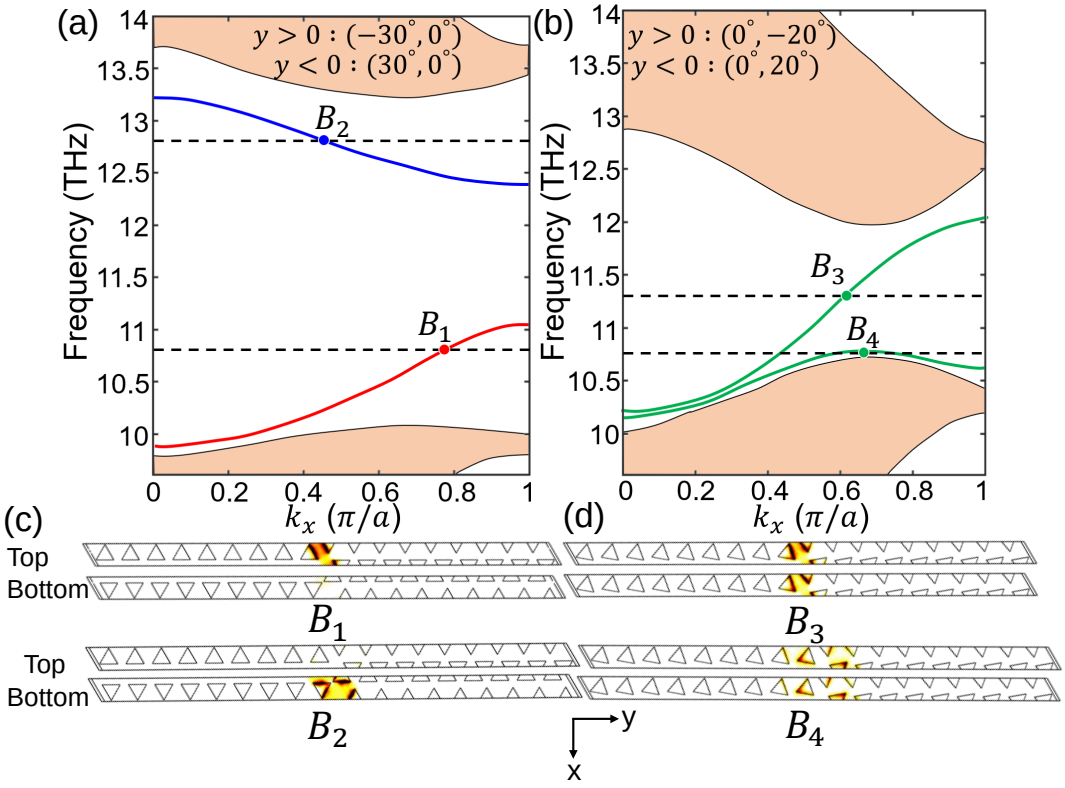

Figure 5.11: (a) Projected band (light orange) structure of the finite supercell by combining two halves of bilayer graphene triangular nanohole crystals with rotation angles $(-30°, 0°)$ and $(30°, 0°)$ in a mirror-symmetric manner, which exhibits a nonzero layer Chern number difference ($\Delta C_L = 2$) across the domain-wall interface. Two nontrivial topological modes localized in different graphene layers are marked by red and blue curves inside the nontrivial bandgap, respectively. (b) Projected band structure determined for finite supercell composed by two halves of bilayer graphene crystals of rotation angles $(0°, -20°)$ and $(0°, 20°)$ with nonzero valley Chern number difference $\Delta C_V = 2$ across the mirror-symmetric domain-wall interface, showing two topological valley modes (green) inside the nontrivial bandgap. (c) Field distribution of two layer-polarized topological modes corresponding to B_1 and B_2 points in (a). (d) Field distribution of two topological valley modes corresponding to B_3 and B_4 points in (b).

face. For the former configuration with nonzero layer Chern number, the bilayer graphene metasurface with -1 layer Chern number for $(30°, 0°)$ orientation of triangular hole and the system with 1 layer Chern number for $(-30°, 0°)$ orientation of triangular hole are placed together, which builds a mirror-symmetric domain-wall interface with $\Delta C_L = 2$. For the latter configuration with nonzero valley Chern number, the topological bilayer systems with ± 1 valley Chern number for $(0°, \pm 20°)$ orientations of triangular holes are utilized to construct a supercell with a mirror-

symmetric domain-wall interface with $\Delta C_V = 2$.

The projected band structures of the layer-polarized and valley-chirality-locking bilayer graphene metasurfaces have been computed numerically and are presented in Figs. 5.11(a) and 5.11(b), respectively. In these calculations we used a supercell with a number of 20 unit cells along the y-axis and periodic boundary conditions along the x-axis. The two domains with different orientations of triangular holes are placed along the y-axis and are mirror symmetric with respect to the x-axis. In Fig. 5.11(a) with $\Delta C_L = 2$, the light orange regions represent the projected bulk bands, whereas two topological modes are formed inside the nontrivial bandgap with opposite group velocities, as marked by red and blue curves. To investigate two topological modes with layer-polarized property, two points B_1 and B_2 of topological valley modes are chosen at the frequency of 10.8 THz and 12.8 THz, respectively. It can be seen in Fig. 5.11(c) that the field distribution of both modes is localized at the domain-wall interface; however, the optical field of B_1 is only confined at the top layer while the optical field of B_2 is confined at the bottom layer. Therefore, the bilayer graphene metasurface with nonzero layer Chern number exhibits layer-polarized topological edge modes with opposite group velocities, and the number of layer-polarized topological modes is equal to the layer Chern number difference across the domain-wall interface.

By contrast, the bilayer graphene metasurface with $\Delta C_V = 2$ possesses two topological valley modes with same group velocity in most of the k-space, as indicated by the green curves in Fig. 5.11(b). At the chosen frequencies of 10.8 THz and 11.3 THz, the electric field of the two topological valley modes (B_3 and B_4) are localized at the domain-wall interface and extended in both graphene layers (see Fig. 5.11(d)). Note that the domain-wall interface constructed by the two halves of bilayer system with $(0^\circ, \pm 20^\circ)$ is the same as the mirror operation of a topological valley system which could connect the valley Chern number between K and K' valleys, so that the domain-wall interfaces in both cases could support chirality-momentum-locked topological interface modes. As we will see later on, this idea has important implications on the nature of topological interface modes of metasur-

faces with more than two layers.

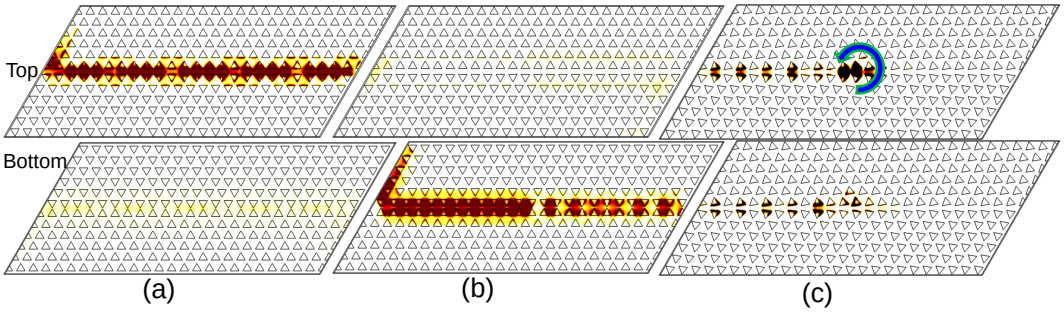

Figure 5.12: (a) Spatial field profile of a layer-polarized topological mode in the finite metasurface with a layer-Hall domain-wall interface, corresponding to B_1 at 10.8 THz in Fig. 5.11(a). (b) same as in (a), but corresponding to B_2 at 12.8 THz in Fig. 5.11(a). (c) Unidirectional field propagation along the negative direction of the x-axis, when the finite metasurface is excited by a right-circularly polarized source at frequency of 11.3 THz (B_3 in Fig. 5.11(b)).

Importantly, we also analyzed the layer-polarized and valley-chirality-locking characteristics of light propagation along the domain-wall interface of bilayer graphene metasurfaces, and the results are displayed in Fig. 5.12. To illustrate the layer-polarized topological light propagation in a finite bilayer graphene metasurface with $(\pm 30^\circ, 0^\circ)$ orientations of triangular holes, a RCP source is placed at the center of top and bottom layers, respectively, which is used to excite topological modes localized at different layers. As expected, when the source with a frequency of 10.8 THz is located at the center of the top graphene layer, the high confinement of electric field in the domain-wall interface of the top graphene layer is observed, as illustrated in Fig. 5.12(a). Similarly, as shown in Fig. 5.12(b), a RCP source with a frequency of 12.8 THz located at the bottom layer, excites the topological interface mode only confined at the domain-wall interface of the bottom layer. It should be noted that the layer-polarized topological modes excited by a RCP source propagate along both positive and negative x-axis, which indicates that the excited topological mode shows only layer-polarized property due to $\Delta C_L \neq 0$ and $\Delta C_V = 0$ across the domain-wall.

Differently, the light propagation in the finite metasurface with $(\pm 0^\circ, 20^\circ)$ triangular hole orientations between the domain-wall interface is indicated in Fig. 5.12(c). Under the excitation of a RCP source with a frequency of 11.3 THz located

at the top graphene layer, unidirectional propagation of light along the negative direction of the x-axis of the domain-wall interface is observed. Specifically, the light field of the topological mode extends at the domain-wall interface throughout both graphene layers and displays unidirectional propagation characteristics, which proves that the nonzero valley Chern number difference only results in the topological modes with valley-chirality-locking properties.

5.4 Three-layer Graphene Triangular Nanohole Crystals

In this section, a three-layer graphene triangular nanohole metasurface is investigated, and the corresponding effective Hamiltonian is derived by considering the interlayer coupling between any two layers, which will be verified by fitting the eigenfrequencies of the first six bands with results of COMSOL simulations. Importantly, there are three topological modes with two different characteristics (layer-polarized and chirality-momentum-locked) inside a nontrivial bandgap, which will be successfully explained by the layer Chern number and valley Chern number of the three-layer graphene metasurface.

5.4.1 Band Diagram of Three-layer Graphene Crystals

So far, we have explained the monolayer graphene nanohole crystal with reduced inversion symmetry, and bilayer graphene triangular nanohole metasurfaces with additional mirror symmetry breaking, which possess a nontrivial bandgap by rotating the triangular hole with respect to the hexagonal lattice. In order to investigate graphene systems with one more layer degree of freedom, a three-layer graphene triangular nanohole metasurface with a mirror-symmetric domain-wall interface composed by three-freestanding graphene layers has been studied as schematically shown in Fig. 5.13(a). The top and bird's eye views of its geometrical configuration are presented in Figs. 5.13(b) and 5.13(c), respectively. It consists of a periodic hexagonal lattice of triangular holes with lattice constant a, with the unit cell in each layer containing a triangular hole with orientation $\theta_{1,2,3}$ with respect to the lat-

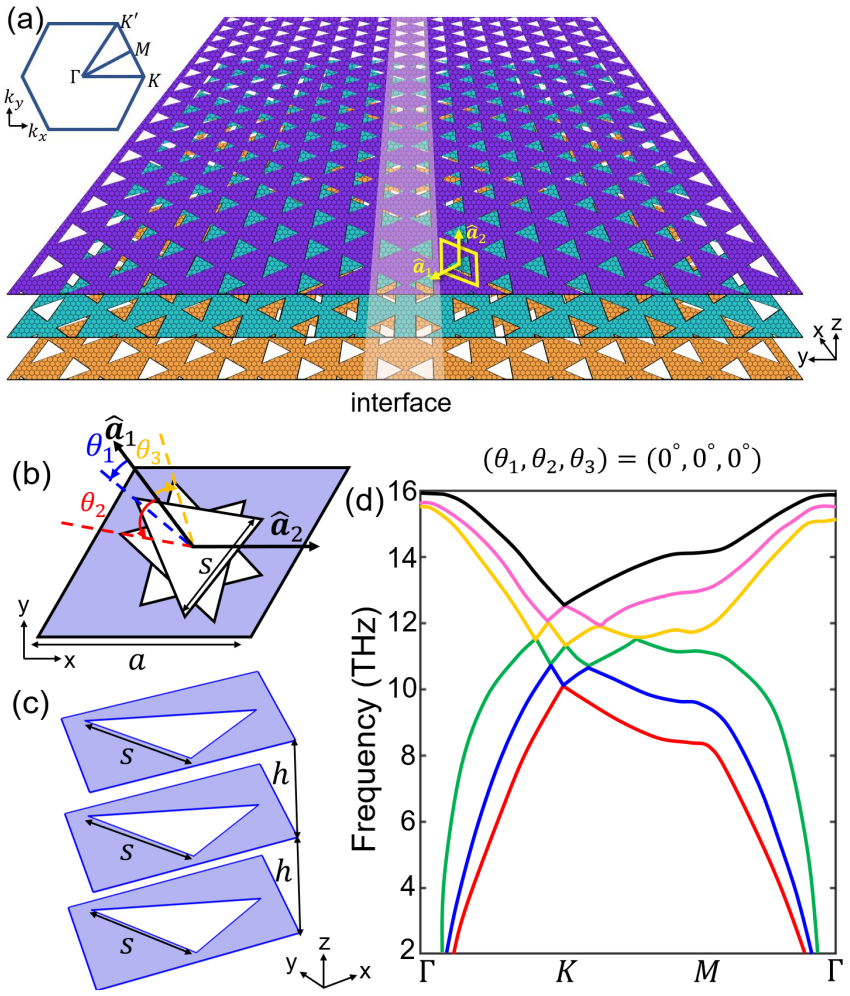

Figure 5.13: (a) Schematic of the three-layer graphene metasurface plasmonic waveguide with a mirror-symmetric domain-wall interface oriented along the x-axis. (b) Top view of unit cell of the three-layer graphene metasurfaces with lattice constant a, of which each layer is composed of a regular triangular nanohole with same sidelength s. The rotation angles of triangular holes in the unit cell from top to bottom layers with respect to the hexagonal lattice are θ_1, θ_2, and θ_3, respectively. (c) Bird's eye view of the unit cell with a separation distance, h, between the two adjacent layers. (d) Bulk band diagram of the infinite three-layer graphene triangular nanohole crystal with orientations of three triangular holes along the direction of lattice vector with $\theta_{1,2,3} = 0^\circ$. By introducing the interlayer coupling between three layers, the symmetry-protected three-layer graphene crystal possesses three frequency-shifted Dirac cones at K point, and the first six bands are depicted in red, blue, green, yellow, magenta, and black, respectively.

tice vector $\boldsymbol{a_1}$. Specifically, we fix the lattice constant $a = 500\,\text{nm}$, the sidelength of triangular nanohole $s = 200\,\text{nm}$, and the separation distance between two adjacent layers $h = 200\,\text{nm}$.

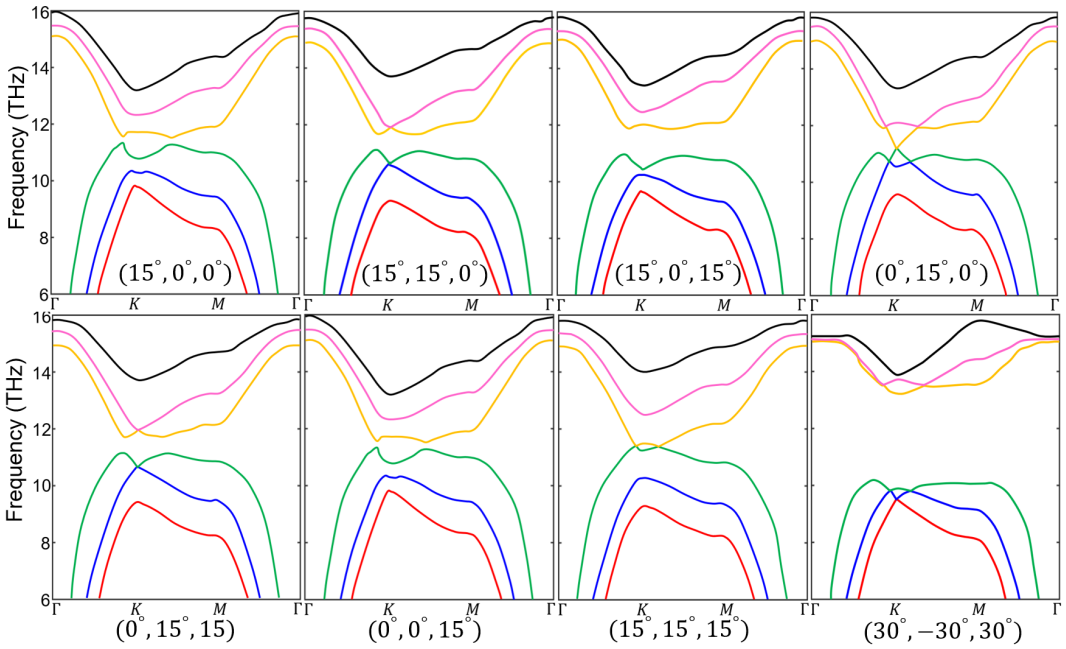

Figure 5.14: First six bulk bands of three-layer graphene triangular nanohole crystals, calculated for various rotation angles $(\theta_1, \theta_2, \theta_3)$ of triangular holes. The inversion symmetry reduction or mirror symmetry breaking results in nontrivial frequency bandgaps between the third and fourth bands.

We show in Fig. 5.13(d) the bulk band structure of the first six bands along the high-symmetry points in the hexagonal FBZ. Without the perturbation of the rotation of triangular holes, the three-layer graphene crystal exhibits three symmetry-protected Dirac cones at the K point. When the interlayer coupling is introduced with the separation distance $h = 200\,\text{nm}$ between any two layers, the Dirac cone of each layer is split along the frequency-axis. Interestingly, the higher and lower Dirac frequencies are symmetric with respect to the middle Dirac frequency at the K point.

To properly identify the frequency band gap when the three-layer graphene system is perturbed by rotating triangular holes so as to reduce the inversion symmetry or break the mirror symmetry, the variation of the first six bulk bands determined for specific orientations $(\theta_1, \theta_2, \theta_3)$ of three triangular holes are presented in Fig. 5.14. For the mirror-symmetric three-layer graphene system for which only the inversion symmetry is reduced ($\theta_1 = \theta_2 = \theta_3 \neq 0°$), three frequency bandgaps emerge around three Dirac points, the size of each increasing with the increment of

rotation angles (see $(15^\circ, 15^\circ, 15^\circ)$ in Fig. 5.14). Hence, a common nontrivial frequency band of the three-layer graphene crystal can appear when the rotation angle reaches a threshold value of 15°.

When aiming to break the mirror symmetry, only the triangular holes in one layer or two layers are rotated by 15°. For the former case, the band diagrams of triangular holes being rotated in top $(15^\circ, 0^\circ, 0^\circ)$ or bottom $(0^\circ, 0^\circ, 15^\circ)$ layers are same and exhibit a narrow bandgap between the third and fourth bands. However, with the $(0^\circ, 15^\circ, 0^\circ)$ orientation of triangular nanohole in the middle layer, the top and bottom layers are still mirror-symmetric and thus preserve one mirror-symmetry-protected Dirac cone at K point, which is independent of the orientation of the triangular holes in the middle layer. When the triangular holes in any two layers are rotated, the band diagram of the lower three bands shows two degenerate bands and one non-degenerate band, and the frequency bandgap between the third and fourth bands is nontrivial. In addition, the maximum frequency bandgap appears for the $(30^\circ, -30^\circ, 30^\circ)$ orientation, in which the relative rotation angle between triangular holes in two adjacent layers reaches the largest possible value of 60°.

Since the three-layer graphene triangular nanohole crystal possesses nontrivial bandgap when its inversion-symmetry or mirror-symmetry is broken, the orientation of energy flow of bulk valley modes in these two typical cases are further investigated, and the results are presented in Fig. 5.15. The three-layer graphene crystal with reduced inversion symmetry via rotating the triangular holes by $(20^\circ, 20^\circ, 20^\circ)$ exhibits three non-degenerate bands below the nontrivial bandgap. To be more specific, in Fig. 5.15(a), the three bulk valley modes are labelled D_1, D_2, and D_3, and each of them has an intrinsic LCP vorticity marked by a clockwise-oriented red arrow. In particular, the electric fields of bulk valley modes D_1 and D_3 are confined around the triangular holes and spread through all three layers, whereas the electric field of D_2 is mostly located at the top and bottom layers, and thus can be viewed as a layer-polarized mode.

When the mirror-symmetry of the three-layer graphene crystals is broken by

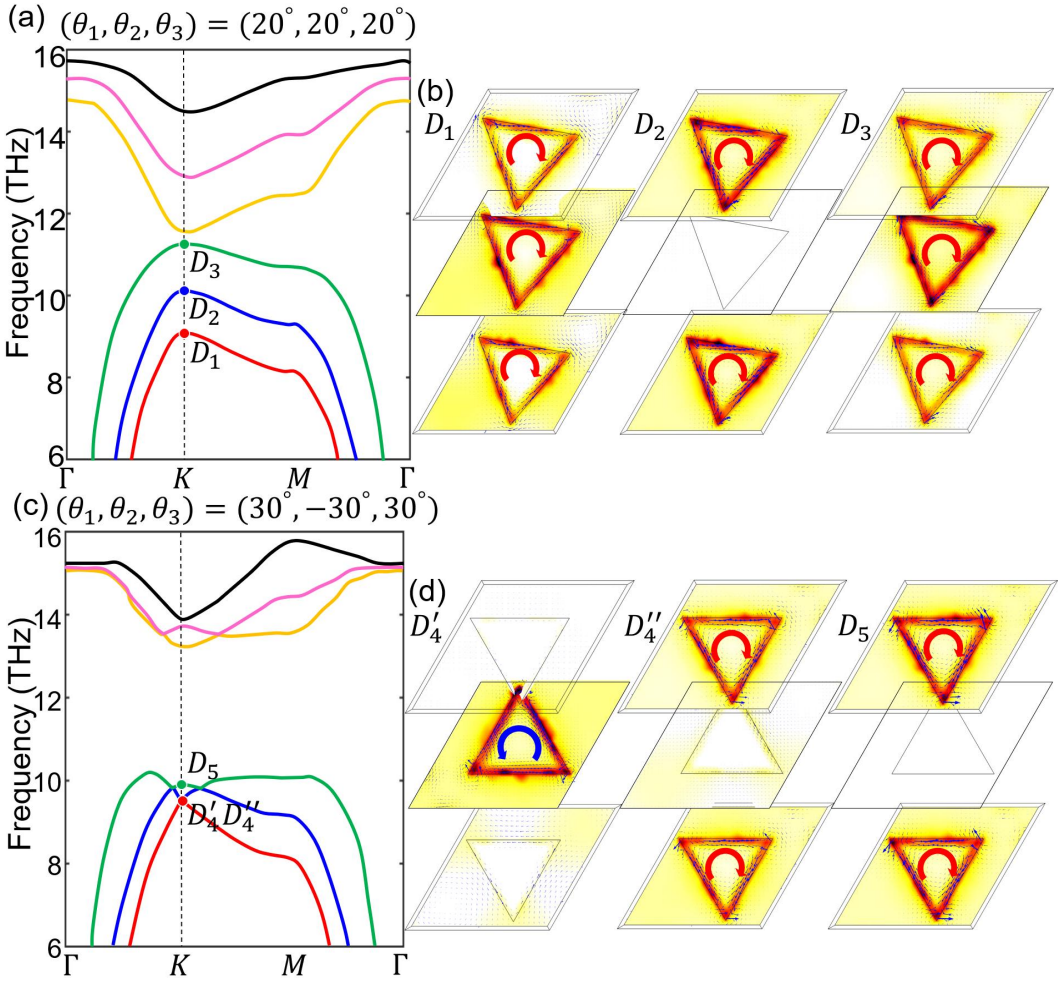

Figure 5.15: (a) First six non-degenerate bulk bands of three-layer graphene triangular nanohole crystals with orientations of three triangular holes $(\theta_1, \theta_2, \theta_3) = (20^\circ, 20^\circ, 20^\circ)$. (b) From the left to right panel, electric fields and Poynting vector distributions of the first three non-degenerate bands at K point correspond to points D_1, D_2, and D_3 in (a), respectively. The red arrows represent LCP energy flow. (c) Band structure of three-layer graphene triangular nanohole crystals with orientations of three triangular holes $(\theta_1, \theta_2, \theta_3) = (30^\circ, -30^\circ, 30^\circ)$. Two bands marked by red and blue curves are degenerate at K point. (d) From the left to right panel, electric fields and Poynting vector distributions of the two degenerate bands and another non-degenerate band at K point correspond to points D_4', D_4'', and D_5 in (c), respectively. The blue arrow represents a RCP energy flow.

relatively rotating the triangular holes in two adjacent graphene layers, the system exhibits the largest nontrivial bandgap with $(30^\circ, -30^\circ, 30^\circ)$ orientations of triangular holes (see Fig. 5.15(c)), in which the lower two bands (D_4' and D_4'') are degenerate at K point. In addition, we present in Fig. 5.15(d) the energy flows of the corresponding first three bands (D_4', D_4'' and D_5) at K point. Interestingly, the elec-

tric field of bulk valley modes from left to right panels is only confined around the triangular holes at the middle or top and bottom layers with layer-polarized characteristics, from which one can see that the intrinsic vorticities of the two degenerate bulk modes at K point are opposite. Moreover, by comparing two similar electric fields of points D_4'' and D_5, the field of D_4'' located at the middle layer is the radiation of the field at the top and bottom layers while there is no optical field in the middle layer of D_5. In this way, the eigenmodes D_4', D_4'', and D_5 can be regarded as the modes of the middle layer, and a symmetric and antisymmetric superpositions of modes of top and bottom layers, respectively.

5.4.2 Effective Hamiltonian of Three-layer Graphene Crystals

To quantitatively describe the topological properties of three-layer graphene metasurfaces with triangular holes, an effective Hamiltonian of this photonic system is constructed. In this process, the challenging part is to define the interlayer coupling for the three layers. First, for the unperturbed three-layer graphene metasurfaces with zero rotation angle ($\theta_{1,2,3} = 0$) of triangular holes in each layer, the symmetry protection leads to the formation of three nonequivalent Dirac cones and six-fold degeneracy of valley states at the K point. Therefore, six eigenstates of the three-layer graphene metasurfaces are chosen as the basis, $\{\psi_{p_1^-}, \psi_{q_1^+}, \psi_{p_2^-}, \psi_{q_2^+}, \psi_{p_3^-}, \psi_{q_3^+}\}$. When the interlayer coupling is not considered, the 6 by 6 Hamiltonian H_u^t of three-layer graphene metasurfaces with triangular hole is the sum of monolayer Hamiltonians in Eq. (5.2) for three layers,

$$\delta H_u^t = \bigoplus_{i=1}^{3} \begin{pmatrix} 2\vartheta\omega_D\theta_i & 2\omega_D v_D(\delta k_x - i\delta k_y) \\ 2\omega_D v_D(\delta k_x + i\delta k_y) & -2\vartheta\omega_D\theta_i \end{pmatrix} \tag{5.10}$$

where all the elements without interlayer coupling are the diagonal term of the 6×6 Hamiltonian. To properly investigate the interlayer coupling among three layers, all off-diagonal entries are estimated based on Eq. (5.5). For the bilayer graphene system, the off-diagonal entries for interlayer coupling Hamiltonian with coupling strength ω_{SA} are defined as $\begin{pmatrix} 2\omega_D\omega_{SA} & 0 \\ 0 & 2\omega_D\omega_{SA} \end{pmatrix}$.

Therefore, when a third layer is introduced into the bilayer system with the same separation distance, the coupling between top and middle layers, and between middle and bottom layers remain unchanged with the same coupling strength ω_{SA}. In this way, the interlayer coupling term for the top and middle layers, middle and bottom layers can be defined as the off-diagonal of $\begin{pmatrix} 2\vartheta\omega_D\theta_1 & 2\omega_D v_D(k_x - ik_y) \\ 2\omega_D v_D(k_x + ik_y) & -2\vartheta\omega_D\theta_1 \end{pmatrix} \oplus \begin{pmatrix} 2\vartheta\omega_D\theta_2 & 2\omega_D v_D(k_x - ik_y) \\ 2\omega_D v_D(k_x + ik_y) & -2\vartheta\omega_D\theta_2 \end{pmatrix}$ and $\begin{pmatrix} 2\vartheta\omega_D\theta_2 & 2\omega_D v_D(k_x - ik_y) \\ 2\omega_D v_D(k_x + ik_y) & -2\vartheta\omega_D\theta_2 \end{pmatrix} \oplus \begin{pmatrix} 2\vartheta\omega_D\theta_3 & 2\omega_D v_D(k_x - ik_y) \\ 2\omega_D v_D(k_x + ik_y) & -2\vartheta\omega_D\theta_3 \end{pmatrix}$ with the same coupling strength, respectively. Importantly, the interlayer coupling term between the top and bottom layer is proposed in the off-diagonal between the first and third layers of Eq. (5.10) with a different and smaller coupling strength ω'_{SA}. In this way, the interlayer coupling Hamiltonian for three-layer graphene metasurfaces becomes,

$$\delta H_c^t = \begin{pmatrix} 0 & 0 & 2\omega_D\omega_{SA} & 0 & 2\omega_D\omega'_{SA} & 0 \\ 0 & 0 & 0 & 2\omega_D\omega_{SA} & 0 & 2\omega_D\omega'_{SA} \\ 2\omega_D\omega_{SA} & 0 & 0 & 0 & 2\omega_D\omega_{SA} & 0 \\ 0 & 2\omega_D\omega_{SA} & 0 & 0 & 0 & 2\omega_D\omega_{SA} \\ 2\omega_D\omega'_{SA} & 0 & 2\omega_D\omega_{SA} & 0 & 0 & 0 \\ 0 & 2\omega_D\omega'_{SA} & 0 & 2\omega_D\omega_{SA} & 0 & 0 \end{pmatrix} \tag{5.11}$$

where the coupling strength between any two layers is expressed as the off-diagonal terms of the corresponding Hamiltonian. Coupling strengths ω_{SA} and ω'_{SA} can be numerically extracted. By combining Eqs. (5.10) and (5.11), the perturbed effective

Hamiltonian of three-layer graphene metasurfaces can be obtained,

$$\delta H^t = \frac{\delta H_u^t + \delta H_c^t}{2\omega_D} = \begin{pmatrix} \vartheta\theta_1 & v_D(\delta k_x - i\delta k_y) & \omega_{SA} & 0 & \omega'_{SA} & 0 \\ v_D(\delta k_x + i\delta k_y) & -\vartheta\theta_1 & 0 & \omega_{SA} & 0 & \omega'_{SA} \\ \omega_{SA} & 0 & \vartheta\theta_2 & v_D(\delta k_x - i\delta k_y) & \omega_{SA} & 0 \\ 0 & \omega_{SA} & v_D(\delta k_x + i\delta k_y) & -\vartheta\theta_2 & 0 & \omega_{SA} \\ \omega'_{SA} & 0 & \omega_{SA} & 0 & \vartheta\theta_3 & v_D(\delta k_x - i\delta k_y) \\ 0 & \omega'_{SA} & 0 & \omega_{SA} & v_D(\delta k_x + i\delta k_y) & -\vartheta\theta_3 \end{pmatrix} \tag{5.12}$$

Utilizing the Pauli matrices, it can be rewritten as,

$$\delta H^t = v_D s_0 \otimes (\delta k_x \sigma_x + \delta k_y \sigma_y) + \vartheta(\alpha s_z + \beta s_0 + \gamma s_d) \otimes \sigma_z + \omega_{SA} s_x \otimes \sigma_0 + \omega'_{SA} s_{ad} \otimes \sigma_0 \tag{5.13}$$

where s_i and σ_i ($i = 0, x, y, z$) are 3×3 and 2×2 Pauli matrices indicating the layered pseudospin and orbital degree of freedoms, respectively. The diagonal spin matrix s_d is defined as $\begin{pmatrix} 1 & 0 & 0 \\ 0 & 0 & 0 \\ 0 & 0 & 1 \end{pmatrix}$ and an anti-diagonal spin matrix s_{ad} is $\begin{pmatrix} 0 & 0 & 1 \\ 0 & 0 & 0 \\ 1 & 0 & 0 \end{pmatrix}$. To simplify the notation, the rotation angle of triangular holes in the top (θ_1), middle (θ_2), and bottom (θ_3) layers are represented by $\alpha+\beta+\gamma$, β, and $-\alpha+\beta+\gamma$, respectively, with 2α being the relative angles between triangular holes of top and bottom layers, and $\pm\alpha+\gamma$ being the relative angles of triangular holes in top and bottom layers with respect to the middle layer. Note that, because the interlayer coupling between the top and bottom layers is different from the coupling to the middle layer, the new interlayer coupling term between the top and bottom layers is added at the end of Eq. (5.13).

By solving the eigenvalue matrix equation $\delta H^t \phi_i = \delta\omega_i \phi_i$ with $i = 1,2,3,4,5,6$, we obtained the frequency dispersion relation of eigenfrequencies and corresponding eigenstates for the first six bands. Then, for various orientations of triangular holes in three-layer graphene metasurfaces, the parameters,

slope of the frequency dispersion curve around the Dirac point $v_D = 4.09$, angular coefficient $\vartheta = 4.03\,\mathrm{deg}^{-1}$, interlayer coupling strength between two adjacent layers $\omega_{SA} = -0.8494$, and coupling strength between top and bottom layers $\omega'_{SA} = 0.0646$, are extracted by fitting the eigenfrequencies around K valley with computed band diagrams from the COMSOL simulations in Fig. 5.14. By comparing the angular coefficient ϑ and interlayer coupling strength between two adjacent layers ω_{SA} of bilayer and three-layer graphene metasurfaces, one can conclude that these two parameters are almost unchanged with the introduction of the additional third layer in the layered system with same lattice constant, triangular hole and separation distance. Moreover, the interlayer coupling strength ω'_{SA} between the top and bottom layers is 10 orders of magnitude smaller than the interlayer coupling ω_{SA} between two adjacent layers.

Figure 5.16 presents the frequency dispersion bands around K point, calculated for various orientations of triangular holes in three-layer graphene metasurfaces by using the effective Hamiltonian (blue curves) with extracted parameters and full-wave COMSOL simulations (red dotted curves), respectively. The x-axis represents the wave vector difference with respect to the K point, whereas the frequency difference relative to the mean Dirac frequency of 11.29 THz is plotted on the y-axis. The good agreement between eigenfrequencies of derived Hamiltonian and the COMSOL simulations around K valley validates the effectiveness of perturbed Hamiltonian for three-layer graphene metasurfaces, even in the cases with reduced inversion symmetry or broken mirror-symmetry.

Since the topological modes in three-layer graphene triangular nanohole metasurfaces show layer-polarized characteristics under the reduced inversion symmetry and mirror-symmetry breaking, the eigenstates $\{\phi_1, \phi_2, \phi_3\}$ of the lower three bands can be regrouped into three new eigenstates $\{\psi_0, \psi_+, \psi_-\}$ based on a layer operator $L = \begin{pmatrix} 0 & 0 & 1 \\ 0 & 0 & 0 \\ 1 & 0 & 0 \end{pmatrix} \otimes I_2$ with I_2 being a 2×2 identity matrix that can represent the field confinement in middle layer with eigenvector as $(0,1,0)^T$ and symmetric and antisymmetric supermodes in top and bottom layers with eigenvectors as $(1,0,1)^T$ and

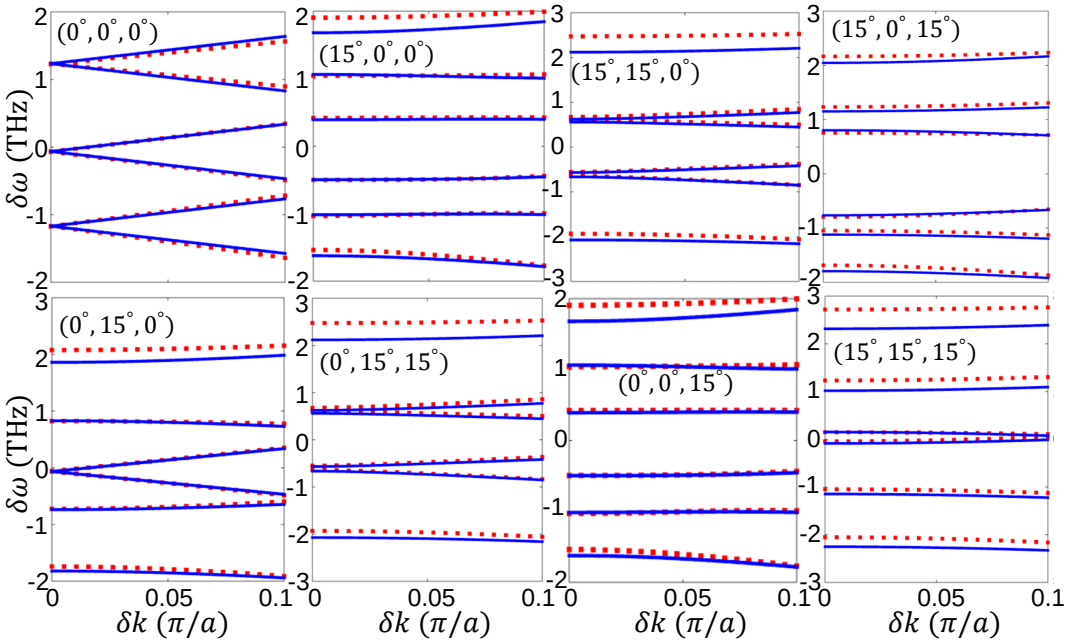

Figure 5.16: Detailed band structure along the k vector difference δk with respect to the K-point, determined for specific orientations $(\theta_1,\theta_2,\theta_3)$ of triangular holes in three-layer graphene metasurfaces. $\delta\omega$ corresponds to the frequency difference of the first six bands with respect to the mean Dirac frequency at 11.29 THz. The blue solid and red dotted curves represent $\delta\omega$ calculated by effective perturbed 6×6 Hamiltonian and COMSOL simulations, respectively.

$(1,0,-1)^T$, respectively. For three eigenvectors below the bandgap, ϕ_1 is an eigenvector corresponding to the field confinement in the middle layer, whereas ϕ_2 and ϕ_3 correspond to symmetric and antisymmetric superpositions of modes confined in the top and bottom layers, respectively. By expressing the layer operator L in the basis of eigenstates of lower three bands $\{\phi_1,\phi_2,\phi_3\}$, the 3×3 matrix representation of layer operator becomes,

$$\langle\phi_i|L|\phi_j\rangle = \begin{pmatrix} \langle\phi_1|L|\phi_1\rangle & \langle\phi_1|L|\phi_2\rangle & \langle\phi_1|L|\phi_3\rangle \\ \langle\phi_2|L|\phi_1\rangle & \langle\phi_2|L|\phi_2\rangle & \langle\phi_2|L|\phi_3\rangle \\ \langle\phi_3|L|\phi_1\rangle & \langle\phi_3|L|\phi_2\rangle & \langle\phi_3|L|\phi_3\rangle \end{pmatrix} = \begin{pmatrix} c & 0 & t \\ 0 & m & 0 \\ t & 0 & u \end{pmatrix} \tag{5.14}$$

where $\langle\phi_1|L|\phi_2\rangle = \langle\phi_2|L|\phi_1\rangle = \langle\phi_2|L|\phi_3\rangle = \langle\phi_3|L|\phi_2\rangle < 10^{-4} = 0$ is obtained by our computational method. The eigenvalues of this matrix are $\{m, \frac{c+u-\sqrt{c^2+4t^2-2cu+u^2}}{2}, \frac{c+u+\sqrt{c^2+4t^2-2cu+u^2}}{2}\}$ with eigenstates $(0,1,0)^T$,

$(\frac{-c+u+\sqrt{c^2+4t^2-2cu+u^2}}{-2t},0,1)^T$, and $(\frac{-c+u-\sqrt{c^2+4t^2-2cu+u^2}}{-2t},0,1)^T$, respectively. By considering middle (ϕ_1), symmetric (ϕ_2), and antisymmetric (ϕ_3) layer-polarized eigenmodes as $(0,1,0)^T$, $(1,0,1)^T$, and $(1,0,-1)^T$, one can obtain the regrouped eigenstates as,

$$\psi_0 = \phi_1, \tag{5.15}$$

$$\psi_+ = \frac{-c+u-2t+\sqrt{c^2+4t^2-2cu+u^2}}{-4t}\phi_2 + \frac{-c+u+2t+\sqrt{c^2+4t^2-2cu+u^2}}{-4t}\phi_3, \tag{5.16}$$

$$\psi_- = \frac{-c+u-2t-\sqrt{c^2+4t^2-2cu+u^2}}{-4t}\phi_2 + \frac{-c+u+2t-\sqrt{c^2+4t^2-2cu+u^2}}{-4t}\phi_3, \tag{5.17}$$

Three types of Berry curvature and corresponding quantized topological invariants could be computational calculated based on the regrouped layer-polarized basis $\{\psi_0,\psi_+,\psi_-\}$. We show in Fig. 5.17 the Berry curvature distribution around K valley for three-layer graphene system with $\pm(20^\circ,20^\circ,20^\circ)$ orientations of triangular holes. Three types of Berry curvatures of the system with $(20^\circ,20^\circ,20^\circ)$ orientations show a maximum at K point indicating $C_0 = C_+ = C_- = 0.5$ valley

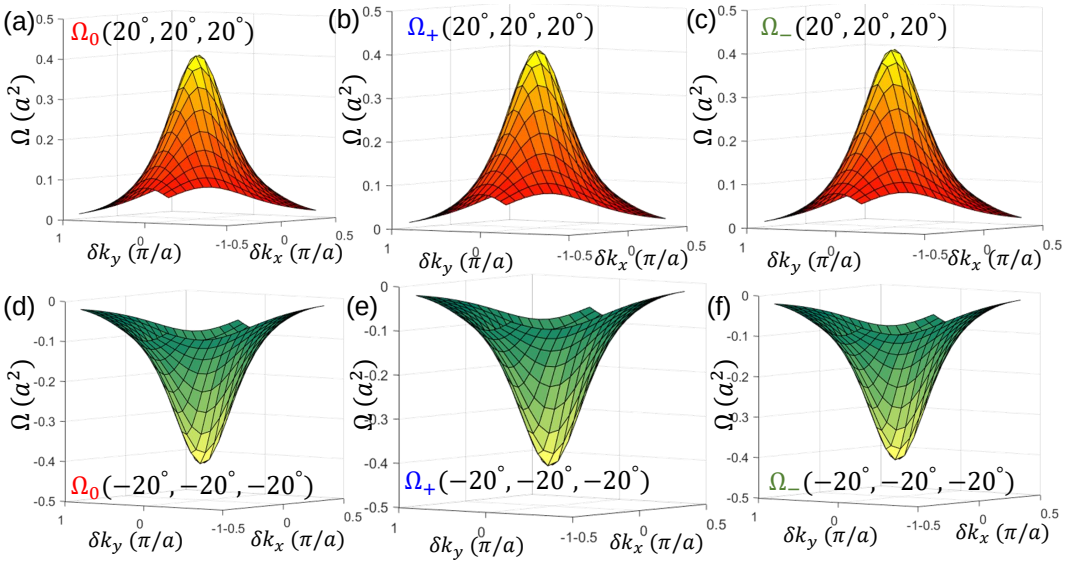

Figure 5.17: Layer-polarized Berry curvature Ω distribution over the K valley computed by the regrouped eigenstate basis ψ_0, ψ_+, and ψ_-. Notations 0, $+$, and $-$ correspond to eigenmodes localized in the middle layer, symmetric, and anti-symmetric supermodes, respectively. (a)-(c) for orientations of triangular holes $(\theta_1,\theta_2,\theta_3) = (20^\circ,20^\circ,20^\circ)$. (d)-(f) Mirror-symmetric to (a)-(c), for orientations of triangular holes $(\theta_1,\theta_2,\theta_3) = (-20^\circ,-20^\circ,-20^\circ)$.

Chern numbers, while the Berry curvature of layer-polarized valley Chern number of the system with $(-20°,-20°,-20°)$ orientations presents a minimum at the K point ($C_0 = C_+ = C_- = -0.5$). Additionally, the sign of valley Chern number is consistent with the intrinsic chiral vorticity of the light flow in Fig. 5.15(b). Specifically, the positive and negative Chern numbers correspond to LCP and RCP energy flows, respectively.

For the three-layer graphene system with $\pm(30°,-30°,30°)$ orientations of triangular holes with mirror symmetry breaking between two adjacent layers, the Berry curvature distribution calculated by $\{\psi_0,\psi_+,\psi_-\}$ around K valley are given in Fig. 5.18. Based on the sign of the calculated topological invariants, the quantized topological invariants for the system with triangular hole orientation along $(30°,-30°,30°)$ are $-C_0 = C_+ = C_- = 0.5$, while the quantized topological invariant for triangular hole orientation $(-30°,30°,-30°)$ have opposite values as compared to the former case, namely $C_0 = -C_+ = -C_- = 0.5$.

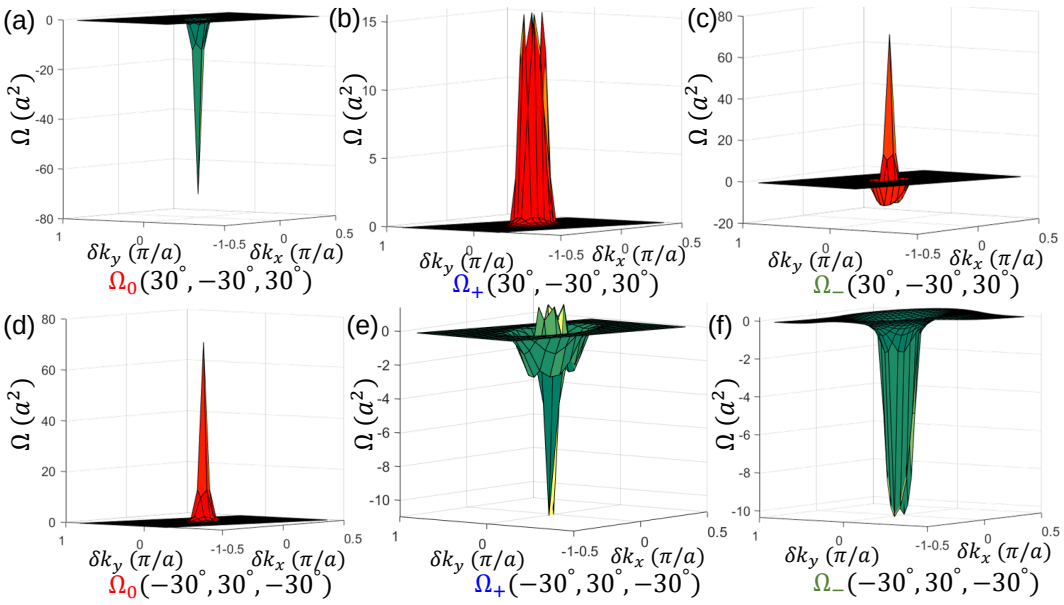

Figure 5.18: Similar to Fig. 5.17, but for two mirror-symmetric specific orientations of three triangular holes. (a)-(c) $(\theta_1,\theta_2,\theta_3) = (30°,-30°,30°)$ and (d)-(f) $(\theta_1,\theta_2,\theta_3) = (-30°,30°,-30°)$.

As a consequence, a layer Chern number and a valley Chern number for the three-layer graphene metasurfaces can be defined, which should represent the number of layer-polarized and valley-chirality-locked topological modes, respec-

tively. As it is well-known, valley Chern number in this three-layer topological system with chirality features is the sum of Chern number below the bandgap, $C_V = C_0 + C_+ + C_-$. Furthermore, the layer Chern number of the three-layer graphene nanohole metasurface is defined, and indicating the number of layer-polarized topological modes as $C_L = C_0 - C_+ - C_-$.

5.4.3 Layer-polarized and Chirality-momentum-locked Topological Modes in Three-layer Graphene Metasurfaces

Since the number of topological modes inside the nontrivial bandgap should be equal to the defined Chern numbers ΔC_L and ΔC_V across the domain-wall interface, the projected band diagrams of a finite three-layer graphene metasurface with inversion-symmetry reduction and mirror symmetry breaking have been computed. This would allows us to validate our definition of the layer and valley Chern numbers.

Consequently, a supercell with 20 unit cells along the y-axis is composed by combing two halves of three-layer graphene supercells with $\pm(20^\circ, 20^\circ, 20^\circ)$ triangular hole orientations in a mirror-symmetric manner, which forms a domain-wall interface with layer Chern number difference $\Delta C_L = 1$ and valley Chern number difference $\Delta C_V = 3$. This means that there should be three valley-chirality-locked topological modes and one layer-polarized topological mode inside the bandgap. We present in Fig. 5.19(a) the projected band diagram of this configuration. In this figure, the orange regions represent the bulk states, and three topological modes can be seen inside the nontrivial bandgap. To gain deeper physical insights into the properties of three topological modes, their field distributions corresponding to three points marked in Fig. 5.19(a) have been investigated, and the results are shown in Fig. 5.19(b). The field distribution of the topological mode T_1 and T_3, are highly confined at the domain-wall interface and dispersed throughout the three layers, whereas the field distribution of the topological mode T_2 is only confined at the domain-wall interface, at the top and bottom layers. To be more specific, the symmetry property of the topological mode T_2 is illustrated in Fig. 5.19(c). For all three components of the electric field, the spatial distribution of T_2 located in the

top layer is opposite to that in the bottom layer, which proves the anti-symmetric property of topological mode T_2 marked by blue curves in Fig. 5.19(a).

In addition, we show in Fig. 5.20(a) the projected band diagram for a three-layer graphene supercell under the breaking of mirror symmetry, which is constructed by two three-layer graphene metasurfaces with $\pm(30°, -30°, 30°)$ rotation angles of triangular holes in a mirror-symmetric manner. This configuration exhibits layer Chern number difference $\Delta C_L = 3$ and valley Chern number difference $\Delta C_V = 1$ across the domain-wall interface. As expected, three topological modes emerge inside the nontrivial bandgap. To distinguish the optical property of the three topological modes, we show in Fig. 5.20(b) from top to bottom panels the spatial field distribution of three topological eigenmodes marked by T_4, T_5, and T_6 in Fig. 5.20(a), respectively. In this figure, all three topological modes localized

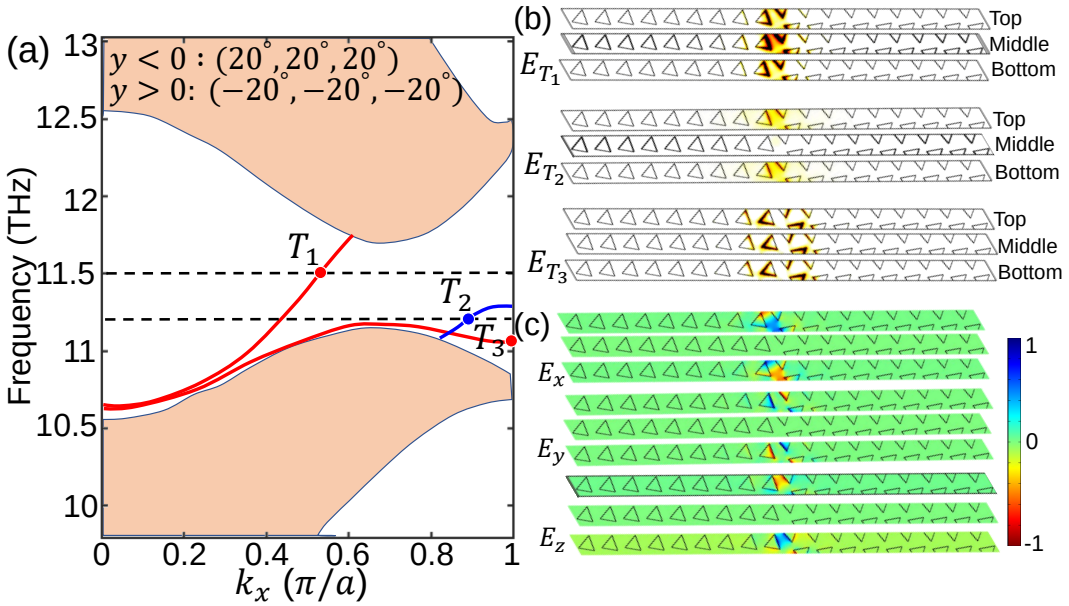

Figure 5.19: (a) Projected band (orange) structure of the finite supercell by combining two halves of three-layer graphene triangular nanohole crystals with rotation angles $(20°, 20°, 20°)$ and $(-20°, -20°, -20°)$ in a mirror-symmetric manner, which exhibits nonzero layer Chern number difference ($\Delta C_L = 1$) and nonzero valley Chern number difference ($\Delta C_V = 3$) across the domain-wall interface. Two topological valley modes without layer-polarized property inside the nontrivial bandgap are marked by red curves while the layer-polarized topological valley mode is depicted in blue. (b) Field distribution of three topological valley modes corresponding to T_1, T_2, and T_3 points in (a). (c) Spatial distribution of the E_x, E_y, and E_z components of the anti-symmetric topological valley modes T_2 in (a).

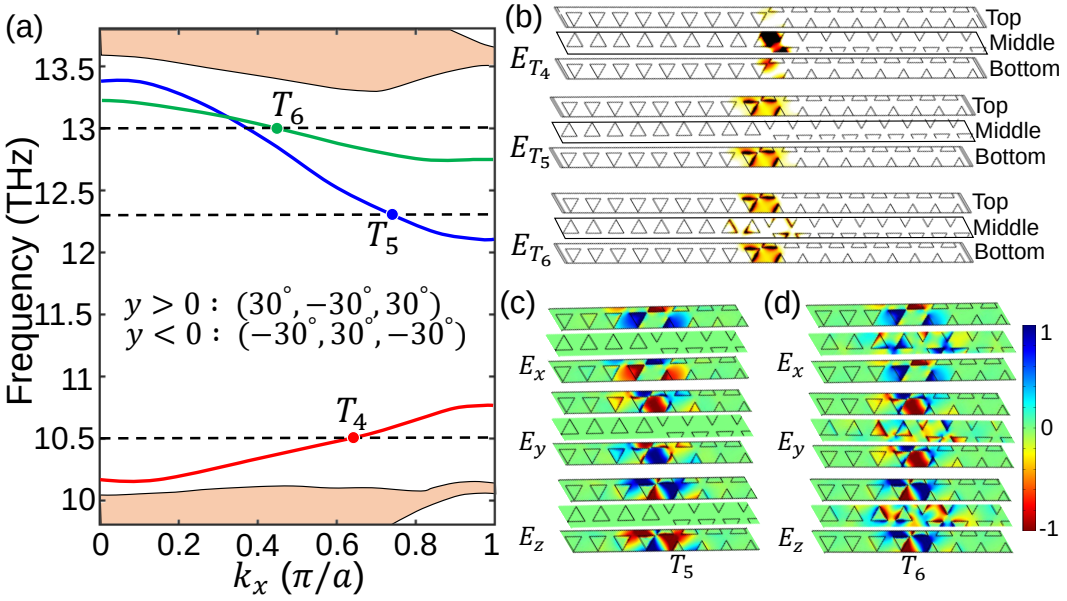

Figure 5.20: (a) Projected band diagram of the finite supercell with a mirror-symmetric domain-wall interface ($\Delta C_L = 3$ and $\Delta C_V = 1$), which is constructed by two three-layer graphene triangular nanohole crystals with rotation angles $(30^\circ, -30^\circ, 30^\circ)$ and $(-30^\circ, 30^\circ, -30^\circ)$. The red, blue, and green curves represent the middle-layer, anti-symmetric, and symmetric topological layer-polarized modes, respectively. (b) Field distribution of three layer-polarized topological modes corresponding to T_4, T_5, and T_6 points in (a). Spatial distribution of the E_x, E_y, and E_z components of the anti-symmetric topological supermode T_5 (c), and the symmetric topological supermode T_6 (d).

at the domain-wall interface show layer-polarized properties. Specifically, the field distribution of T_4 shows high confinement in the middle layer whereas the optical fields of T_5 and T_6 are highly confined at the top and bottom layers. We further show in Figs. 5.20(c) and 5.20(d) the spatial distribution of the topological modes T_5 and T_6 in three electric field components, respectively. As can be seen, for all three field components, the fields of T_5 are anti-symmetric with respect to the top and bottom layers whereas the fields of T_6 are symmetric with respect to these layers. In this way, this graphene system possesses three topological modes with middle-, antisymmetric- and symmetric-layer-polarized properties, as marked by red, blue, and green curves in Fig. 5.20(a), respectively.

Since the layer-polarized characteristics can be observed from the field distribution of the eigenmode, the light propagation of all topological modes in the finite three-layer graphene metasurfaces has been investigated in order to better under-

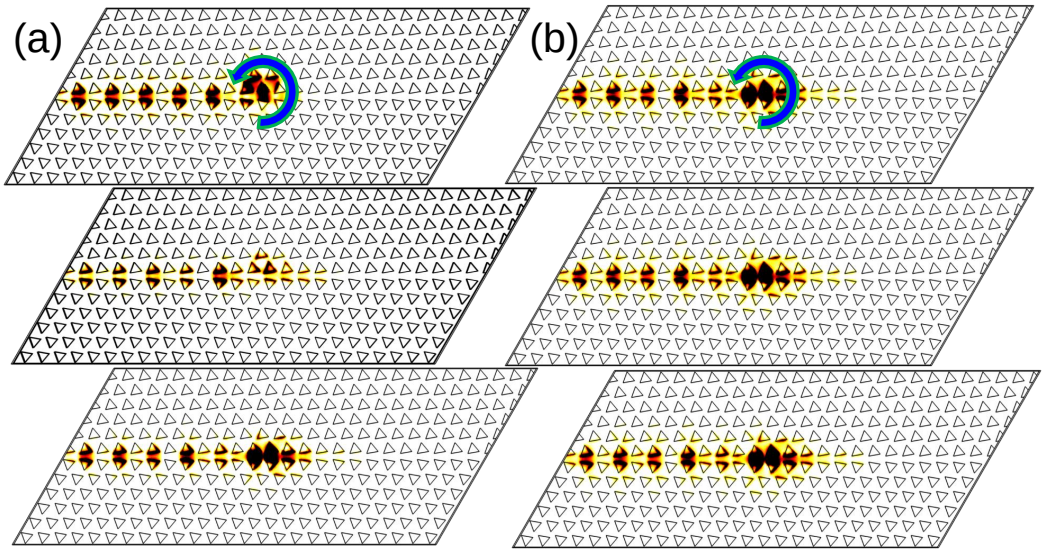

Figure 5.21: (a) Unidirectional field propagation along the negative direction of the x-axis, when a right-circularly polarized source at frequency of 11.2 THz is placed at the top layer of finite three-layer graphene metasurface with triangular hole orientations $(20^\circ, 20^\circ, 20^\circ)$ and $(-20^\circ, -20^\circ, -20^\circ)$. (b) The same as in (a), but for the excitation frequency at 11.5 THz.

stand the valley-chirality-locking property of the topological modes. A monochromatic RCP excitation source is placed at the center of the graphene layer, which is utilized to excite topological modes along the negative x-axis of domain-wall interface with negative group velocity. More specifically, we present in Fig. 5.21 the unidirectional character of light propagation along the domain-wall interface of three-layer graphene waveguide with $\pm(20^\circ, 20^\circ, 20^\circ)$ triangular hole orientations. At the frequency of 11.2 THz, a RCP light source placed at the center of the top layer of the three-layer graphene metasurface, excites unidirectional light propagation of topological mode along the negative x-axis of the domain-wall interface in the three layers (see Fig. 5.21(a)), which is the mixed optical field of red and blue topological bands at the lower dotted frequency line in Fig. 5.19(a). Since the topological mode depicted in blue is antisymmetric-layer-polarized at the top and bottom layers, the optical field at the top and bottom graphene layers is significantly stronger than that at the middle graphene layer. Similarly, as shown in Fig. 5.21(b), a RCP source with frequency of 11.5 THz excites unidirectional light propagation of topological mode along the negative x-axis of the domain-wall interface, corresponding to the

red band at the 11.5 THz dotted frequency line in Fig. 5.19(a). Because all three topological modes exhibit valley-chirality-locking property, the number of topological valley modes is equal to the valley Chern number $\Delta C_V = 3$. In addition, one of the topological valley modes is antisymmetric-layer-polarized, which is consistent with the layer Chern number $\Delta C_L = 1$.

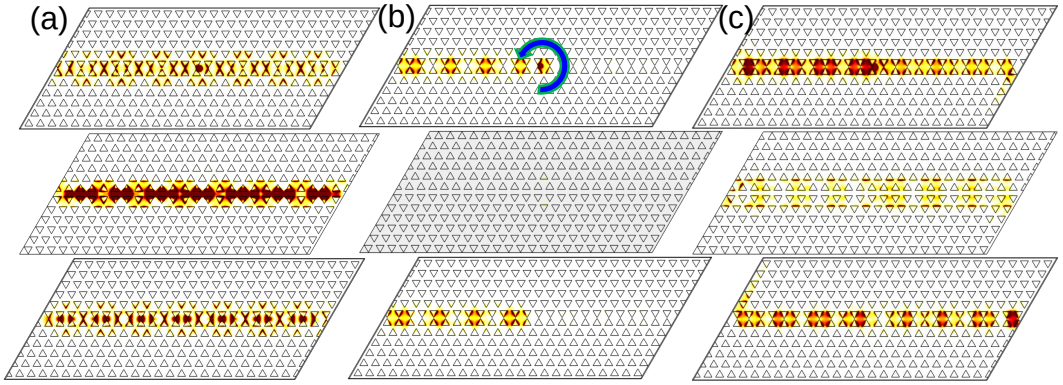

Figure 5.22: From left to right panels, light propagation in the finite three-layer graphene metasurfaces with triangular hole orientations $(30^\circ, -30^\circ, 30^\circ)$ and $(-30^\circ, 30^\circ, -30^\circ)$, determined for excitation frequency at 10.5 THz, 12.3 THz, and 13 THz of a RCP source placed at the top layer, respectively.

For the three-layer graphene metasurfaces of $\pm(30^\circ, -30^\circ, 30^\circ)$ triangular hole orientations with $\Delta C_L = 3$ and $\Delta C_V = 1$ across the domain-wall interface, the light propagation of topological modes determined for different frequencies is shown in Fig. 5.22. Since the eigenmode at the frequency of 10.5 THz corresponding to the red band in Fig. 5.20(a) exhibits middle-layer-polarized property, a RCP source is placed at the center of the middle graphene layer. It can be seen in Fig. 5.22(a) that, as expected, the light is markedly more confined along the domain interface at the middle layer rathen than at the other two layers. Differently, as presented in Fig. 5.22(b), a RCP light source with a frequency of 12.3 THz located at the top layer excites a topological mode that propagates along the negative x-axis of the domain interface, at the top and bottom graphene layers, which shows a good agreement with the antisymmetric eigenmode of blue band in Fig. 5.20(a). When the excitation frequency of the RCP source is increased to 13 THz, as indicated in Fig. 5.22(c), the excited propagating mode is mainly confined at the domain-wall interface of the top and bottom graphene layers. Additionally, a larger amount of

optical energy propagates along the negative direction of the x-axis as compared to the amount propagating along the opposite direction, which suggests a mixture of modes corresponding to blue (unidirectional and antisymmetric) and green (symmetric) bands at the 13 THz frequency line in Fig. 5.20(a). Hence, the number of layer-polarized topological modes is equal to the layer Chern number $\Delta C_L = 3$, of which one antisymmetric topological mode shows unidirectional propagation with the value of the valley Chern number $\Delta C_V = 1$.

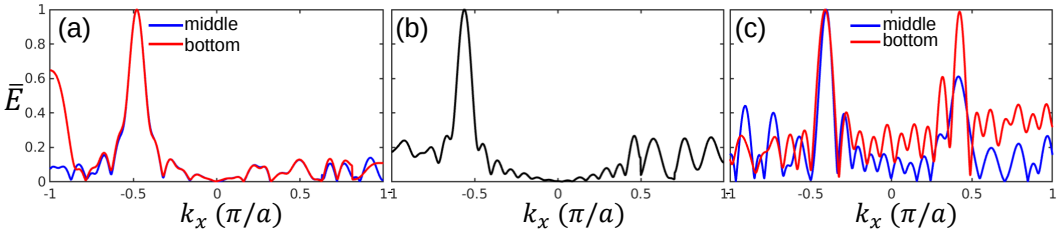

Figure 5.23: From leftmost to the rightmost panels, Fourier transform of normalized electric fields shown in Fig. 5.21(a), Fig. 5.21(b), and Fig. 5.22(c), respectively. The blue and red curves represent the normalized electric fields localized in middle and bottom graphene layers, respectively.

To properly distinguish the mixing of optical fields in Fig. 5.21(a), Fig. 5.21(b), and Fig. 5.22(c), the value of wave-vectors of the optical field propagating in different graphene layers can be extracted by Fourier transforming the field profiles $E(\boldsymbol{r})$ to the momentum space $\overline{E}(\boldsymbol{k})$, and the results are present in Fig. 5.23. The blue and red curves represent the light propagation confined in the middle and bottom graphene, respectively. As illustrated in Fig. 5.23(a) corresponding to the mixed light propagation in Fig. 5.22(a), the field spectrum at the middle graphene layer displays one peak around $k_x = -0.45\pi/a$ while there are two peaks around $k_x = -0.45\pi/a$ and $k_x = -0.9\pi/a$ for the field spectrum of the bottom graphene layer. This demonstrates that the peaks located at negative k_x wave-vectors correspond to backward-propagating modes. Specifically, two peaks of the bottom layer indicate the mixed mode between red and blue bands in Fig. 5.19(a) whereas one peak of the middle layer corresponds to the red band in Fig. 5.19(a), which has a good agreement with the layer-polarized antisymmetric topological mode depicted in blue. Similarly, for the field spectrum of the pure valley-chirality-locked

topological mode in Fig. 5.21(b), we show in Fig. 5.23(b) that the field spectra of all three graphene layers have only one peak around $k_x = -0.55\pi/a$, corresponding to the unidirectional propagation of topological mode T_1 in Fig. 5.19(a). Moreover, we present in Fig. 5.23(c) the Fourier field spectra of the mixed optical field in Fig. 5.22(c). The field spectrum of the middle graphene layer exhibits two peaks around $k_x = \pm 0.4\pi/a$, which corresponds to the optical field of layer-polarized symmetric mode T_6 in Fig. 5.20(a). However, there are three peaks around $k_x = \pm 0.4\pi/a$ and $k_x = 0.35\pi/a$ in the field spectrum of the bottom graphene layer, from which one can see that a new valley-chirality-locking optical field with unidirectional propagation (blue band in Fig. 5.20(a)) is mixed with the former layer-polarized symmetric mode T_6 in the bottom layer.

5.5 Conclusion

In this chapter, we presented the topological properties of layered graphene triangular nanohole metasurfaces with valley-chirality-locking and layer-polarized characteristics. Starting from a monolayer graphene metasurface, we proved that the specific orientations of triangular nanohole with respect to the hexagonal lattice could reduce the inversion symmetry and open a nontrivial bandgap with chirality-momentum-locking features. By introducing additional second and third layers, the new layer degree of freedom brings layer pseudospins into the bilayer and three-layer graphene systems, which can be achieved by rotating the triangular holes of each graphene layer to break the mirror symmetry of the bilayer and three-layer graphene metasurfaces. Based on the inversion symmetry breaking perturbation of monolayer system, a key thrust of the work presented in this chapter represents the derivation of an effective perturbation Hamiltonian by considering the nonzero interlayer coupling in bilayer and three-layer systems, whose predictions show a good agreement with COMSOL simulations.

Moreover, for the bilayer graphene metasurface, the layer Chern number and valley Chern number are defined as the difference and the sum of the pseudospin valley Chern numbers, respectively. Our computational results show a phase dia-

gram of layer and valley Chern number parameterized by rotation angles. For the three-layer graphene metasurface, in addition to the valley Chern number as a sum of Chern numbers ($C_V = C_0 + C_+ + C_-$) calculated using a specially defined basis of eigenmodes, the layer Chern number is defined as $C_L = C_0 - C_+ - C_-$. Specifically, two kinds of mirror-symmetric domain-wall interfaces with nonzero layer and valley Chern number differences are constructed and analyzed. The results of our numerical computations show that, as conjectured, the number of layer-polarized and valley-chirality-locking topological modes is equal to the layer Chern number and valley Chern number across the domain-wall interface, respectively.

Bibliography

[1] J. Lu, C. Qiu, W. Deng, X. Huang, F. Li, F. Zhang, S. Chen, and Z. Liu, "Valley Topological Phases in Bilayer Sonic Crystals," Phys. Rev. Lett. **120**, 116802 (2018).

[2] M. Gao, S. Wu, and J. Mei, "Acoustic topological devices based on emulating and multiplexing of pseudospin and valley indices," New J. Phys. **22**, 013016 (2020).

[3] X. Chen, X. He, and J. Dong, "All-dielectric layered photonic topological insulators," Laser Photonics Rev. **13**, 1900091 (2019).

[4] X. Wu, Z. Li, J. Chen, X. Li, J. Tian, Y. Huang, S. Wang, W. Lu, B. Hou, C. T. Chan, and W. Wen, "Interlayer topological transport and devices based on layer pseudospins in photonic Valley-Hall phases," Adv. Opt. Mater. **7**, 1900872 (2019).

[5] Z. Zhu, *et al.* "Acoustic valley Spin Chern insulators," Phys. Rev. Applied **16**, 014058 (2021).

[6] X. Xu, W. Yao, D. Xiao, and T. F. Heinz, "Spin and pseudospins in layered transition metal dichalcogenides," Nat. Phys. **10**, 343-350 (2014).

[7] X. T. He, E. T. Liang, J. J. Yuan, H. Y. Qiu, X. D. Chen, F. L. Zhao, and J. W. Dong, " A silicon-on-insulator slab for topological valley transport," Nat. Commun. **10**, 1-9 (2019).

[8] J. Lu, C. Qiu, L. Ye, X. Fan, M. Ke, F. Zhang, and Z. Liu, "Observation of topological valley transport of sound in sonic crystals," Nat. Phys. **13**, 369-374 (2017).

[9] J. Lu, C. Qiu, S. Xu, Y. Ye, M. Ke, and Z. Liu, "Dirac cones in two-dimensional artificial crystals for classical waves," Phys. Rev. B **89**, 134302 (2014).

[10] S. Wong, M. Saba, O. Hess, and S. S. Oh, "Gapless unidirectional photonic transport using all-dielectric kagome lattices," Phys. Rev. Res. **2**, 012011 (2020).

[11] X. D. Chen, F. L. Zhao, M. Chen, and J. W. Dong, "Valley-contrasting physics in all-dielectric photonic crystals: Orbital angular momentum and topological propagation," Phys. Rev. B **96**, 020202 (2017).

[12] O. Bleu, D. D. Solnyshkov, and G. Malpuech, "Quantum valley Hall effect and perfect valley filter based on photonic analogs of transitional metal dichalcogenides," Phys. Rev. B **95**, 235431 (2017).

[13] Z. Gao, Z. Yang, F. Gao, H. Xue, Y. Yang, J. Dong, and B. Zhang, "Valley surface-wave photonic crystal and its bulk/edge transport," Phys. Rev. B **96**, 201402 (2017).

[14] X. D. Chen, *et al.* "Tunable electromagnetic flow control in valley photonic crystal waveguides," Phys. Rev. App. **10**, 044002 (2018).

[15] H. Raza, *Graphene Nanoelectronics: metrology, synthesis, properties and applications* (Springer Science & Business Media, 2012).

[16] E. Prodan, "Robustness of the spin-Chern number," Phys. Rev. B **80**, 125327 (2009).

[17] Y. Yang, Z. Xu, L. Sheng, B. Wang, D. Y. Xing, and D. N. Sheng, "Time-reversal-symmetry-broken quantum spin Hall effect," Phys. Rev. Lett. **107**, 066602 (2011).

Chapter 6

Conclusions and future work

Photonic topological insulators are the extension of topological insulators from solid state physics into the area of optics, which is mostly studied on photonic crystals. As part of these developments in topological photonics, new phenomena and applications, such as unidirectional, topologically protected light propagation in which disorder-induced backscattering is suppressed, have been successfully demonstrated. By introducing the time-reversal and spatial-inversion symmetry breaking into the periodic photonic system, the symmetry-protected Dirac cone will be gapped out which generates a nontrivial frequency bandgap. When the domain-wall interface is properly designed with nonzero Chern number difference, the topologically protected edge mode can emerge inside the nontrivial bandgap and the corresponding light propagation is localized at the domain-wall interface. Moreover, nonlinear topological photonics has been attracting increasing research interest, as it provides an exciting photonic platform that combines the advantages of active all-optical control offered by nonlinear optics with the unique features of topological photonic systems, such as different spatial profiles among topologically protected edge modes, trivial edge modes, and bulk modes. Specifically, photonic topological insulators under spatial-inversion symmetry have been being less explored in 2D photonic platforms, including graphene. Taking advantage of key factors of graphene metasurfaces, such as tunable chemical potential, long intrinsic relaxation times, large near-field enhancement of plasmons, and large third-order susceptibility, the graphene-based topological photonic system shows great poten-

tial in the development of active and robust integrated photonic nanodevices with high frequency, low loss and ultralow optical power.

This dissertation proposed the topological valley plasmon transport on graphene nanohole metasurfaces, and achieved the need for computational design of active optically and chemically controllable nanodevices, respectively. I developed three configurations of graphene metasurfaces possessing valley topological plasmonic modes inside a nontrivial frequency bandgap: i) a single graphene nanohole metasurface with spatial-inversion symmetry reduction by introducing extra nanoholes (chapter 3), ii) bilayer graphene metasurfaces with mirror symmetry breaking via a horizontal shift (chapter 6) and iii) layered graphene triangular nanohole metasurfaces (chapter 8) with inversion symmetry reduction and mirror symmetry breaking by rotating triangular holes. In particular, a domain-wall interface is constructed by placing together two graphene metasurfaces with opposite valley Chern numbers, and topologically protected valley modes propagate along the domain-wall interface with unidirectional features.

Taking advantage of the strong Kerr effect and tunable chemical potential of graphene, I developed an active all-optical switch in chapter 4 and an efficient approach of coupling topological and trivial edge modes in chapter 5, by optically tuning the frequency bandgap of a monolayer graphene nanohole metasurface via optical Kerr effect. Moreover, a molecular gas sensor based on the fact that the Fermi energy of graphene varies upon chemical doping is investigated on bilayer graphene metasurfaces in chapter 7. The presented theoretical results and designs may not only provide deeper insights into topological valley photonic systems with spatial-inversion or mirror-symmetry breaking, but also lead to active photonic nanodevices implemented in integrated and robust graphene-based topological systems.

My original contributions to the field of the graphene-based topological photonic systems will be summarized in the next section and the future perspectives in the area of topological photonics will be described in Sec. 6.2.

6.1 Contributions

There are two main contributions of this thesis in the development of topological photonics in two-dimensional photonic platforms, including graphene. First, our theoretical and computational works develop various graphene-based topological photonic systems with a new layer degree of freedom, in which the spatial-inversion symmetry and novel mirror symmetry breaking can be achieved. In particular, monolayer, bilayer, and three-layer graphene nanohole plasmonic waveguides have been proposed, and possess plasmonic topological valley-chirality-locked interface modes with unidirectional characteristics. In addition, the layer-polarized topological modes is observed at the domain-wall interface of layered graphene metasurfaces with the nonzero layer Chern number. Second, our work can facilitate and spur the development of new or improved active graphene-based photonic devices that combine the unidirectional feature in topological photonics with tunable advantages, whose functionality can be provided by nonlinear optics or chemical potential of graphene. Specifically, I have studied the influence of Kerr effect in a monolayer graphene topological photonic system, which can tune the refractive index of graphene via an extended pump beam. Since the variation of refractive index can result in a frequency shift of bandgap, an active all-optical switch and an effective nonlinear mode coupler can be implemented in this monolayer topologically-protected graphene nanohole metasurface. Furthermore, I have designed a graphene-based molecular gas sensor based on the fact that the chemical potential of graphene can be tuned *via* gas molecule adsorption. This effect induces a strong variation of the transmission of the topological interface modes, which is employed as the underlying working principle of gas sensing devices.

To be more specific, several valuable and remarkable findings can be summarized in this thesis, which may contribute to the development of graphene-based topological photonics and its applications:

- **Graphene-based topological valley photonic system** Topological valley-Hall photonic modes have been mostly studied in bulk materials, such as photonic crystals, being less explored in graphene. This 2D material is becoming

a promising platform to achieve passive and active topologically protected plasmonic modes at an extremely deep subwavelength scale, due to its high carrier mobility, long relaxation time, and low loss at the Terahertz range.

- **Novel mirror symmetry breaking** By introducing the additional layer with a new layer degree of freedom, I studied the mirror symmetry breaking of bilayer graphene nanohole plasmonic waveguides. Valley topological plasmonic modes are realized on a bilayer graphene metasurface by horizontally shifting in opposite directions the lattice of holes of the top layer with respect to the bottom layer. In addition to the chirality-momentum-locked topological mode, the bilayer and three-layer graphene metasurfaces with specific orientations of triangular holes exhibit nontrivial bandgaps, in which topological valley modes emerge with layer-polarized properties.

- **Effective Hamiltonian of three-layer graphene metasufaces** Starting from the effective perturbed Hamiltonian of monolayer graphene triangular nanohole crystal, I derived an effective Hamiltonian of three-layer graphene triangular nanohole metasurfaces by considering the interlayer coupling between two adjacent layers and another interlayer coupling term between the top and bottom layers, which is well-fitted by the results of COMSOL simulation.

- **Valley Chern number calculation** Based on the Wilson-loop approach, the valley Chern number has been calculated over the K valley by the eigenfields obtained from Hamiltonian and COMSOL simulations, respectively. Our computational results prove that the absolute value of valley Chern number depends on the perturbation applied to the system and a 0.5 value of valley Chern number can be achieved only for infinitesimal perturbations at K point.

- **Layer and valley Chern number** To distinguish layer-polarized and valley-chirality-locked topological modes, the layer Chern number and valley Chern number have been defined in the bilayer and three-layer graphene triangular hole metasurfaces.

- **Combination of topological photonics and nonlinear optics** The unique properties of graphene-based topological systems, in conjunction with strong nonlinear optical interactions occurring in graphene, can be employed to develop nonlinear photonic devices and systems, which can be used to optically control topologically-protected defect-immune light propagation at the nanoscale. In particular, an all-optical switch has been achieved in graphene metasurfaces under various optical pump powers, due to large optical near-field enhancement and extended life-time of plasmons in graphene metasurfaces with strong Kerr nonlinearity. .

- **Efficient coupler for transferring light to topological modes** With the aim of developing efficient excitation techniques that would allow one to couple optical power from external sources to topological modes of photonic structures, I design and theoretically analyze an effective coupling between trivial edge mode and an interface topological mode of a monolayer graphene metasurface, which can be tuned through Kerr effect induced by a pump beam injected by a bulk mode. This functionality is achieved by the variation of the power-dependent refractive index leading to a change of phase-mismatch between topological and trivial edge modes.

- **Slow light regime** By choosing a bulk mode in the slow-light (SL) regime as a pump beam to induce the Kerr effect in the graphene topological systems, I proved that the required pump power can be significantly reduced if the device is operated in the SL regime, which is particularly effective for increasing the efficiency of nonlinear wave interactions.

6.2 Future Perspectives

The novel and unique properties of topological photonics, such as unidirectional, defect-immune, and scattering-free propagation of light, have a great potential to contribute to the development of robust on-chip ultracompact nanophotonic devices. Key factors, such as large, tunable carrier densities and long intrinsic relaxation times up to the picosecond range, make graphene an ideal platform for topological

plasmonics at high frequency, low loss, and large topological bandgaps. My theoretical and computational study of the topological valley transport on graphene metasurfaces, proposed various graphene-based topological photonic systems, which are further applied to optically- or chemically- controllable nanodevices. In addition, there are two future perspectives for my research work that can be developed. One is to thoroughly explore the change of Chern number of layered graphene metasurfaces when the orientations of triangular holes are totally opposite, another is to develop active topological photonic devices relying on nonlinear processes.

Since the topological modes with valley-chirality-locked features can only be achieved inside a mirror-symmetric domain-wall interface, it is significant to explore the Chern number difference between two graphene systems with opposite rotation angles of triangular holes, namely in a mirror-symmetric manner. Hence, if an analytic relation between Chern numbers of opposite rotation angles can be derived, it will reduce 50% computation time. Specifically, the opposite sign of rotation angles directly influences the effective Hamiltonian, which results in the change of eigenvectors with the same eigenfrequencies. In this way, the valley Chern numbers calculated using the eigenvectors or a specially defined basis may change their signs with opposite triangular hole orientations.

The most important potential extension of topological photonics focuses on the investigation of the nonlinear optical response of such photonic systems. Key functionalities of active photonic devices, such as tunability, optical frequency generation, and sensing, can most effectively be implemented by employing the nonlinear optical response of the underlying materials. To this end, active topological photonic devices relying on nonlinear optical effects, including Kerr effect, second-harmonic generation (SHG), third-harmonic generation (THG), and four-wave mixing (FWM), may possess new or improved functionality. Since the significant nonlinearity enhancement of graphene makes it promising to achieve strong nonlinear interaction in topological photonic systems, frequency-mixing processes between phase-matched topological edge modes, such as FWM and THG, can be further studied in graphene-based topological plasmonic metasurfaces.